TUNABLE SYNTHESIS AND CHARACTERIZATION OF PHYTOCONJUGATED NANOPARTICLES FOR WATER REMEDIATION

Thesis submitted to the University of Calicut
in partial fulfillment of the requirement
for the award of

DOCTOR OF PHILOSOPHY IN
CHEMISTRY

By
JULIA GARVASIS

DEPARTMENT OF CHEMISTRY
UNIVERSITY OF CALICUT
KERALA, INDIA
DECEMBER
2022

Dr. Abraham Joseph
Sr. Professor
Department of Chemistry
University of Calicut

CERTIFICATE

This is to certify that the thesis entitled "Tunable synthesis and characterization of phytoconjugated nanoparticles for water remediation" submitted to the University of Calicut, for the award of the degree of Doctor of Philosophy in Chemistry by Ms. Julia Garvasis, embodies the results of the original research work carried out by her under my supervision and guidance in the Department of Chemistry, University of Calicut, and the thesis has not previously formed the basis for the award of any degrees, diploma, associateship or other similar title or recognition. The contents of this thesis have been checked for plagiarism using the software 'Ouriginal' and the similarity index falls under permissible limit. The corrections recommended by the adjudicators have been incorporated in the thesis and the contents in the thesis and the softcopy are one and the same.

University of Calicut

Dr. Abraham Joseph
Research Supervisor

DECLARATION

I hereby declare that the work presented in this thesis entitled "Tunable synthesis and characterization of phytoconjugated nanoparticles for water remediation" submitted to the University of Calicut, as partial fulfillment of Ph.D. program for the award of degree of Doctor of Philosophy in Chemistry is original and carried out by me under the supervision of Dr. Abraham Joseph, Sr. Professor, Department of Chemistry, University of Calicut. This has not been submitted earlier either in part or full to any university or institution for the award of any degree or diploma.

University of Calicut

Julia Garvasis

ACKNOWLEDGMENT

Doctoral study at the University of Calicut has been one of the most exciting and challenging chapters of my life and many people have supported me in this memorable journey. I would like to express my deepest gratitude to my supervisor, Prof. Abraham Joseph, for accepting me to be a part of his group and for supporting me through the difficulties of doctoral research. All the success and experiences that I gained during my time as a doctoral student are largely due to his unwavering patience and guidance. I am also grateful that he gave me free rein to decide the course of my research, allowing me to develop the necessary initiative and skills as an independent scientist.

I am extremely grateful to Dr. A. I. Yahya, Head of the Department, Chemistry, University of Calicut and former HoDs for providing the essential laboratory facilities during my doctoral program. Sincere thanks to Prof. P. Raveendran, Prof. N. K. Renuka, Prof. M. T. Ramesan and all other faculties of the department for their timely suggestions and encouragement.

I express my deepest gratitude to the Council of Scientific & Industrial Research (CSIR), HRDG, Govt. of India for the Senior Research Fellowship, without which this journey would have been more challenging.

I am indebted to my former mentor, Mr. Aravind K., who cultured the art of asking the right questions in me. I sincerely thank all my former teachers; from the scariest maths teacher to the sweetest malayalam teacher, for the invaluable time and experiences they have shared with me.

I acknowledge the support and critical suggestions (and the occasional coffee) provided by my group members. It would be ungrateful of me to not mention the immense support of Dr. K. K. Anupama., Dr. Anupama R. Prasad, Dr. Sabeel M. Basheer and Dr. Shamsheera K. O., throughout my doctoral program. I am very thankful to Mr. Deepak Joshy, Ms. Anjitha T., Dr. Jijil C. P., and all other research scholars for their valuable assistance in the laboratory. Sincere thanks to all the non-teaching staffs of the department.

I am thankful to Prof. Santhosh Nampy, Prof. A. K. Pradeep, Prof. K. K. Elyas, Dr. Ajayan K. V., Ms. Reshmi. S., Dr. Hareesh E. S., and Mr. Vishnu Mohan of the University of Calicut for providing valuable technical assistance during the period of study.

I acknowledge the analytical services provided by the Central Sophisticated Instrument Facility (CSIF) of the University of Calicut, The Indian Nanoelectronics Users Program (INUP) of IISc, Bangalore, Sophisticated Analytical Instrument Facility (SAIF), IIT Madras, Sophisticated Test and Instrumentation Centre (STIC), CUSAT, Kochi, Athmic Biotech Solutions-Trivandrum, PSG Infotech, Coimbatore and Central Instrumentation Facility (CIF), IISER Trivandrum. I duly acknowledge the technical support from the DST-FIST Facility and KSCSTE Facility at CCS, Department of Chemistry, University of Calicut.

I admire the patience and effort taken by my husband Mr. Nidheesh Roy T. A., to design and illustrate the layouts for my research work and to design a beautiful thesis cover page (plus, to learn cooking). Without your honest suggestions and support, this thesis would not have taken this form. I appreciate the support of my parents and siblings which kept me sane through the last few years.

Layla, I am eagerly waiting for the day you will read this thesis and be proud of your mother.

“This thesis has surpassed two major floods, a deadly
epidemic, and a pandemic. I am honestly grateful
to the *entity* that kept me alive”

- Dedicated to the unconditional love and memory of Bailey -

CONTENTS

CHAPTER 4:

CHAPTER 5:

CHAPTER 6:

List of publications and presentations

Preface

The boom in anthropogenic activities and improper handling of resources have caused an alarming hike of heavy metal ions in the ecosystem. Chromium exists in its trivalent and hexavalent state in nature. Cr(III) is considered an essential human dietary element whereas Cr(VI) is highly toxic and acts as carcinogens, mutagens, and teratogens in biological systems. It is well established that the toxicity of Cr(VI), is higher than that of Cr(III), due to the increased solubility of Cr(VI) species compared to Cr(III), and easy absorption and accumulation in kidneys, stomach, and liver. Extensive use of hexavalent chromium in various industries including electroplating, leather tanning, metal fabrication, and finishing has exacerbated Cr(VI) contamination in water bodies. Existing literature indicates the presence of unacceptable quantities of Cr(VI) in drinking water, soil and plants which demands immediate and effective remediation strategies. The hazards caused by another inorganic toxin, Pb(II) are more extensive than any other pollutant out there. Though the use of leaded petrol has been restricted in many countries, the metal is still found in several other products including paint, plumbing pipes, ceramics, pottery glaze, cosmetics, and batteries. Lead is used in food adulteration and traditional medicines. It’s a highly poisonous, cumulative contaminant that persists at the disposal site as a source of exposure for long periods. Even the lowest measurable blood lead levels can compromise the reproductive, neurological, and cardiovascular systems of an adult. Chronic and high lead exposure can cause hematological effects and neurological disturbances, lethargy, muscle weakness, ataxia, tremors, and paralysis, and even death. Compared to adults, children are more vulnerable to the irreversible adversities of lead exposure. Neurological disorders, retarded growth, and juvenile delinquency are closely associated with infantile lead exposure. Lead is a recyclable metal therefore the establishment of safe and efficient recycling infrastructures can help in regulating the lead levels in water and soil. Another important pollutant are dyes used in textile sector. Industry has polluted the planet extensively that rarely any component of the ecosystem remains untouched. The dyeing industry is accountable for polluting many rivers, turning them black, pushing some to the brink of death. While color is a catalyst within the fashion industry, it is a huge contributor to water consumption and pollution.

Although adsorption is widely used to remove toxic metal ions from water, fabrication of promising adsorbent systems is very challenging due to multiphase synthesis routes and the expensive chemicals involved. Another demerit of the adsorption process is the laborious separation of the exhausted adsorbent at the end of the process. Usually, multiple centrifugations or filtration steps are performed to separate the analyte free of the loaded adsorbent. In this regard, iron oxide NPs (IONPs) are highly exploited for their magnetic properties which provide fast separation and easy recycling. IONPs represent one of the most important classes of inorganic materials. They are nontoxic, biodegradable, biocompatible, and efficiently cleared from the human body through iron metabolism pathways. However pure IONPs are prone to agglomeration which decelerates their absorption capacity. Possibilities of using biogenic resources for the removal of heavy metals has recently gained global attention. Phytogenic synthesis of IONPs provides a sustainable and facile one pot alternative for the fabrication of surface modified IONPs. Plant extract-mediated synthesis of IONPs offers strategic synthesis of different iron oxide nanoparticles such as goethite, hematite, maghemite and magnetite. Magnetite nanoparticles are frequently opted for water remediation over other IONPs owing to their low toxicity, ease of functionalization and easy separation ability. There are substantial reports on the use of crude phytoextracts for the synthesis of iron oxide nanoparticles. The plant metabolites (polyphenols, amino acids, polysaccharides, alkaloids, etc.) present in these phytoextracts act as effective reducing and capping agents. The incorporation of organic functional groups onto the phytogenic nanoparticle surface makes it a potential candidate for the recovery of aqueous heavy metal ions.

Alum is the most commonly and frequently used coagulant for water treatment. The use of inorganic coagulants is now revised due to the high dosage, voluminous sludge produced post flocculation, inconsistent performance with pH, and temperature. Intensive studies to find suitable replacements are in trend. An optimal coagulant must be efficient at lower dosages with minimal sludge production and reusability. Although certain biomass is extensively used as natural coagulants release of secondary metabolites and fouling prevents them from commercial scaling up.

The thesis is an interpretation of a question or subject and not the subject itself. This thesis explores the possibility of adapting weed extracts as effective and versatile phytoreagents for metal oxide nanoparticle synthesis. This work demonstrates the potential of strategic management of phytogenic synthesis processes to generate pure NPs of different phases with significant water remediation abilities.

Chapter 1 presents a very brief overview of the background of the study, different aspects of green synthesis, the scope of green alternatives etc. The chapter proceeds through a review of literature relevant to the topic of study. Chapter 1 winds up with a glimpse of the total work presented in this thesis. The details of the materials used, collected plants instrumental techniques and analytical procedures involved in the study are explained in **Chapter 2**.

Chapter 3 explains the steps involved in procuring superparamagnetic phytogenic magnetite NPs(PMNPs) from *Chromolaena odorata* flower extract via ultrasonic-assisted hydrothermal reaction and their characterization using field emission scanning electron microscopy (FESEM), high-resolution transmission electron microscopy (HRTEM), X-Ray diffraction (XRD) patterns, selected area diffraction patterns (SAED), Fourier transform infrared (FTIR) spectra, energy dispersive X-ray spectroscopy (EDX), X-ray photoelectron spectroscopy (XPS), vibrating sample magnetometer(VSM) and zeta potential analysis. The chapter analyses the performance of the PMNPs in removing Cr(VI) and Pb(II) from the aquatic environment. The details of the batch adsorption studies are summarized here to evaluate the efficiency of the proposed HMI-adsorbent. The *C. odorata* derived NPs; CMN-8 removed 49.6 mg g^{-1} of Cr(VI) from an initial concentration of 100mg L^{-1} in under 10 minutes at pH~2. At the inherent pH of the simulated Pb(II) effluent CMN-8 removed 66.43 mg g^{-1} Pb(II) in under 10 minutes. Coexisting ions did not alter the efficiency of the adsorbents considerably and the exhausted adsorbents were recovered and used up to 5 consecutive cycles without deterioration in adsorption capacity. The morphological, compositional, and magnetic changes of the exhausted adsorbents are also described to provide a better understanding of the removal mechanism.

Chapter 4 explores the possibility of reproducibility of the method adopted in the previous chapter by employing another vicious weed, *Sphageneticola trilobata* leaf extracts to procure magnetite NPs (SMNs). The chapter outlines the adopted changes in the method to obtain PMNPs with similar efficiencies and the characterization results. There was an increase in the duration of the hydrothermal reaction period (12 hr) owing to the low TPC and TFC in the extract. The product was characterized using assorted instrumental techniques and the formation of the magnetite phase was confirmed. The adsorptive capacity of the PMNPs was evaluated using standard analytical procedures. It was observed that SMN-12 facilitated complete reduction of Cr(VI) and a partial reduction of Pb(II). A probable mechanism for the reduction of HMIs with respect to the increased phytoconjugate content on the surface is described in this chapter.

Chapter 5 presents side-to-side viewpoints on the tunable synthesis of IONPs using the phytoreagents prepared in chapter 3&4. It discusses the preparation of hematite, maghemite and magnetite NPs by controlling the pH of the reactant system. Effects of various reaction constraints like reaction time and neutralizing agent are mentioned here. The studies revealed a promising combination of strong pigmentation along with mild antioxidant abilities of the NPs. The chapter then extends to the formulation of different lifestyle products using the phytogenic pigments. The in-vitro cytotoxicity analysis of the phytogenic iron oxide nanopigments revealed the nontoxic nature of the nanopigments and proved that these products can be safely used for cosmetic applications. It was noted that the pigments were of no harm to the skin microflora even at higher concentrations.

Chapter 6 discusses the formation of Aluminum sulfate NPs (AS-6) and γ-alumina NPs (AS-10) using *Hemigraphis alternata* leaf extract with minimal use of corrosive solvents. The material was characterized by FTIR, XRD, TGA, FESEM, EDX, HR-TEM and zeta potential analysis. We were able to suggest a probable mechanism for the formation of AS-6 from the phytoextract. AS-6 displayed superior coagulation ability compared to the adsorption capacity of AS-10 towards congo red and fluoride. Coagulation efficiency of AS-6 for congo red dye and fluoride solution was explored under various constraints like coagulant dosage, initial concentration, pH, temperature, presence of inorganic ions and settling time. 140mgL^{-1} of AS-6 removed 99.5% of congo red dye (100 mgL^{-1}) and 2.5mgL^{-1} of AS-6 removed 99.8% of 10mgL^{-1} of fluoride solution. The variation in pH of the solution in the range 3–9 and the increase in temperature from 30 to 70°C did not affect the efficiency of the nanocoagulant. The AS-6 also displayed high coagulation efficiency and rapid settling ability. The sludge produced is less and thermally decomposable. The coagulant can be reused for up to five cycles with negligible compromise in efficiency. Thus, phytogenic AS-6 is a promising candidate for the removal of congo red and fluoride in terms of cost efficiency, low dose, high coagulation efficiency, sludge management, and shelf life. The novel synthesis route adapted in the chapter lights up the sparsely investigated area of phytogenic synthesis of $Al_2(SO4)_3/Al_2O_3$ NPs, its possibilities, and challenges.

The thesis ends with future perspectives on possible diverse applications and modifications of the procured materials.

CHAPTER 1

INTRODUCTION

> Water is life's matter and matrix, mother and medium.
> There is no life without water.
>
> \- Albert Szent-Gyorgyi

The scarcity of safe drinking water has started rising concerns across global borders. The fact that out of the total amount of water present on earth, only 0.5% is available for all living beings to survive is scary enough to prompt us to begin remediation measures. Green adsorbents, coagulants and safe pigments provides an alternative strategy to produce efficient materials for the same. Use of weeds for phytogenic synthesis of nanoparticles is a comparatively novel, potential area of research.

The rising needs fuelled by the increasing population has made the development of science and technology marginally unsustainable. Cultivation of exotic species, inefficient management of resources, poor recycling strategies, poor waste management and lack of evidence-based knowledge in several sectors have severely compromised the quality of life. The burst of invasive weeds controlling and gradually eliminating the native biodiversity and triggering global ecological disturbances has attracted research interest lately. The menace of water pollution has established an irreversible nature alongside. Water quality is one of the major challenges that mankind will face soon, threatening human welfare, altering the ecological balance, and hindering economic advancements. Water quality degradation translates directly into severe environmental, social, and economic consequences in turn demanding urgent attention and awareness from the global community.

1.1 Alien invasive species - an emerging threat.

India is bestowed with a wide range of climatic condition, landscapes, and soil types; the agriculture and farming systems are adapted accordingly. The diversity is extended to the weed abundance too. Most weeds now challenging the native biodiversity are exotic in nature and were introduced for ornamental/commercial purposes or accidently through foreign trade. Weeds compete with crops for moisture, nutrients, light and space thus depriving the crops their vital requirements. Weeds cause huge crop yield loss besides quality impairment of the produce, disturbances in ecoservices, and health hazards[1]. Invasive weeds are a great threat to the eco diversity and is a major constraint that limit crop production. Moreover, allelopathic weeds inhibits the growth of plants native to the land threatening the existence of several ethnic, valuable plant species. Their aggressive growth rates aid them in thriving in ecological hot spots causing disturbances in global plant diversity[2]. Despite the presence of several national and international regulations and mandates to prevent and control the spread of alien invasive species (AIS), the records are profusely increasing, owing to factors such as soil disturbances, climate change, and an increasing diversity, frequency, and intensity of anthropogenic vectors globally. AIS numbers are burgeoning across the globe, with the number of established alien species expected to increase by 36% in the next three decades[3,4]. The International Union for the Conservation of Nature's (IUCN's) Invasive Species Specialist Group has shown that of the world's100 most invasive species, 36 are plant species, and these invasive plant species may seriously affect biodiversity worldwide[5]. Though the accurate scale of the socio-economic costs associated with AIS is unknown, it is estimated that the direct impacts of AIS and their management cost the global economy billions of US$ annually[6]. Under ineffective control measures AIS can suffocate our land and economy drastically.

Despite the surge in science and technology, weed management in India still involves considerable human labour. Manual weeding, cultural measures, chemical and biological control measures are the main control methods adopted to regulate weeds[7]. However, these measures are expensive, temporary and unsustainable. Therefore, development of economical and effective weed management strategies is of prime importance at this hour. Among other strategies adapted to prevent and reduce the spread of AIS, the exploitation of weed raw materials economically is a viable, yet not exhaustively explored one[8]. The present work investigates the possibilities of using three obnoxious weeds to fabricate functional nanomaterials for environmental applications.

1.2 The right to safe drinking water.

The United Nations General Assembly in 2010 recognized “the access to safe and clean drinking water and sanitation as a human right" essential for our lives and well-being[9]. Out of all the available water, only 2.5% is freshwater, with 98.8% being stored in ice and groundwater[10]. Water scarcity is a major global concern and the number of people who do not have access to safe drinking water is increasing every day. The disposal of large quantities of poorly treated, or untreated, industrial effluents into aquatic systems worsens the water pollution menace[11-14]. Furthermore, newly emerging pollutants from personal care products, pharmaceuticals, pesticides, industrial and household chemicals, represent a new, complex water quality challenge, with still unknown long-term impacts on human health and ecosystems[15].

Insufficiently treated/ recycled or untreated industrial effluents is the major reason behind the rising levels of heavy metal ions (HMIs) in waterbodies across the globe. Metal processing and mining are other major contributors to HMI pollution. Approximately 40% of the global aquatic systems has been polluted by HMIs[14,16]. Non-essential heavy metals are toxic to living organisms, as are the essential ones at high concentrations. They trigger muscular, physical and neurological degenerative processes. Whereas long exposure lead to muscular dystrophy, Alzheimer's disease, different types of cancer and multiple sclerosis. Damaged or decreased central nervous and mental activities, damage to the lungs, liver, kidneys, blood compositions, are also closely associated with heavy metal exposure[17-20]. Cadmium, arsenic, chromium, mercury, and lead are among heavy metals commonly found in industrial effluents. The permissible levels of different HMIs, their anthropogenic sources and health hazards are given in Table 1[21,22].

Textile industry has a crucial role in the growth of human civilization, it adds color and texture to the mundane life events. However, the industry has polluted the planet extensively that rarely any component of the ecosystem remains untouched. The dyeing industry is accountable for polluting many rivers, turning them black, pushing some to the brink of death[23-26]. While color is a catalyst within the fashion industry, it is a huge contributor to water consumption and pollution. For example, producing a single pair of jeans consumes ~7500 liters from growing raw cotton to finished product[27,28]. The industry highlights a new trend/color every year which adds new pigments, catalysts, and other associated chemicals to the effluent. Textile industry pollution is alarmingly rising in Asian countries, as they are the hub of garment industries due to availability of cheap labor.

Table 1. HMIs, source and effect on human health

Heavy metal	Anthropogenic source	Allotted level in water ($\mu g\ L^{-1}$)	Adverse effect on health
Lead (Pb)	Metal purifying, pesticides, vehicular emissions, coal, fertilizers, gasoline	10	Neurotic and kidney disorders, mental retardation, cancer
Cadmium (Cd)	Electroplating and metallurgic industry, petroleum products, insecticides, synthetic chemicals	3	Hepatic toxicity, lung cancer, respiratory disorders, and reproductive organ damage
Mercury (Hg)	Fossil fuel combustion, electronics and plastic industries, paper and pulp industry	6	Damages to brain, liver, kidney, reproductive and respiratory systems
Chromium (Cr)	Leather tanning, textile and electroplating industries, industrial sewage, and anticorrosive products	50	Skin inflammation, liver and kidney damage, pulmonary congestion, vomiting and ulcer

Arsenic (As)	Electronics production, pesticides, livestock manures, composts, sewage and sludge, fly ash, irrigation with municipal & industrial wastewater	10	Skin damage, circulatory system, issues, increases the risk of getting cancer
Copper (Cu)	Mining industries, metallurgy and chemical manufacturing, steel industries, electroplating industries, fertilizers and pesticides	2000	Hair loss, anaemia, kidney damage and headache
Nickel (Ni)	Metal alloys, battery plants. Electroplating industries, pulp and paper mills, fertilizers, petroleum refineries	70	Dry cough, chest pain, breathing issues, nausea, skin eruption, pulmonary fibrosis, gastrointestinal ache, diarrhoea, renal edema

The discharge is often a mix of carcinogenic chemicals, dyes, salts and heavy metals that not only harm the environment but pollute essential drinking water sources. Due to poor monitoring and weak law enforcement, most of the effluents are disposed directly into water streams where it enters the food chain. Most synthetic dyes used in the textile industry contain azo functions often linked to an aromatic ring which makes them highly toxic, non-biodegradable, carcinogenic, and mutagenic for human and aquatic life[24,29-31]. Also, under specific conditions, azo dyes can be decomposed to produce more than 20 kinds of carcinogenic aromatic amines[29,32-34]. Though several countries have banned these dyes they are still used for their bright colours and colour fastness. Another sector that widely consumes and pollutes water is the lifestyle/cosmetic industry[35]. Hygiene products and cosmetics contain harmful chemicals including UV filters, plasticizers, pigments and microplastics. The critical concern regarding these chemicals is that they don't simply wash away down the drain and get disappeared. Cosmetics pose more ecological concerns compared to pharmaceuticals because they are used in much larger quantities and throughout the course of life and, being intended for external application, are not subjected to metabolic transformation; therefore, they end up in the environment unaltered in large amounts. Another unfortunate factor causing severe troubles is the inability of sewage treatment plants to effectively treat the cosmetic-wash off[36-40]. Long-lasting, highly stained vibrant pigments pose both environmental and health hazards. Synthetic organic pigments are preferred in the cosmetic industry for vivid and bright hues they produce. Many FD&C approved dyes are toxic and are legally allowed to contain low levels of lead and other heavy metals[41]. There are several reports on the presence of lead in lip cosmetics[42,43]. Over time, these heavy metals build up in the body and pollute the environment. Upon long run they cause health issues including cancer, allergies, reproductive and developmental disorders, neurological problems, memory loss, mood swings, muscle disorders, kidney and renal problems, lung damage, hair loss, nausea, and headaches[44].

There is an urgent global need for sustained investment to improve wastewater management. Effective wastewater treatment strategies are crucial for the future of water security. Along with stringent regulations, awareness regarding slow fashion, domestic waste management and safe use of chemicals (bleach, hair dyes, herbicides, pesticides etc.) should be provided to the consumers.

1.3 The green alternatives

From facial wipes to vaccine delivery systems nanotechnology has proved its efficacy in improving the quality of human life. Nanomaterials, when carefully curated, can offer inexpensive and efficient treatment of wastewater to drinking water. Several conventional techniques are adopted for the removal of heavy metals and other dyestuff from water. It includes chemical precipitation, coagulation-flocculation, ion exchange, adsorption, membrane filtration and electrochemical methods[45-48]. Usually, the most effective technique should be economical, efficient, produce low sludge, should work over a large range of concentrations and be recyclable[49]. However, the method adopted varies relatively with the nature of the involved industries. For instance, metallurgical industries require recovery of the certain metal ions which demands use of selective tools and techniques.

1.3.1 Green adsorbents

The versatility, efficiency and low cost of the adsorption process have attracted interest for the adsorption process and hundreds of new adsorbents and natural materials have been researched for their heavy metal removal capabilities. The types of nano-adsorbents used for heavy metals include carbon-based adsorbents, mesoporous silica-based adsorbents and aerogels, polymeric materials, metal oxides NPs and composite materials to name a few[50-56]. Metallic and metal oxide have been thoroughly researched for HMI removal properties owing to their superior performance compared to the traditional alternatives (like clay, silica, etc.)[57-59]. One of the rigorously studied metal oxide NPs is iron oxide nanoparticles (IONPs)[60-65].

Due to their abundance, high surface reactivities, and affinity for ions, iron (hydro)oxides are excellent sinks for various nutrients as well as environmental contaminants[66]. There are six non-hydrated crystalline iron oxide phases identified so far, they are frequently classified according to the valence state of iron in their crystal structure. FeO (wüstite) has only Fe^{2+} ions in its cubic crystal structure and is thermodynamically unstable and paramagnetic at room temperature. Fe_2O_3, or ferric oxide, contains only Fe^{3+} ions and displays polymorphism. Four widely studied Fe_2O_3 polymorphs are (i) α-Fe_2O_3, hematite, with a rhombohedral-centered hexagonal crystal structure (ii) β- Fe_2O_3 with a cubic-body-centered crystal structure of a bixbyite type (iii) γ- Fe_2O_3, maghemite, with a cubic crystal structure of inverse spinel type and (iv) ε- Fe_2O_3 with an orthorhombic crystal structure. The last non-hydrated iron oxide phase, Fe_3O_4, magnetite, has both Fe^{2+} and Fe^{3+} ions distributed over a cubic inverse spinel crystal structure. However, only Fe_3O_4 and γ-Fe_2O_3 are commonly preferred due to their superior magnetic properties for technological, environmental, and biological applications. They are both strong ferrimagnetic materials with two magnetic sublattices mirroring tetrahedral (T_d) and octahedral (O_h) sites, the two non-equivalent cation positions in their crystal lattice. In stoichiometric Fe_3O_4, Fe^{3+} ions are distributed over all (T_d) sites and half the O_h sites whereas Fe^{2+} ions occupy the remaining O_h sites leaving no vacant places. On the other hand, in stoichiometric γ-Fe_2O_3, Fe^{3+} ions are located at all the T_d sites and 5/3rd of O_h sites; the remaining 1/3rd of O_h sites are left vacant[67]. Hematite is widely used as a pigment due to its red color from ancient times. The possible crystal structures of hematite, maghemite and magnetite are shown in Fig.1[68]. When the size of γ-Fe_2O_3 or Fe_3O_4 nanoparticles falls below a certain threshold (usually below~20 nm), they display superparamagnetism, a relaxation phenomenon associated with thermally activated spontaneous oscillations of the nanoparticle spin. The spin orient itself along the easy axes of magnetization, energetically favoured by the magnetic anisotropy of the nanoparticle. In a superparamagnetic regime, γ-Fe_2O_3 and Fe_3O_4 nanoparticles exhibit a strong magnetic response in a relatively low applied magnetic field (less than 1 T)[69,70]. Like all other iron oxide phases, γ-Fe_2O_3 and Fe_3O_4 are nontoxic (at low dosage), biodegradable and biocompatible, significantly raising their application potential in several fields. However, the γ-Fe_2O_3 and Fe_3O_4

nanoparticle surfaces must be modified by suitable capping agents to (i) prevent the degradation of iron oxide nanoparticles in a foreign environment[71], (ii) suppress the aggregation of iron oxide nanoparticles by suppressing their magnetic interactions[72] and (iii) provide anchors for the attachment of active compounds (e.g., drug, enzymes, etc.)[73], (iv) increase the adsorption capacity[74,75].

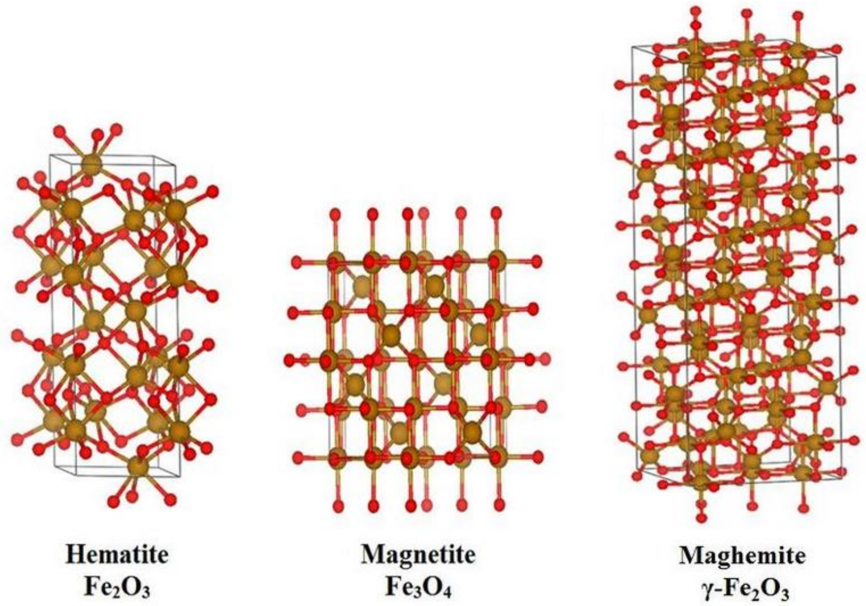

Fig.1. Crystal structure of three commonly studied iron oxides.

Functionalization of the surface enables modulation of IONPs behaviour in solution, such as colloidal stability, pH response, overall toxicity, and inclination to bind and transport other substances. Many synthetic routes for the preparation of IONPs of various shapes and morphologies have been reported which can be commonly classified as (i) synthesis in constrained environments[76], (ii) hydrothermal synthesis[77], (iii) solgel reactions[78], (iv) flow injections[79], (v) microwave-assisted processes[80], and (vi) coprecipitation processes[81]. However, most of these techniques provide bare IONPs which must be functionalized later. Surface functionalization of IONPs is a multistep process demanding sophisticated experimental setups and expertise. Green synthesis provides a novel route for the one-pot reduction and surface functionalization of IONPs[82,83].

Green synthesis primarily aims at resourcing natural materials and employing them as reducing and capping agents for producing functionalized metal oxide nanoparticles; in most of the cases, they are one-pot processes. Biological entities possess a huge potential to produce NPs. Green synthesis, a bottom-up approach, is like chemical reduction where an expensive and hazardous synthetic reducing agent is replaced by extract of a natural product. The green reagent is derived from a wide range of natural source materials comprising plants (leaves, flowers, peels, seeds, bark & roots), microorganisms (yeast, algae, bacteria, fungi), and animal waste[84]. Biogenic reduction of metal salts takes place in the presence of polyphenols, sugars, enzymes and proteins harvested from these sources. In most scenarios, the reduction is followed by capping and stabilization of formed NPs. Fig.2 illustrates various aspects of green synthesis of nanoparticles[83]. As per the studies conducted by Dhillon et al., the nanoparticles prepared from microorganisms have low dispersion, and slow rate of formation when compared to phytogenic synthesis[85]. In 2010 Kalaiarasi et al., reported that plant-based synthesis of metallic nanoparticles is facile, most cost-efficient with high repeatability and reproducibility[86]. It has been proved that plant extracts are appropriate for producing highly stable metal NPs at rapid rates and large quantities[82]. Phytomediated nanomaterial synthesis is preferred due to the abundance of natural robust biomolecular reducing agents that can be extracted from various plants. Different phytochemicals in the plant extracts, contribute to the reduction and stabilization of nanoparticles. Flavonoids are water soluble secondary metabolites present in plants. The scavenging ability of oxygen molecules in flavonoids is linked to their electron-donating capability. Phenolic compounds contain organic carboxylic acids, hydroxyl groups and phenolic rings and can bind with various metallic ions[87-89]. The hydroxyl groups can reduce metal ions into phytoconjugated nanoparticles[60]. The literature contains a commendable amount of reports on the synthesis of metal NPs (Au, Ag, Zn, Fe, Pb, Pd, Mn etc.), metal oxide NPs (ZnO, CuO, TiO_2, Fe_3O_4, Fe_2O_3 etc.) and even bimetallic NPs[59,82,90]. Among these, iron oxide nanoparticles (IONPs) - a flexible potential material combined with low toxicity - were extensively studied and numerous green strategies were developed to produce them. The last decade has witnessed a plethora of reports on green especially phytogenic synthesis of several iron oxide NPs[60,84,91]

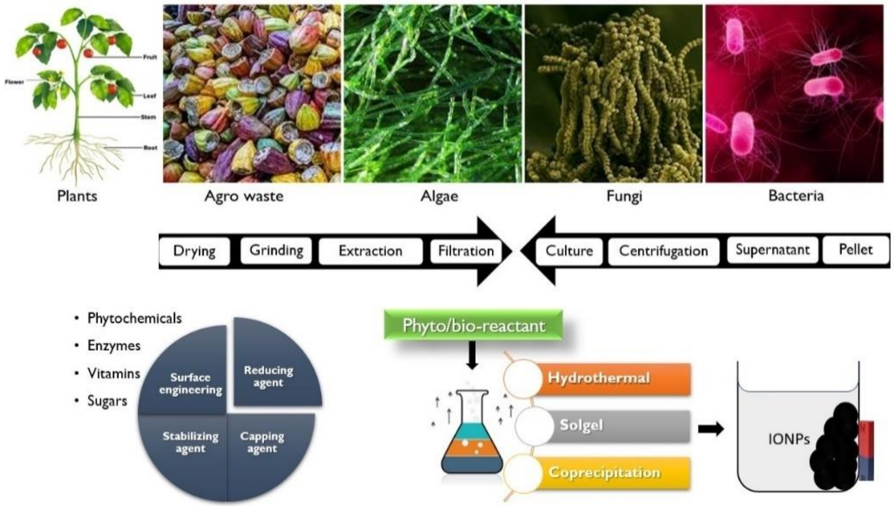

Fig.2. Various green strategies to produce IONPs

Among different synthesis techniques, hydrothermal synthesis, originated from geology and initiated from stimulating hydrothermal conditions by geologists in the 19th century to study the formation of minerals, has become useful in synthesizing nanoparticles with precise morphologies. The hydrothermal reactions are performed in a well-sealed reactor/autoclave in aqueous media, where the pressure of ~2000 psi and temperature of 100-200ºC are maintained. The dehydration of metal salts and low solubility of oxides in aqueous phase supersaturate the medium leading to the formation of highly crystalline NPs[92-94].

1.3.2 Green coagulants

Among various types of water treatment technologies developed in the last few decades, coagulation remains to be one of the oldest processes that continue to be widely employed in many water and wastewater treatment plants. Coagulation removes the impurities, especially suspended particles, and colloids in water by destabilizing and agglomerating the particles into larger aggregates. The aggregates settle down quickly and are subsequently separated from the water[95]. A schematic representation is shown in Fig.3. It's considered as one of the simplest and most economical methods for water treatment. There are several types of coagulants to be chosen for water and wastewater treatment. Conventional chemical coagulants are classified into three large groups which are, i) synthetic cationic polymers (aminomethyl polyacrylamide, polydiallyldimethyl ammonium chloride (polyDADMAC) etc.), ii) pre-hydrolyzing metallic salts (polyferrous sulfate, polyaluminium chloride (PAC), etc.), and iii) hydrolyzing metallic salts (aluminum sulphate $Al_2(SO_4)_3$, ferric chloride ($FeCl_3$) etc.)[96-99]. Among inorganic coagulants iron and aluminum salts are frequently used due to their effective coagulation ability, dispersibility, shelf life, as well as low cost. However, their usage in water treatment pose alarming concerns including the generation of huge volume of sludge, the requirement for alkalinity and pH adjustment and the notable concentration of residual metals in the treated water[100]. There has been a remark on the possible link of the pathogenesis of Alzheimer's disease to the neurotoxicity of aluminum found in wastewater sludge[101]. Another common drawback of conventional coagulants is the mandatory assistance of flocculant aids for faster coagulation. These drawbacks have inspired the search for natural coagulants which are generally claimed to be sustainable in terms of production, usage, and sludge volume.

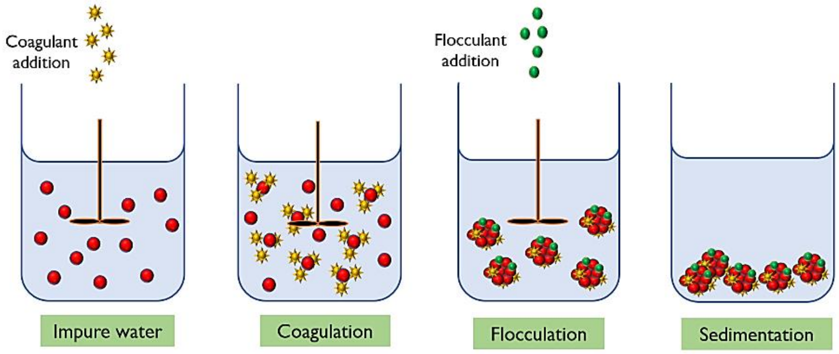

Fig. 3. Schematic representation of coagulation process.

The usage of natural coagulants for water and wastewater remediation has been noted for more than two millennia in China, Africa, and India. Natural coagulants are generally classified into two groups based on the main coagulating compound as polysaccharides and proteins [102,103]. Chitosan, starch, and mucilage belong to the first category while protein-based natural coagulants mainly originated from plants. They can be cationic, anionic, or non-ionic in nature. The presence of active functional groups including hydroxyl and amino groups on these compounds contributes to the coagulation capability. One of the most researched plants for procuring natural coagulants is *Moringa olifera.* Various extraction processes of compounds with coagulation activity from Moringa have been reported[104–106]. Other largely investigated compounds for coagulation properties are tannins[107] and chitosan derivatives[108,109]. Unfortunately, natural coagulants have a lot of disadvantages that restrict their use on commercial levels. Despite appreciable performance and other benefits proven by bench-scale studies, concern arises about its cost-effectiveness and performance consistency in actual treatment processes. Unlike conventional inorganic coagulants where the physicochemical characteristics of the materials can be controlled precisely, the quality of most natural coagulants is difficult to control. It's mainly ascribed to the presence of considerable amounts of noncoagulating impurities that remain in the natural coagulant extract at the final stage. The presence of such impurities severely affects the coagulation efficiency and degrades the quality of the treated water. The uncertainties in quality control resulting from the variation in the performance of natural coagulants with source and extraction approaches hinder it’s use in industrial water treatment sectors. Even though further purification and subsequent modification processes can be performed, the additional expenses render the “cost-saving” aspect of the natural coagulants unattractive[110,111]. Therefore, it becomes mandatory to explore other effective and yet eco-friendly alternatives with commercial possibilities.

1.3.3 Safe pigments

The inorganic mineral pigments like mica, oxides and ultramarines were generally regarded as much healthier alternatives to artificial dyes. Primitive people discovered that hematite, the most abundant ore of iron, could be crushed and used as a paint or cosmetic. The name hematite originates from the Greek word "haimatitis" which means "blood-red." That name stems from the color of hematite when it has been crushed to a fine powder. Iron-oxide mineral deposits have been collected and prepared as pigment for use in art (Fig.4), personal adornment, and mortuary practices by paleolithic people[112–114]. Iron oxide is available in various hues of red, brown, black, and yellow. It’s an ancient, versatile pigment used as a colorant for ceramic glazes, glass, paper, plastic, rubber and textiles as well as in cosmetics and magnetic ink and toner[113]. Micaceous iron oxide has been used to coat industrial tanks, refineries, chemical plants, drilling rigs and bridges, and even on the Eiffel Tower[115]. Natural pigments, especially red pigments, containing hematite are identified to have a major role in human evolutionary development, social interaction, and behavioral complexity[116]. Hematite continues to be one of the most important pigment minerals. Mineral pigments are well suited in cosmetics due to their ability to produce warm earthy tones, and dispersibility in formulations. However, later, it was found that mineral pigments sourced from the earth might contain toxic heavy metals and synthetic production of mineral pigments were initiated for consumer safety[117,118]. Although inorganic mineral pigments are comparatively safer to human beings the sourcing of these materials are often unsustainable and include child labour. Attempts to produce sustainable and safe inorganic pigments are undertaken extensively.

Fig. 4. Prehistoric cave paintings from India[119] & France[120]

1.4 Review of literature

Owing to its versatile and nontoxic nature, phytogenic IONPs are extensively reported globally. Different reaction parameters like temperature, pH, stirring, metal salt concentration and volume of extract are very crucial to obtain nanoparticles of desired shape, size, crystallinity, purity, stability, and morphology. In phytomediated nanoparticle synthesis, the choice of the starting material is very crucial as each part of the plant varies in the concentration of reducing agents like flavones, terpenoids, sugars, ketones, amides, anthracenes, alkaloids etc.[91]. Leaf extract is considered as the best source for the synthesis of metal oxide NPs as it contains high concentration of phytochemicals and foraging of leaves are possible throughout the year without destructing the plant itself. Many researchers have demonstrated various plant extract-based synthesis strategies for iron-based NPs. *Rosa damascene* leaves, *Thymus vulgaris* leaves, *Camelia sinensis* leaves, *Utrica dioica* leaves, *Azadirachta indica* leaves and $FeCl_3$ as a metal precursor were employed to make nano zero valent iron[121–123]. Magnetite NPs were prepared using $FeSO_4.7H_2O$ and $FeCl_3.6H_2O$ and *Musa ornate* and *Passiflora tripartirta* flower sheath as phytoreducing agents[124,125]. *Ocimum sanctum* and *Carica papaya* leaf extracts were employed as reducing agents for the synthesis of hematite NPs and *Terminalia chebula* fruit extracts were used as reducing agents for the manufacture of iron oxide NPs[126–128].

Green synthesis of magnetite using iron precursor and tangerine peel extract at pH 10 produced brown precipitate yielding magnetite NPs on purification[129,130]. Magnetite NPs were achieved by mixing seaweed extract with an iron precursor solution. The color of the mixture changed at pH 11, upon addition of NaOH; the mixture was stirred to obtain magnetically active magnetite nanoparticles were formed[131]. Sathya et al., used coriander leaves as a reducing agent to produce magnetite nanoparticles. An equal amount of leaf extract and iron precursor solution are mixed and ultrasonicated to produce black magnetite[132]. Spherical magnetite NPs of 6-30nm was obtained hydrothermally using aloe vera extract as the reductant and ferric acetyl acetonate as the precursor[133].

The leaf extract of *Avicennia marina,* a grey mangrove variety, was used to produce maghemite nanoparticles. The sudden color change in mixing extract and iron precursor indicated a reduction of iron precursor salt to spherical maghemite NPs [134]. Carolina et al., reported the use of pumpkin leaves and beet stalks as a phytoreducing reagent to produce a mixture of maghemite and goethite NPs. The extract was mixed with the iron precursor to generate a black solution yielding a mixture of 2nm goethite and 20nm maghemite nanoparticles [135].

In 2017, Patra and Baek reported the photo-catalyzed synthesis of magnetic IONPs using hairs of corn and outer leaves of Chinese cabbage[136]. The aqueous extracts of both materials were reacted with a mixture of iron (II) chloride and iron (III) chloride under photocatalytic conditions. The extracts acted as reducing agents in the reaction while sodium hydroxide was used to enable uniform precipitation of nanoparticles. Prasad et al., synthesized well-dispersed magnetic iron oxide nanoparticles of uniform size of 45–60nm using aqueous *Punica granatum* (pomegranate) leaf extract. The phytoextracts were reacted with iron (III) chloride solution as a precursor in the ratio 1:2. Appearance of black colour indicated the formation of nanoparticles[137]. Dried tangerine peels were milled, boiled with distilled water and the resulting solution was then reacted with iron (II) solution and iron (III) solution to obtain uniform, spherical nanoparticles with size ranging from 50–200 nm. 25 % hydroxylamine was added to the mixture to facilitate uniform precipitation[138].

Pomegranate seeds extract and the iron salt solution was stirred and heated to produce a black colour solution spherical hematite NPs[139]. Similarly, Miswak was used as a source for producing hematite nanoparticles wherein, the extract was mixed with an equal amount of iron precursor solution and heated with pH adjusted to 11 to produce hematite[140]. Ahmmad et al., using green tea (*Camellia sinensis*) leaf extract, through the hydrothermal synthesis method successfully prepared pure hematite α-Fe_2O_3 nanoparticles[141]. Literature survey revealed the simultaneous use of multiple phytoextracts to procure IONPs. Ramalingam et al., successfully synthesized hematite nanoparticles using a mixture of aqueous extracts of guava and drumstick leaves together as a phytoreagent. A ferric salt solution was added to the extract, stirred for an hour, and purified to obtain hematite NPs. Table 2 shows a list of magnetite NPs prepared by green methods.

Table 2. List of magnetite NPs prepared by green methods

Source	**Particulars**	**Reference**
Carob extract	Spherical, 16 nm	[142]
Juglans regia	5.7 nm	[143]
Plantain peels	Spherical, 50 nm, magnetic	[144]
Syzygium cumini	Spherical, 20 nm, Superpramagnetic	[145]
Withania coagulans	Rectangular plates, 10–20 nm	[146]
Azadirachta indica hot water extract	Spherical, 9–14 nm, 82 emu/g	[147]
Platanus orientalis L.	7.69 nm	[148]
Andean blackberry	Spherical 54.5 nm	[149]
Urea and gram-bean (GBE, *Cicer arietinum L.)*	13 nm	[150]
Cicer arietinum L.	Poly-dispersed, 20–105 nm	[151]
Passiflora tripartite, methanol/water extract	Spherical, 18.23-24.65 nm	[124]
Soya bean sprouts	SPION Cubic, 8 nm, 37.1 emu/g	[152]
Chromolaena odorata root	6-17 nm, Spherical, agglomerated	[153]

Mimosa pudica root	Spherical, 67 nm, 55.40 emu/g	[151]
Rhus coriaria	Spherical 53 nm	[154]
Flax seed extract	Spherical, 30-40 nm, 51 emu/g	[155]
Padina pavonica	Spherical, 10-19.5 nm	[156]
Sargassum acinarium	Spherical, 21.6-27.4 nm	[156]

In general, IONPs are synthesized by mixing the plant extract and iron precursor in a specific ratio and heating in a thermostat for a specified time interval. The lack of control on morphology and phase of the formed iron/IONPs has lead modification of the process by incorporating techniques like microwave treatment and ultrasonication. The probable complexation of iron with the polyphenols as suggested by Wang et.al., is given below in Fig.5[157].

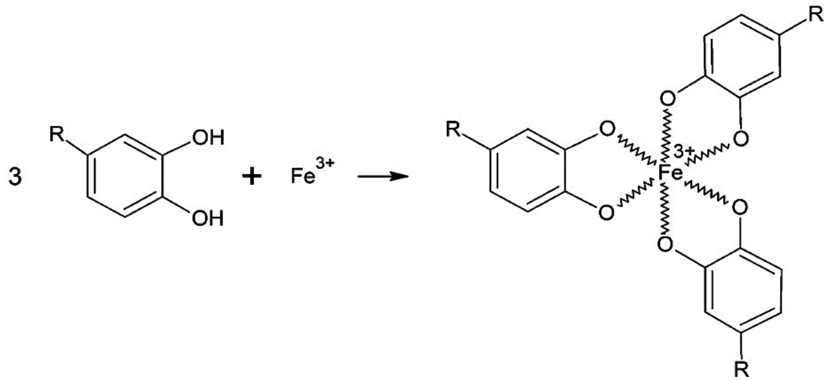

Fig.5. Proposed structure of Fe-polyphenol complex. R groups are typically H, OH, galloyl esters, or carbohydrate groups, depending on the compound.

The phytochemicals present in the extract further reduces the Fe-polyphenol complex. An alkaline environments stimulates the uniform precipitation and reduction of the Fe(III)-polyphenol complexes. High pH along with the presence of phytochemicals containing multiple iron chelating sites prevent the re-oxidation of iron[87]. Subsequent hydrothermal treatments dissolve the precipitated mixture and initiates nucleation of nanoparticles upon attaining the right temperature and pressure. The evolution of CO_2 acts a trigger for the nucleation events. The thermal gradient in the reactor vessels is considered to accelerate the conversion of hydroxide to oxides resulting in IONPs.

IONPs prepared using assorted synthetic routes are extensively used in water remediation owing to their reduction and high adsorption capacity resulting from their larger specific surface area, high porosity, and strong magnetic response. Laboratory findings showed that iron oxide NPs act as an effective sink to a series of heavy metals, such as Pb^{2+}, Hg^{2+}, Cd^{2+}, Cu^{2+}, Cr^{6+} etc. In an experiment conducted by Nassar it was observed that Fe_3O_4 NPs shows maximum adsorption for Pb(II) ions of 36.0mgg^{-1}. It was found that small sized Fe_3O_4 NPs efficiently promoted the diffusion of metal ions from solution onto the active sites of the adsorbent surface[151]. Powdered activated carbon (PAC) and granular activated carbon (GAC) composites with magnetite NPs were synthesized using green tea extract as reducing agent and was used for the removal of Cu from aquatic environment [158]. Magnetic IONPs prepared using *P. granatum* rind and then capped with dimercaptosuccinic acid was applied as a reusable adsorbent for the removal of Pb(II). The removal of Pb (II) ions increased as the pH increased from 2 to 5 and decreased at pH 6 and 7 due to the formation of hydroxides of lead at higher pH. On the other side at low pH the adsorption decreased due to the competition between Pb(II) and H^+ ions[159]. Nanoscale iron oxides, particularly magnetite NPs are found effective in arsenic adsorption. Wu et al., synthesized Fe_3O_4 which were used to disperse nano-Fe(0) for Cr (VI) mitigation. Fe_3O_4 prevents the agglomeration of Fe(0) nanoparticles and maintains the high efficiency of the adsorbent for Cr(VI) reduction. The results showed that high amount of Fe_3O_4 in the nano composites leads to the rise in Cr (VI) reduction[160]. Green synthesized IONPs are effective in immobilizing and reducing HMIs from water and soil. A list of recent reports on removal of HMIs by iron-based/ iron oxide NPS are presented in Table3.

Table 3. Recent reports on removal of HMIs by green IONPs

Phytogenic source	**HMI**	**HMI dosage**	**Removal efficiency**	**Time (min)**	**pH**	**Ref.**
			Magnetite			
Lemon peel extract	Pb(II) Cd(II) As(III)	20mg/L	98% 46% 48%	20	5.5	[161]
Tangerine peel extract	Pb(II)	33mg/L	95%	95	4.5	[162]
Emblica officinalis extract	Pb		46.18 mgg^{-1}			[163]
Hevea bark extract	Cd	20mg/L	90%	30	6	[164]
Cnidium monnieri (L) C. Seed extract	Pb(II) Cr(III)	10mg/L	95%	100	4	[165]
Padina pavonica (Linnaeus) Thivy	Pb(II)		91%		4	[156]
Sargassum acinarium (Linnaeus) Setchell 1933	Pb(II)	75mg/L	78%	75	4	[156]
Averrhoa carambola leaf extract	Cr(VI) (ground water, 3ppm)		99.34%	15 min	5	[166]
Thymus schimperi leaf extract	Cr(VI) Hg(II)		86% 90%	60 90	5 7	[167]
Portulaca oleracea	Pb(II) Cd(II) 50mg/L		100 % 95.32	70	6	[168]

Others						
Tangerine peel extract-IONPs	Cd(II)	15 mg/L	89.6%	90	7	[169]
Green tea extract MWCNT-Au/Fe_3O_4	Pb(II)	1000 mg/L	70%	240	7	[170]
Sugarcane bagasse Nano-IOS	*Pb(II), Cd(II), Ni(II), Cu(II), and Zn(II)*	10mg/L	80, 82, 84, 87 & 88%	70	5	[171]
Cordia myxa leaf extract. Fe_3O_4@Al-B nanocomposite	Pb(II)	10mg/L	98%	60	7	[172]
Lemon extract Chitosan-Fe_2O_3	Pb(II) Cd(II)	50mg/L	93.8 mgg^{-1} 88.88 mgg^{-1}	180		[173]
Saw dust EDTA@ Fe_3O_4/SC nano composites	Cd(II)	30mg/L	84%	120	6.5	[174]

Despite the existence of large number of reports on green synthesis of various pure and mixed iron oxide NPs, the pigment properties of IONPs are rarely investigated. Iron oxide pigments (IOPs) were produced using citrus pectin as a colloidal template resulting in the generation of different shades of pigment. The same batch generates different colours for the hematite phase as function of calcination temperature. This sustainable novel method does not produce waste, requires a quantity of water proportional to the volume of the prepared colloid, and does not involve any additional purification methods. Six IOPs belonging to yellow, red and purple shades were prepared using iron (II) sulphate and iron (III) sulphate as precursor salts[175]. Another instance of green synthesis is the production of iron oxide based ceramic pigments from industrial waste by encapsulation of hematite in crystalline and amorphous silica matrix. Iron oxide from a metal sheet rolling process was used as chromophore in the process. Conventional, high-energy milling was used to homogenize hematite and silica milling. The powders were calcined between 1050 and 1200°C for 2 hours and the obtained pigments were applied to ceramic enamel and porcelain body[176].

The extract of *Sargassum ilicifolium* was used as a bioreductant as well as a stabilizing agent to produce alumina NPs. The X-Ray diffractogram revealed that after calcination at ~ 1200°C, the α-Al_2O_3 nanoparticles were crystalline in nature with a diameter of 35nm and had a rhombohedral structure. TEM indicated that the spherical alumina NPs were well-dispersed with an average size of 20 ± 2.1nm[177].

Microwave assisted synthesis of semicrystalline alumina NPs using extracts of *Syzygium aromaticum, Origanum vulgare, Origanum majorana, Theobroma cacao and Cichorium intybus* were performed by Hasanpoor et al., and it was observed that nanoparticles possessed quasi-spherical morphology. Average size of clusters of nanoparticles varied with different routes from 60nm to 300nm. AFM images showed that individual nanoparticles were less than 10nm[178]. *Cymbopogan citratus* (Lemongrass) was used to synthesize Al_2O_3 NPs using leaf extracts of lemongrass and Aluminium nitrate. The X-ray diffraction data revealed the average size of the spherical Al_2O_3-NPs as 34.5nm. The hydrodynamic size in Milli Q water and zeta potential were determined to be 254nm and +52.2mV, respectively[179]. Another study demonstrated Al_2O_3 NPs synthesis using tragacanth (*Astragalus gummifer*) gel as a biotemplate via sol-gel method at different calcination temperatures. The synthesized NPs were characterized by XRD, FTIR, FESEM, and EDX. The XRD analysis indicated that the catalyst calcined at 500°C was amorphous while the one calcined at 900°C was crystalline with gamma phase[180]. Various green extracts like tea, coffee and thriphala were also reported to yield alumina NPs using bulk aluminium nitrate[181]. However, none of these reports lead to generation of coagulants or coagulant aids. Although there is plenitude of reports on isolation of green coagulants from biomaterials, alternative green methods for production of modified inorganic coagulants which are highly superior to green coagulants are scarce.

1.5 Present study

Though phytosynthesis is considered as a more sustainable option to chemical processes, exploitation of food and commercially important crops for nanoparticle synthesis reduces the overall efficacy of the biosynthetic process because of competition for use as food materials for other economic purposes. In this study three aggressive weeds have been used to procure different NPs. All three selected plants are known for their ethnomedicinal properties and are currently studied for antioxidant, antibacterial, antidiabetic and anticancer properties. Iron oxide NPs of different phases were synthesized using *Chromolaena odorata* flower extract and *Sphageneticola trilobata* leaf extract through hydrothermal approach. Fine phytogenic magnetite nanoparticles (PMNPs) produced using the plant extracts were used to immobilize and remove heavy metal ions including Cr(VI) and Pb(II) from aquatic environment. The PMNPs proved to be efficient in removing the HMIs even in repeated cycles. The hematite and maghemite NPs prepared using the plant extracts were characterized using assorted analytical techniques including XPS. The antioxidant capacity and cytotoxicity studies of the pigments were conducted and was then incorporated into cosmetic formulations. Another potential weed native to the land, *Hemigraphis alternata* was used to produce alumina and aluminium sulphate NPs which were tested for their water purification capacities. The nano aluminium sulphate obtained in this route used for the preparation of γ-alumina NPs displayed appreciable coagulation ability towards organic and inorganic anionic impurities. The work explores a sustainable way for effective utilization and management of plant wastes and biomass to resolve the gripping issues of water purification. Since the phytogenic synthesis uses minimal chemicals and instrumental setups to produce stable and efficient nanoparticle systems the method can be scaled up economically.

References

[1] Spitters CJT, Van Den Bergh JP. Competition between crop and weeds: A system approach. In: Holzner W, Numata M, editors. Biology and ecology of weeds, Dordrecht: Springer Netherlands; 1982, p. 137–48. https://doi.org/10.1007/978-94-017-0916-3_12.

[2] Del Fabbro C, Güsewell S, Prati D. Allelopathic effects of three plant invaders on germination of native species: a field study. Biol Invasions 2014;16:1035–42. https://doi.org/10.1007/s10530-013-0555-3.

[3] Padayachee AL, Irlich UM, Faulkner KT, Gaertner M, Procheş Ş, Wilson JRU, et al. How do invasive species travel to and through urban environments? Biol Invasions 2017;19:3557–70. https://doi.org/10.1007/s10530-017-1596-9.

[4] Charles H, Dukes JS. Impacts of Invasive Species on Ecosystem Services. In: Nentwig W, editor. Biological Invasions, vol. 193, Berlin, Heidelberg: Springer Berlin Heidelberg; 2007, p. 217–37. https://doi.org/10.1007/978-3-540-36920-2_13.

[5] GISD n.d. http://www.iucngisd.org/gisd/species.php?sc=47 (accessed July 18, 2022).

[6] Invasive alien species and sustainable development. IUCN n.d. https://www.iucn.org/resources/issues-brief/invasive-alien-species-and-sustainable-development (accessed December 7, 2022).

[7] Rao AN, Chauhan BS. Weeds and Weed Management in India - A Review. In: Rao VS, Yaduraju NT, Chandrasena NR, Hassan G, Sharma AR, editors., Hyderabad: Indian Society of Weed Science; 2015, p. 87–118.

[8] Sajeev T, Sankaran K, Suresh T. Are Alien Invasive Plants a Threat to Forests of Kerala? n.d.:28.

[9] Water | United Nations n.d. https://www.un.org/en/global-issues/water (accessed December 7, 2022).

[10] Water Facts - Worldwide Water Supply | ARWEC| CCAO | Area Offices | California-Great Basin | Bureau of Reclamation n.d. https://www.usbr.gov/mp/arwec/water-facts-ww-water-sup.html (accessed December 7, 2022).

[11] Haseena M. Water pollution and human health. 2017;1:4.

[12] Nazir F. Factors Effecting Water Pollution 2018.

[13] Ghangrekar MM, Chatterjee P. Water Pollutants Classification and Its Effects on Environment. In: Das R, editor. Carbon Nanotubes for Clean Water, Cham: Springer International Publishing; 2018, p. 11–26. https://doi.org/10.1007/978-3-319-95603-9_2.

[14] Verma R, Dwivedi P. Heavy metal water pollution-A case study. Recent Research in Science and Technology 2013;5:98–9.

[15] Singh J, Yadav P, Pal AK, Mishra V. Water Pollutants: Origin and Status. In: Pooja D, Kumar P, Singh P, Patil S, editors. Sensors in Water Pollutants Monitoring: Role of Material, Singapore: Springer; 2020, p. 5–20. https://doi.org/10.1007/978-981-15-0671-0_2.

[16] Kaushik A, Kansal A, Santosh, Meena, Kumari S, Kaushik CP. Heavy metal contamination of river Yamuna, Haryana, India: Assessment by Metal Enrichment Factor of the Sediments. Journal of Hazardous Materials 2009;164:265–70. https://doi.org/10.1016/j.jhazmat.2008.08.031.

[17] Briffa J, Sinagra E, Blundell R. Heavy metal pollution in the environment and their toxicological effects on humans. Heliyon 2020;6:e04691. https://doi.org/10.1016/j.heliyon.2020.e04691.

[18] Duruibe J, C O, Egwurugwu J. Heavy Metal Pollution and Human Biotoxic Effects. Int J Phys Sci 2007;2:112–8.

[19] Jaishankar M, Tseten T, Anbalagan N, Mathew BB, Beeregowda KN. Toxicity, mechanism and health effects of some heavy metals. Interdiscip Toxicol 2014;7:60–72. https://doi.org/10.2478/intox-2014-0009.

[20] Tchounwou PB, Yedjou CG, Patlolla AK, Sutton DJ. Heavy Metal Toxicity and the Environment. In: Luch A, editor. Molecular, Clinical and Environmental Toxicology: Volume 3: Environmental Toxicology, Basel: Springer; 2012, p. 133–64. https://doi.org/10.1007/978-3-7643-8340-4_6.

[21] Gupta K, Joshi P, Gusain R, Khatri OP. Recent advances in adsorptive removal of heavy metal and metalloid ions by metal oxide-based nanomaterials. Coordination Chemistry Reviews 2021;445:214100. https://doi.org/10.1016/j.ccr.2021.214100.

[22] Rahman Z, Singh VP. The relative impact of toxic heavy metals (THMs) (arsenic (As), cadmium (Cd), chromium (Cr)(VI), mercury (Hg), and lead (Pb)) on the total environment: an overview. Environ Monit Assess 2019;191:419. https://doi.org/10.1007/s10661-019-7528-7.

[23] Khan S, Malik A. Environmental and Health Effects of Textile Industry Wastewater. In: Malik A, Grohmann E, Akhtar R, editors. Environmental Deterioration and Human Health: Natural and anthropogenic determinants, Dordrecht: Springer Netherlands; 2014, p. 55–71. https://doi.org/10.1007/978-94-007-7890-0_4.

[24] Yusuf M. Synthetic Dyes: A Threat to the Environment and Water Ecosystem. Textiles and Clothing, John Wiley & Sons, Ltd; 2019, p. 11–26. https://doi.org/10.1002/9781119526599.ch2.

[25] Rajaram T, Das A. Water pollution by industrial effluents in India: Discharge scenarios and case for participatory ecosystem specific local regulation. Futures 2008;40:56–69. https://doi.org/10.1016/j.futures.2007.06.002.

[26] Selvakumar S, Chandrasekar N, Kumar G. Hydrogeochemical characteristics and groundwater contamination in the rapid urban development areas of Coimbatore, India. Water Resources and Industry 2017;17:26–33. https://doi.org/10.1016/j.wri.2017.02.002.

[27] Pal H, Chatterjee KN, Sharma D. 5 - Water footprint of denim industry. In: Muthu SS, editor. Sustainability in Denim, Woodhead Publishing; 2017, p. 111–23. https://doi.org/10.1016/B978-0-08-102043-2.00005-8.

[28] Denim & Water – TEXINLIFE n.d. https://texinlife.com/denim-water/ (accessed December 7, 2022).

[29] Chung K-T. Azo dyes and human health: A review. Journal of Environmental Science and Health, Part C 2016;34:233–61. https://doi.org/10.1080/10590501.2016.1236602.

[30] Yaseen DA, Scholz M. Textile dye wastewater characteristics and constituents of synthetic effluents: a critical review. Int J Environ Sci Technol 2019;16:1193–226. https://doi.org/10.1007/s13762-018-2130-z.

[31] Ali H. Biodegradation of Synthetic Dyes—A Review. Water Air Soil Pollut 2010;213:251–73. https://doi.org/10.1007/s11270-010-0382-4.

[32] Alves de Lima RO, Bazo AP, Salvadori DMF, Rech CM, de Palma Oliveira D, de Aragão Umbuzeiro G. Mutagenic and carcinogenic potential of a textile azo dye processing plant effluent that impacts a drinking water source. Mutation Research/Genetic Toxicology and Environmental Mutagenesis 2007;626:53–60. https://doi.org/10.1016/j.mrgentox.2006.08.002.

[33] Gregory P. Azo dyes: Structure-carcinogenicity relationships. Dyes and Pigments 1986;7:45–56. https://doi.org/10.1016/0143-7208(86)87005-X.

[34] Yahagi T, Degawa M, Seino Y, Matsushima T, Nagao M, Sugimura T, et al. Mutagenicity of carcinogenic azo dyes and their derivatives. Cancer Letters 1975;1:91–6. https://doi.org/10.1016/S0304-3835(75)95563-9.

[35] Juliano C, Magrini GA. Cosmetic Ingredients as Emerging Pollutants of Environmental and Health Concern. A Mini-Review. Cosmetics 2017;4:11. https://doi.org/10.3390/cosmetics4020011.

[36] Anagnosti L, Varvaresou A, Pavlou P, Protopapa E, Carayanni V. Worldwide actions against plastic pollution from microbeads and microplastics in cosmetics focusing on European policies. Has the issue been handled effectively? Marine Pollution Bulletin 2021;162:111883. https://doi.org/10.1016/j.marpolbul.2020.111883.

[37] Uter W, Strahwald J, Hallmann S, Johansen JD, Havmose MS, Kezic S, et al. Systematic review on skin adverse effects of important hazardous hair cosmetic ingredients with a focus on hairdressers. Contact Dermatitis n.d.;n/a. https://doi.org/10.1111/cod.14236.

[38] Canavez ADPM, de Oliveira Prado Corrêa G, Isaac VLB, Schuck DC, Lorencini M. Integrated approaches to testing and assessment as a tool for the hazard assessment and risk characterization of cosmetic preservatives. Journal of Applied Toxicology 2021;41:1687–99. https://doi.org/10.1002/jat.4156.

[39] Kim K-B, Kwack SJ, Lee JY, Kacew S, Lee B-M. Current opinion on risk assessment of cosmetics. Journal of Toxicology and Environmental Health,PartB,2021;24:137–61. https://doi.org/10.1080/10937404.2021.1907264.

[40] Suaria G, Aliani S, Merlino S, Abbate M. The Occurrence of Paraffin and Other Petroleum Waxes in the Marine Environment: A Review of the Current Legislative Framework and Shipping Operational Practices. Frontiers in Marine Science 2018;5.

[41] Arshad H, Mehmood MZ, Shah MH, Abbasi AM. Evaluation of heavy metals in cosmetic products and their health risk assessment. Saudi Pharmaceutical Journal 2020;28:779–90. https://doi.org/10.1016/j.jsps.2020.05.006.

[42] Ghosh A, Das S, Kundu S, Maiti PK, Sahoo P. Rapid estimation of lead in lipsticks. Sensors and Actuators B: Chemical 2018;266:80–5. https://doi.org/10.1016/j.snb.2018.03.105.

[43] Bioaccessible trace metals in lip cosmetics and their health risks to female consumers. Environmental Pollution 2018;238:554–61. https://doi.org/10.1016/j.envpol.2018.03.072.

[44] Marinovich M, Boraso MS, Testai E, Galli CL. Metals in cosmetics: An a posteriori safety evaluation. Regulatory Toxicology and Pharmacology 2014;69:416–24. https://doi.org/10.1016/j.yrtph.2014.05.005.

[45] Qasem NAA, Mohammed RH, Lawal DU. Removal of heavy metal ions from wastewater: a comprehensive and critical review. Npj Clean Water 2021;4:1–15. https://doi.org/10.1038/s41545-021-00127-0.

[46] Malik LA, Bashir A, Qureashi A, Pandith AH. Detection and removal of heavy metal ions: a review. Environ Chem Lett 2019;17:1495–521. https://doi.org/10.1007/s10311-019-00891-z.

[47] Fu F, Wang Q. Removal of heavy metal ions from wastewaters: A review. Journal of Environmental Management 2011;92:407–18. https://doi.org/10.1016/j.jenvman.2010.11.011.

[48] Qin H, Hu T, Zhai Y, Lu N, Aliyeva J. The improved methods of heavy metals removal by biosorbents: A review. Environmental Pollution 2020;258:113777. https://doi.org/10.1016/j.envpol.2019.113777.

[49] Rajendran S, Priya TAK, Khoo KS, Hoang TKA, Ng H-S, Munawaroh HSH, et al. A critical review on various remediation approaches for heavy metal contaminants removal from contaminated soils. Chemosphere 2022;287:132369. https://doi.org/10.1016/j.chemosphere.2021.132369.

[50] Fei Y, Hu YH. Design, synthesis, and performance of adsorbents for heavy metal removal from wastewater: a review. J Mater Chem A 2022;10:1047–85. https://doi.org/10.1039/D1TA06612A.

[51] Chakraborty R, Asthana A, Singh AK, Jain B, Susan ABH. Adsorption of heavy metal ions by various low-cost adsorbents: a review. International Journal of Environmental Analytical Chemistry 2022;102:342–79. https://doi.org/10.1080/03067319.2020.1722811.

[52] Feng X, Long R, Wang L, Liu C, Bai Z, Liu X. A review on heavy metal ions adsorption from water by layered double hydroxide and its composites. Separation and Purification Technology 2022;284:120099. https://doi.org/10.1016/j.seppur.2021.120099.

[53] Li J, Yang Z, Ding T, Song Y-J, Li H-C, Li D, et al. The role of surface functional groups of pectin and pectin-based materials on the adsorption

of heavy metal ions and dyes. Carbohydrate Polymers 2022;276:118789. https://doi.org/10.1016/j.carbpol.2021.118789.

[54] Ibrahim Adil H, R. Thalji M, A. Yasin S, A. Saeed I, A. Assiri M, Feng Chong K, et al. Metal–organic frameworks (MOFs) based nanofiber architectures for the removal of heavy metal ions. RSC Advances 2022;12:1433–50. https://doi.org/10.1039/D1RA07034G.

[55] Damiri F, Andra S, Kommineni N, Balu SK, Bulusu R, Boseila AA, et al. Recent Advances in Adsorptive Nanocomposite Membranes for Heavy Metals Ion Removal from Contaminated Water: A Comprehensive Review. Materials 2022;15:5392. https://doi.org/10.3390/ma15155392.

[56] Liang W, Wang G, Peng C, Tan J, Wan J, Sun P, et al. Recent advances of carbon-based nano zero valent iron for heavy metals remediation in soil and water: A critical review. Journal of Hazardous Materials 2022;426:127993. https://doi.org/10.1016/j.jhazmat.2021.127993.

[57] Naseem T, Durrani T. The role of some important metal oxide nanoparticles for wastewater and antibacterial applications: A review. Environmental Chemistry and Ecotoxicology 2021;3:59–75. https://doi.org/10.1016/j.enceco.2020.12.001.

[58] Lv Z, Zhang J, Zhang Y, Li K, Ye X, Fang M, et al. Selective and efficient removal of radioactive ions from water with well-dispersed metal oxide nanoparticles@N-doped carbon. Separation and Purification Technology 2022;285:120366. https://doi.org/10.1016/j.seppur.2021.120366.

[59] Verma A, Bharadvaja N. Plant-Mediated Synthesis and Characterization of Silver and Copper Oxide Nanoparticles: Antibacterial and Heavy Metal Removal Activity. J Clust Sci 2022;33:1697–712. https://doi.org/10.1007/s10876-021-02091-8.

[60] Selvaraj R, Pai S, Vinayagam R, Varadavenkatesan T, Kumar PS, Duc PA, et al. A recent update on green synthesized iron and iron oxide nanoparticles for environmental applications. Chemosphere 2022;308:136331. https://doi.org/10.1016/j.chemosphere.2022.136331.

[61] Venkatraman Y, Priya AK. Removal of heavy metal ion concentrations from the wastewater using tobacco leaves coated with iron oxide nanoparticles. Int J Environ Sci Technol 2022;19:2721–36. https://doi.org/10.1007/s13762-021-03202-8.

[62] Park JE, Shin J-H, Oh W, Choi S-J, Kim J, Kim C, et al. Removal of Hexavalent Chromium(VI) from Wastewater Using Chitosan-Coated Iron Oxide Nanocomposite Membranes. Toxics 2022;10:98. https://doi.org/10.3390/toxics10020098.

[63] Hammad EN, Salem SS, Mohamed AA, El-Dougdoug W. Environmental Impacts of Ecofriendly Iron Oxide Nanoparticles on Dyes Removal and Antibacterial Activity. Appl Biochem Biotechnol 2022;194:6053–67. https://doi.org/10.1007/s12010-022-04105-1.

[64] Perwez M, Fatima H, Arshad M, Meena VK, Ahmad B. Magnetic iron oxide nanosorbents effective in dye removal. Int J Environ Sci Technol 2022. https://doi.org/10.1007/s13762-022-04003-3.

[65] Özdemir S, Serkan Yalçın M, Kılınç E. Preconcentrations of Ni(II) and Pb(II) from water and food samples by solid-phase extraction using Pleurotus

ostreatus immobilized iron oxide nanoparticles. Food Chemistry 2021;336:127675. https://doi.org/10.1016/j.foodchem.2020.127675.

[66] Facile synthesis and characterization of polypyrrole - iron oxide – seaweed (PPy-Fe3O4-SW) nanocomposite and its exploration for adsorptive removal of Pb(II) from heavy metal bearing water. Chemosphere2021;278:130400. https://doi.org/10.1016/j.chemosphere.2021.130400.

[67] Hola K, Markova Z, Zoppellaro G, Tucek J, Zboril R. Tailored functionalization of iron oxide nanoparticles for MRI, drug delivery, magnetic separation and immobilization of biosubstances. Biotechnology Advances 2015;33:1162–76. https://doi.org/10.1016/j.biotechadv.2015.02.003.

[68] Kuchma E, Kubrin S, Soldatov A. The Local Atomic Structure of Colloidal Superparamagnetic Iron Oxide Nanoparticles for Theranostics in Oncology.Biomedicines,2018;6:78. https://doi.org/10.3390/biomedicines6030078.

[69] Mahmoudi M, Sant S, Wang B, Laurent S, Sen T. Superparamagnetic iron oxide nanoparticles (SPIONs): Development, surface modification and applications in chemotherapy. Advanced Drug Delivery Reviews 2011;63:24–46. https://doi.org/10.1016/j.addr.2010.05.006.

[70] Qiao R, Yang C, Gao M. Superparamagnetic iron oxide nanoparticles: from preparations to in vivo MRI applications. J Mater Chem 2009;19:6274–93. https://doi.org/10.1039/B902394A.

[71] Neouze M-A, Schubert U. Surface Modification and Functionalization of Metal and Metal Oxide Nanoparticles by Organic Ligands. Monatsh Chem 2008;139:183–95. https://doi.org/10.1007/s00706-007-0775-2.

[72] Zhu N, Ji H, Yu P, Niu J, Farooq MU, Akram MW, et al. Surface Modification of Magnetic Iron Oxide Nanoparticles. Nanomaterials 2018;8:810. https://doi.org/10.3390/nano8100810.

[73] Banerjee SS, Chen D-H. Grafting of 2-Hydroxypropyl-β-Cyclodextrin on Gum Arabic-Modified Iron Oxide Nanoparticles as a Magnetic Carrier for Targeted Delivery of Hydrophobic Anticancer Drug. International Journal of Applied Ceramic Technology 2010;7:111–8. https://doi.org/10.1111/j.1744-7402.2008.02332.x.

[74] Mahdavi M, Ahmad MB, Haron MJ, Namvar F, Nadi B, Rahman MZA, et al. Synthesis, Surface Modification and Characterisation of Biocompatible Magnetic Iron Oxide Nanoparticles for Biomedical Applications. Molecules 2013;18:7533–48. https://doi.org/10.3390/molecules18077533.

[75] Huo L, Zeng X, Su S, Bai L, Wang Y. Enhanced removal of As (V) from aqueous solution using modified hydrous ferric oxide nanoparticles. Sci Rep 2017;7:40765. https://doi.org/10.1038/srep40765.

[76] Allen M, Willits D, Mosolf J, Young M, Douglas T. Protein Cage Constrained Synthesis of Ferrimagnetic Iron Oxide Nanoparticles. Advanced Materials 2002;14:1562–5. https://doi.org/10.1002/1521-4095(20021104)14:21<1562::AID-ADMA1562>3.0.CO;2-D.

[77] Ge S, Shi X, Sun K, Li C, Uher C, Baker JRJr, et al. Facile Hydrothermal Synthesis of Iron Oxide Nanoparticles with Tunable Magnetic Properties. J Phys Chem C 2009;113:13593–9. https://doi.org/10.1021/jp902953t.

[78] F. Hasany S, H. Abdurahman N, R. Sunarti A, Jose R. Magnetic Iron Oxide Nanoparticles: Chemical Synthesis and Applications Review. Current Nanoscience 2013;9:561–75.

[79] Novel flow injection synthesis of iron oxide nanoparticles with narrow size distribution. Chemical Engineering Science 2006;61:4625–33. https://doi.org/10.1016/j.ces.2006.02.032.

[80] Kozakova Z, Kuritka I, Kazantseva NE, Babayan V, Pastorek M, Machovsky M, et al. The formation mechanism of iron oxide nanoparticles within the microwave-assisted solvothermal synthesis and its correlation with the structural and magnetic properties. Dalton Trans 2015;44:21099–108. https://doi.org/10.1039/C5DT03518J.

[81] Besenhard MO, LaGrow AP, Hodzic A, Kriechbaum M, Panariello L, Bais G, et al. Co-precipitation synthesis of stable iron oxide nanoparticles with NaOH: New insights and continuous production via flow chemistry. Chemical Engineering Journal 2020;399:125740. https://doi.org/10.1016/j.cej.2020.125740.

[82] Iravani S. Green synthesis of metal nanoparticles using plants. Green Chem 2011;13:2638–50. https://doi.org/10.1039/C1GC15386B.

[83] Nasrollahzadeh M, Atarod M, Sajjadi M, Sajadi SM, Issaabadi Z. Plant-Mediated Green Synthesis of Nanostructures: Mechanisms, Characterization, and Applications. Interface Science and Technology, vol. 28, Elsevier; 2019, p. 199–322. https://doi.org/10.1016/B978-0-12-813586-0.00006-7.

[84] Shanker U, Jassal V, Rani M, Kaith BS. Towards green synthesis of nanoparticles: From bio-assisted sources to benign solvents. A review. International Journal of Environmental Analytical Chemistry 2016;96:801–35. https://doi.org/10.1080/03067319.2016.1209663.

[85] Dhillon GS, Brar SK, Kaur S, Verma M. Green approach for nanoparticle biosynthesis by fungi: current trends and applications. Critical Reviews in Biotechnology 2012;32:49–73. https://doi.org/10.3109/07388551.2010.550568.

[86] Kalaiarasi R, Jayallakshmi N, Venkatachalam P. Phytosynthesis of nanoparticles and its applications. Plant Cell Biotechnology and Molecular Biology 2010;11:1–16.

[87] Morel I, Lescoat G, Cogrel P, Sergent O, Pasdeloup N, Brissot P, et al. Antioxidant and iron-chelating activities of the flavonoids catechin, quercetin and diosmetin on iron-loaded rat hepatocyte cultures. Biochemical Pharmacology 1993;45:13–9. https://doi.org/10.1016/0006-2952(93)90371-3.

[88] Deng J, Yang H, Capanoglu E, Cao H, Xiao J. 9 - Technological aspects and stability of polyphenols. In: Galanakis CM, editor. Polyphenols: Properties, Recovery, and Applications, Woodhead Publishing; 2018, p. 295–323. https://doi.org/10.1016/B978-0-12-813572-3.00009-9.

[89] Elhabiri M, Carrër C, Marmolle F, Traboulsi H. Complexation of iron(III) by catecholate-type polyphenols. Inorganica Chimica Acta 2007;360:353–9. https://doi.org/10.1016/j.ica.2006.07.110.

[90] Mittal AK, Chisti Y, Banerjee UC. Synthesis of metallic nanoparticles using plant extracts. Biotechnology Advances 2013;31:346–56. https://doi.org/10.1016/j.biotechadv.2013.01.003.

[91] Priya, Naveen, Kaur K, Sidhu AK. Green Synthesis: An Eco-friendly Route for the Synthesis of Iron Oxide Nanoparticles. Frontiers in Nanotechnology 2021;3.

[92] Khalil M, Yu J, Liu N, Lee RL. Hydrothermal synthesis, characterization, and growth mechanism of hematite nanoparticles. J Nanopart Res 2014;16:2362. https://doi.org/10.1007/s11051-014-2362-x.

[93] Morey GW. Hydrothermal Synthesis. Journal of the American Ceramic Society 1953;36:279–85. https://doi.org/10.1111/j.1151-2916.1953.tb12883.x.

[94] Sōmiya S, Roy R. Hydrothermal synthesis of fine oxide powders. Bull Mater Sci 2000;23:453–60. https://doi.org/10.1007/BF02903883.

[95] Lam S-M, Low X-ZD, Wong K-A, Sin J-C. Sequencing coagulation–photodegradation treatment of Malachite Green dye and textile wastewater through ZnO micro/nanoflowers. Chemical Engineering Communications 2018;205:1143–56. https://doi.org/10.1080/00986445.2018.1434163.

[96] Edzwald JK. Coagulation in Drinking Water Treatment: Particles, Organics and Coagulants. Water Science and Technology 1993;27:21–35. https://doi.org/10.2166/wst.1993.0261.

[97] Sinha S, Yoon Y, Amy G, Yoon J. Determining the effectiveness of conventional and alternative coagulants through effective characterization schemes. Chemosphere 2004;57:1115–22. https://doi.org/10.1016/j.chemosphere.2004.08.012.

[98] Gregory J, Duan J. Hydrolyzing metal salts as coagulants. Pure and Applied Chemistry 2001;73:2017–26. https://doi.org/10.1351/pac200173122017.

[99] Lee KE, Morad N, Teng TT, Poh BT. Development, characterization and the application of hybrid materials in coagulation/flocculation of wastewater: A review. Chemical Engineering Journal 2012;203:370–86. https://doi.org/10.1016/j.cej.2012.06.109.

[100] Teh CY, Budiman PM, Shak KPY, Wu TY. Recent Advancement of Coagulation–Flocculation and Its Application in Wastewater Treatment. Ind Eng Chem Res 2016;55:4363–89. https://doi.org/10.1021/acs.iecr.5b04703.

[101] Lau Y-Y, Wong Y-S, Teng T-T, Morad N, Rafatullah M, Ong S-A. Degradation of cationic and anionic dyes in coagulation–flocculation process using bi-functionalized silica hybrid with aluminum-ferric as auxiliary agent. RSC Adv 2015;5:34206–15. https://doi.org/10.1039/C5RA01346A.

[102] Choy SY, Prasad KMN, Wu TY, Raghunandan ME, Ramanan RN. Utilization of plant-based natural coagulants as future alternatives

towards sustainable water clarification. Journal of Environmental Sciences 2014;26:2178–89. https://doi.org/10.1016/j.jes.2014.09.024.

[103] Shamsnejati S, Chaibakhsh N, Pendashteh AR, Hayeripour S. Mucilaginous seed of Ocimum basilicum as a natural coagulant for textile wastewater treatment. Industrial Crops and Products 2015;69:40–7. https://doi.org/10.1016/j.indcrop.2015.01.045.

[104] Ndabigengesere A, Subba Narasiah K. Quality of water treated by coagulation using Moringa oleifera seeds. Water Research 1998;32:781–91. https://doi.org/10.1016/S0043-1354(97)00295-9.

[105] Ndabigengesere A, Narasiah KS, Talbot BG. Active agents and mechanism of coagulation of turbid waters using Moringa oleifera. Water Research 1995;29:703–10. https://doi.org/10.1016/0043-1354(94)00161-Y.

[106] Ueda Yamaguchi N, Cusioli LF, Quesada HB, Camargo Ferreira ME, Fagundes-Klen MR, Salcedo Vieira AM, et al. A review of Moringa oleifera seeds in water treatment: Trends and future challenges. Process Safety and Environmental Protection 2021;147:405–20. https://doi.org/10.1016/j.psep.2020.09.044.

[107] Ibrahim A, Yaser AZ, Lamaming J. Synthesising tannin-based coagulants for water and wastewater application: A review. Journal of Environmental Chemical Engineering 2021;9:105007. https://doi.org/10.1016/j.jece.2020.105007.

[108] Bhalkaran S, Wilson LD. Investigation of Self-Assembly Processes for Chitosan-Based Coagulant-Flocculant Systems: A Mini-Review. International Journal of Molecular Sciences 2016;17:1662. https://doi.org/10.3390/ijms17101662.

[109] Renault F, Sancey B, Badot P-M, Crini G. Chitosan for coagulation/flocculation processes – An eco-friendly approach. European Polymer Journal 2009;45:1337–48. https://doi.org/10.1016/j.eurpolymj.2008.12.027.

[110] Owodunni AA, Ismail S. Revolutionary technique for sustainable plant-based green coagulants in industrial wastewater treatment—A review. Journal of Water Process Engineering 2021;42:102096. https://doi.org/10.1016/j.jwpe.2021.102096.

[111] Oladoja NA. Headway on natural polymeric coagulants in water and wastewater treatment operations. Journal of Water Process Engineering 2015;6:174–92. https://doi.org/10.1016/j.jwpe.2015.04.004.

[112] Sharma A, Singh MR. A Review on Historical Earth Pigments Used in India's Wall Paintings. Heritage 2021;4:1970–94. https://doi.org/10.3390/heritage4030112.

[113] Hradil D, Grygar T, Hradilová J, Bezdička P. Clay and iron oxide pigments in the history of painting. Applied Clay Science 2003;22:223–36. https://doi.org/10.1016/S0169-1317(03)00076-0.

[114] Emerson D. Haematite: the Bloodstone. Preview 2017;2017:43–53. https://doi.org/10.1071/PVv2017n191p43.

[115] MacDonald BL, Stalla D, He X, Rahemtulla F, Emerson D, Dube PA, et al. Hunter-Gatherers Harvested and Heated Microbial Biogenic Iron

Oxides to Produce Rock Art Pigment. Sci Rep 2019;9:17070. https://doi.org/10.1038/s41598-019-53564-w.

[116] Doménech-Carbó MT, Vázquez de Agredos-Pascual ML, Osete-Cortina L, Doménech-Carbó A, Guasch-Ferré N, Vidal-Lorenzo C. Funerary colors in Pre-classical Maya culture: the red pigment in the 19th tomb of Rio Azul (Peten, Guatemala). Heritage Science 2020;8:47. https://doi.org/10.1186/s40494-020-00386-z.

[117] Affat SS. Classifications, Advantages, Disadvantages, Toxicity Effects of Natural and Synthetic Dyes: A review. University of Thi-Qar Journal of Science 2021;8:130–5.

[118] Jansen M, Letschert HP. Inorganic yellow-red pigments without toxic metals. Nature 2000;404:980–2. https://doi.org/10.1038/35010082.

[119] The Prehistoric Paintings of the Pachmarhi Hills n.d. https://www.bradshawfoundation.com/india/pachmarhi/index.php (accessed December 19, 2022).

[120] The Cave Art Paintings of the Lascaux Cave n.d. https://www.bradshawfoundation.com/lascaux/ (accessed December 19, 2022).

[121] Fazlzadeh M, Rahmani K, Zarei A, Abdoallahzadeh H, Nasiri F, Khosravi R. A novel green synthesis of zero valent iron nanoparticles (NZVI) using three plant extracts and their efficient application for removal of Cr(VI) from aqueous solutions. Advanced Powder Technology 2017;28:122–30. https://doi.org/10.1016/j.apt.2016.09.003.

[122] Devatha CP, K J, Patil M. Effect of Green synthesized iron nanoparticles by Azardirachta Indica in different proportions on antibacterial activity. Environmental Nanotechnology, Monitoring & Management 2018;9:85–94. https://doi.org/10.1016/j.enmm.2017.11.007.

[123] Geneti ST, Mekonnen GA, Murthy HCA, Mohammed ET, Ravikumar CR, Gonfa BA, et al. Biogenic Synthesis of Magnetite Nanoparticles Using Leaf Extract of *Thymus schimperi* and Their Application for Monocomponent Removal of Chromium and Mercury Ions from Aqueous Solution. Journal of Nanomaterials 2022;2022:e5798824. https://doi.org/10.1155/2022/5798824.

[124] Kumar B, Smita K, Cumbal L, Debut A. Biogenic synthesis of iron oxide nanoparticles for 2-arylbenzimidazole fabrication. Journal of Saudi Chemical Society 2014;18:364–9. https://doi.org/10.1016/j.jscs.2014.01.003.

[125] Saranya S, Vijayarani K, Pavithra S. Green Synthesis of Iron Nanoparticles using Aqueous Extract of Musa ornata Flower Sheath against Pathogenic Bacteria. Indian Journal of Pharmaceutical Sciences 2017;79:688–94. https://doi.org/10.4172/pharmaceutical-sciences.1000280.

[126] Jena A, Kumar Sahoo P, Ghosal A, Kumar Sahoo N. Bioinspired synthesis of iron-based nanomaterials and nanocomposite: For environmental remediation. Materials Today: Proceedings 2022;67:1090–6. https://doi.org/10.1016/j.matpr.2022.07.058.

[127] Bhuiyan MdSH, Miah MY, Paul SC, Aka TD, Saha O, Rahaman MdM, et al. Green synthesis of iron oxide nanoparticle using Carica papaya leaf extract: application for photocatalytic degradation of remazol yellow RR dye and antibacterial activity. Heliyon 2020;6:e04603. https://doi.org/10.1016/j.heliyon.2020.e04603.

[128] Mohan Kumar K, Mandal BK, Siva Kumar K, Sreedhara Reddy P, Sreedhar B. Biobased green method to synthesise palladium and iron nanoparticles using Terminalia chebula aqueous extract. Spectrochimica Acta Part A: Molecular and Biomolecular Spectroscopy 2013;102:128–33. https://doi.org/10.1016/j.saa.2012.10.015.

[129] Lingamdinne LP, Vemula KR, Chang Y-Y, Yang J-K, Karri RR, Koduru JR. Process optimization and modeling of lead removal using iron oxide nanocomposites generated from bio-waste mass. Chemosphere 2020;243:125257. https://doi.org/10.1016/j.chemosphere.2019.125257.

[130] Lingamdinne LP, Koduru JR, Rao Karri R. Green Synthesis of Iron Oxide Nanoparticles for Lead Removal from Aqueous Solutions. Key Engineering Materials 2019;805:122–7. https://doi.org/10.4028/www.scientific.net/KEM.805.122.

[131] Yew YP, Shameli K, Miyake M, Kuwano N, Bt Ahmad Khairudin NB, Bt Mohamad SE, et al. Green Synthesis of Magnetite (Fe3O4) Nanoparticles Using Seaweed (Kappaphycus alvarezii) Extract. Nanoscale Research Letters 2016;11:276. https://doi.org/10.1186/s11671-016-1498-2.

[132] Sathya K, Saravanathamizhan R, Baskar G. Ultrasound assisted phytosynthesis of iron oxide nanoparticle. Ultrasonics Sonochemistry 2017;39:446–51. https://doi.org/10.1016/j.ultsonch.2017.05.017.

[133] Phumying S, Labuayai S, Thomas C, Amornkitbamrung V, Swatsitang E, Maensiri S. Aloe vera plant-extracted solution hydrothermal synthesis and magnetic properties of magnetite (Fe3O4) nanoparticles. Appl Phys A 2013;111:1187–93. https://doi.org/10.1007/s00339-012-7340-5.

[134] Ramalingam V, Dhinesh P, Sundaramahalingam S, Rajaram R. Green fabrication of iron oxide nanoparticles using grey mangrove Avicennia marina for antibiofilm activity and in vitro toxicity. Surfaces and Interfaces 2019;15:70–7. https://doi.org/10.1016/j.surfin.2019.01.008.

[135] de Lima Barizão AC, Silva MF, Andrade M, Brito FC, Gomes RG, Bergamasco R. Green synthesis of iron oxide nanoparticles for tartrazine and bordeaux red dye removal. Journal of Environmental Chemical Engineering 2020;8:103618. https://doi.org/10.1016/j.jece.2019.103618.

[136] Patra JK, Baek K-H. Green biosynthesis of magnetic iron oxide (Fe3O4) nanoparticles using the aqueous extracts of food processing wastes under photo-catalyzed condition and investigation of their antimicrobial and antioxidant activity. Journal of Photochemistry and Photobiology B: Biology 2017;173:291–300. https://doi.org/10.1016/j.jphotobiol.2017.05.045.

[137] Prasad C, Karlapudi S, Venkateswarlu P, Bahadur I, Kumar S. Green arbitrated synthesis of Fe3O4 magnetic nanoparticles with nanorod structure from pomegranate leaves and Congo red dye degradation

studies for water treatment. Journal of Molecular Liquids 2017;240:322–8. https://doi.org/10.1016/j.molliq.2017.05.100.

[138] Bachheti RK, Konwarh R, Gupta V, Husen A, Joshi A. Green Synthesis of Iron Oxide Nanoparticles: Cutting Edge Technology and Multifaceted Applications. In: Husen A, Iqbal M, editors. Nanomaterials and Plant Potential, Cham: Springer International Publishing; 2019, p. 239–59. https://doi.org/10.1007/978-3-030-05569-1_9.

[139] Bibi I, Nazar N, Ata S, Sultan M, Ali A, Abbas A, et al. Green synthesis of iron oxide nanoparticles using pomegranate seeds extract and photocatalytic activity evaluation for the degradation of textile dye. Journal of Materials Research and Technology 2019;8:6115–24. https://doi.org/10.1016/j.jmrt.2019.10.006.

[140] Miri A, Khatami M, Sarani M. Biosynthesis, Magnetic and Cytotoxic Studies of Hematite Nanoparticles. J Inorg Organomet Polym 2020;30:767–74. https://doi.org/10.1007/s10904-019-01245-6.

[141] Ahmmad B, Leonard K, Shariful Islam Md, Kurawaki J, Muruganandham M, Ohkubo T, et al. Green synthesis of mesoporous hematite (α-Fe2O3) nanoparticles and their photocatalytic activity. Advanced Powder Technology 2013;24:160–7. https://doi.org/10.1016/j.apt.2012.04.005.

[142] Hernández-Hernández AA, Aguirre-Álvarez G, Cariño-Cortés R, Mendoza-Huizar LH, Jiménez-Alvarado R. Iron oxide nanoparticles: synthesis, functionalization, and applications in diagnosis and treatment of cancer. Chem Pap 2020;74:3809–24. https://doi.org/10.1007/s11696-020-01229-8.

[143] Izadiyan Z, Shameli K, Miyake M, Hara H, Mohamad SEB, Kalantari K, et al. Cytotoxicity assay of plant-mediated synthesized iron oxide nanoparticles using Juglans regia green husk extract. Arabian Journal of Chemistry 2020;13:2011–23. https://doi.org/10.1016/j.arabjc.2018.02.019.

[144] Venkateswarlu S, Rao YS, Balaji T, Prathima B, Jyothi NVV. Biogenic synthesis of Fe3O4 magnetic nanoparticles using plantain peel extract. Materials Letters 2013;100:241–4. https://doi.org/10.1016/j.matlet.2013.03.018.

[145] Venkateswarlu S, Natesh Kumar B, Prasad CH, Venkateswarlu P, Jyothi NVV. Bio-inspired green synthesis of Fe3O4 spherical magnetic nanoparticles using Syzygium cumini seed extract. Physica B: Condensed Matter 2014;449:67–71. https://doi.org/10.1016/j.physb.2014.04.031.

[146] Atarod M, Nasrollahzadeh M, Mohammad Sajadi S. Green synthesis of Pd/RGO/Fe3O4 nanocomposite using Withania coagulans leaf extract and its application as magnetically separable and reusable catalyst for the reduction of 4-nitrophenol. Journal of Colloid and Interface Science 2016;465:249–58. https://doi.org/10.1016/j.jcis.2015.11.060.

[147] Zambri NDS, Taib NI, Abdul Latif F, Mohamed Z. Utilization of Neem Leaf Extract on Biosynthesis of Iron Oxide Nanoparticles. Molecules 2019;24:3803. https://doi.org/10.3390/molecules24203803.

[148] Nurbas M, Ghorbanpoor H, Avci H. AN ECO-FRIENDLY APPROACH TO SYNTHESIS AND CHARACTERIZATION OF MAGNETITE (Fe3O4) NANOPARTICLES USING PLATANUS ORIENTALIS L. LEAF EXTRACT n.d.

[149] Kumar B, Smita K, Cumbal L, Debut A, Galeas S, Guerrero VH. Phytosynthesis and photocatalytic activity of magnetite (Fe3O4) nanoparticles using the Andean blackberry leaf. Materials Chemistry and Physics 2016;179:310–5. https://doi.org/10.1016/j.matchemphys.2016.05.045.

[150] Koli RR, Phadatare MR, Sinha BB, Sakate DM, Ghule AV, Ghodake GS, et al. Gram bean extract-mediated synthesis of Fe3O4 nanoparticles for tuning the magneto-structural properties that influence the hyperthermia performance. Journal of the Taiwan Institute of Chemical Engineers 2019;95:357–68. https://doi.org/10.1016/j.jtice.2018.07.039.

[151] El-Gendy NSh, Nassar HN. Biosynthesized magnetite nanoparticles as an environmental opulence and sustainable wastewater treatment. Science of The Total Environment 2021;774:145610. https://doi.org/10.1016/j.scitotenv.2021.145610.

[152] Cai Y, Shen Y, Xie A, Li S, Wang X. Green synthesis of soya bean sprouts-mediated superparamagnetic Fe3O4 nanoparticles. Journal of Magnetism and Magnetic Materials 2010;322:2938–43. https://doi.org/10.1016/j.jmmm.2010.05.009.

[153] Nnadozie EC, Ajibade PA. Green synthesis and characterization of magnetite (Fe3O4) nanoparticles using Chromolaena odorata root extract for smart nanocomposite. Materials Letters 2020;263:127145. https://doi.org/10.1016/j.matlet.2019.127145.

[154] Barzinjy AA, Abdul DA, Hussain FHS, Hamad SM. Green synthesis of the magnetite (Fe3O4) nanoparticle using Rhus coriaria extract: a reusable catalyst for efficient synthesis of some new 2-naphthol bis-Betti bases. Inorganic and Nano-Metal Chemistry 2020;50:620–9. https://doi.org/10.1080/24701556.2020.1723027.

[155] Fahmy HM. Oxidative Impact of Carob Leaf Extract–Synthesized Iron Oxide Magnetic Nanoparticles on the Kidney, Liver, Testis, and Spleen of Wistar Rats. BioNanoSci 2020;10:54–61. https://doi.org/10.1007/s12668-019-00704-1.

[156] El-Kassas HY, Aly-Eldeen MA, Gharib SM. Green synthesis of iron oxide (Fe3O4) nanoparticles using two selected brown seaweeds: Characterization and application for lead bioremediation. Acta Oceanol Sin 2016;35:89–98. https://doi.org/10.1007/s13131-016-0880-3.

[157] Wang X, Zhao Y, Jiang X, Liu L, Li X, Li H, et al. In-situ self-assembly of plant polyphenol-coated Fe3O4 particles for oleaginous microalgae harvesting. J Environ Manage 2018;214:335–45. https://doi.org/10.1016/j.jenvman.2018.03.019.

[158] The efficiency of activated carbon/magnetite nanoparticles composites in copper removal: Industrial waste recovery, green synthesis, characterization, and adsorption-desorption studies | Elsevier Enhanced Reader n.d. https://doi.org/10.1016/j.micromeso.2020.110692.

[159] Rehman AU, Nazir S, Irshad R, Tahir K, ur Rehman K, Islam RU, et al. Toxicity of heavy metals in plants and animals and their uptake by magnetic iron oxide nanoparticles. Journal of Molecular Liquids 2021;321:114455. https://doi.org/10.1016/j.molliq.2020.114455.

[160] Bhateria R, Singh R. A review on nanotechnological application of magnetic iron oxides for heavy metal removal. Journal of Water Process Engineering 2019;31:100845. https://doi.org/10.1016/j.jwpe.2019.100845.

[161] Lung I, Stan M, Opris O, Soran M-L, Senila M, Stefan M. Removal of Lead(II), Cadmium(II), and Arsenic(III) from Aqueous Solution Using Magnetite Nanoparticles Prepared by Green Synthesis with Box–Behnken Design. Analytical Letters 2018;51:2519–31. https://doi.org/10.1080/00032719.2018.1446974.

[162] Lingamdinne LP, Vemula KR, Chang Y-Y, Yang J-K, Karri RR, Koduru JR. Process optimization and modeling of lead removal using iron oxide nanocomposites generated from bio-waste mass. Chemosphere 2020;243:125257. https://doi.org/10.1016/j.chemosphere.2019.125257.

[163] Fahmy HM, Mohamed FM, Marzouq MH, Mustafa ABE-D, Alsoudi AM, Ali OA, et al. Review of Green Methods of Iron Nanoparticles Synthesis and Applications. BioNanoSci 2018;8:491–503. https://doi.org/10.1007/s12668-018-0516-5.

[164] Sebastian A, Nangia A, Prasad MNV. Cadmium and sodium adsorption properties of magnetite nanoparticles synthesized from Hevea brasiliensis Muell. Arg. bark: Relevance in amelioration of metal stress in rice. Journal of Hazardous Materials 2019;371:261–72. https://doi.org/10.1016/j.jhazmat.2019.03.021.

[165] Biogenic reductive preparation of magnetic inverse spinel iron oxide nanoparticles for the adsorption removal of heavy metals | Elsevier Enhanced Reader n.d. https://doi.org/10.1016/j.cej.2016.08.067.

[166] Devi AP, Mishra PM, Pothal JK, Ramasamy B, Pradhan N. Sustainable synthesis of emerging bio-based magnetite nanoparticles for efficient removal of Cr(VI) from groundwater. Biomass Conv Bioref 2022. https://doi.org/10.1007/s13399-022-02863-w.

[167] Geneti ST, Mekonnen GA, Murthy HCA, Mohammed ET, Ravikumar CR, Gonfa BA, et al. Biogenic Synthesis of Magnetite Nanoparticles Using Leaf Extract of Thymus schimperi and Their Application for Monocomponent Removal of Chromium and Mercury Ions from Aqueous Solution. Journal of Nanomaterials 2022;2022:1–15. https://doi.org/10.1155/2022/5798824.

[168] Hassan PB, Rasheed RO, Zargoosh K. Cadmium and Lead Removal from Aqueous Solution Using Magnetite Nanoparticles Biofabricated from *Portulaca oleracea* Leaf Extract. Journal of Nanomaterials 2022;2022:e1024554. https://doi.org/10.1155/2022/1024554.

[169] Ehrampoush MH, Miria M, Salmani MH, Mahvi AH. Cadmium removal from aqueous solution by green synthesis iron oxide nanoparticles with tangerine peel extract. J Environ Health Sci Engineer 2015;13:84. https://doi.org/10.1186/s40201-015-0237-4.

[170] Zondo BZ, Sadare OO, Simate GS, Moothi K. Removal of Pb2+ ions from synthetic wastewater using functionalized multi-walled carbon nanotubes decorated with green synthesized iron oxide-gold nanocomposite. Water SA 2022;48:304–16. https://doi.org/10.17159/wsa/2022.v48.i3.3959.

[171] Garg R, Garg R, Khan MA, Bansal M, Garg VK. Utilization of biosynthesized silica-supported iron oxide nanocomposites for the adsorptive removal of heavy metal ions from aqueous solutions. Environ Sci Pollut Res 2022:1–14. https://doi.org/10.1007/s11356-022-21111-2.

[172] Ghohestani E, Samari F, Yousefinejad S. An efficient removal of methylene blue and lead(II) from aqueous solutions by green synthesized iron oxide/pillared bentonite nanocomposite. Materials Chemistry and Physics 2022;287:126266. https://doi.org/10.1016/j.matchemphys.2022.126266.

[173] Ahmad R, Mirza A. Facile one pot green synthesis of Chitosan-Iron oxide (CS-Fe2O3) nanocomposite: Removal of Pb(II) and Cd(II) from synthetic and industrial wastewater. Journal of Cleaner Production 2018;186:342–52. https://doi.org/10.1016/j.jclepro.2018.03.075.

[174] Kataria N, Garg VK. Green synthesis of Fe3O4 nanoparticles loaded sawdust carbon for cadmium (II) removal from water: Regeneration and mechanism. Chemosphere 2018;208:818–28. https://doi.org/10.1016/j.chemosphere.2018.06.022. magnetic anisotropy

[175] Mariani FQ, Borth KW, Müller M, Dalpasquale M, Anaissi FJ. Sustainable innovative method to synthesize different shades of iron oxide pigments. Dyes and Pigments 2017;137:403–9. https://doi.org/10.1016/j.dyepig.2016.10.024.

[176] Prim SR, Folgueras MV, de Lima MA, Hotza D. Synthesis and characterization of hematite pigment obtained from a steel waste industry. Journal of Hazardous Materials 2011;192:1307–13. https://doi.org/10.1016/j.jhazmat.2011.06.034.

[177] Koopi H, Buazar F. A novel one-pot biosynthesis of pure alpha aluminum oxide nanoparticles using the macroalgae Sargassum ilicifolium: A green marine approach. Ceramics International 2018;44:8940–5. https://doi.org/10.1016/j.ceramint.2018.02.091.

[178] Hasanpoor M, Fakhr Nabavi H, Aliofkhazraei M. Microwave-Assisted Synthesis of Alumina Nanoparticles Using Some Plants Extracts. Journal of Nanostructures 2017;7:40–6. https://doi.org/10.22052/jns.2017.01.005.

[179] Ansari MA, Khan HM, Alzohairy MA, Jalal M, Ali SG, Pal R, et al. Green synthesis of Al2O3 nanoparticles and their bactericidal potential against clinical isolates of multi-drug resistant Pseudomonas aeruginosa. World J Microbiol Biotechnol 2015;31:153–64. https://doi.org/10.1007/s11274-014-1757-2.

[180] Atrak K, Ramazani A, Taghavi Fardood S. Green synthesis of amorphous and gamma aluminum oxide nanoparticles by tragacanth gel and comparison of their photocatalytic activity for the degradation of

organic dyes. J Mater Sci: Mater Electron 2018;29:8347–53. https://doi.org/10.1007/s10854-018-8845-2.

[181] Sutradhar P, Debnath N, Saha M. Microwave-assisted rapid synthesis of alumina nanoparticles using tea, coffee and triphala extracts. Adv Manuf 2013;1:357–61. https://doi.org/10.1007/s40436-013-0043-0.

CHAPTER 2

MATERIALS AND METHODS

> Science, for me, gives a partial explanation for life.
> In so far as it goes, it is based on fact, experience, and experiment.
>
> \- Rosalind Franklin

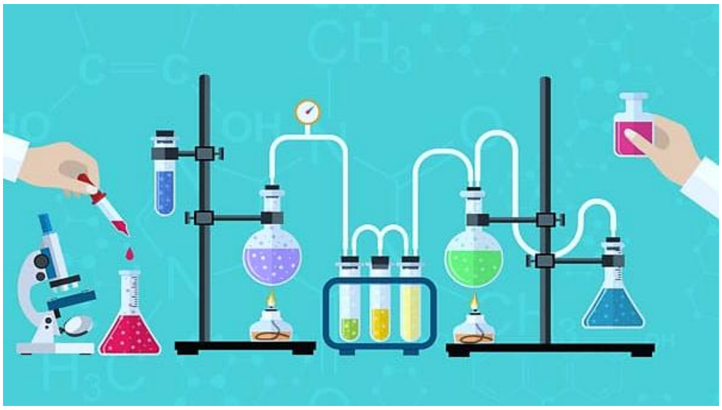

The rising need for sustainable and ethical alternatives in chemistry led chemists to explore and experiment with different bioactive compounds derived from plants, algae, fungi, and bacteria to procure efficient nano-metal/metal oxide systems. Owing to the eternal supply and diversity, plant parts remain to be the major source for yielding green reagents for nanoparticle synthesis. This chapter familiarizes the three plants used for procuring IONPs and alumina NPs, their extraction & phytochemistry, ecological and ethnomedicinal reputation. The chapter also discusses the set of analytical tools used in the study.

2.1 Chemicals used

The work explores the possible utilization, of three plants which belong to the list of ‘World’s 100 worst alien invasive species’ prepared by IUCN. *Chromolaena odorata, Hemigraphis alternata* and *Sphageneticola trilobata* were chosen for the study owing to their invasive nature. The plants were collected from the localities of the University of Calicut. The particulars of each plant were identified by Prof. Pradeep A. K., Department of Botany, University of Calicut. The plant specimens were deposited at the Calicut University Herbarium (CALI) for future reference.

Table 1. List of chemicals used for the synthesis of NPs

Sl. No	Name of the Compound	Molecular formula	Purity	Manufacturer
1	Aluminium chloride	$AlCl_3$	98%	Avra
2	Aluminium nitrate nonahydrate	$Al(NO_3)_3.9H_2O$	98%	Merck
3	Aluminium sulfate 16 hydrate	$Al_2(SO_4)_3.16H_2O$	98%	Merck
4	Ferric chloride hexahydrate	$FeCl_3.6H_2O$	99.9%	Merck
5	Sodium bicarbonate	$NaHCO_3$	98%	Merck

Table 2. List of chemicals used in water remediation studies

Sl. No	Name	Molecular formula	Purity	Manufacturer
1	Acetone	CH_3COCH_3	99.5%	Merck
2	Ammonium fluoride	NH_4F	99.9%	Merck
3	Congo red	$C_{32}H_{22}N_6Na_2O_6S_2$	99.9%	Merck

4	1,5-Diphenylcarbazide	$((C_6H_5)NHNH)_2CO$	99.9%	Merck
5	Ethanol	C_2H_5OH	99.5%	Merck
6	Hydrochloric acid	HCl	99.8%	Merck
7	Lead nitrate	$Pb(NO_3)_2$	99.5%	Merck
8	Potassium dichromate	$K_2Cr_2O_7$	99.5%	Merck
9	Sodium hydroxide	$NaOH$	98%	Merck
10	SPADNS reagent		99.9%	Merck
11	Conc. Sulphuric acid	H_2SO_4	98%	Merck

2.2 Plants used in the study

A non-native organism that triggers detrimental ecological or economic changes in a new environment is called an invasive species. These species can harm the natural resources in an ecosystem and alter the ecosystem's services. Invasive species compete with native organisms for limited resources and endanger native plants and animals, reducing biodiversity. Invasive species are widely accepted as one of the leading direct causes of biodiversity loss[1]. Loss of food resources, reduction in crop yield and climatic changes are the major concerns posed by aggressive plants. Alien Invasive Species (AIS) demands worldwide attention as being the second most important irreversible impact on landscapes next to habitat destruction[2]. Despite the overwhelming evidence of these impacts and a growing appreciation for ecosystem services, researchers and policymakers rarely address the direct connection between invasions and ecosystem services. Globally, various attempts have been made to account and address the ecosystem processes that are affected by invasive species.

Kerala Forest Research Institute (KFRI), Peechi has identified 38 alien invasive species in the forests of Kerala out of which 10 are of high risk. Few of the plants included in this list are *Acacia mearnsii*, *Chromolaena odorata, Lantana camara, Merrimia vitifolia, Spahgeneticola trilobata and Mucuna bracteate.* Some of these species were introduced owing to their nitrogen fixing ability and for ornamental purposes. However, the high adapting capacity and wide ecological tolerance of these plants enabled their invasive growth. The report says that for those AIS which have established themselves in large tracts, manual removal would be laborious and impractical. The use of herbicides to control these weeds pose another major environmental concern. Therefore, systematic restoration strategies should be taken up as follows: i) Identifying probable uses of the AIS. ii) Prepare a management plan which includes the use of the AIS, products which can be made, marketing structures, and its economics. A new study at KFRI has identified that the recent floods and landslides in Kerala have released/reintroduced several invasive species of plants into the State's water bodies, posing a threat to the native[2].

With their extensive impact on native biodiversity and landscape levels, AIS is an important concern in the forests of Kerala which warrants immediate action. In this work we intend to explore the abundance of two invasive species, *Chromolaena odorata* and *Sphageneticola trilobata* (Fig 1a, b) in the state, to produce tailormade materials for environmental and personal applications, sustainably. The study also investigates another potential weed, *Hemigraphis alternata* (Fig 1c).

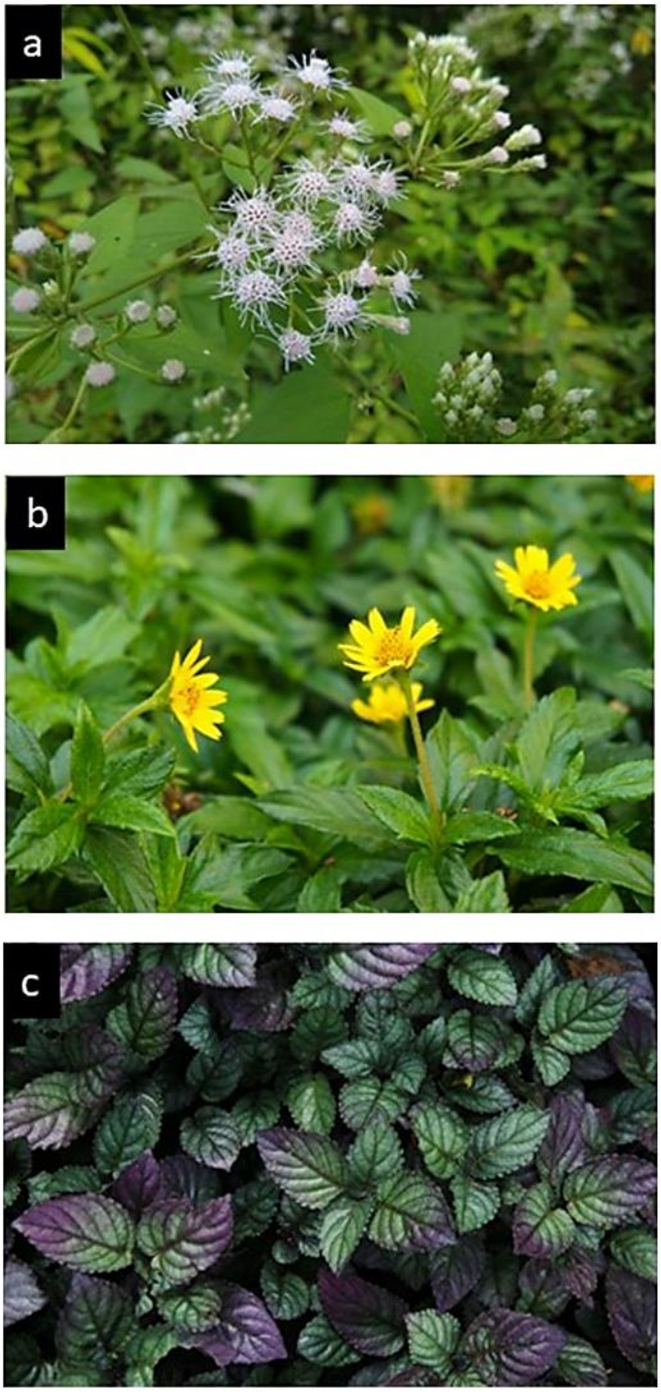

Fig.1. a) *Chromolaena odorata* b) *Sphageneticola trilobata*
c) *Hemigraphis alternata*

2.2.1 *Chromolaena odorata*

Chromolaena odorata (Asteraceae family), commonly known as Siam weed (Communist pacha), is a perennial shrub, native to South America and Central America. The plant was introduced to tropical Asia, West Africa, and parts of Australia where it is considered a noxious weed and is listed in the '100 of the world's worst invasive alien species' by the Global Invasive Species Database (IUCN, GISD)[3]. *C. odorata* might have reached India via introduction to the Calcutta Botanic Garden (now known as Acharya Jagadish Chandra Bose Indian Botanic Garden) in West Bengal. A study conducted by researchers at KFRI suggests that Siam weed made its way to the state mainly through the returning laborers who were recruited to Assam by the British government and agencies for World War II[4]. The plant forms a bushy habit with very dense thicket thriving in almost pure stands and is now found in abundance across India[3]. The ability of the plant to thrive in a wide range of soils and habitats makes it a nuisance in agricultural and commercial plantations. Flowering is seasonal and generally occurs in the summer followed by enormous seed production. The seeds are wind-disseminated and can survive up to 6 years in the soil. Prolific reproduction, fast growth, efficient root system, phenotypic plasticity and branching habit of *C. odorata* suppresses other species[5]. A preliminary study conducted in Kerala revealed the ability of the phytochemicals in the plant to prevent seed germination[6]. Depending on the intensity of the summer season large areas covered with *C. odorata* also pose severe fire hazards because of the presence of volatile oils in stems and leaves[7]. In Asia and Africa, the plant is popular for its ethnomedicinal uses. Recently various parts of the plant are investigated for their wound healing[8,9], antioxidant, antimicrobial[10], and anticancer properties[11,12]. Several mechanical, chemical, and biological control methods have been adopted to restrict the environmental and economic impact of *C. odorata*. Fig.2 represents the herbarium specimen of the plant.

CALICUT UNIVERSITY HERBARIUM (CALI)
Department of Botany, Calicut University, Kerala - 673 635, India
No. 148269 Date. 6/01/2022 Alt.
Locality. C.U Campus, Malappuram District
Name. Chromolaena odorata (L.) King & Robins.
Family. Asteraceae
Notes.
Coll. Julia Garvasis Det.
CUP/9174/12/100X500

Fig. 2. Herbarium specimen of *Chromolaena odorata (L) King & Robins.*

2.2.2 *Sphageneticola trilobata*

Sphageneticola trilobata or Singapore daisy (Asteraceae family) is a herbaceous perennial with bright yellow flowers contrasting its shiny green leaves. It's native to tropical America and has spread rapidly threatening the native flora in many countries after its introduction as an ornamental species[13]. It can propagate through seeds and stem cuttings. Generally, the propagules are spread intentionally across the ground to develop thick carpets in gardens and plantations. The plant has appreciable ornamental value in setting landscapes which is the main reason behind its deliberate spreading. However, the live stem cuttings, when disposed carelessly cause unintended aggressive growth under favorable conditions, making the spread nearly uncontrollable.

S. trilobata has a history of repeated introductions outside its natural range and is becoming widely naturalized throughout the tropics. It is a noxious weed in agricultural areas, along roadsides and trails, in open areas, waste ground, irrigated lawns, rubbish dumps, natural grasslands and disturbed sites. *S. trilobata* has become naturalized along rivers, canals, the margins of mangrove forests and in coastal vegetation. The plant can thrive in wide variety of conditions and will cover dry rocky land or wet drainage ditches and tolerates some degree of trampling. It can destroy crops, reduce water availability, and soil fertility in its region of invasion. The allelopathic effects of the plant is a hot topic under investigation[6].

The IUCN has listed *S. trilobata* in its 100 of the world's worst invasive alien species[13]. The species, which can pose serious environment and biodiversity threat, has found mention in the list of invasive species prepared by the Kerala State Biodiversity Board and the Handbook of Invasive Species of Kerala. It was also featured in the list of Invasive Alien Plants in the Asia Pacific region. In the Kerala handbook, the species was included in the red category, considering the high risk posed by it [2]. This species continues to be available as an ornamental and is therefore likely to spread further. However, several countries have started implementing plans to eradicate it. Recently, an attempt to beautify the Cochin International airport, India using *S. trilobata* ground cover was vehemently opposed by botanists considering its invasive and allelopathic capacity[14]. Fig.3 represents the herbarium specimen of the collected sample.

No. 7085

CALICUT UNIVERSITY HERBARIUM (CALI)
Department of Botany, Calicut University, Kerala - 673 635, India
No. Date 15/12/2021 Alt.
Locality C.U Campus , Malappuram (Dist)
Name Spageneticola trilobata(L.) Pruski; Nem
Family Astoraceae
Notes
Coll. Julia Garvasis Det.
CUP/9174/12/100X500

Fig.3. Herbarium specimen of *Spageneticola trilobata(L) Pruski; Nem*

2.2.3 *Hemigraphis alternata*

Hemigraphis alternata or red flame ivy is an ornamental plant known for its dense attractive foliage in the Acanthaceae family. The local name of the plant is ‘murikootti’ and in ayurveda it’s called ‘vranaropani’; both names literally translate to ‘wound healer’ which reveals the commendable wound healing properties of the plant. Fig. 4 shows the herbarium specimen of the plant. *H. alternata* is a creeping herb native to Indonesia and Malaysia that has been widely commercialized as an ornamental plant, mainly due to its metallic green and purple foliage and white flower[15]. It is often planted as a ground cover in gardens, but the occasional pruning and dumping of the live stem cuttings in the near area, triggers it’s spread into large areas. Once established, the species grows forming large dense carpets that completely cover the ground, displacing native vegetation particularly in forest and other shaded land.

It has been widely commercialized and introduced as an ornamental plant into tropical and subtropical countries across Asia, America, the Caribbean and into many islands in the Indian and Pacific Ocean. The ethnomedicinal use of the plant is also a cause for its cultivation across the globe. The anti-oxidant, anti-inflammatory potential, hypoglycemic and anti-diabetic properties of *H. alternata* are being investigated rigorously [10,16,17]. Although the plant does not show aggressive invasion yet, the plant has weedy characteristics and can thrive in shades. Thus, the plant should be handled with care while pruning and transport to avoid potential invasion by the species.

CALICUT UNIVERSITY HERBARIUM (CALI)
Department of Botany, Calicut University, Kerala - 673 635, India

No. Date 15.04.2022 Alt. ± 50m
Locality C. U Campus, Malappuram (Dist), Kerala
Name Hemigraphis alternata (Burm. f.) T. Anderson
Family Acanthaceae
Notes Cultivated ornamental foliage plant. Often used in medicine to cure fresh wounds.
Coll. Julia Gervasis Det. AK Pradeep.
CUP/9174/12/100X500

No. 7112

Fig.4. Herbarium specimen of *Hemigraphis alternata* (Burm. F.) T. Anderson

All three plants discussed in this study are widely distributed across continents (Fig.5) and can damage the native biodiversity and alter the ecosysytem services to a large extent.

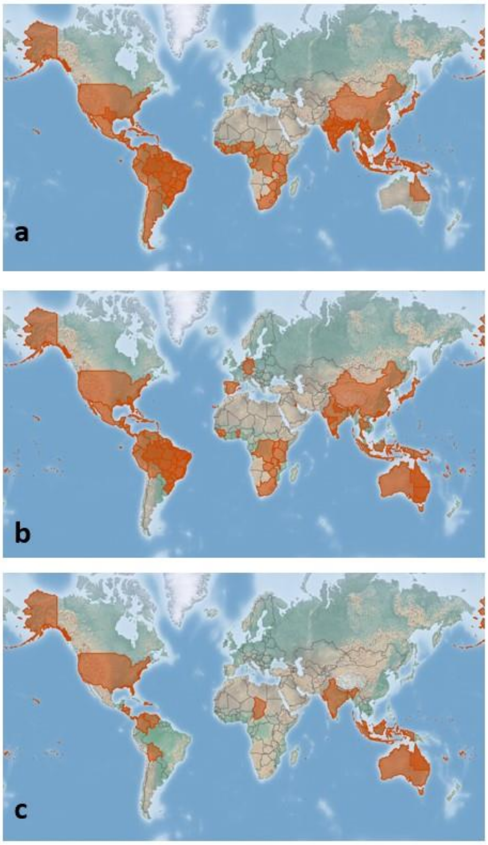

Fig.5. Global distribution of a) *C. odorata*, b) *S. trilobata* and c) *H. Colorata* as per CABI database

2.3 Preparation of the phytoreagents

The foraged leaves/flowers were washed thoroughly in tap water to remove any soil or debris. Selected healthy/uninfected leaves/flowers were stripped off from the stem and desiccated naturally. To prepare the extract, ~10g of desiccated plant-parts were added into ~150mL of double distilled water in a glass vessel and then stirred magnetically for 3 hours, at 80^{0}C to obtain the decoction. The temperature of the system was maintained at 40^{0}C overnight for effective leaching of phytochemicals into the solvent. The cooled crude mixture was then strained through a folded muslin cloth to obtain the plant extract. The mixture was kept at 4^0C before use and was used within two weeks of preparation.

2.4 Primary phytochemical analysis

Standard qualitative analysis was carried out to identify the presence of various secondary metabolites such as alkaloids, terpenoids, polyphenols, tannins, resins, flavonoids and saponins, in aqueous extracts of leaves of plants following reports given elsewhere[18-20].

2.4.1 Test for alkaloids

To a few ml of each plant sample extract, two drops of Mayer's reagent was added along the sides of test tube. The appearance of white creamy precipitate indicates the presence of alkaloids.

2.4.2 Test for polyphenols

a) To 5 mL of dilute extract few drops of neutral 5% ferric chloride solution was added. A dark green colour indicates the presence of phenolic compounds. b) To an aqueous solution of the extract 10% ammonium hydroxide solution was added. Yellow fluorescence indicates the presence of flavonoids.

2.4.3 Test for saponins

The diluted extract was shaken in a graduated cylinder for 15 minutes. A two cm layer of foam indicates the presence of saponins.

2.4.4 Test of tannins

The diluted extract was boiled in a vial and then filtered. In the filtrate 0.1% $FeCl_3$ solution was added and the appearance of brownish green colour shows the presence of tannins.

2.4.5 Test of steroids

To 2ml of extract, H_2SO_4 and acetic anhydride (2mL each) were mixed in a test tube and reaction mixture. The change in colour from violet to bluish green shows the presence of steroids in the extract.

2.4.6 Test of terpenoids

Terpenoid content was determined by mixing 5mL of the extract with chloroform (2mL) and concentrated H_2SO_4 (3mL). The reaction mixture was continuously stirred, formation of reddish-brown colour shows the absence of terpenoids or terpenes.

2.4.7 Test of glycosides

To the 1mL of the extract, 1mL of conc. sulphuric acid is added and allowed to stand for 2 min, a reddish colour precipitate shows the presence of glycosides.

2.4.8 Test for fixed oils and fats - spot test

A small quantity of extract is pressed between two filter papers. Oil stain on the paper indicates the presence of fixed oils.

2.4.9 Test for gum and mucilage

To the extract, 2mL of absolute alcohol is added with constant stirring. White or cloudy precipitate indicates the presence of gums/mucilage.

2.4.10 Total phenol content

Total phenol content of the extracts was determined using the Folin-Ciocalteu (FC) method with some modifications. From a gallic acid stock solution (0.5g/L), a range of methanolic solutions has been prepared (0–200 µg/ml). 200µL of the plant extract is mixed with 1mL of the FC reagent (10%), after 20 min incubation in the dark, 800µL Na_2CO_3 (7.5% (w/v)) is added. The mixture is stirred and incubated in the dark room at temperature for 3 h and the absorbance is measured at 765nm by a UV spectrophotometer. The results are expressed in µg gallic acid equivalent/mg dry plant matter by reference to the calibration curve of gallic acid[21].

2.4.11 Total flavonoid content

To determine the total flavonoid content of the plant extracts 500µl of each plant extract is added to 1500µL of methanol (95 %),100µL $AlCl_3$ (10% (m/v), 100µL CH_3COONa (1M) and 2.8mL distilled water. The mixture is stirred and incubated in the dark room at temperature for 1h. The absorbance is measured at 415nm using a UV spectrophotometer. The results are expressed in µg quercetin equivalent/mg dry plant matter with reference to the quercetin calibration curve[21].

2.5 Characterization techniques

Proper characterization is the basis of the advancement and largescale implementation of nanotechnology. This section introduces assorted nanomaterial characterization techniques adopted in this work.

2.5.1 UV-Visible spectroscopy

UV-Visible spectroscopy is a frequently used analytical technique in material characterization and is vital for analyzing the optical properties of materials. It measures the number of discrete wavelengths of UV or visible light that are absorbed by or transmitted through a solid/liquid sample in comparison to a reference. This property is primarily influenced by the sample composition and provides crucial information regarding the constitution of the sample and its concentration. The analysis provides both qualitative and quantitative information on nanoparticle characterization[22]. It helps in deducing sample interaction in case of analytical studies like adsorption and coagulation. It's an economical, versatile, rapid, and facile characterization technique used in nanomaterial studies. The study used a JascoV-770 UV-Vis-NIR spectrophotometer available at the Dept. of Chemistry, University of Calicut for characterization and analytical investigations.

2.5.2 FTIR spectroscopy

Fourier transform infrared spectroscopy (FTIR) is another familiar analytical technique for qualitative analysis. It uses the mathematical process (Fourier transform) to translate the raw data (interferogram) into the actual spectrum. The spectrum reveals crucial information about the functional groups in the sample of concern. Thus, it is frequently employed for surface analysis of samples including nanomaterials[23,24]. FTIR can identify the transformation of precursors to targeted nanomaterials and can recognize specific interactions between the nanomaterials and biomolecules/dye/heavy metal ions. FTIR can aid in the identification of the surface-active sites responsible for surface reactivity. The work employed a Jasco FTIR-4600 spectrophotometer, available at the Dept. of Chemistry, University of Calicut for characterization and analytical purposes.

2.5.3 XRD analysis

X-Ray diffraction analysis (XRD) is a non-destructive technique which is based on the constructive interference of monochromatic X-rays and a sample. XRD imparts precise information about the crystallographic structure, average crystallite size, crystal defects, composition heterogeneity, and physical properties of a material. For qualitative analysis, the obtained X-ray diffractogram is compared with existing standard crystallographic databases to identify the phase of the analyzed material. The shape of peaks in the diffractogram provides primary information about the size of the crystallites. In this study, XRD analysis had a major role in the preliminary identification of the phases of synthesized iron oxide nanoparticles[25]. XRD (Malvern PANanalytical) available at CSIF, University of Calicut was used for powder-XRD analysis of materials involved in the study.

2.5.4 SAED analysis

Qualitative selected area electron diffraction (SAED) is used alongside electron microscopy instrument and consists of observation of the pattern of diffraction spots/rings obtained from a randomly oriented particle. The nature of the observed pattern indicates the crystallinity of the material. It also provides information regarding lattice parameters, crystal structure, and orientation. It can be used for the structure determination of unknown samples[26]. Jeol/JEM 2100 high-resolution transmission electron microscope, facilitated by STIC-CUSAT, Kochi, was used for SAED analysis for the study.

2.5.5 ESCA/XPS analysis

X-ray Photoelectron Spectroscopy (XPS) or Electron Spectroscopy for Chemical Analysis (ESCA) is a frequently used sensitive surface analysis technique that can be applied to a wide range of materials and provides valuable quantitative and chemical state information from the surface of the material being analyzed. The average depth of analysis for an XPS measurement is approximately 5-10nm. Although the post-analysis procedures are elaborate and tricky, the binding energy and intensity of photoelectron peaks aid in determining the elemental identity, chemical state, and quantity of a detected element[27]. XPS has found extensive use in the investigation of the surface composition of phytogenic nanomaterials. The instrument at CIF-IISER (XPS, Omicron Nanotechnology), Thiruvananthapuram, Kerala, was used for XPS analysis of the synthesized iron oxide nanoparticles during the study.

2.5.6 EDX Spectroscopy

Energy dispersive X-ray spectroscopy (EDX) is a standard analytical method for the identification and quantification of the surface elemental composition of solid samples. The EDX setup is generally attached to an electron microscopy instrument such as transmission electron microscopy (TEM) or scanning electron microscopy (SEM). EDX profile displays the peaks correlated to the surface elemental composition of the sample. In addition, the elemental mapping of a sample can be created with this characterization technique. EDX offers valuable semi-qualitative and semi-quantitative information about the investigated sample[28]. Energy dispersive X-ray spectroscopy (Bruker Nano X-Flash Detector) at PSG-TECH, Coimbatore and CSIF, University of Calicut was used for EDX analysis of samples involved in this study.

2.5.7 FESEM imaging

Field emission scanning electron microscopy (FESEM) is a topographical analytical tool and provides high-resolution images containing morphological data of the material under investigation[28]. FESEM possesses higher magnification in the range of 10–300,000x which makes it suitable for the characterization of nanomaterials. Carl-Zeiss (Sigma) field emission scanning electron microscope at CSIF, University of Calicut and PSG-TECH Coimbatore was used for FESEM imaging in this study.

2.5.8 HRTEM imaging

High resolution transmission electron microscopy (HRTEM) or phase contrast TEM provides direct imaging of the nanoparticle at the atomic scale. It uses both transmitted and diffracted electron beams to create an interference image, in which the phase contrast of modulated electron waves passing through the sample can be recorded with the resolution down to the angstrom level. HRTEM monitors the interference of the electron beam by the sample, which gives a higher resolution, which is invaluable when studying nanoparticles. This technique is widely used in the advanced characterization of materials, allowing the acquisition of information about crystal structures, defects in the crystal, grain boundaries and individual atoms[25,26]. HRTEM analysis of nanomaterials in the study was carried out at STIC-CUSAT, Kochi on a Jeol/JEM 2100 high-resolution transmission electron microscope.

2.5.9 Zeta potential analysis

Zeta potential, or ζ potential, is an abbreviation for electro kinetic potential in colloidal systems. Zeta potential analysis determines the surface charge of particles in a colloidal solution. Zeta potential is the potential difference between the mobile dispersion medium and the stationary layer of the dispersion medium attached to the dispersed particle[29]. It is determined through velocity measurement of the charged particles moving toward the electrode across the sample solution in the presence of an external electric field. pH plays a crucial role in determining the zeta potential of the NPs or in other words, the zeta potential of NPs changes with pH. The magnitude of the zeta potential predicts the colloidal stability of NPs. Brookhaven PALS zeta potential analyzer Ver.5.60. at INUP, CeNse, IISc, Bangalore was used for the zeta potential analysis of NPs involved in the study.

2.5.10 BET analysis

The Brunauer-Emmett-Teller (BET) method is generally used to compute the specific surface area based on nitrogen adsorption isotherm measurements. This is commonly used to directly determine NPs surface area, pore structure, pore size and pore volume under high vacuum conditions[30]. In a typical BET analysis, NPs surface area is determined from the volume of N_2 gas adsorbed on the NPs. N_2 gas is assumed to have access to the entire NPs surface. The surface area measurements are based on adsorption of gas molecules in infinite layers with no interlayer interaction. Belsorp-mini, Japan, was used for BET analysis of NPs synthesized in this work. Brunauer-Emmett-Teller (BET) analysis (Belsorp) facilitated at CSIF, University of Calicut was used for surface area analysis and porosity determination.

2.5.11 VSM analysis

Vibrating sample magnetometry (VSM) belongs to the direct class of magnetic measuring techniques, where the macroscopic magnetization of the sample is sensed. VSM is a versatile technique for measuring the magnetic moment of the entire sample, when it is vibrated perpendicularly to a uniform magnetizing field. The vibration of the investigated magnetic material within a uniform magnetic field, generates an electric current in properly placed sensing coils. The resulting voltage developed in the sensing coils varies in proportion to the magnetic moment of the specimen. The nature of plot of magnetic field v/s magnetic moment aids in identification of magnetic behavior of the material. The magnetization, hysteresis, and coercivity of ferrimagnetic and ferromagnetic can be accurately determined with this method[31]. Since its introduction, the technique has gained widespread acceptance due to its accuracy, versatility, and ease of use. The present study uses VSM as tool for identifying the magnetic behavior of synthesized IONPs. Lakeshore VSM 7410 at SAIF-IITM was employed for magnetic characterization of the NPs in the study.

2.6 Adsorption experiments

A stock solution of 500mgL^{-1} was prepared for Cr(VI) and Pb(II) in double distilled water for adsorption studies. The adsorptive capacity of two different phytogenic magnetite nanoparticles (PMNPs) against Cr(VI) and Pb(II) were investigated separately. Pilot adsorption studies for optimization of adsorbent dosage were conducted in glass vessels containing 20mL of simulated effluent (100mgL^{-1}) at room temperature using PMNPs as adsorbents. A platform shaker was employed to maximize the adsorbent-adsorbate interaction. At periodic intervals the supernatant solution was recovered under an external magnetic field to analyze the residual heavy metal ion (HMI) concentration. UV/Visible spectroscopy using 1,5 diphenyl carbazide reagent[32] and atomic absorption spectroscopy were used for estimating the residual concentration of Cr(VI) and Pb(II) in the procured analyte respectively.

The equilibrium adsorption capacity (q_e) was calculated as

$$q_e = \frac{(C_0 - C_e)v}{m} \tag{1}$$

where C_0 and C_e are the initial and equilibrium concentration of the HMI under study respectively. Here *v* is the volume of pollutant (ml) considered and *m* denoted the mass (mg) of the adsorbent taken.

Constraints including pH, temperature and initial HMI concentration of the experiments were altered to finalize the optimum conditions to facilitate maximum removal of the HMI. Possible detrimental factors, like the presence of competing ions affecting the adsorption capacity, were also investigated using equimolar mixtures of selected competing ion and the concerned HMI.

For commercial applications regeneration and recyclability of the adsorbent is of prime concern. The magnetic property of the PMNPs facilitated facile separation of the exhausted adsorbent from the bulk solution. The Cr(VI) loaded PMNPs were recovered by rinsing with double distilled water whereas Pb(II) loaded PMNPs were rinsed with HCl (1M). The cleaned PMNPs were dried at 70°C in an air oven before repeating adsorption experiments to estimate changes in adsorption efficiency up on continuous usage.

2.7 Antioxidant assay

Antioxidant activity of all obtained phytogenic iron oxide pigments (PIOPs) were tested by assessing the radical scavenging activity of the test sample against stable 2, 2-diphenyl 2 picrylhydrazyl hydrate (DPPH) according to standard protocol. DPPH reacts with an antioxidant compound, which can donate hydrogen, and reduce DPPH. The change in colour from deep violet to light yellow, was measured at the optical density 515nm on a UV visible spectrophotometer. Ascorbic acid was used as the reference for the study. 200μL of 60μM methanolic solution of DPPH was mixed with 50μl of the test sample at various concentrations (1.5-1500μg/mL). The plates were kept in the dark for 15 minutes at room temperature and the decrease in absorbance was measured at 515nm[21].

Radical scavenging activity was calculated by the following formula

$$\%\,inhibition = \frac{Absorbance\ of\ control - Absorbance\ of\ sample}{Absorbance\ of\ control}\ x\ 100 \quad (2)$$

2.8 Antibacterial studies

Agar well diffusion method was used to evaluate the antimicrobial activity of the PMNPs against different microbes. Inoculums were procured from the Microbial Type Culture Collection and Gene Bank (MTCC) Chandigarh. The culture medium used was Muller Hinton Agar medium (HIMEDIA- M173). 15-20mL of sterilized Mueller-Hinton agar was poured to glass petri plates of the same size. After the solidification of the agar medium, 4 wells/ plate were made with a sterile cork borer of diameter 8mm (20mm apart from one another). The standardized inoculum of the test organism was uniformly spread on the surface of the solidified media using sterile cotton swab. The test volumes (40μL & 80μL from 10mg/mL) of the PMNPs at desired concentrations were added to the first 2 wells, 80mcg of Gentamycin was added to 3rd well as positive control and the last one with DMSO as negative control. Then, the agar plates were incubated in incubator under 37°C for 24 hr. After incubation, clear zone was measured in mm[33].

2.9 *In-vitro* cytotoxicity studies

The cytotoxicity profile was examined using human skin epithelial A431cells. The cell line was acquired from American Type Culture Collection (ATCC) (Manassas, VA, USA). Cells were cultured in DMEM medium supplemented with 10% FBS and 100U/mL penicillin-streptomycin at 37°C. At 85% confluence, cells were harvested using 0.25% trypsin and were sub-cultured into 75 cm^2 96-well plates. Viability of cells after exposure to IONPs was assessed by MTT assay as described by Mossman with some modifications[34]. The MTT assay assesses the mitochondrial function by measuring the ability of viable cells to reduce the yellow tetrazolium salt (3-(4,5-dimethylthiazol-2-yl)-2,5-diphenyltetrazolium bromide or MTT) to purple formazan crystals. The phytogenic pigments were diluted to appropriate concentrations (100-1000µg/mL) via sonication and were then suspended in cell culture for 24 hours. At the end of exposure medium was removed from each well to avoid interference of nanoparticles and replaced with new medium containing MTT solution in an amount equal to 10% of culture volume and incubated for 3 h at 37°C until the formation of purple color. The resulted formazan product was dissolved in acidified isopropanol. Then, a 100µL supernatant was transferred to other fresh wells of 96-well plate and absorbance was measured at 570nm by using a microplate reader.

2.10 Coagulation experiments

Coagulation efficiency of synthesized ASNPs was conducted in a faux jar test setup. A stock solution of 1000mgL^{-1} of congo red and 500mgL^{-1} fluoride was prepared in tap water and diluted accordingly. The optimum coagulant dosage was determined using a 100mgL^{-1} congo red dye and 10mgL^{-1} fluoride solution at pH 7. Weighed coagulant was added to 25ml of the pollutant solution at room temperature. The mixture was initially stirred at 190 rpm for 60 seconds and then at 90 rpm for 2 minutes. After a 30-minute settling period, about 4ml of the supernatant solution was retrieved and filtered to remove any flocs. For monitoring congo red concentration, the clear solution was examined using a Jasco-v-750 UV-Vis spectrophotometer, λm was set to 498nm. Whereas the residual fluoride concentration was monitored spectrophotometrically with the aid of SPADNs reagent at 570 nm[35]. The coagulation efficiency was calculated using the given equation.

$$\%\, Coagulation\ Efficiency = \frac{(C_0 - C)}{C_0}\ x\ 100 \qquad (3)$$

Where C_0 and C represent the initial and final concentration of the pollutant solution, respectively. A Stemi 508 stereomicroscope attached with an axiocam 105 colour cam was employed to attain the optical images of the flocs. The sludge volume index (SVI) was calculated using the given equation.

$$SVI\ (\mathrm{mL}\ g^{-1}) = \frac{Settled\ sludge\ volume\ (mL\ L^{-1})}{Suspended\ solids\ concentration (g\ L^{-1})}\ X\ 1000 \qquad (4)$$

Settled sludge volume was determined from 30-minute settling experiment using a graduated container.

Variation of the coagulation efficiency with variables like initial pollutant concentration (Congo red - 50-200mgL^{-1}, Fluoride - 1-50mgL^{-1}), temperature (30-70^{0}C), and pH (3-9) were also monitored. To monitor the ionic interference and to rule out if any, chosen cations and anions were introduced into the pollutant solution prior to coagulant addition. The efficacy of the AS-6 in the presence of various ions was investigated at optimum constraints.

The settled sludge was collected and dried in an air oven at 70°C for 48 hours to obtain a thin film of sludge. The film was then collected and ground to powder. The powdered sludge was then washed thoroughly with ethanol and water repeatedly to separate out the coagulant from the adhered pollutant molecules. The white slurry of AS-6 so obtained was dried at 100°C to regenerate AS-6 and weighed. The efficiency of the recovered AS-6 was investigated using fresh analyte solutions. The recyclability of the coagulant was monitored for multiple cycles following the same procedure. All the experiments were performed in triplicates.

2.11 Software used for data analysis and drafting.

Sl no.	Name of the software	Purpose
1	XPS41	XPS analysis and plotting
2	Origin Pro	Plotting of graphs, statistical calculations
3	MS office	Drafting, Analytical calculations
4	Adobe photoshop	Schematic illustrations
5	ImageJ	Size distribution analysis, SAED analysis
6	Zotero	Bibliography

References

[1] Charles H, Dukes JS. Impacts of Invasive Species on Ecosystem Services. In: Nentwig W, editor. Biol. Invasions, vol. 193, Berlin, Heidelberg: Springer Berlin Heidelberg; 2007, p. 217–37. https://doi.org/10.1007/978-3-540-36920-2_13.

[2] Sajeev T, Sankaran K, Suresh T. Are Alien Invasive Plants a Threat to Forests of Kerala? n.d.:28.

[3] GISD n.d. http://www.iucngisd.org/gisd/species.php?sc=47 (accessed July 18, 2022).

[4] Communist Pacha's entry to state had political reasons - Times of India. Times India n.d.

https://timesofindia.indiatimes.com/city/kozhikode/communist-pachas-entry-to-state-had-political-reasons/articleshow_new/77771824.cms (accessed July 22, 2022).

[5] Gautier L. Taxonomy and distribution of a tropical weed: Chromolaena odorata (L.) R. King & H. Robinson. Candollea 1992;47:645–62.

[6] Jose AM, Gopi A, Shaji F. Allelopathic Effects of Aqueous Leaf Extracts of Two Invasive Plants (Chromolaena Odorata (L.) R. M. King 8 H. Rob. and Sphagneticola Trilobata (L.) Pruski) on Seed Germination of Amaranthus Cruentus L. J Adv Sci Res 2020;11:198–201.

[7] Macdonald I a. W. Alien trees, shrubs and creepers invading indigenous vegetation in the Hluhluwe-Umfolozi Game Reserve Complex in Natal. Bothalia 1983;14:949–59. https://doi.org/10.4102/abc.v14i3/4.1268.

[8] Pandith H, Zhang X, Liggett J, Min K-W, Gritsanapan W, Baek SJ. Hemostatic and Wound Healing Properties of *Chromolaena odorata* Leaf Extract. ISRN Dermatol 2013;2013:1–8. https://doi.org/10.1155/2013/168269.

[9] Sirinthipaporn A, Jiraungkoorskul W. Wound Healing Property Review of Siam Weed, Chromolaena odorata. Pharmacogn Rev 2017;11:35–8. https://doi.org/10.4103/phrev.phrev_53_16.

[10] Vijayaraghavan K, Rajkumar J, Seyed MA. Phytochemical screening, free radical scavenging and antimicrobial potential of Chromolaena odorata leaf extracts against pathogenic bacterium in wound infections– a multispectrum perspective. Biocatal Agric Biotechnol 2018;15:103–12. https://doi.org/10.1016/j.bcab.2018.05.014.

[11] Olawale F, Olofinsan K, Iwaloye O. Biological activities of Chromolaena odorata: A mechanistic review. South Afr J Bot 2022;144:44–57. https://doi.org/10.1016/j.sajb.2021.09.001.

[12] Adedapo A, Oyagbemi A, Fagbohun O, Omobowale T, Yakubu M. Evaluation of the anticancer properties of the methanol leaf extract of Chromolaena odorata on HT-29 cell line. J Pharmacogn Phytochem E-ISSN 2278-4136 2016;52:52–7.

[13] GISD n.d. http://www.iucngisd.org/gisd/species.php?sc=44 (accessed August 3, 2022).

[14] Sudhi KS. Singapore Daisy could spell doom, warn experts. The Hindu 2020.

[15] Rojas-Sandoval J. Hemigraphis alternata (red ivy). Invasive Species Compendium; 2020. https://doi.org/10.1079/ISC.121880.20203483479.

[16] Adangampurath S, Sudhakaran S. Antiinflammatory potential of flavonoids from Hemigraphis colorata. Int J Life Sci 2018;6:569–74.

[17] Scariya S, Davis D, Hameed J, Babu M. An In-vitro Evaluation on Anthelmintic activity of different extracts of Hemigraphis colorata leaves. Res J Pharm Technol 2019;12:4394–6.

[18] Shaikh JR, Patil M. Qualitative tests for preliminary phytochemical screening: An overview. Int J Chem Stud 2020;8:603–8. https://doi.org/10.22271/chemi.2020.v8.i2i.8834.

[19] Galili S, Hovav R. Determination of Polyphenols, Flavonoids, and Antioxidant Capacity in Dry Seeds. Polyphenols Plants, Elsevier; 2014, p. 305–23. https://doi.org/10.1016/B978-0-12-397934-6.00016-4.

[20] Nguyen MT, Nguyen VT, Le VM, Trieu LH, Lam TD, Bui LM, et al. Assessment of preliminary phytochemical screening, polyphenol content, flavonoid content, and antioxidant activity of custard apple leaves (Annona squamosa Linn.). IOP Conf Ser Mater Sci Eng 2020;736:062012. https://doi.org/10.1088/1757-899X/736/6/062012.

[21] Hayat J, Akodad M, Moumen A, Baghour M, Skalli A, Ezrari S, et al. Phytochemical screening, polyphenols, flavonoids and tannin content, antioxidant activities and FTIR characterization of Marrubium vulgare L. from 2 different localities of Northeast of Morocco. Heliyon 2020;6:e05609. https://doi.org/10.1016/j.heliyon.2020.e05609.

[22] Holbrook RD, Galyean AA, Gorham JM, Herzing A, Pettibone J. Chapter 2 - Overview of Nanomaterial Characterization and Metrology. In: Baalousha M, Lead JR, editors. Front. Nanosci., vol. 8, Elsevier; 2015, p. 47–87. https://doi.org/10.1016/B978-0-08-099948-7.00002-6.

[23] Nasrollahzadeh M, Atarod M, Sajjadi M, Sajadi SM, Issaabadi Z. Plant-Mediated Green Synthesis of Nanostructures: Mechanisms, Characterization, and Applications. Interface Sci. Technol., vol. 28, Elsevier; 2019, p. 199–322. https://doi.org/10.1016/B978-0-12-813586-0.00006-7.

[24] Ismail AA, van de Voort FR, Sedman J. Chapter 4 Fourier transform infrared spectroscopy: Principles and applications. In: Paré JRJ, Bélanger JMR, editors. Tech. Instrum. Anal. Chem., vol. 18, Elsevier; 1997, p. 93–139. https://doi.org/10.1016/S0167-9244(97)80013-3.

[25] Titus D, James Jebaseelan Samuel E, Roopan SM. Chapter 12 - Nanoparticle characterization techniques. In: Shukla AK, Iravani S, editors. Green Synth. Charact. Appl. Nanoparticles, Elsevier; 2019, p. 303–19. https://doi.org/10.1016/B978-0-08-102579-6.00012-5.

[26] Lábár JL. Electron Diffraction Based Analysis of Phase Fractions and Texture in Nanocrystalline Thin Films, Part I: Principles. Microsc Microanal 2008;14:287–95. https://doi.org/10.1017/S1431927608080380.

[27] Engelhard MH, Droubay TC, Du Y. X-Ray Photoelectron Spectroscopy Applications. In: Lindon JC, Tranter GE, Koppenaal DW, editors. Encycl. Spectrosc. Spectrom. Third Ed., Oxford: Academic Press; 2017, p. 716–24. https://doi.org/10.1016/B978-0-12-409547-2.12102-X.

[28] Abd Mutalib M, Rahman MA, Othman MHD, Ismail AF, Jaafar J. Chapter 9 - Scanning Electron Microscopy (SEM) and Energy-Dispersive X-Ray (EDX) Spectroscopy. In: Hilal N, Ismail AF, Matsuura T, Oatley-Radcliffe D, editors. Membr. Charact., Elsevier; 2017, p. 161–79. https://doi.org/10.1016/B978-0-444-63776-5.00009-7.

[29] Shnoudeh AJ, Hamad I, Abdo RW, Qadumii L, Jaber AY, Surchi HS, et al. Chapter 15 - Synthesis, Characterization, and Applications of Metal Nanoparticles. In: Tekade RK, editor. Biomater. Bionanotechnol., Academic Press; 2019, p. 527–612. https://doi.org/10.1016/B978-0-12-814427-5.00015-9.

[30] Scherdel C, Reichenauer G, Wiener M. Relationship between pore volumes and surface areas derived from the evaluation of N2-sorption data by DR-, BET- and t-plot. Microporous Mesoporous Mater 2010;132:572–5. https://doi.org/10.1016/j.micromeso.2010.03.034.

[31] Faraji M, Yamini Y, Salehi N. 3 - Characterization of magnetic nanomaterials. In: Ahmadi M, Afkhami A, Madrakian T, editors. Magn. Nanomater. Anal. Chem., Elsevier; 2021, p. 39–60. https://doi.org/10.1016/B978-0-12-822131-0.00014-5.

[32] Onchoke KK, Sasu SA. Determination of Hexavalent Chromium (Cr(VI)) Concentrations via Ion Chromatography and UV-Vis Spectrophotometry in Samples Collected from Nacogdoches Wastewater Treatment Plant, East Texas (USA). Adv Environ Chem 2016;2016:e3468635. https://doi.org/10.1155/2016/3468635.

[33] Bawazeer S, Rauf A, Shah SUA, Shawky AM, Al-Awthan YS, Bahattab OS, et al. Green synthesis of silver nanoparticles using Tropaeolum majus: Phytochemical screening and antibacterial studies. Green Process Synth 2021;10:85–94. https://doi.org/10.1515/gps-2021-0003.

[34] Young FM, Phungtamdet W, Sanderson BJS. Modification of MTT assay conditions to examine the cytotoxic effects of amitraz on the human lymphoblastoid cell line, WIL2NS. Toxicol In Vitro 2005;19:1051–9. https://doi.org/10.1016/j.tiv.2005.05.001.

[35] How to measure Fluoride: SPADNS Spectrophotometric Method n.d.:26.

CHAPTER 3

Synthesis, characterization, and Cr(VI) and Pb(II) adsorption of PMNPs engineered using *Chromolaena odorata* flower extract

> A neat and orderly laboratory is unlikely.
> It is, after all, so much a place of false starts and multiple attempts.
>
> \- Isaac Asimov

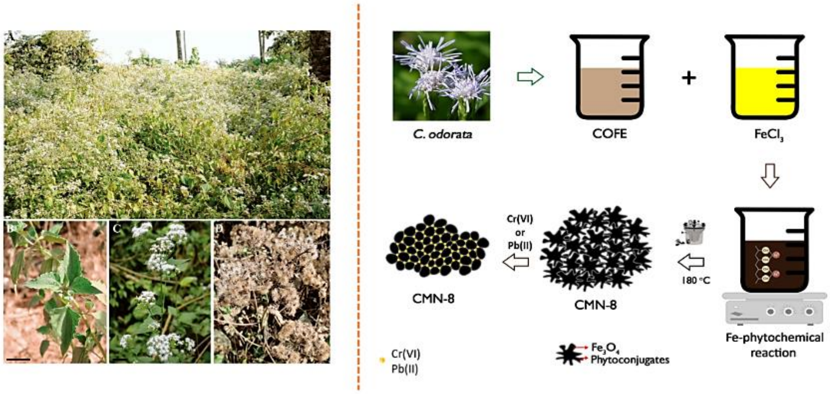

Magnetite, maghemite, and hematite are the most common forms of iron oxides existing naturally. IONPs have potential applications in areas such as magnetic recording, magnetic data storage devices, toners, and inks for xerography, magnetic resonance imaging (MRI), wastewater treatment, bioseparation, theranostics and medicine. Phytogenic synthesis of IONPs produce surface stabilized NPs with active functional groups capable of immobilizing different target molecules.

Erratic climatic events along with alarmingly polluted soil, air, and water, have awakened the communities to the need for safer and sustainable alternatives in different realms of their life. Safer, non-toxic, reusable, renewable and biodegradable replacements are now in the pursuit more than ever. As a part of the community, green chemists are rigorously engaged in substituting corrosive chemicals and hazardous experimental procedures with safe reactants and trouble-free experimental scaffolds. Utilizing phytogenic resources for procuring different metal and metal oxide NPs are highly pursued due to the abundance of versatile raw materials and the simplicity of the procedure[1]. Among the large set of phytogenic metallic/bimetalic oxide NPs, iron oxide nanoparticles (IONPs) hold a special mention owing to their rare combination of electric and magnetic qualities. They are extensively explored for heavy metal removal, data storage devices and biomedical technologies[2,3].

Chromolaena odorata, commonly known as Siam weed, is an invasive, allelopathic tropical species that cause severe impacts on the eco-diversity during its propagation (see Chapter 2). Siam weed extracts are reported to possess appreciable antioxidant properties, iron chelation ability, antimicrobial properties, and minimal cytotoxic effects. About 6000 types of flavonoids have been extracted from *C. odorata* [4,5]. The plant is widely used in traditional medicines against several ailments and wound healing[6]. However, to the best of our knowledge, there are no reports on the reductive and capping abilities of the siam weed flower extracts. This study explores the simultaneous use of the siam weed flower extract as a reductant and a capping agent in the synthesis of *C. odorata* derived magnetite nanoparticles (CMNs). The obtained samples were characterized using assorted analytical techniques. The CMNs were subsequently analyzed for their heavy metal adsorption properties.

3.1 Synthesis of CMNs

To 50mL of the *C. odorata* flower extract, 30mL of 0.032M $FeCl_3$ solution was added under vigorous magnetic stirring. The decline in the pH of the medium was adjusted by the gradual addition of 0.52g of $NaHCO_3$. The resultant black precipitate was homogenized using Branson 150 D Sonifier with an immersed ultrasonic probe (2.38mm, 25kHz) for 15 minutes and was then magnetically stirred for 1 hour at room temperature. The mixture was then exposed to hydrothermal treatment at 180°C and autogenous pressure for 8 hours in a teflon-lined autoclave. The black, solid product formed was magnetically separated, and sequentially washed with ethanol and water to remove any adhered reactant residues. The slurry was then dried at 70°C in an air oven to obtain CMN-8. The procedure was repeated for varying the hydrothermal treatment periods to 12 and 24 hours to obtain CMN-12 and CMN-24.

3.2 Characterization of CMNs

The physical, morphological, and structural properties of the synthesized samples were analytically investigated with various methodical and technical aids.

3.2.1 FTIR analysis

FTIR analysis is a versatile tool in investigating the nanomaterials' surface. FTIR spectra of the flower extract and the dried precursor (CMN-P) illustrated in Fig.1a indicate the presence of several functional groups. The broad peak ~570cm^{-1} in CMN-P can be attributed to the formation of Fe-OH bonds after precipitation. Fig.1b represents the FTIR spectra of as synthesized phytoconjugated CMNs. The strong peak around 3435cm^{-1} is attributed to hydroxyl groups from polyphenols. The peaks at 2927cm^{-1} and 1457cm^{-1} refer to alkyl C-H stretching and bending vibrations respectively while the peaks at 1556, 1378cm^{-1} and 1156cm^{-1} represent aromatic skeletal vibrations.

The peak at 1260cm^{-1} indicate presence of aromatic C-O groups. The peaks appeared in the range 811-870cm^{-1} represents C=C moieties [7–9]. The distinct peak at 575cm^{-1} corresponding to the metal-oxygen vibrational band (Fe–O) at the tetrahedral site, in CMNs verifies the formation of magnetite. Thus, FTIR confirms the formation of iron oxide conjugated with active functional groups derived from the phytoreagent [6].

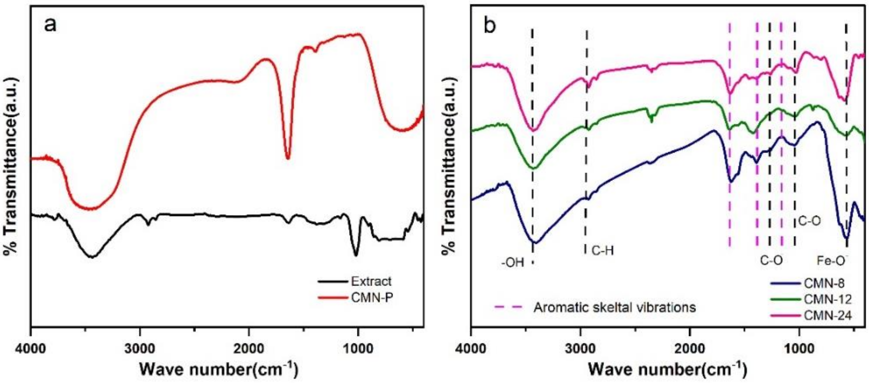

Fig.1. FTIR spectra of, a) plant extract and precursor and b) CMNs

3.2.2 XRD and SAED analysis

XRD analysis aids in confirming the crystalline phase, size, and possible defects in the synthesized materials. The XRD studies confirmed the formation of inverse spinel magnetite nanoparticles after hydrothermal treatment. Fig.2a depicts X-ray diffraction patterns of the CMN-P and CMN-12. CMN-P displays highly amorphous nature whereas all the peaks of CMN-12 matched well with the normal diffraction patterns of inverse spinel Fe_3O_4 and can be indexed to PDF no. 19–0629[9,10]. Peaks formed at 2θ values of 30.1°, 35.5 °, 43.2 °, 53.6°, 57.1°, and 62.7°, correspond to Miller indices of 220, 311, 400, 422, 511, and 440 respectively. Fig.2b depicts the X-ray diffractograms of CMNs formed after hydrothermal reaction at different durations. Crystallite size was calculated from the high-intensity peak (311) using Scherrer’s equation as given below,

$$D = \frac{K\lambda}{\beta cos\theta} \qquad (1)$$

where D is the crystallite size, k is known as the Scherer's constant (K=0.94) which denotes the shape of the particle, λ is the X-ray wavelength (1.54178Å), β is full width at half maximum (FWHM) of the diffraction peak, and θ is the angle of diffraction. The Scherrer equation accounts for the broadening of the diffraction peaks solely due to crystallite size[11]. The broadening of the peaks depicts the formation of very fine magnetite NPs. Crystallite size was calculated using Scherrer's equation using the line broadening of the most intense (311) diffraction peak and was found to be ~6.1, 7.2 and 8.2nm for CMN-8, CMN-12 and CMN-24 respectively. The computed lattice parameter was 8.39, 8.37, and 8.36Å for CMN-8, CMN-12 and CMN-24 respectively, which correlated well with the reference file further confirming magnetite formation. The absence of other peaks indicates the purity of the formed iron oxide phase and the absence of any impurities derived from the plant extract.

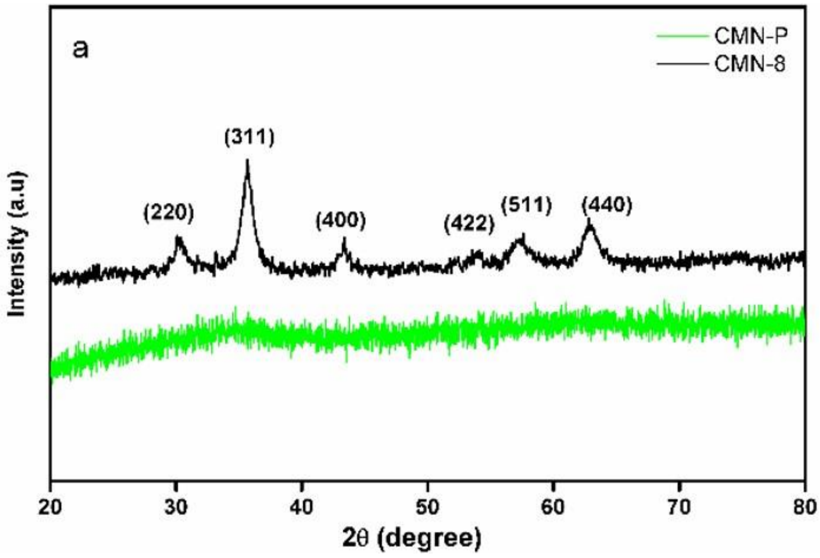

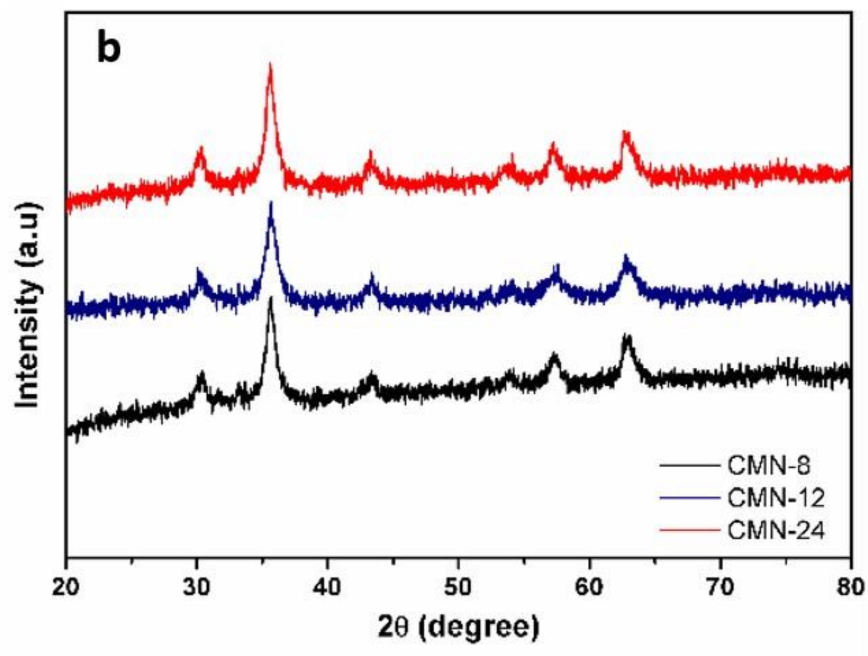

Fig.2. XRD diffraction patterns of, a) precursor and CMN-8 and b) CMNs

The selected area electron diffraction (SAED) pattern of CMNs displayed in Fig.3, in the selected area exhibits five distinguishable crystal planes of (440), (511), (400), (311), and (220) which agrees with the XRD results [12]. It indicates that the precursor was fully converted to pure Fe_3O_4 NPs. The evaluation of SAED pattern showed that the prepared sample is polycrystalline in nature with a cubic inverse spinel crystal structure. The interplanar spacing of approximately 1.8, 2.4, 2.8 Å observed for CMN-8, CMN-12 and CMN-24 concurs well with the lattice spacing of the (422), (311) and (220) planes in crystalline magnetite nanoparticles [13]. SAED patterns also suggest that crystallinity of CMNs increase with increase in the hydrothermal reaction period.

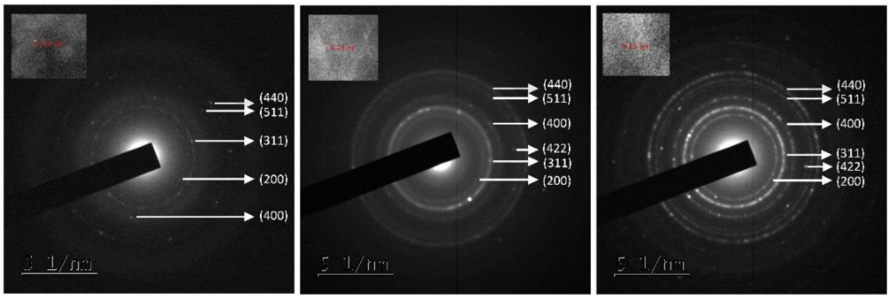

Fig.3. SAED patterns of, a) CMN-8 b) CMN-12 and c) CMN-24; inset displaying the *d-spacing*

3.2.3 HRTEM analysis

Microscopy is the most effective method of particle size analysis since it is the only method in which individual particles are observed and measured. HRTEM provides crucial information on the particle size distribution and the morphological characteristics of the material. The HRTEM profiling of all three obtained samples were conducted to identify the most promising material. CMN-8 exhibited nearly spherical and well-resolved particles (Fig.4 a, b) owing to the low hydrothermal treatment period and effective capping by the phytochemicals. However, the increase in hydrothermal treatment period resulted in larger agglomerated particles as evident from HRTEM images (Fig.4c-f). The estimated average particle diameter from size distribution analysis is approximately 6.14±0.25, 7.7±0.34 and 8.7 ±0.52nm for CMN-8, CMN-12, and CMN-24 respectively (Fig.5). The close correlation of the calculated size of the CMNs from XRD and HRTEM suggests that the phytoconjugate exist as a thin layer around the magnetite core. The increase in particle size is attributed to the accelerated grain growth under prolonged reaction periods that overtake the otherwise occurring nucleation events. Increased reaction periods might also promote interparticle magnetic interactions leading to agglomeration which is further accelerated by poor phytochemical capping at larger reaction hours.

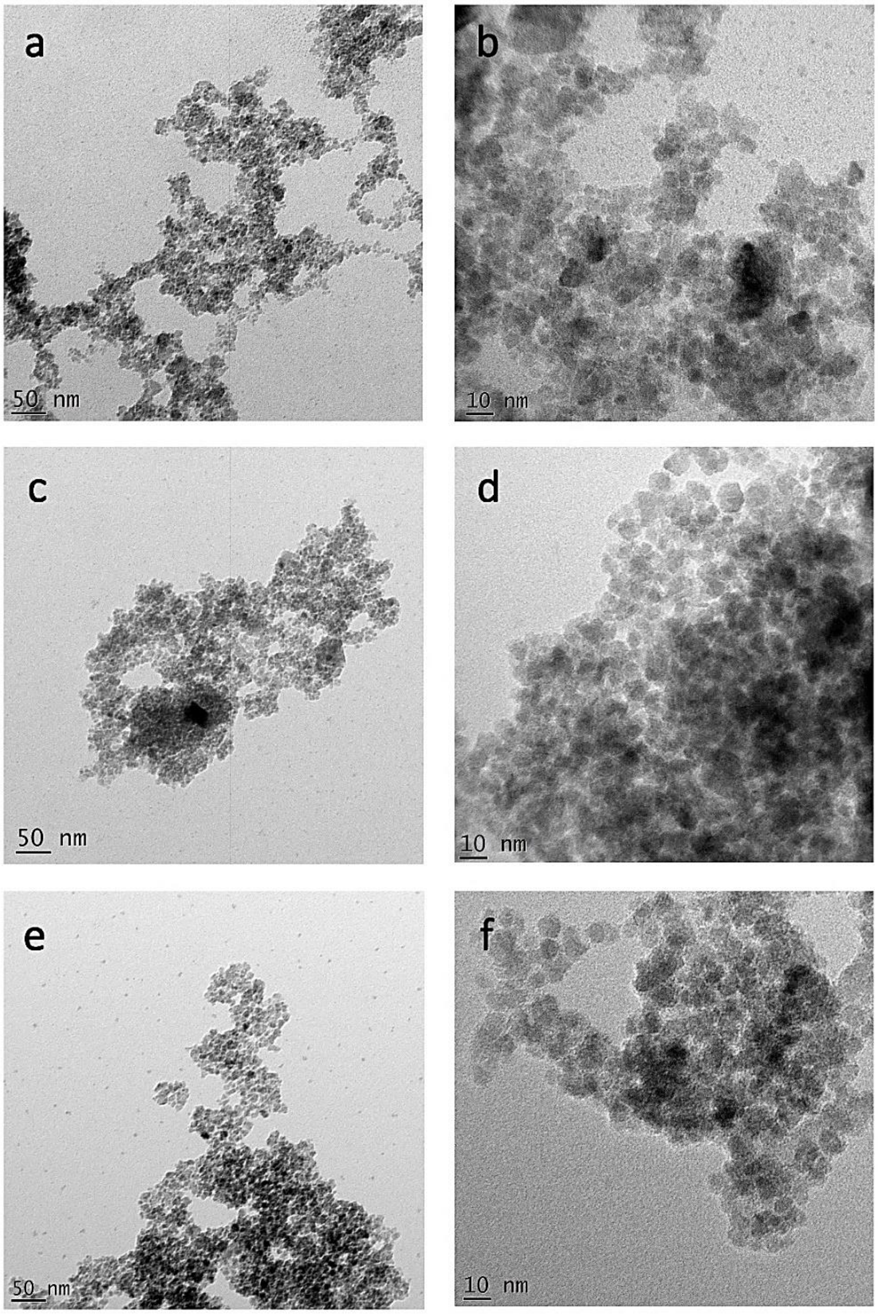

Fig.4. HRTEM images of a,b) CMN-8, c,d) CMN-12 and e,f) CMN-24

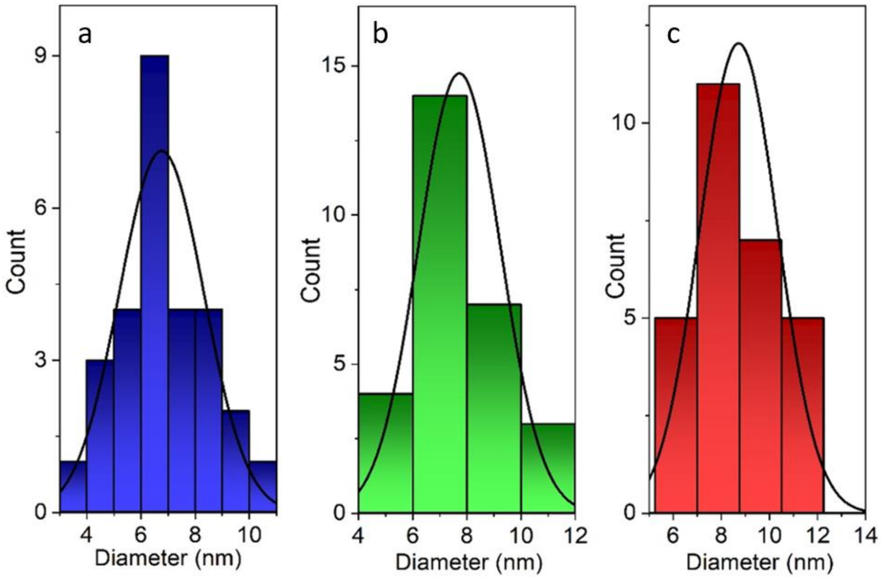

Fig.5. Size distribution analysis of a) CMN-8 b) CMN-12 & c) CMN-24

3.2.4 Point of zero charge and zeta potential study

Zeta potential (ZP) is a measure of the effective electric charge on the surface of the particles in colloidal solution/dispersion. The surface charge prevalent over the surface controls the electrostatic interactions initiated in the material surface[14,15]. pH of the medium plays a crucial role in dictating the surface charge of nanomaterials altering its responses to external stimulants. The pH_{pzc} of the CMNs were determined using the pH drift method to understand the surface electrostatic interactions of the material and to predict its possible applications[16]. The results illustrated in Fig.6 shows that at pH above ~4.6 the surface of CMN-8 and CMN-12 is negatively charged. Upon decreasing the pH below 4.6 the charge reveres altering the electrostatic properties of the material. Zeta potential values of CMN-8, CMN-12 and CMN-24 at neutral pH were -26.4, -24.5 and -33.5mV respectively.

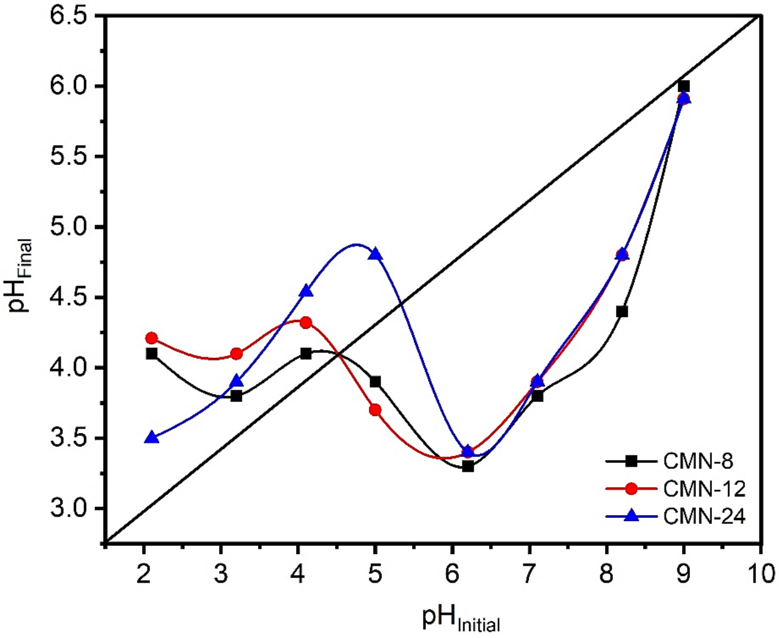

Fig.6. Surface charge analysis of CMNs by pH drift method

3.2.5 BET analysis

Low temperature N_2 adsorption-desorption isotherms were obtained to determine the surface area and nature of the porosity of CMN-8 (based on superior adsorption properties). Though the result (Fig.7) resembles type-IV isotherm, the absence of plateau region in the higher-pressure region categorizes it as a pseudo- type II isotherm. The presence of hysteresis loop at p/p_0=0.6-0.9 indicates a typical H3 type hysteresis indicating the presence of grooves created by non-rigid aggregated particles. Pore distribution analysis by Barrett-Joyner-Halenda's (BJH) method revealed multiple peaks indicating the presence of pores of different types. The peaks represent the interstices created by the boundaries of the nanoparticles. The specific surface area and the mean pore diameter obtained for CMN-8 calculated were 8.12m^2g^{-1} and 28.2nm respectively. The average pore volume calculated was 0.05cm^3g^{-1} indicating the low porosity of the material. Though BET method sheds light on crucial surface properties of the material, the pore availability and surface area change with the adsorbate-adsorbent pair[17].

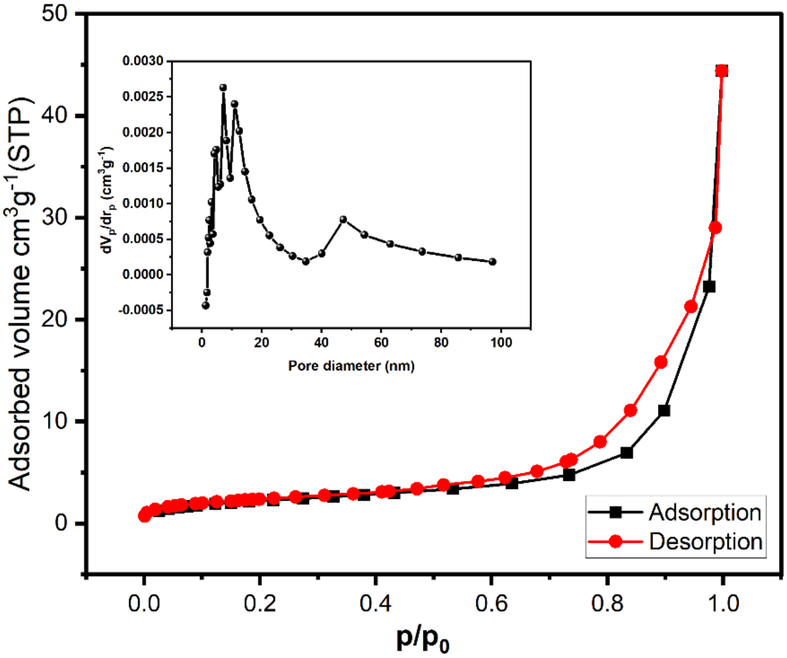

Fig.7. BET plot of CMN-8; inset showing the BJH plot

3.3 Mechanism of CMNs formation

The aqueous extracts of aerial parts of *Chromolaena odorata* are reported to contain an appreciable number of polyphenols and flavonoids in addition to other hydrophilic biomolecules like saponins. According to literature, the plant extract contains complex mixtures of flavonoids and other phenolic compounds like salivigenin, sakuranetin, chalcones, protocatechuic acid, p-hydroxy benzoic acid, p-coumaric acid, ferulic acid and vanillic acids[4,5,18,19]. These phytochemicals provide a variety of iron-binding sites such as 6,7-di-hydroxy moieties, B-ring catechol, and 2,3 double bonds. The reductive nature of these phytochemicals aids in metallic reduction under favourable conditions[9,20]. Primary phytoscreening of the aqueous *C. odorata* flower extract used in this work revealed the presence of saponins, tannins, polyphenols, flavonoids, alkaloids, and glycosides in the aqueous extract. The total phenolic content (TPC) and total flavonoid content (TFC) estimated were 175.69±1.21mg GAE/g and 24.72±0.87mg QE/g respectively. The high amount of TPC and TFC approves the effective extraction procedure adopted and the potency of the extract to reduce Fe^{3+} ions.

The instantaneous change in the brown colour and transparency of the extract to dirty green precipitate upon the addition of $FeCl_3$ indicates the complexation of Fe^{3+} ions with polyphenols/flavonoids[21,22]. The addition of $NaHCO_3$ neutralizes the acid formed in the reaction medium enabling the active components of the extract to reduce Fe^{3+} ions. The higher pH further destabilizes the polyphenols promoting iron chelation at multiple sites. Hydrothermal treatment helps in the generation of single phased iron oxide from the crude mixture of iron-polyphenol complexes. It can be speculated that $NaHCO_3$ along with the phytochemicals generates heterogeneous nucleating centres during the hydrothermal treatment. The evolution of CO_2 suggests a plausible gas template mechanism of nucleation[23]. The local temperature gradient formed on the surface of the nanoparticles accelerates hydroxide to oxide conversion. The reactant mixture containing brine solution ($NaCl+ H_2O+CO_2$) along with complexed iron under hydrothermal conditions mimic geothermal events producing iron oxide of pure magnetite phase[24]. The presence of hydrophilic phytochemicals in the reaction medium has a significant role in decreasing the frequency of collisions between the newly formed nanoparticles. As the collisions decrease, the oriented attachment and Ostwald ripening rate diminish, resulting in smaller crystallite size. Self-capping of phytochemical fragments controls the aggregation of nanoparticles, providing them a surface with active functional groups and appreciable wettability, which in turn facilitates its use in water remediation.

3.4 Removal of HMIs by CMNs-Analytical study

Among all the dreadful water contaminants, heavy metal ions (HMIs) call for immediate remediation owing to their severe and irreversible toxicological effects on human health. The synthesized CMNs were tested for possible removal activity against several HMIs. The pilot study demonstrated that CMNs actively adsorb Cr(VI) and Pb(II) under suitable conditions. Adsorption batch experiments were performed systematically to evaluate the effect and extent of Cr(VI) and Pb(II) adsorption by CMN-8,CMN-12 and CMN-24.

3.4.1 Adsorption batch experiments

Initially the CMNs were tested to identify the order of adsorptive removal and it was found that CMN-8 displayed superior removal capacities (Fig.8) towards both the target ions and therefore, was chosen as the ideal candidate for further studies. The optimal conditions standardized for the appreciable removal of Cr(VI) & Pb(II) at ambient temperature are summarized in Table 1. Experimental constraints including initial concentration (10-500mgL^{-1}) temperature (30-60°C) and pH (2-9) of the adsorbent-adsorbate systems were varied to evaluate the efficiency of CMN-8 in heavy metal detoxification.

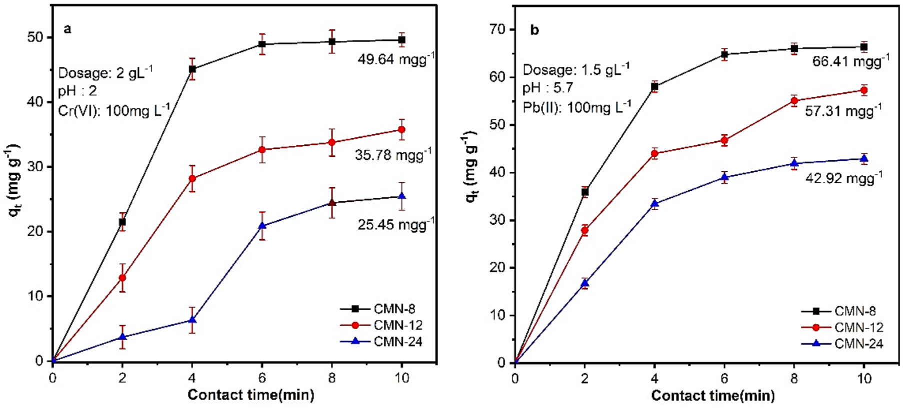

Fig.8. Adsorption capacity of CMNs towards a) Cr(VI) & b) Pb(II)

Table 1. Optimized conditions for adsorption of Cr(VI) & Pb(II) by CMN-8

	Initial dosage	Initial conc.	pH	Contact time (min)	Adsorption capacity (mg g^{-1})
Cr(VI)	2 gL^{-1}	100 mgL^{-1}	2	10	49.64
Pb(II)	1.5 gL^{-1}	100 mgL^{-1}	5.6	10	66.41

pH has a major role in determining the surface charge and hence the electrostatic interactions between the adsorbent-adsorbate pair. The variation of the adsorbent surface charge is already explained in section 3.2.4. The speciation of HMIs also changes with pH of the solution resulting in different surface with altered charge magnitude or polarity. Fig.9 depicts the distribution of speciation of Cr(VI) & Pb(II) with pH [25,26]. The negatively charged chromium species that exist in solutions with low pH is attracted to the oppositely charged CMN-8 surface initiating the adsorption process. As the pH of the solution increases beyond 4, CMN-8's surface charge reverses and the negative chromium species gets repelled from the adsorbent surface terminating the adsorption process. This corroborated the drastic decrease in the adsorption capacity of CMN-8 towards Cr(VI) with increase in pH (Fig.10).

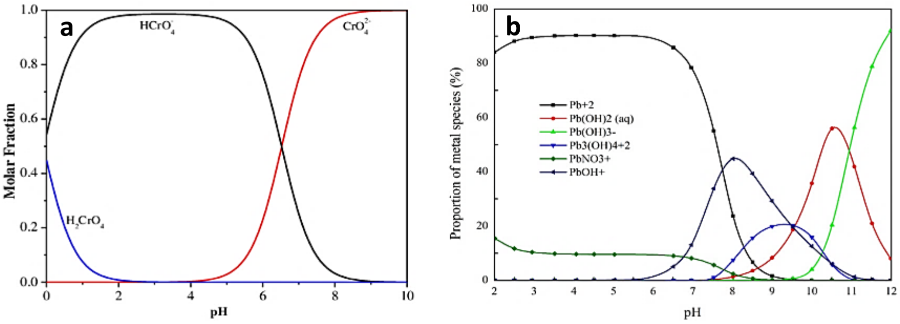

Fig.9. The speciation of a) chromium and b) lead with pH.

At lower and neutral pH, lead moieties exhibit positive charge and can be sequestrated by the negative CMN-8 surface when the pH of the system is above 4. The ambient pH of the lead nitrate solution was 5.7 and adsorption capacity recorded at this pH was 66.4mgg^{-1}. Though adsorption should increase upon increasing the pH according to the electrostatic theory, the alkalinity of the solution cause Pb^{2+} ions to precipitate and consequently lowering the adsorption capacity (Fig.10).

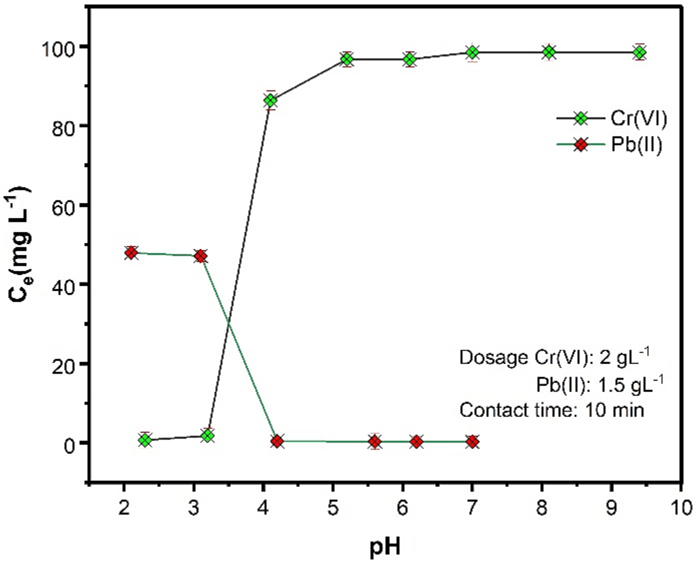

Fig.10. Change in adsorption efficiency with pH

Industrial effluents are concoctions of ions that have a secret recipe. For use in commercial applications, the adsorbent must be able to work selectively against the target HMIs to help with metal ion recycling. Additionally, the presence of other ions shouldn't impair the adsorbent's ability to absorb them. Therefore, the target ion solution containing known concentrations of an extra ion was prepared separately, and adsorption studies were carried out, to examine the commercial viability of CMN-8. The results of the study are compiled in Fig.11. At lower concentration of competing anions CMN-8 showed appreciable adsorption towards Cr(VI). However, the adsorption capacity deteriorated evidently in presence of carbonate and phosphate ions. These ions compete with $HCrO_4^-$ ions for active sites on the adsorbent. Moreover, higher affinity of these anions towards iron may decelerate the adsorption of Cr(VI) by blocking the reactive sites. The study revealed that the adsorption of Pb(II) by CMN-8 was uninterrupted in presence of several other divalent cations displaying the selectivity of the adsorbent towards the target metal ion. The selective adsorptive removal is attributed to the combined effect of the size of hydrated ions and hydration energy. The metal ions with high free energy of hydration tend to remain in the aqueous phase reducing the possibility of interaction with the adsorbent surface. The free energy of hydration follows the order, $Ni^{+2} > Cu^{+2} > Hg^{+2} > Co^{+2} > Cd^{+2} > Pb^{2+}$ [27-29] .The lower free energy of hydration of Pb^{2+} ions, compared to the other divalent cation of choice, resulted in a lower hydrated radius, thereby enhancing the chances of reaching the adsorbent surface for adsorption [30]. Moreover, the larger ionic radius of Pb^{+2} ions make it fit the active sites and facilitates binding to several surface groups simultaneously.

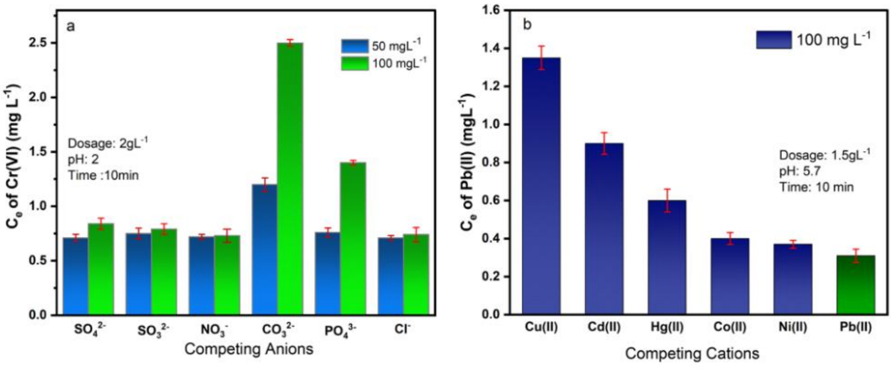

Fig.11. Adsorption efficiency of CMN-8 towards a) Cr(VI) b)Pb(II) in presence of interfering ions.

3.4.2 Adsorption isotherm, kinetic and thermodynamic study

Batch equilibrium adsorption experiments were used for adsorption assessment by simulating plots of both Langmuir, Freundlich and Temkin adsorption models[31]. According to Langmuir model, for homogenous systems,

$$q_e = \frac{q_m b C_e}{1+bC_e} \qquad (2)$$

where q_e is the amount of Cr(VI)/Pb(II) adsorbed at equilibrium, q_m is the maximum amount of Cr(VI))/Pb(II) adsorbed per unit weight of the adsorbent (mg g^{-1}) and b is the Langmuir adsorption isotherm constant[32]. The Freundlich model can account for multilayer and non-equivalent adsorption sites. According to the Freundlich adsorption model

$$q_e = K_F C_e^{1/n} \qquad (3)$$

Where K_F and n are Freundlich adsorption isotherm constants and n is the measure of the heterogeneity of the system[33]. Temkin adsorption isotherm equation, which considers both monolayer and multilayer adsorption, is given as

$$q_e = \frac{RT}{B_T} \, lnK_T C_e \qquad (4)$$

where, B_T is the Temkin isotherm constant and K_T is Temkin isotherm equilibrium binding constant[34].

Table 2 indicated that the Langmuir model effectively describes the adsorption of Cr(VI) & Pb(II) onto CMN-8 as dominantly monolayer adsorption. The maximum adsorption capacity (q_m) for CMN-8 towards Cr(VI) & Pb(II) was 173.12 and 355.43mgg^{-1}, which corresponds to the complete monolayer coverage on the CMN-8 surface.

Table 2. Results of the adsorption isotherm modelling study

Isotherm Models	Parameters	
	Cr(VI)	Pb(II)
Langmuir	q_m(mg g^{-1}) =173.12	q_m(mg g^{-1}) =315.43
	K_L =1.02	K_L =0.787
	R^2=0.924	R^2=0.988
Freundlich	K_F =79.78	K_F =120.12
	n =3.5	n =0.359
	R^2=0.684	R^2=0.955
Temkin	K_T (Lg^{-1}) = 32.58	K_T (Lg^{-1}) = 7.43
	B(Jmol^{-1}) = 21.25	B(Jmol^{-1}) = 120.18
	R^2= 0.746	R^2= 0.983

The affinity between the adsorbent and adsorbate is quantified by evaluating the dimensionless separation factor R_L which is given by the equation,

$$R_L = \frac{1}{1 + bC_0} \qquad (5)$$

where C_0 is the highest initial adsorbate concentration. For favorable adsorption $0 < R_L < 1$ and for unfavorable adsorption $R_L > 1$ or $R_L = 1$. The R_L value obtained for adsorption of Cr(VI) on CMN-8 was 0.0097. From the obtained R_L value, a favorable parameter K_{C0} can be derived.

$$K_{C_0} = \frac{1}{R_L} - 1 \qquad (6)$$

The adsorption is considered favorable when the K_{C0} value is between 1 and 10. K_{C0} values higher than 10 denote spontaneous and highly probable adsorption[35]. The derived value of K_{C0} for Cr(VI) adsorption is 525.32 and it indicated the highly favorable nature of its adsorption. The R_L value obtained for adsorption of Pb(II) on CMN-8 was 0.0025 and the corresponding K_{C0} was 394.25. The parameters derived from the Langmuir adsorption indicated the highly favorable nature of adsorption of the target metal ions on the prepared magnetite nanoparticles. The simulated isotherms for both target ions are illustrated in Fig. 12.

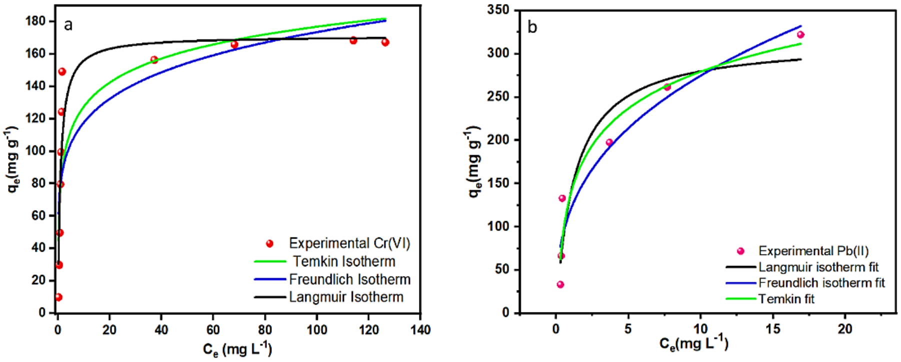

Fig.12. Fitted adsorption isotherms for a) Cr(VI) and b) Pb(II)

The HMIs removal occurred at the highest rate for the first 4 minutes in both cases for owing to the high concentration gradient on the solid-liquid interface in the beginning. The rate of adsorption of the HMIs by CMN-8 can be determined by employing different kinetic models. Here we have considered pseudo-first order, pseudo-second order, and Elovich models for kinetic studies[36,37] as depicted in Fig.13. Pseudo first order kinetics is generally used in the form,

$$q_t = q_e\left(1 - e^{-k_1 t}\right) \qquad (7)$$

Where q_t is the adsorption capacity at time t, q_e is the equilibrium adsorption capacity and k_1 is the pseudo first order rate constant. It is generally used to explain the adsorption process during the initial stage. The linearized equation is expressed as,

$$log\ (q_e - q_t) = log q_e - \frac{k_1 t}{2.303} \qquad (8)$$

The commonly used form of pseudo second order is given below,

$$q_t = \frac{q_e^2 k_2 t}{1 + q_e k_2 t} \qquad (9)$$

Here, k_2 represents the pseudo second order rate constant. The model can be linearized as,

$$\frac{t}{q_t} = \frac{1}{k_2 q_e^2} + \frac{t}{q_e} \tag{10}$$

Elovich kinetics is another frequently used model to collect information about the kinetics of adsorption. The equation is given as below,

$$q_t = \frac{1}{b} ln(1 + abt) \tag{11}$$

a and b represent the initial rate of adsorption and the extent of surface coverage respectively. The model is represented in linear form as,

$$q_t = \frac{1}{b} ln(ab) + \frac{1}{b} ln(t) \tag{12}$$

The conforming fit was determined by the R^2 value and closeness of the predicted equilibrium adsorption capacity to the experimental value. From the regression analysis(table 3), it was observed that the experimental results correlated well with pseudo-first order adsorption.

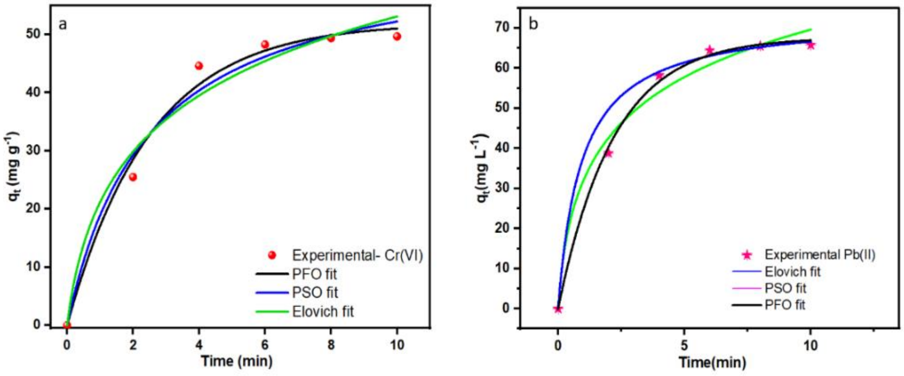

Fig.13. Fitted kinetic models for, a) Cr(VI) and b) Pb(II) adsorption

Table 3. Results of kinetic modelling studies

Kinetic models	Parameters	
	Cr(VI)	Pb(II)
Pseudo first order	q_e (mg g^{-1}) =51.98 k_1(h^{-1}) =0.397 R^2= 0.988	q_e (mg g^{-1}) =67.66 k_1(h^{-1}) =0.454 R^2= 0.997
Pseudo second order	q_e (mg g^{-1}) =64.92 k_2(g (mg h)$^{-1}$) =0.0063 R^2= 0.973	q_e (mg g^{-1}) =72.79 k_2(g (mg h)$^{-1}$) =0.0148 R^2= 0.995
Elovich	a (mg g^{-1}) =44.72 b =0.063 R^2= 0.964	a (mg g^{-1}) =90.67 b =0.056 R^2= 0.973

The effect of temperature on the adsorption process was investigated by conducting adsorption experiments at different temperatures. In this work, the batch thermodynamic experiments were studied between 303 and 333K, and the following equations were applied to compute the thermodynamic parameters for the adsorption of Cr(VI) & Pb(II) ions.

$$K_d = \frac{q_e}{C_e} \tag{13}$$

$$lnK_d = \frac{-\Delta H}{RT} + \frac{\Delta S}{R} \tag{14}$$

$$G = \Delta H - T\Delta S \tag{15}$$

where K_d represents the equilibrium constant. Fig.14 shows the simulated plot of ln K_d against 1/T for adsorption of Cr(VI) & Pb(II) ions on CMN-8 at different temperatures[38]. Table 4 summarizes the obtained thermodynamic parameters. The positive ΔH value indicated the endothermic nature of the adsorption. The positive ΔS values suggested the rising disorder at the interface during the adsorption of the HMIs onto CMN-8. The high negative values of ΔG indicated the spontaneity of the process.

Fig.14. Thermodynamic investigation of, a) Cr(VI) and b) Pb(II) adsorption

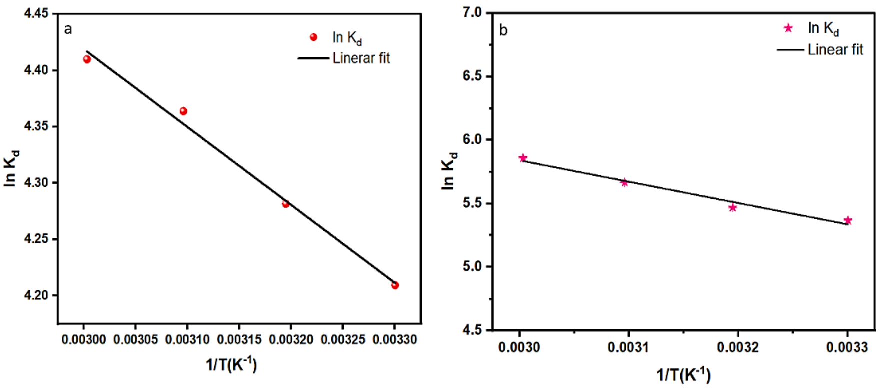

Table 4. Details of thermodynamic investigation on adsorption of HMIs on CMN-8

	Temperature (K)	ΔG (kJmol^{-1}K^{-1})	ΔH (kJ mol^{-1}K^{-1})	ΔS (Jmol^{-1}K^{-1})
Cr(VI) Adsorption	303	-10.608	5.744	53.97
	313	-11.148		
	323	-11.687		
	333	-12.227		
Pb(II) Adsorption	303	-7.167	34.147	136.356
	313	-8.532		
	323	-9.895		
	333	-11.26		

3.4.3 Elucidation of adsorption mechanism with the aid of XPS studies

Surface charge studies on CMN-8 revealed the prevalence of a negative surface above pH 3.7. FTIR studies identified the presence of phytoconjugates and surface hydroxyls on CMN-8. These surface moieties undergo protonation under acidic environment inversing the inherent negative charge on the surface. The positive charge prevailing on the surface of CMN-8 up to pH 3.7 enables electrostatic attraction towards $HCrO_4^-$ species initiating the adsorption process. It's highly speculative to assume that the surface hydroxyls close to the Fe_3O_4 core are less available for extensive protonation.

The inherent pH of the simulated Pb(II) effluent was 5.6. The lead species detected to dominate in solution at this pH is primarily Pb^{2+} ions. This triggers an electrostatic interaction between the adsorbent and positively charged lead species in the medium, initiating the adsorption process.

Fig.15-18 illustrates the XPS profile of CMN-8 before and after adsorption of target metal ions. XPS confirms the formation of pure magnetite with phyto-conjugate stabilization. The Fe 2p core-level spectrum of CMN-8 has two peaks at ~710.8eV and ~724.1eV verifying the magnetite phase[39]. The fitted Fe 2p spectrum consists of peaks at 710.1, 711.3, 713.1, 723.4, 724.1 and 725.3eV. The peaks at 710.1 and 723.4eV correspond to the presence of Fe^{2+} species in the octahedral (O_h) site. Fe^{3+} species in the octahedral sites are found at a binding energy of 711.3 and 724.1eV. The peaks at 713.1 and 725.3eV are attributed to Fe^{3+} in tetrahedral sites (T_d). A weak shoulder displayed at ~719.2eV corresponds to vacancy cascade(VC) commonly observed in iron oxide species.[39,40]. A slight chemical shift to the higher binding energy from that of pure magnetite can be attributed to the phyto-conjugation on the surface of CMN-8. The O 1s core-level spectrum exhibits peaks at ~529.4eV and 530.6eV correlated to Fe-O and C-O moieties. The peak with higher binding energy at 531.9 eV is attributed to surface hydroxyl groups adhered to CMN-8[41,42]. The C 1s profile of CMN-8 was fitted into four peaks with binding energies ~285, 286.5, 289.3, and 292.3eV corresponding to C-C, C-O, C=O moieties, and π-π interactions respectively[43]. However, upon adsorption of chromium, the peak at ~292.3eV disappeared whereas the peak at 289.3eV displayed a chemical shift to 288.5eV. There was a concomitant increase in the percentage composition of C-C and C-O bonds and a decrease in C=O bonds. O 1s spectra also displayed evident post adsorption changes. Dissolution of the peak at 531.9eV indicated active participation of surface hydroxyl groups in adsorption of Cr(VI). The prominent increase in percentage composition of the peak corresponding to the Fe-O (metal–O) bond (529.4eV) assisted with peak shift to higher binding energy (529.8eV) confirms the deposition of chromium to CMN surface through Cr-O bonds. Fe 2p spectrum exhibited a chemical shift to lower binding energies and the weak shoulder at ~719.2 disappeared possibly due to the association of O-Cr on the CMN-8 surface. Cr 2p core-level spectra displayed peaks at 576.6eV and 578.2 eV corresponding to Cr(III) and Cr(VI) respectively evincing the reduction of toxic hexavalent chromium on the CMN-8 surface[41].

Pb(II) moieties were detected on the surface of CMN-8-Pb indicating lead adsorption. Deconvolution of the Pb 4f spectra exposed the presence of two different Pb(II) moieties on the surface. Accordingly, the peaks at 137.9 and 143.25eV were assigned to Pb-O bonds whereas the peaks at 139.1 and 144.2eV represent Pb interacting with the hydroxyl groups[44]. The peak at 530.6eV in O 1s core spectra displayed an increase in intensity owing to the increase in the total number of metal-OH bonds formed on the surface. The association of Pb(II) on the surface produced slight chemical shifts in Fe 2p and C 1s spectra of CMN-8-Pb towards higher binding energy values. The changes in the C 1s spectra may be attributed to the involvement of π electrons in the adsorption process.

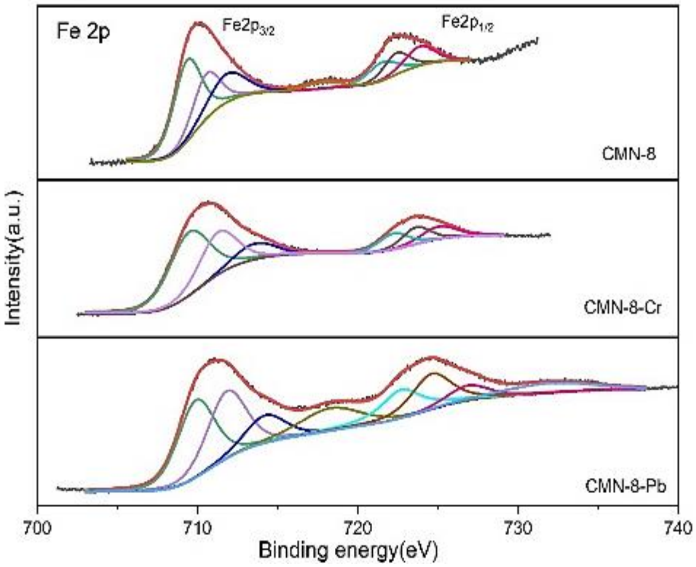

Fig.15. Fe 2p core spectra of bare and exhausted adsorbents.

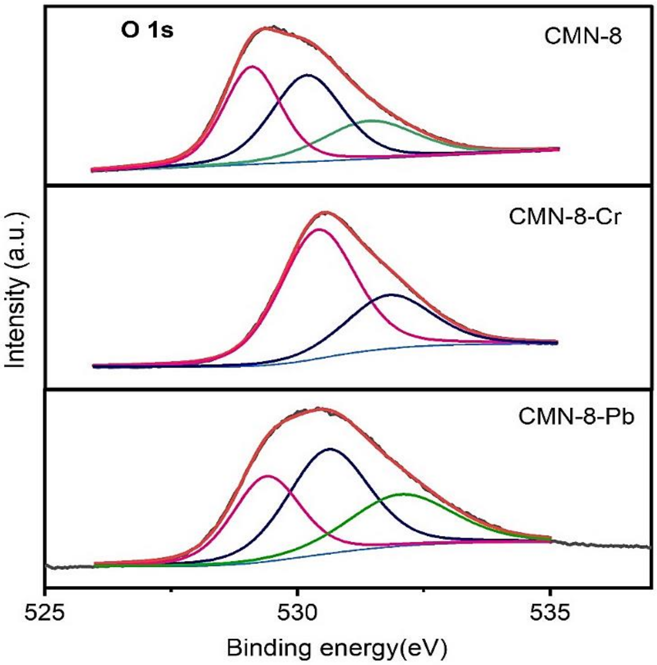

Fig.16. O 1s core spectra of bare and exhausted adsorbents.

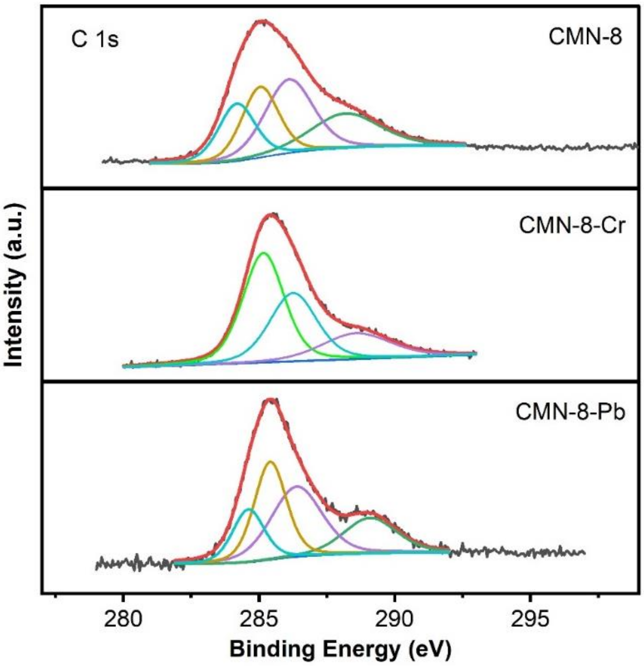

Fig.17. C 1s core spectra of bare and exhausted adsorbents.

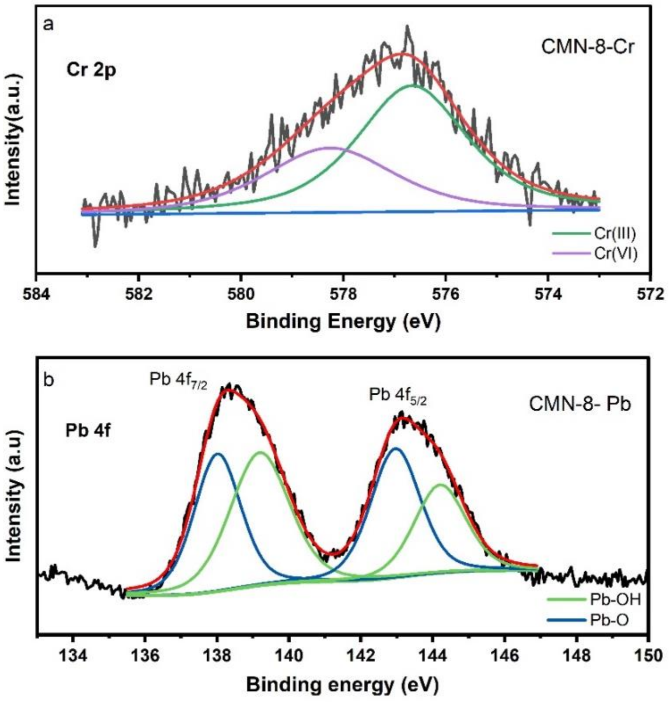

Fig.18. a) Cr 2p and b) Pb 4f core spectra of exhausted adsorbents.

The above results indicated that, 1) adsorptive removal of Cr(VI) is initiated through electrostatic attraction, 2) the variations inflicted in XPS spectrum of CMN-8 after adsorption of chromium corroborates the following: CMN-8 appreciably reduces Cr(VI) to Cr(III) through redox reactions of surface hydroxyl groups and phytoconjugates with Cr(VI) and 3) since the PXRD profile of CMN-8 did not alter after adsorption it is reasonable to speculate that there might be an amorphous $Cr_xFe_{1-x}(OH)_3$ on post-adsorption.

3.4.4 Effect of adsorption on magnetic properties

The change in magnetic properties of magnetic adsorbents after adsorption is rarely investigated. Magnetic properties of CMN-8 before and after adsorption (Fig.19) differed prominently. Owing to the smaller size of particles CMN-8 exhibited superparamagnetic nature with a saturation magnetization (M_s) of 38.78 emug^{-1}. The lower saturation magnetization value originated from the small size of CMN-8 and the nonmagnetic phytochemical capping derived from COFE. M_s after adsorption of Cr(VI) increased up to 52.05 emug^{-1}. A similar rise in saturation magnetization is reported for iron oxide nanoparticles upon doping with chromium owing to the inherent paramagnetic nature and high magnetic moment of chromium[45]. Ferromagnetic nature post adsorption originated from the obvious increase in the size of particles due to bulk chromium association. The remarkable broadening in the hysteresis upon adsorption further substantiates the deposition of chromium on the CMN-8 surface.

The interactions with diamagnetic materials attenuate the inherent magnetic properties of a material. Here, the adsorption of Pb(II) caused a drastic decrease in the saturation magnetization value of CMN-8 as evident from Fig.19. The M_s for Pb(II) loaded CMN-8 was recorded as 22.65 emug^{-1}. The adsorbed layer of diamagnetic lead moieties on the magnetite surface reduces the magnetic moment of both adsorbents without interfering with the superparamagnetic nature of the adsorbents[46]. Despite the reduction in the M_s value, an external magnet could effectively separate the exhausted adsorbent from the analyte. Table 4 summarizes the details of the study.

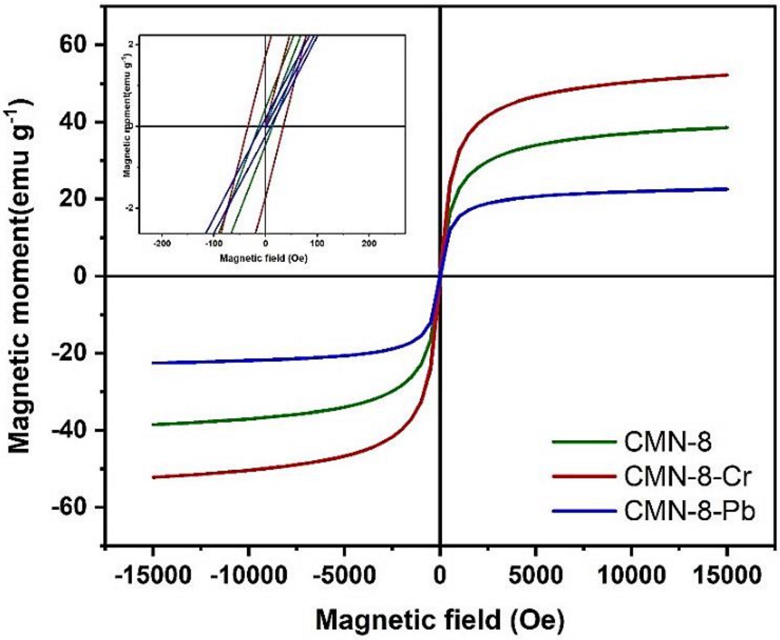

Fig.19. VSM plots of bare and exhausted adsorbents.

Table 4. Magnetic measurements of CMN-8 pre & post adsorption of HMI

Sample	Coercivity H_c (Oe)	Remanence M_r (emu g^{-1})	Saturation magnetization M_s (emu g^{-1})
CMN-8	13.24	0.465	38.78
CMN-Cr	34.04	1.719	52.05
CMN-Pb	9.221	0.186	22.65

3.4.5 Effect of adsorption on surface morphology

Scanning electron microscopy equipped with energy dispersive spectroscopy (FESEM-EDX) was used to investigate morphological and compositional changes on CMN-8's surface post adsorption. The FESEM images (Fig.20) of CMN-8 illustrate a unique morphology of an assembly of tiny nanobuds resembling a 'broccoli head'. There are numerous void interstices surrounding each cluster of nanobuds as predicted by the N_2 sorption analysis. These interstices act as interlinking channels that facilitate the easy transport and anchoring of heavy metal species on the adsorbent surface. Up on adsorption of target metal ions, surface morphology of CMN-8 changed evidently. More protruding clusters appeared on the surface and the void interstices were filled with deposition of the adsorbed species in case of Cr(VI) (Fig.20c,d). Lead caused a uniform deposition with lesser growth filling the interstices (Fig.20 e,f). Images of elemental investigation on exhausted adsorbents are displayed in Fig.21. EDX spectra of CMN-8 revealed the presence of Fe, O and C confirming the phytoconjugation on the iron oxide surface (Fig.21 a). Whereas EDX analysis of Cr-CMN-8 and Pb-CMN-8 displayed the presence of Cr (Fig.21 b) and Pb (Fig.21 c) respectively along with noticeable changes in the composition of carbon and oxygen indicating the participation of phytoconjugate in adsorption. The changes in the composition of iron in both cases were negligible.

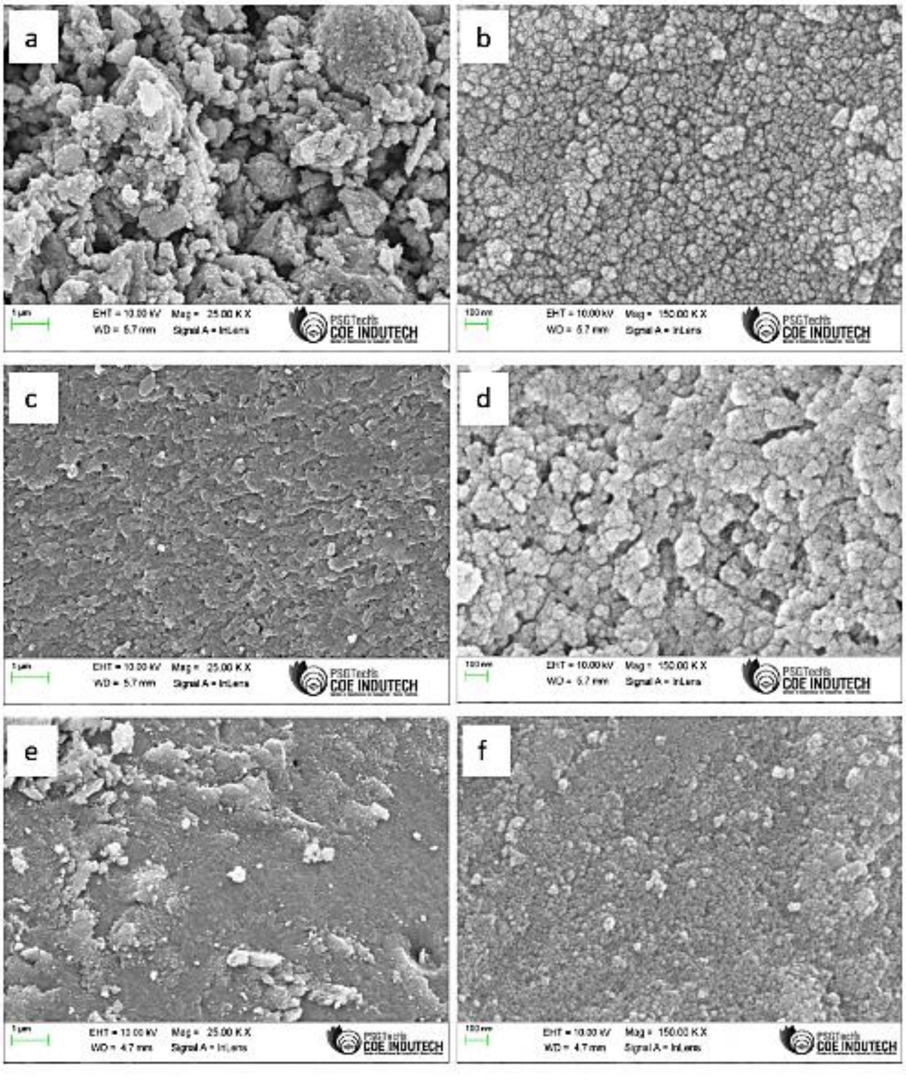

Fig.20. FESEM images of a,b) CMN-8, c,d) Cr-CMN-8 &e,f) Pb-CMN-8

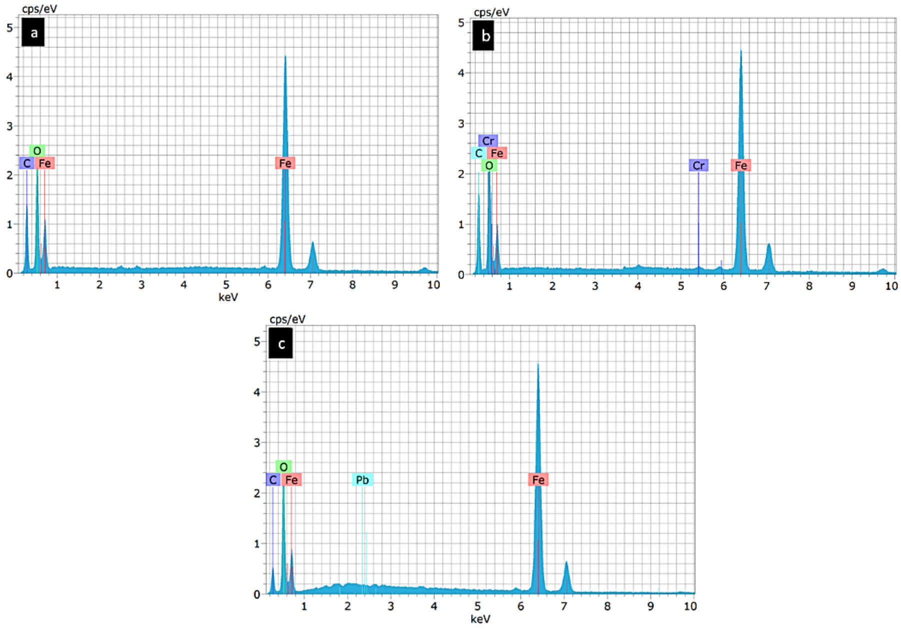

Fig.21. EDX spectra of a) CMN-8 b) Cr-CMN-8 and c) Pb-CMN-8

The details compositional analysis from XPS and EDX studies are displayed in table 5.

Table 5. Details of compositional analysis.

	EDX (atomic wt%)				XPS (atomic wt%)			
	Fe	O	C	Cr/Pb	Fe	O	C	Cr/Pb
CMN-8	21.34	24.75	53.91	-	9.15	40.57	50.28	-
CMN-8-Cr	20.25	30.23	47.39	2.13	8.76	45.79	43.61	1.84
CMN-8-Pb	19.64	31.45	46.25	2.66	8.93	46.31	42.68	2.08

The plausible pathway of Cr(VI) removal by CMN-8 proceeds through 1) electrostatic attraction of chromate anions on to CMN-8 surface, 2) partial reduction of Cr(VI) ions by the nearby electron donor groups, 3) surface hydroxyl groups on CMN-8 now sequestrates the reduced Cr^{3+} and Cr^{6+} ions. Since the PXRD profile of CMN-8 did not alter after adsorption it is reasonable to speculate that there might be an amorphous layer of chromium post-adsorption which lead to the higher saturation magnetization moment. FESEM images of exhausted adsorbents also support extensive deposition of chromium species on the surface. A schematic representation of the mechanism is illustrated in Fig.22.

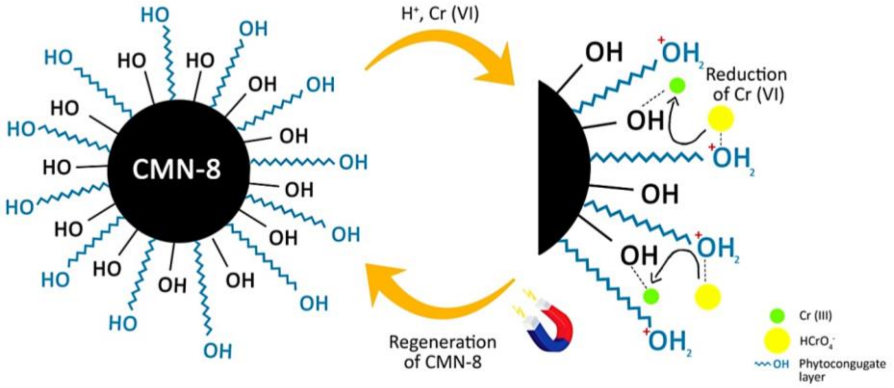

Fig.22. Schematic illustration of Cr(VI) reduction and removal

The removal of Pb(II) by CMN-8 primarily involves the following attributes. 1) Physical adsorption: the possible enhancement of surface area achieved through appreciable reduction of particle size instigates adsorption of the target metal ions onto CMN-8. 2) Electrostatic interactions: the strong electrostatic interactions between the negatively charged adsorbent surface and the cationic lead species further promote the adsorptive removal of lead by CMN-8. 3) Interfacial interactions: the adsorption proceeds through the interactions of the surface hydroxyl groups of CMN-8 with Pb^{2+} ions. Elimination of a fraction of H^+ ions by Pb^{2+} resembling an ion exchange process subsequently gives rise to two different lead species on the adsorbent surface. A schematic representation of the proposed mechanism is given in Fig.23.

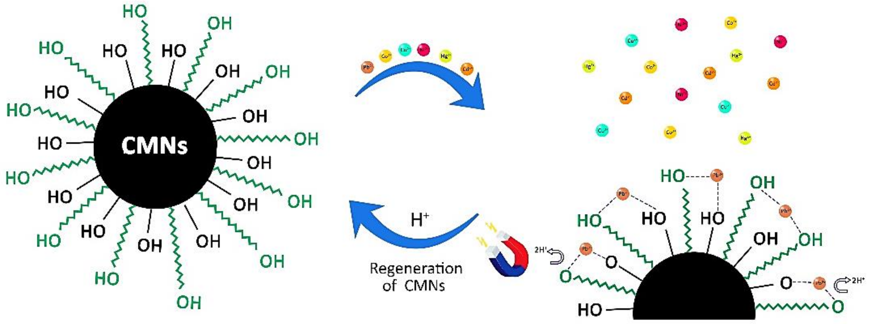

Fig.23. Schematic representation of Pb(II) removal by CMN-8

The considerable decrease in the saturation magnetization indicated the deposition of diamagnetic lead species on CMN-8 surface. The decrease in adsorption capacity with increase in duration of hydrothermal treatment can be correlated to the decrease in the phytoconjugate content evident from the XRD and EDX results. The increase in crystallinity of the samples suggest lower phytoconjugation in CMN-12 and CMN-24, which along with increased agglomeration reduce the efficiency of adsorption.

3.5 Regeneration and recyclability of CMN-8

The magnetic property of the adsorbent made recovery and regeneration of the exhausted adsorbent easy and fast. The exhausted adsorbents were regenerated using 10 ml of 0.1M HCl (for CMN-8-Pb) and distilled water (for CMN-8-Cr) as an eluent at room temperature in both cases. The sudden change in pH of the system triggered electrostatic charge reversal on the adsorbent surface resulting in the desorption of the pollutant. The efficiency of CMN-8 for five consecutive adsorption-desorption cycles is illustrated in

Fig.24. The loss of adsorbent mass during recycling was minimal due to the easy and effective magnetic separation. Regenerated adsorbents displayed sustained adsorption capacities throughout the cycles. The invariable adsorption capacity demonstrates the effectiveness of the adapted regeneration method and the high stabilization derived from phytochemical capping.

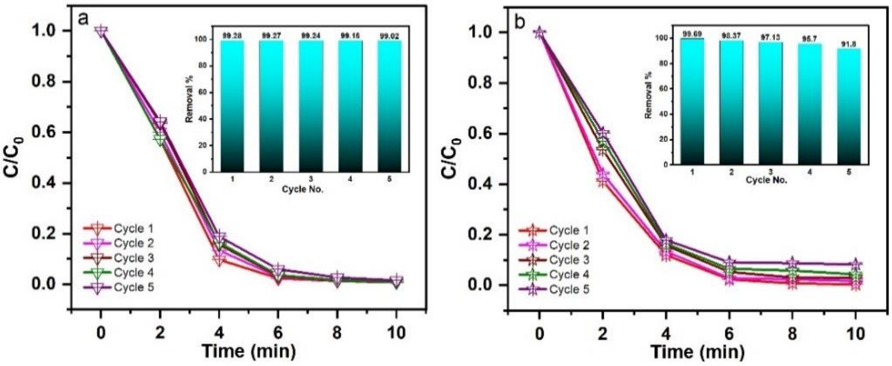

Fig.24. Recyclability studies on CMN-8 for a) Cr(VI) removal and b) Pb(II) removal

3.6 Summary

In this work, a facile one-pot strategy was developed for the synthesis of superparamagnetic small magnetite nanoparticles by using siam weed flower extracts for the first time. The synthesized nanoparticles were characterized using assorted instrumental techniques including XRD, FTIR, HRTEM, VSM, and XPS. The reasonable reduction in size and the monodispersity attained through ultrasonic homogenization is evident in the TEM micrographs. The self-capping of the plant metabolites provided number of active sites for the target metal ions to bind. At lower pH CMN-8 showed an appreciable adsorption capacity of 49.6 mg g^{-1} towards hexavalent chromium under 10 minutes. Majority of chromium adsorbents reported elsewhere requires longer contact periods to attain appreciable removal. At the inherent pH of the simulated effluent containing Pb(II), the adsorption capacity of CMN-8 reached 66.43 mg g^{-1} in under 10 minutes. CMN-8 exhibited superior adsorptive properties owing to the enhanced surface area and effective phytoconjugation. The adsorption equilibrium and adsorption kinetics for both target ions conformed well to the Langmuir adsorption isotherm model and pseudo first order kinetics model respectively. The selectivity of the CMN-8 towards Cr(VI) & Pb(II) can aid in the recovery of the metal ion from effluent mixtures in practical scenarios. The adsorbents were regenerated and used to confirm their economic viability. The results of the study indicate the potential of CMN-8 as an efficient, selective, and recyclable magnetic adsorbents for aqueous Cr(VI) & Pb(II). Furthermore, the economic and greener synthesis route that might serve as an effective weed control upon scaling up makes CMN-8 more promising.

- *The results of the study are published in the Journal of Hazardous Materials Advances and Materials Research Bulletin.*

References

[1] Nasrollahzadeh M, Atarod M, Sajjadi M, Sajadi SM, Issaabadi Z. Plant-Mediated Green Synthesis of Nanostructures: Mechanisms, Characterization, and Applications. Interface Science and Technology, vol. 28, Elsevier; 2019, p. 199–322. https://doi.org/10.1016/B978-0-12-813586-0.00006-7.

[2] Das C, Sen S, Singh T, Ghosh T, Paul SS, Kim TW, et al. Green Synthesis, Characterization and Application of Natural Product Coated Magnetite Nanoparticles for Wastewater Treatment. Nanomaterials 2020;10:1615. https://doi.org/10.3390/nano10081615.

[3] El-Gendy NSh, Nassar HN. Biosynthesized magnetite nanoparticles as an environmental opulence and sustainable wastewater treatment. Science of The Total Environment 2021;774:145610. https://doi.org/10.1016/j.scitotenv.2021.145610.

[4] Adedapo A, Oyagbemi A, Fagbohun O, Omobowale T, Yakubu M. Evaluation of the anticancer properties of the methanol leaf extract of Chromolaena odorata on HT-29 cell line. Journal of Pharmacognosy and Phytochemistry E-ISSN: 2278-4136 2016;52:52–7.

[5] Kouamé PB-K, Jacques C, Bedi G, Silvestre V, Loquet D, Barillé-Nion S, et al. Phytochemicals Isolated from Leaves of Chromolaena odorata: Impact

on Viability and Clonogenicity of Cancer Cell Lines. Phytotherapy Research 2013;27:835–40. https://doi.org/10.1002/ptr.4787.

[6] Pandith H, Zhang X, Liggett J, Min K-W, Gritsanapan W, Baek SJ. Hemostatic and Wound Healing Properties of *Chromolaena odorata* Leaf Extract. ISRN Dermatology 2013;2013:1–8. https://doi.org/10.1155/2013/168269.

[7] Ricci A, Olejar KJ, Parpinello GP, Kilmartin PA, Versari A. Application of Fourier Transform Infrared (FTIR) Spectroscopy in the Characterization of Tannins. Applied Spectroscopy Reviews 2015;50:407–42. https://doi.org/10.1080/05704928.2014.1000461.

[8] Wang Z, Fang C, Megharaj M. Characterization of Iron–Polyphenol Nanoparticles Synthesized by Three Plant Extracts and Their Fenton Oxidation of Azo Dye. ACS Sustainable Chem Eng 2014;2:1022–5. https://doi.org/10.1021/sc500021n.

[9] Wang X, Zhao Y, Jiang X, Liu L, Li X, Li H, et al. In-situ self-assembly of plant polyphenol-coated Fe3O4 particles for oleaginous microalgae harvesting. J Environ Manage 2018;214:335–45. https://doi.org/10.1016/j.jenvman.2018.03.019.

[10] Cai W, Wan J. Facile synthesis of superparamagnetic magnetite nanoparticles in liquid polyols. Journal of Colloid and Interface Science 2007;305:366–70. https://doi.org/10.1016/j.jcis.2006.10.023.

[11] Drits V, Środoń J, Eberl DD. XRD Measurement of Mean Crystallite Thickness of Illite and Illite/Smectite: Reappraisal of the Kubler Index and the Scherrer Equation. Clays Clay Miner 1997;45:461–75. https://doi.org/10.1346/CCMN.1997.0450315.

[12] Mohamed Khalith SB, Rishabb Anirud R, Ramalingam R, Karuppannan SK, Dowlath MJH, Pandion K, et al. Synthesis and characterization of magnetite carbon nanocomposite from agro waste as chromium adsorbent for effluent treatment. Environmental Research 2021;202:111669. https://doi.org/10.1016/j.envres.2021.111669.

[13] Sitthichai S, Pilapong C, Thongtem T, Thongtem S. CMC-coated Fe3O4 nanoparticles as new MRI probes for hepatocellular carcinoma. Applied Surface Science 2015;356:972–7. https://doi.org/10.1016/j.apsusc.2015.08.140.

[14] Cacua K, Ordoñez F, Zapata C, Herrera B, Pabón E, Buitrago-Sierra R. Surfactant concentration and pH effects on the zeta potential values of alumina nanofluids to inspect stability. Colloids and Surfaces A: Physicochemical and Engineering Aspects 2019;583:123960. https://doi.org/10.1016/j.colsurfa.2019.123960.

[15] Xiang C, Yang F, Li M, Jaridi M, Wu N. Experimental and statistical analysis of surface charge, aggregation and adsorption behaviors of surface-functionalized titanium dioxide nanoparticles in aquatic system. J Nanopart Res 2013;15:1293. https://doi.org/10.1007/s11051-012-1293-7.

[16] Al-Degs YS, El-Barghouthi MI, El-Sheikh AH, Walker GM. Effect of solution pH, ionic strength, and temperature on adsorption behavior of reactive dyes on activated carbon. Dyes and Pigments 2008;77:16–23. https://doi.org/10.1016/j.dyepig.2007.03.001.

[17] Sing KSW, Williams RT. Physisorption Hysteresis Loops and the Characterization of Nanoporous Materials. Adsorption Science & Technology 2004;22:773–82. https://doi.org/10.1260/0263617053499032.

[18] Scariya S, Davis D, Hameed J, Babu M. An In-vitro Evaluation on Anthelmintic activity of different extracts of Hemigraphis colorata leaves. Research Journal of Pharmacy and Technology 2019;12:4394–6.

[19] Pel P, Chae H-S, Nhoek P, Kim Y-M, Khiev P, Kim GJ, et al. A stilbene dimer and flavonoids from the aerial parts of Chromolaena odorata with proprotein convertase subtilisin/kexin type 9 expression inhibitory activity. Bioorganic Chemistry 2020;99:103869. https://doi.org/10.1016/j.bioorg.2020.103869.

[20] Xiao Z, Yuan M, Yang B, Liu Z, Huang J, Sun D. Plant-mediated synthesis of highly active iron nanoparticles for Cr (VI) removal: Investigation of the leading biomolecules. Chemosphere 2016;150:357–64. https://doi.org/10.1016/j.chemosphere.2016.02.056.

[21] Wang Z, Yu C, Fang C, Mallavarapu M. Dye removal using iron–polyphenol complex nanoparticles synthesized by plant leaves. Environmental Technology & Innovation 2014;1–2:29–34. https://doi.org/10.1016/j.eti.2014.08.003.

[22] Elhabiri M, Carrër C, Marmolle F, Traboulsi H. Complexation of iron(III) by catecholate-type polyphenols. Inorganica Chimica Acta 2007;360:353–9. https://doi.org/10.1016/j.ica.2006.07.110.

[23] Kozakova Z, Kuritka I, Kazantseva NE, Babayan V, Pastorek M, Machovsky M, et al. The formation mechanism of iron oxide nanoparticles within the microwave-assisted solvothermal synthesis and its correlation with the structural and magnetic properties. Dalton Trans 2015;44:21099–108. https://doi.org/10.1039/C5DT03518J.

[24] Barton MD. ALTERNATIVE Brine Sources for Fe-Oxide(-Cu-Au) Systems: Implications for Hydrothermal Alteration and Metals n.d.:18.

[25] Anthony ET, Oladoja NA. Process enhancing strategies for the reduction of Cr(VI) to Cr(III) via photocatalytic pathway. Environ Sci Pollut Res 2022;29:8026–53. https://doi.org/10.1007/s11356-021-17614-z.

[26] Wang X, Wang L, Wang Y, Tan R, Ke X, Zhou X, et al. Calcium Sulfate Hemihydrate Whiskers Obtained from Flue Gas Desulfurization Gypsum and Used for the Adsorption Removal of Lead. Crystals 2017;7:270. https://doi.org/10.3390/cryst7090270.

[27] Kepp KP. Free Energies of Hydration for Metal Ions from Heats of Vaporization. J Phys Chem A 2019;123:6536–46. https://doi.org/10.1021/acs.jpca.9b05140.

[28] Fan X, Liu H, Anang E, Ren D. Effects of Electronegativity and Hydration Energy on the Selective Adsorption of Heavy Metal Ions by Synthetic NaX Zeolite. Materials (Basel) 2021;14:4066. https://doi.org/10.3390/ma14154066.

[29] Smith DW. Ionic hydration enthalpies. Journal of Chemical Education 1977;54:540–2. https://doi.org/10.1021/ed054p540.

[30] Cheng TW, Lee ML, Ko MS, Ueng TH, Yang SF. The heavy metal adsorption characteristics on metakaolin-based geopolymer. Applied Clay Science 2012;56:90–6. https://doi.org/10.1016/j.clay.2011.11.027.

[31] Kinniburgh DG. General purpose adsorption isotherms. ACS Publications 2002. https://doi.org/10.1021/es00151a008.

[32] Mittal A, Kurup L, Mittal J. Freundlich and Langmuir adsorption isotherms and kinetics for the removal of Tartrazine from aqueous solutions using hen feathers. Journal of Hazardous Materials 2007;146:243–8. https://doi.org/10.1016/j.jhazmat.2006.12.012.

[33] Jaroniec M. Adsorption on heterogeneous surfaces: The exponential equation for the overall adsorption isotherm. Surface Science 1975;50:553–64. https://doi.org/10.1016/0039-6028(75)90044-8.

[34] A.O D, Olalekan A, Olatunya A, Dada AO. Langmuir, Freundlich, Temkin and Dubinin–Radushkevich Isotherms Studies of Equilibrium Sorption of Zn 2+ Unto Phosphoric Acid Modified Rice Husk. J Appl Chem 2012;3:38–45. https://doi.org/10.9790/5736-0313845.

[35] Joshy D, Chakko S, Ismail YA, Periyat P. Surface basicity mediated rapid and selective adsorptive removal of Congo red over nanocrystalline mesoporous CeO2. Nanoscale Adv 2021;3:6704–18. https://doi.org/10.1039/D1NA00412C.

[36] Simonin J-P. On the comparison of pseudo-first order and pseudo-second order rate laws in the modeling of adsorption kinetics. Chemical Engineering Journal 2016;300:254–63. https://doi.org/10.1016/j.cej.2016.04.079.

[37] Günay A, Arslankaya E, Tosun i. Lead removal from aqueous solution by natural and pretreated clinoptilolite: Adsorption equilibrium and kinetics. Journal of Hazardous Materials 2007;146:362–71. https://doi.org/10.1016/j.jhazmat.2006.12.034.

[38] Kul AR, Koyuncu H. Adsorption of Pb(II) ions from aqueous solution by native and activated bentonite: Kinetic, equilibrium and thermodynamic study. Journal of Hazardous Materials 2010;179:332–9. https://doi.org/10.1016/j.jhazmat.2010.03.009.

[39] Yamashita T, Hayes P. Analysis of XPS spectra of Fe2+ and Fe3+ ions in oxide materials. Applied Surface Science 2008;254:2441–9. https://doi.org/10.1016/j.apsusc.2007.09.063.

[40] Poulin S, França R, Moreau-Bélanger L, Sacher E. Confirmation of X-ray Photoelectron Spectroscopy Peak Attributions of Nanoparticulate Iron Oxides, Using Symmetric Peak Component Line Shapes. J Phys Chem C 2010;114:10711–8. https://doi.org/10.1021/jp100964x.

[41] Zou H, Zhao J, He F, Zhong Z, Huang J, Zheng Y, et al. Ball milling biochar iron oxide composites for the removal of chromium (Cr(VI)) from water: Performance and mechanisms. Journal of Hazardous Materials 2021;413:125252. https://doi.org/10.1016/j.jhazmat.2021.125252.

[42] McCafferty E, Wightman JP. Determination of the concentration of surface hydroxyl groups on metal oxide films by a quantitative XPS method. Surface and Interface Analysis 1998;26:549–64. https://doi.org/10.1002/(SICI)1096-9918(199807)26:8<549::AID-SIA396>3.0.CO;2-Q.

[43] Lei Z, Shi F, Lu L. Incorporation of MnO2-Coated Carbon Nanotubes between Graphene Sheets as Supercapacitor Electrode. ACS Appl Mater Interfaces 2012;4:1058–64. https://doi.org/10.1021/am2016848.

[44] Thomas JM, Tricker MJ. Electronic structure of the oxides of lead. Part 2.—An XPS study of bulk rhombic PbO, tetragonal PbO, β-PbO2 and Pb3O4. J Chem Soc, Faraday Trans 2 1975;71:329–36. https://doi.org/10.1039/F29757100329.

[45] Riaz S, Akbar A, Naseem S. Ferromagnetic Effects in Cr-Doped Fe2O3 Thin Films. IEEE Transactions on Magnetics 2014;50:1–4. https://doi.org/10.1109/TMAG.2014.2312977.

[46] Ullah Z, Atiq S, Naseem S. Influence of Pb doping on structural, electrical and magnetic properties of Sr-hexaferrites. Journal of Alloys and Compounds 2013;555:263–7. https://doi.org/10.1016/j.jallcom.2012.12.061.

CHAPTER 4

Synthesis, characterization and heavy metal removal of PMNPs engineered using *Sphageneticola trilobata* leaf extract

> Biodiversity is the greatest treasure we have.
> Its diminishment is to be prevented at all costs.
>
> \- Thomas Eisner

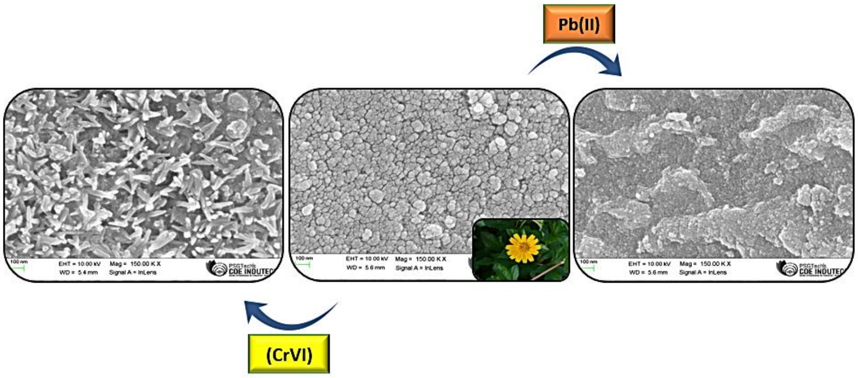

Singapore daisy is an invasive herb capturing acres of land in the State causing a huge economical loss for farmers. The allelopathic nature of the plant prevents any crop to sprout/growing in its area of invasion. The aqueous extract of the plant leaves, containing abundant iron chelating biomolecules was used to procure phytoconjugated superparamagnetic IONPs. The obtained NPs were used to reduce and remove hazardous pollutants from water. The magnetic nature of the NPs facilitated easy removal and regeneration of the exhausted adsorbents.

The boom in anthropogenic activities and improper handling of resources have caused an alarming hike in the heavy metal concentration in the ecosystem. Magnetite NPs are one of the most popularly used adsorbents for the removal of HMIs from the aquatic environment. One of the noxious weeds, *Sphagneticola trilobata* (L.) Pruski, commonly known as 'Singapore daisy' was chosen as a reducing and capping agent to produce phytoconjugated magnetite NPs. The aerial parts of the plant are reported to contain active secondary metabolites which can help in the reduction followed by the stabilization of the metal precursor. Phytogenic nanoparticles generally face high aggregation, therefore ultrasonic assistance was employed to control the extent of aggregation and to control the size of particles. The obtained samples were characterized using assorted analytical techniques. The obtained magnetite NPs were studied for their heavy metal detoxification properties.

4.1 Synthesis of SMNs

To 50mL of the *S. trilobata* leaf extract, 30mL of 0.032M freshly prepared $FeCl_3$ solution was added under vigorous magnetic stirring followed by stepwise addition of 0.52g of $NaHCO_3$. The instant appearance of dirty green precipitate indicated the formation of iron hydroxide. The mixture obtained was ultrasonicated for 15 minutes on a Sonics vibra-cell sonicator with an immersed ultrasonic horn (6.8mm, 25kHz) and was then magnetically stirred for 1 hour at room temperature. The mixture was transferred into a teflon-lined autoclave followed by hydrothermal treatment at 180^0C for 12 hours. The black product formed was magnetically separated, sequentially leached with ethanol and water, dried at 60^0C and was ground to obtain *S. trilobata* - magnetite NPs (SMNs). The effect of hydrothermal duration time on the morphological and physicochemical properties was studied by varying the reaction time to 24 and 36 hours. The obtained samples were named as SMN-12, SMN-24 and SMN-36.

4.2 Characterization of SMNs

The physicochemical characteristics of the procured samples were examined using various analytical techniques.

4.2.1 XRD and SAED Analysis

The diffraction patterns of SMNs (Fig.1 & 2) match well with the normal diffraction patterns of inverse spinel Fe_3O_4 and all peaks are indexed to PDF no. 19-0629. Peaks formed at 2θ values of 30.1°, 35.5°, 43.3°, 53.8°, 57.2°, and 62.9°, correspond to Miller indices of (220), (311), (400), (422), (511), and (440) respectively[1]. Crystallite size can be extracted from the high-intensity peak (311) using Scherrer's equation as given below,

$$D = \frac{K\lambda}{\beta cos\theta} \tag{1}$$

where D is the crystallite size, K is known as the Scherer's constant (K=0.94) which denotes the shape of the particle, λ is the X-ray wavelength (1.54178Å), β is full width at half maximum (FWHM) of the diffraction peak, and θ is the angle of diffraction. The Scherrer equation accounts for the broadening of the diffraction peaks solely due to crystallite size[2]. The recorded crystallite size for SMN-12, SMN-24, and SMN-36 are ~7.24, 11.53 and 13.18nm respectively. The increase in the crystallite size with an increase in reaction time is due to the enhancement in grain growth that occurs with more available reaction time. The increase in the intensity of peaks with an increase in the reaction time indicates the increase in crystallinity attained by altering the hydrothermal treatment time.

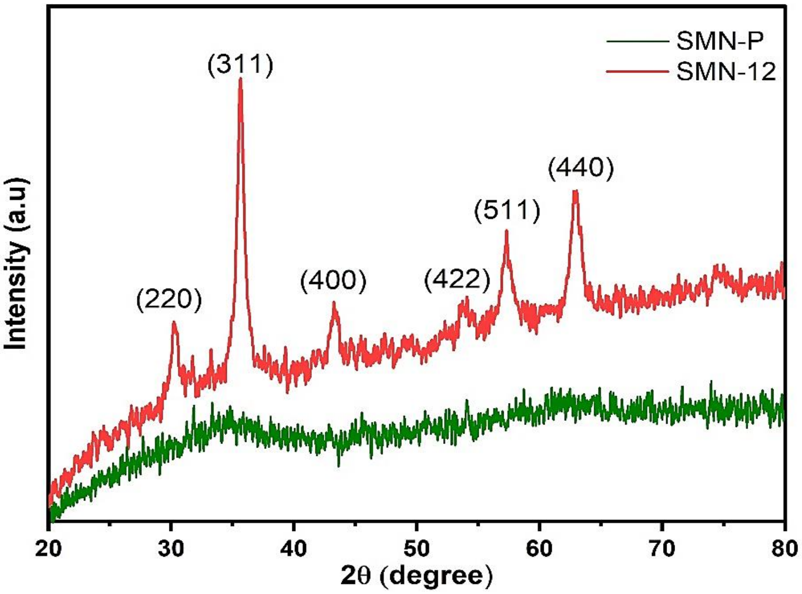

Fig. 1. XRD pattern of dried precursor, SMN-P and SMN-12

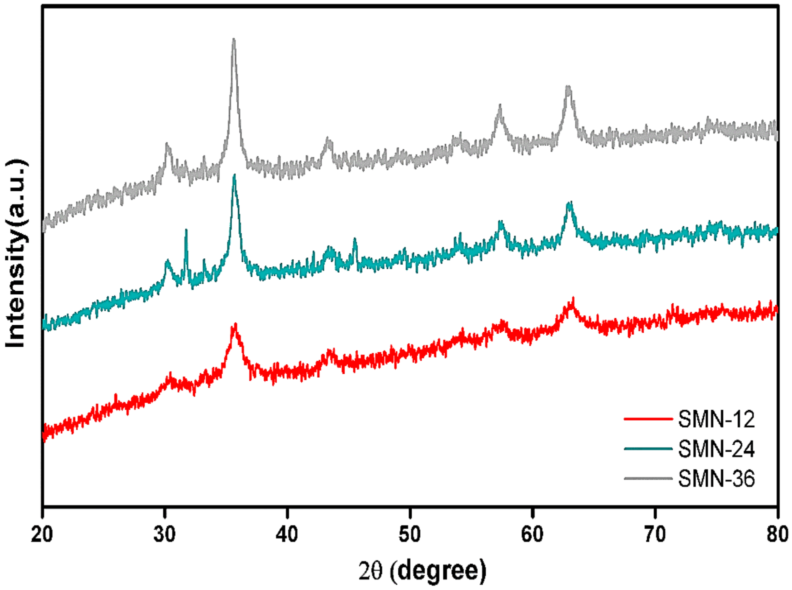

Fig.2. XRD patterns of obtained SMNs

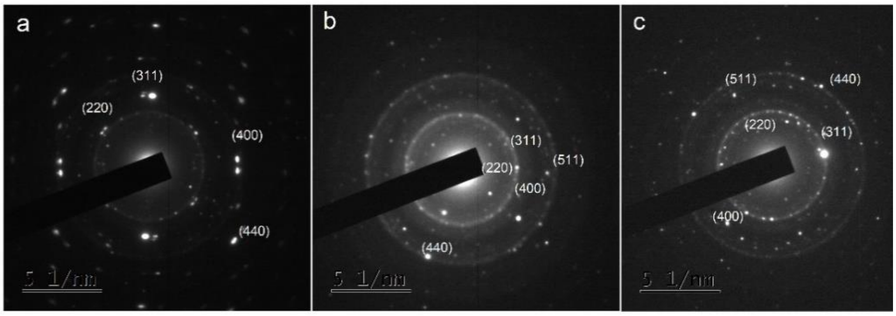

Fig.3. SAED pattern of a) SMN-12, b) SMN-24 and c) SMN-36

The results of the SAED analysis further confirm the phase of the iron oxide nanoparticles formed. The selected area electron diffraction (SAED) pattern of the SMNs (Fig.3) in the selected area exhibits five distinguishable crystal planes of (440), (511), (400), (311), and (220) which agrees with the XRD result. The bright spots in the SAED images depict the crystalline nature of SMNs. The obtained lattice parameters, are 8.406, 8.381and 8.401Å for SMN-12, SMN-24 and SMN-36 respectively, calculated from the SAED date corresponds with the spinel crystal structure of bulk Fe_3O_4 (8.396 Å)[3].

4.2.2 FTIR analysis

FTIR spectra of the leaf extract, the precursor before hydrothermal treatment and the SMN-12 are illustrated in Fig.4. The peaks around 343cm^{-1}, 1454cm^{-1} and 1373cm^{-1} in the extract are attributed to OH stretching and bending vibrations. The peak at 2928cm^{-1} was assigned to C-H stretching vibration and the peaks appeared around 1631 and 856cm^{-1} were assigned to conjugated C=C stretching and bending vibrations from polyphenols, respectively. While the peak at 1034cm^{-1} corresponds to C-O bending vibrations of the biomolecules[4]. A weak peak at ~592cm^{-1} appeared in the precursor indicating the initiation of the metal-oxygen bond. The strong peak around 3435cm^{-1} in SMNs is attributed to hydroxyl groups from polyphenols. The peaks at 2927cm^{-1} and 1457cm^{-1} refer to alkyl

C-H stretching and bending vibrations respectively while the peaks at 1556, 1378cm^{-1} and 1156cm^{-1} represent aromatic skeletal vibrations. The peak at 1260cm^{-1} indicate presence of aromatic C-O groups. The peaks appeared in the range of 811-870cm^{-1} represents C=C moieties. The increased intensity of the peak ~572cm^{-1} in SMNs confirmed transformation of precursor to magnetite whereas the reoccurrence of several peaks in the extract verifies conjugation of the formed iron oxide core with various phytochemical fragments derived from the leaf extract[3].

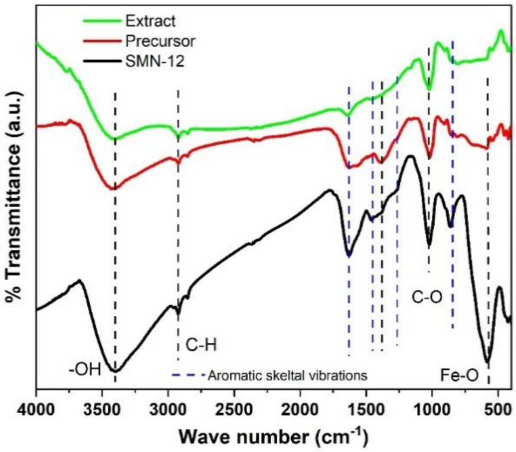

Fig.4. FTIR spectra of *S. trilobata* extract, dried precursor & SMN-12

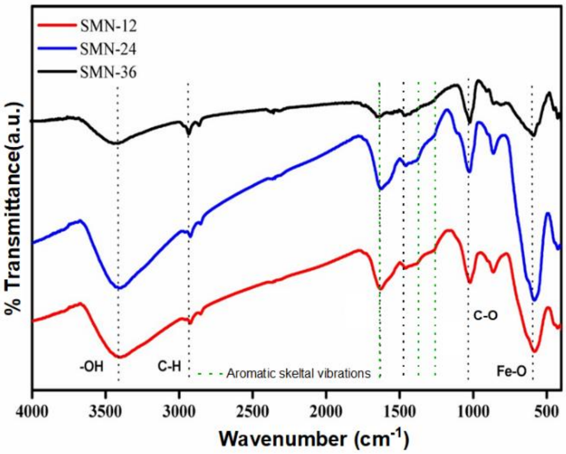

Fig.5. FTIR spectra of SMNs

4.2.3 HRTEM analysis

The HR-TEM micrograph (Fig.6) exhibits the formation of nearly spherical and slightly agglomerated particles in SMN-12. Agglomeration is a common occurrence in the case of phytogenic metal oxide nanoparticles and ultrasonic assistance possibly has enhanced the surface refinement in SMN-12. The agglomeration may also have originated from magnetic interactions between the SMNs particles[5]. However, with the increase in the duration of hydrothermal reaction time particle size and agglomeration tendency also increased, owing to the accelerated degradation of phytoconjugates and high surface energy of particles. HRTEM micrographs indicate formation of elliptical NPs with increase in reaction time. The average particle size computed from size distribution analysis for SMN-12, SMN-24 and SMN-36 is 7.01, 9.44 and 10.39nm respectively (Fig.7). The close correlation between calculated size from HRTEM and XRD indicates that phytochemical exists as a thin layer around the magnetite core and the particles exists mostly as single crystals.

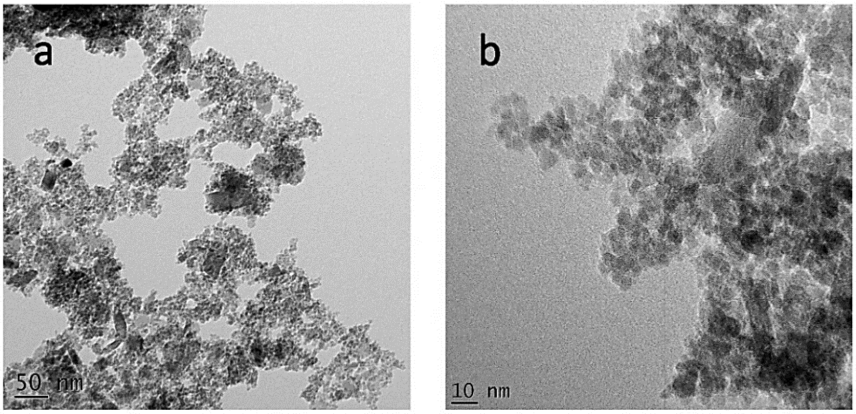

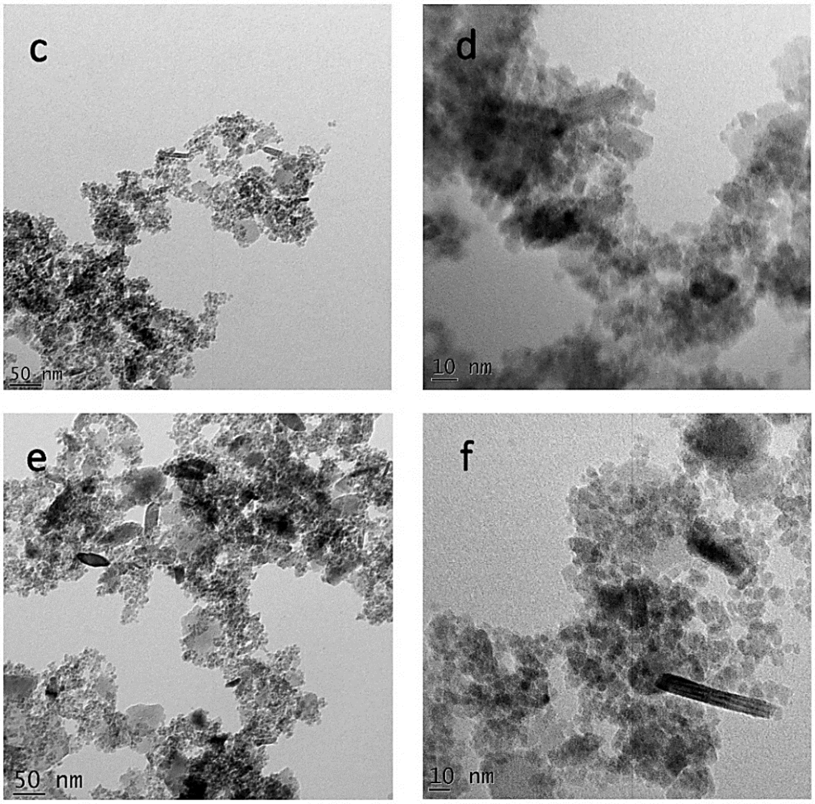

Fig.6. HRTEM micrographs of a,b) SMN-12, c,d) SMN-24 & e,f)SMN-36

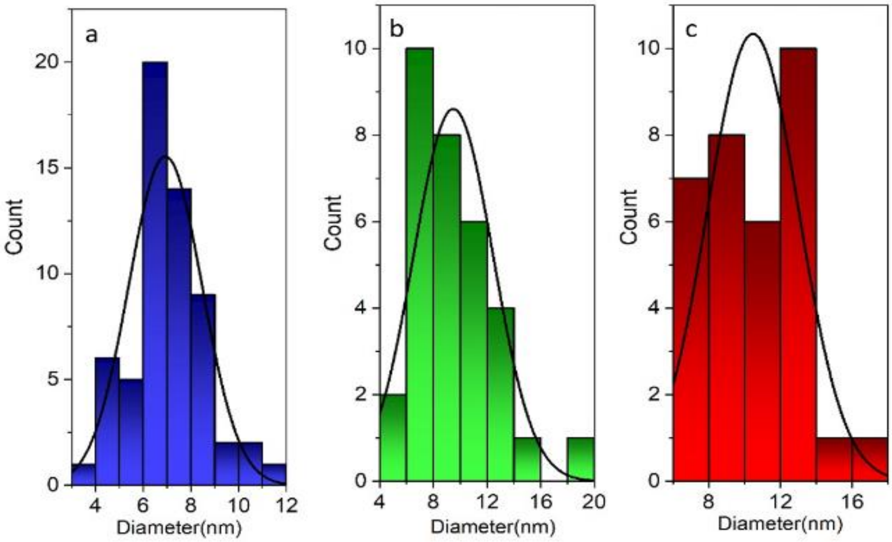

Fig.7. Size distribution analysis of a) SMN-12 b) SMN-24 & c) SMN-36

4.2.4 Zeta potential and the point of zero charge

The magnitude of zeta potential (ZP) is one of the multiple indications of the physical stability of the material in solution/dispersion. ZP values typically range from +100 to −100mV. NPs with ZP values >+25mV or <−25mV generally have an appreciable degree of stability. ZP is crucial in adsorption studies as it provides information on the possible electrostatic interactions between adsorbent-adsorbate pair[6]. The ZP values of SMN-12, SMN-24, and SMN-36 were -29.52, -25.31 and -31.81mV respectively.

The point of zero charge (pH_{PZC}) defines the conditions(pH) for which the surface density of positive charges (contribution of cations) equals that of negative charges (anions). Below pH_{PZC} the surface is positively charged and above the pH_{PZC} the surface exhibits negative charge. pH_{PZC} determination plots for SMNs displayed in Fig.5 reveals that the surface of SMN-12 and SMN-24 is negatively charged above pH of ~4.6 however, SMN-36 surface has a lower pH_{PZC} value of 2.7.

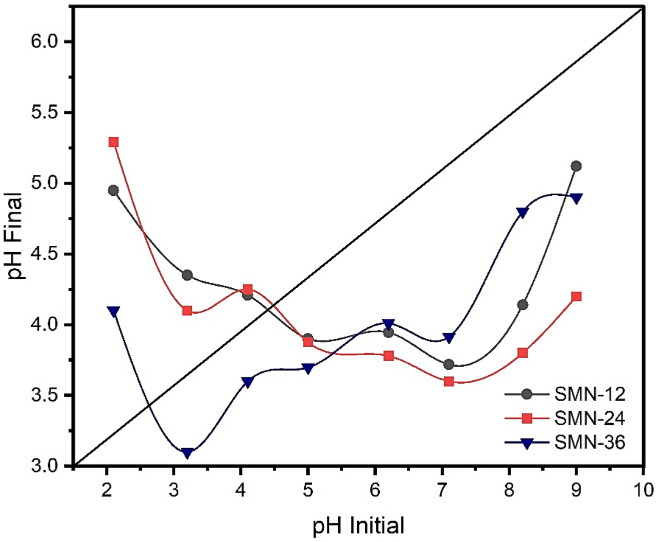

Fig.8. pH drift method for detecting pH_{ZPC} of SMNs

4.2.5 BET analysis

The specific surface area and degree of porosity of SMNs were measured using BET method by N_2 sorption-desorption isotherms. The study yielded a pseudo- type II isotherm. The presence of a hysteresis loop at p/p_0=0.6-0.9 indicates a typical H3 type hysteresis indicating the presence of grooves created by non-rigid aggregated particles. The pore distribution analysis by Barrett-Joyner-Halenda's (BJH) method revealed two peaks indicating the presence of pores of different types[7]. The peaks represent the interstices created by the boundaries of the nanoparticles. The specific surface area and the mean pore diameter obtained for SMN-12 calculated were 7.01m^2g^{-1} and 17.41nm respectively. The average pore volume calculated was 0.03cm^3g^{-1} indicating the low porosity of the material.

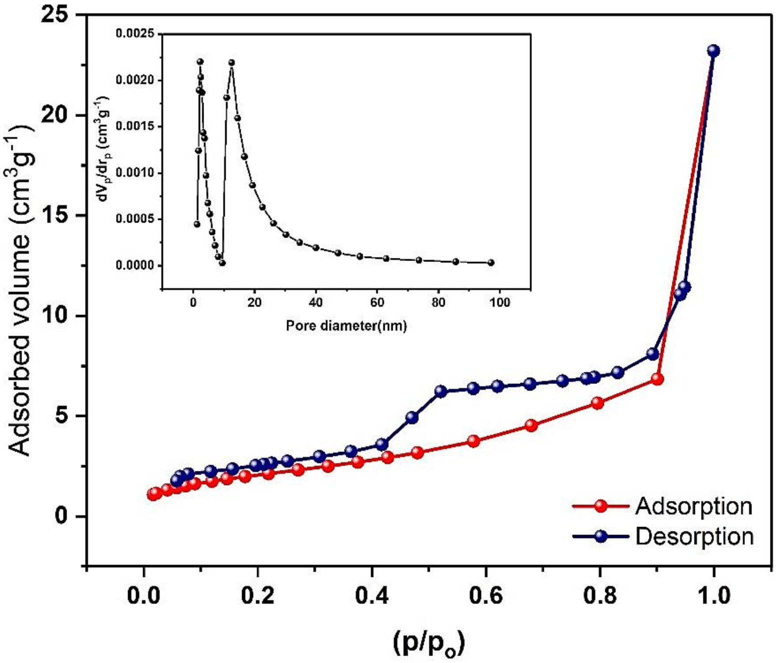

Fig.9. N_2 adsorption isotherm analysis of SMN-12; inset showing BJH plot

4.3 Mechanism of SMNs formation

Literature suggests the presence of an appreciable amount of active secondary metabolites like polyphenols specially flavonoids in addition to other active secondary metabolites including terpenoids and sugars in the aerial parts of the *S. trilobata*. Flavonoids are one of the major phytoconstituent in the stems and leaves of the plant. The iron chelating and reducing ability of flavonoids are reported elsewhere[8]. Fe(III) generally chelates with flavonoids containing catechol/gallol groups to form tris-complexes and undergo subsequent reduction to Fe(II)[9,10]. The iron chelating sites in the flavonoids are the hydroxyl groups in the flavonoid framework, the keto group in the B ring and 2,3 double bonds. Phytoconstituents with multiple iron binding sites prevent the re-oxidation of Fe(II)[11]. The important flavonoids present in the plant are caffeic acid, apigenin, and diosmetin which are reported for its ability to chelate with iron and to subsequently reduce it. The aerial parts of the plant contain benzene derivatives like benzeneacetic acid 2- phenylethenyl ester, isocinnamic acid, 4-methoxycatechol, caffeic acid, and protocatechualdehyde[12,13]. The leaves of the plant also contain isoflavonoids and wedelolactone. Primary phytoscreening of the aqueous leaf extract from *S. trilobata* indicates that tannin, saponins, flavonoids, phenol, and terpenoids are the plant's main phytoconstituents. The estimated TPC and TFC were 142.13±1.27mg GAE/g and 21.52±1.35mg QE/g respectively. The addition of $FeCl_3$, generates a thick black precipitate indicating the complexation of Fe^{3+} ions with active biomolecules in the extract.

The addition of $NaHCO_3$ increases the pH of the reaction mixture to 7.2. At this pH, the mild reducing phytochemicals partially reduce the Fe^{3+} ions in the solution. Ultrasonication of the colloidal solution provides homogenization leading to effective incorporation of phytochemicals around the newly formed nanoparticles. The partial degradation of phytochemicals in the hydrothermal reactor creates heterogenous nucleating centres. The mixture of NaCl, H_2O and CO_2 at higher temperature and suitable pressure initiate the hydroxide-oxide conversion. The phytochemicals present in the reaction medium has a significant role in reducing the frequency of collisions between the premature nanoparticles, resulting in smaller crystallite size. Self-capping of phytochemicals prevents aggregation of nanoparticles and provides SMNs an interactive surface, which can be made use for diverse applications.

4.4 Removal of HMIs by SMNs – analytical study

Exposure to Cr(VI) typically occurs in both occupational and environmental settings. The majority of Cr(VI) exposure for the general public comes by ingestion, whereas occupational dangers happen through inhalation and cutaneous intake. Cr(VI) can reach infants through breast milk and foetus through placenta[14,15]. Considering the noxious nature of this contaminant stringent strategies to monitor, control and eliminate Cr(VI) should be of prime concern.

Another dangerous metal that has been utilised by mankind from the beginning of time is lead. The use of lead in a variety of commercial and domestic applications has been outlawed or severely regulated by the authorities. However, the public is still exposed to lead through drinking water and air pollution from lead smelters and vehicles that use leaded gasoline. Decanters made of lead crystal or ceramic pottery have the potential to contaminate food or various liquids. At the workplace, workers may be exposed to dust and vapours containing lead. The use of conventional ethnic medicines and food adulterants is a surprising source of lead[16]. Even at modest levels of lead exposure, there is growing concern about neurologic disorders, particularly in children[17].

Considering the hazardous nature of these contaminants stringent strategies to monitor, regulate and remove them should be of utmost concern. Based on the pH_{PZC} study, the SMNs were investigated for their heavy metal removal properties. At particular experimental conditions, SMNs demonstrated considerable adsorptive removal against Cr(VI) and Pb(II). A brief discussion of the details of the associated experiments and the obtained results are provided below.

4.4.1 Adsorption batch experiments

Pilot experiments were conducted to choose the finest adsorbent from the SMNs series. Three SMNs were taken in different dosages to find the potential adsorbent and the suitable dosage. SMN-12 exhibited superior adsorption performance compared to SMN-24 and SMN-36, owing to less agglomerated morphology and high phytoconjugate content. Therefore SMN-12 was chosen as the adsorbent for further experiments. The optimum dosage of 2 gL^{-1} for Cr(VI) and 1.5 gL^{-1} for Pb(II) (Fig.10), and a contact period of 10 minutes were kept constant to study the effect of pH (2-9), temperature(30-60°C), initial HMI concentration and selected competing ions.

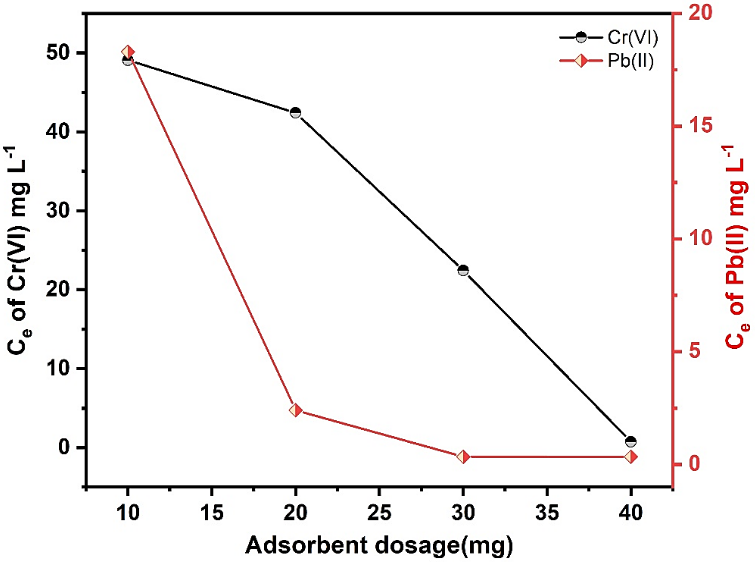

Fig.10. Dosage studies of SMN-12 for removal of Cr(VI) and Pb(II)

The adsorptive efficiency of SMN-12 towards anionic Cr(VI) and cationic Pb(II) was based on the electrostatic interactions between the adsorbate-adsorbent pair, which crucially depended on the pH of the solution. pH_{PZC} for SMN-12 was found to be 4.6, below which the surface is positively charged and can attract anionic species. A prominent increase in the adsorption efficiency of SMN-12 towards Cr(VI) with a decrease in the pH is evident in Fig.11. Maximum Cr(VI) adsorption efficiency of SMN-12 was observed at pH 2. The speciation of Cr(VI) in aqueous solution also varies with pH. $HCrO_4^-$ predominates when pH is below 4.6, however, as the pH increases CrO_4^{2-} dominates in the solution. The lower adsorption free energy of $HCrO_4^-$compared to CrO_4^{2-}make it more susceptible to adsorption [30]. At lower pH the SMN-12 surface is sufficiently protonated yielding electrostatic attraction towards $HCrO_4^-$. Whereas an increase in pH generates more negative charge on the surface of SMN-12 initiating electrostatic repulsion between Cr(VI) species and the adsorbent, thus reducing Cr(VI) adsorption onto SMN-12.

The negative surface formed while increasing the pH aids in the adsorption of Pb(II) species. The Pb(II) species dominating in solution up to pH 7 are Pb^{+2} and $Pb(OH)^+$ which are electrostatically attracted on to the negatively charged SMN-12 surface (L. Giraldo, 2008). The inherent pH of the stimulated lead solution was 5.7 and it was observed that optimum adsorption of Pb(II) ions occurred at pH higher than this(Fig.11). However increasing pH above 6 caused precipitation of $Pb(OH)_2$ causing a decline in the initial concentration of the pollutant prior to the adsorbent addition. Therefore, the inherent pH of the simulated Pb(II) solution was considered as the optimum for the adsorptive removal. The effects of pH on adsorption of the selected HMIs are illustrated in Fig.11.

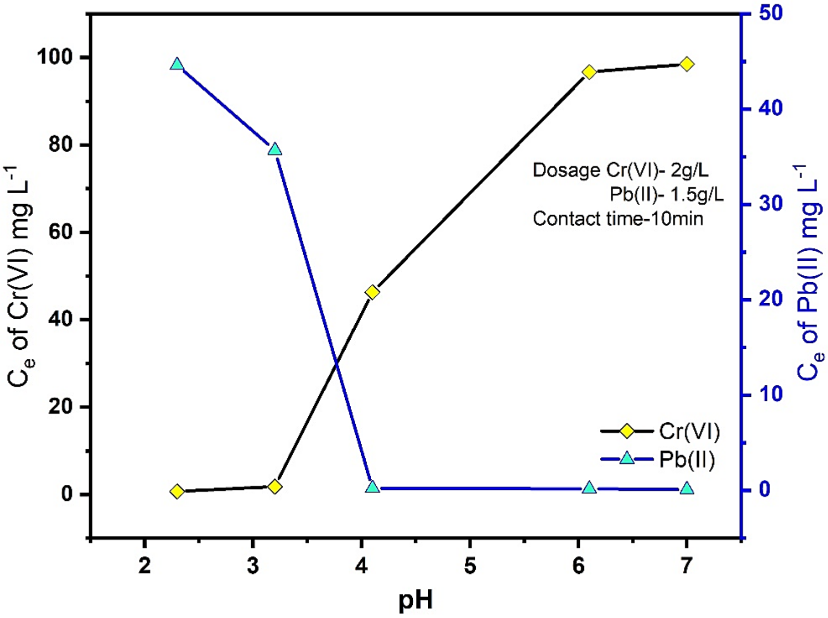

Fig.11. Effect of pH on adsorption of Cr(VI) and Pb(II) by SMN-12

The potential of SMN-12 adsorbent in presence of interfering anions was investigated. The experiments testified that SMN-12 is a promising adsorbent against Cr(VI) and Pb(II) even at higher concentrations of various anions and cations respectively. However, adsorption capacity towards Cr(VI) deteriorated evidently in presence of carbonate and phosphate ions(Fig.12). These ions can compete with $HCrO_4^-$ ions for active sites on the adsorbent. Moreover, higher affinity of these anions towards iron may decelerate the adsorption of Cr(VI) by blocking the reactive sites. As depicted in Fig. 12, SMN-12 showed appreciable removal efficiency and selectivity towards Pb(II) in presence of other cations like Ni^{+2}, Cu^{+2}, Hg^{+2}, Cd^{+2} and Co^{2+}. Atomic absorbance spectroscopy confirmed the absence of any leached iron in the solution after adsorption even after multiple uses.

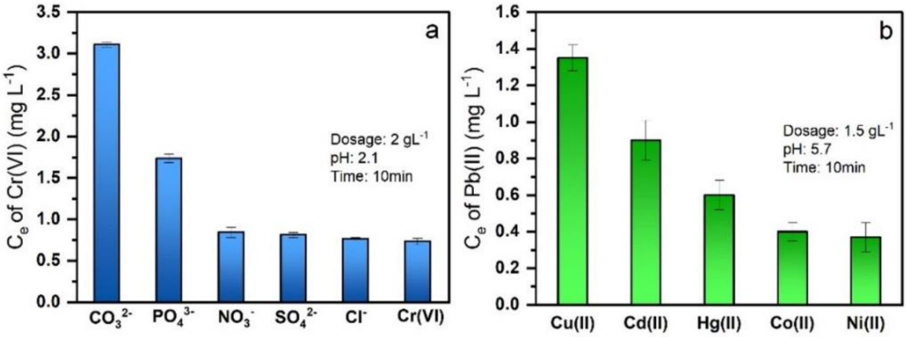

Fig. 12. Effect of competing ions on adsorption of a) Cr(VI) & b) Pb(II)

4.4.2 Adsorption isotherm, kinetic and thermodynamic study

The effect of initial concentration of Cr(VI) was studied to analyse the loading capacity of the adsorbent. The adsorption capacity increased from 25.21 to 184.56 mgg^{-1} and from 32.91 to 323.71 mgg^{-1} for Cr(VI) and Pb(II) respectively with increase in initial concentration (50 to 500 mgL^{-1}). The adsorption isotherms were applied to display the equilibrium between the remaining metal ion concentrations (C_e) and the amount of adsorbed metal ions onto adsorbent surface (q_e). The isotherms were fitted using three different models 1) Langmuir isotherm 2) Freundlich isotherm and 3) Temkin isotherm (Fig.13 a&b)[18]. The correctness of the fit was determined from the R^2 value and closeness of the obtained maximum adsorption capcity (Q_m) to the experimental value. The results of the adsorption equilibrium studies are compiled in Table 1. The study established that adsorption of Cr(VI) and Pb(II) on to SMN-12 followed Langmuir adsorption isotherm model. The affinity between the adsorbent and adsorbate is quantified by evaluating the dimensionless separation factor R_L which is given by the equation.

$$R_L = \frac{1}{1+bC_0} \qquad (1)$$

here C_0 is the highest initial adsorbate concentration and b is the Langmuir adsorption isotherm constant. The R_L value obtained for adsorption of Cr(VI) and Pb(II) on SMN-12 was 0.0022 and 0.0025 respectively. From the obtained R_L-value a favourable parameter K_{C0} can be derived as per equation 2.

$$K_{C_0} = \frac{1}{R_L} - 1 \qquad (2)$$

K_{C0} values higher than 10 denotes a spontaneous and highly probable adsorption isotherm. The derived value of K_{C0} for SMN-12 is 453.54 and 399 for Cr(VI) and Pb(II) adsorption. These values approve the highly favorable nature of the adsorption isotherms.

The effect of contact time on adsorption of Cr(VI) and Pb(II) was estimated by varying the shaking time. The adsorption capacities increased rapidly in the first four minutes attaining more than 85% of adsorption before attaining equilibrium in 10 minutes. The maximum adsorption capacity was recorded as 49.57 and 66.07 mgg^{-1} for 100 mgL^{-1} of Cr(VI) and Pb(II) solutions respectively. The kinetics of adsorption was studied by monitoring the change in adsorbate concentration with time. For a better understanding on kinetics and reaction mechanisms, the experimental data was fitted into three different kinetic models: (1) pseudo-first-order, (2) pseudo-second-order, and (3) Elovich, which are illustrated in Fig.13 c & d[19]. The validity of the predicted models was determined using values of R^2, and closeness to experimental equilibrium adsorption capacity(q_e). The results of kinetic modelling studies are presented in Table 1. Adsorption of both target metal ions on to SMN-12 followed pseudo first order kinetics.

Table 1. Details of adsorption isotherm and kinetic models for adsorption

		Parameters	
		Cr(VI)	**Pb(II)**
Isotherm models	*Langmuir*	$q_m(mg\ g^{-1}) = 182.88$ $K_L = 0.894$ $R^2 = 0.851$	$q_m(mg\ g^{-1}) = 315.38$ $K_L = 0.788$ $R^2 = 0.0.926$
	Freundlich	$K_F = 91.77$ $n = 0.17$ $R^2 = 0.638$	$K_F = 120.12$ $n = 0.359$ $R^2 = 0.89$
	Temkin	$K_T(Lg^{-1}) = 38.09$ $B(Jmol^{-1}) = 22.20$ $R^2 = 0.67$	$K_T(Lg^{-1}) = 9.58$ $B(Jmol^{-1}) = 61.25$ $R^2 = 0.883$
Kinetic models	*Pseudo first order*	$q_e(mg\ g^{-1}) = 53.39$ $k_1(h^{-1}) = 0.346$ $R^2 = 0.979$	$q_e(mg\ g^{-1}) = 68.68$ $k_1(h^{-1}) = 0.431$ $R^2 = 0.996$
	Pseudo second order	$q_e(mg\ g^{-1}) = 69.36$ $k_2(g\ (mg\ h)^{-1}) = 0.0046$ $R^2 = 0.961$	$q_e\ (mg\ g^{-1}) = 83.12$ $k_2(g\ (mg\ h)^{-1}) = 0.0057$ $R^2 = 0.986$
	Elovich	$a\ (mg\ g^{-1}) = 31.380$ $b = 0.0538$ $R^2 = 0.947$	$a\ (mg\ g^{-1}) = 78.03$ $b = 0.0532$ $R^2 = 0.981$

The adsorption of Cr(VI) & Pb(II) ions as a function of system temperature was investigated[20]. The batch thermodynamic experiments were studied between 303 and 333K, and it was revealed that increase in temperature caused notable spike in the adsorption efficiency. The following equations were applied to compute the thermodynamic parameters for adsorption of Cr(VI) and Pb(II) ions.

$$K_d = \frac{q_e}{C_e} \qquad (3)$$

$$lnK_d = \frac{-\Delta H}{RT} + \frac{\Delta S}{R} \qquad (4)$$

$$\Delta G = \Delta H - T\Delta S \qquad (5)$$

where K_d represents the equilibrium constant. Fig.13 e&f shows the simulated plot of ln K_d against 1/T for both target metal ions at different temperatures. Table 2 summarizes the derived thermodynamic parameters for adsorption of heavy metal ions on SMN-12. The positive ΔH value indicated the endothermic nature of the adsorption. The positive ΔS values suggested the rising disorder at the interface during the adsorption of target metal ions onto SMN-12. The high negative values of ΔG indicated the spontaneity of the adsorption process.

Table 2. Details of thermodynamic studies

	Temperature (K)	ΔG ($kJmol^{-1}$ K^{-1})	ΔH (kJ mol^{-1} K^{-1})	ΔS ($Jmol^{-1}$ K^{-1})
Cr(VI) Adsorption	303	-12.76926	2.19	42.15
	313	-13.19076		
	323	-13.61226		
	333	-14.03376		
Pb(II) Adsorption	303	-28.99349	15.757	95.744
	313	-29.95089		
	323	-30.90829		
	333	-31.86569		

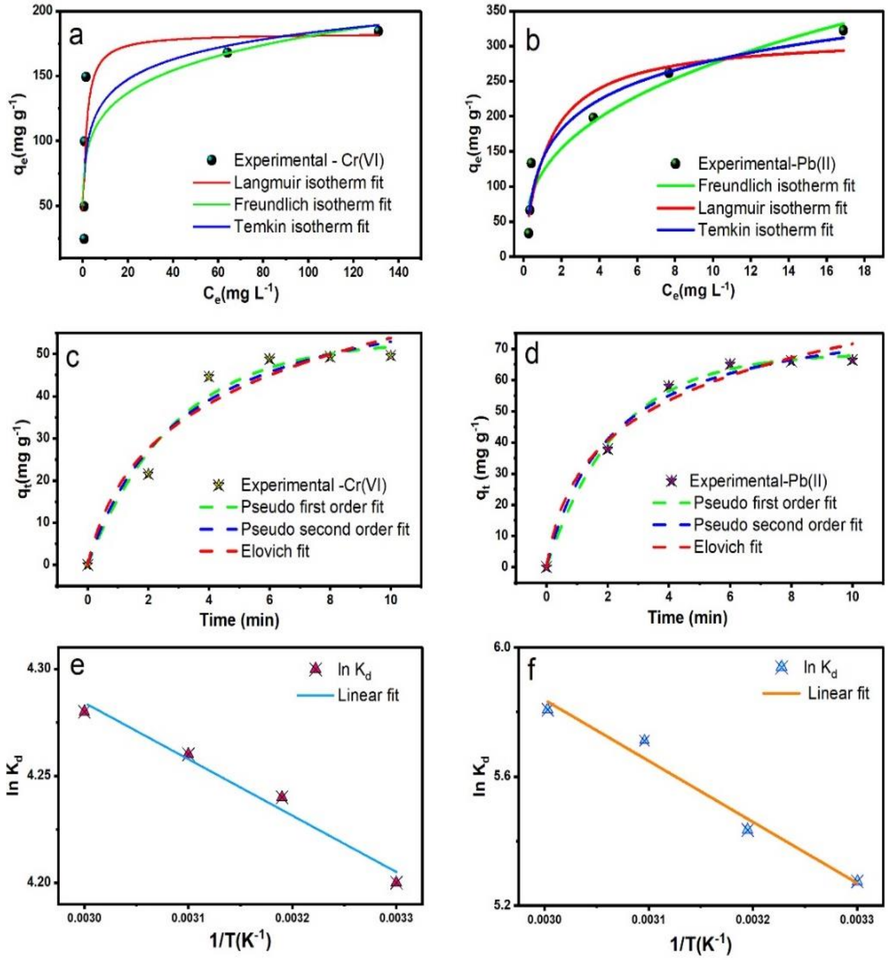

Fig.13. Simulated adsorption isotherms for a) Cr(VI), b) Pb(II) adsorption, simulated kinetic plots for c) Cr(VI), d) Pb(II) adsorption, thermodynamic studies of e) Cr(VI), f) Pb(II).

4.4.3 Surface composition analyses.

Owing to the displayed appreciable adsorption characteristics, SMN-12 was further analyzed using XPS and EDX technique for comprehending the adsorption mechanism of phytoconjugate magnetite nanoparticles and to identify the speciation of the adsorbed ions on the adsorbent surface. XPS profiling of SMN-12 confirmed the presence of Fe, O, C and Fe, O, C, Pb/Cr before and after adsorption respectively. The core-level spectra of each element were peak fitted and examined after aligning the C-C component of C 1s at 284.2eV. The Fe 2p core-level spectrum of SMN-12 displayed two peaks corresponding to Fe $2p_{3/2}$ and Fe $2p_{1/2}$ at ~710.7 eV and ~724.1eV respectively, verifying the magnetite phase. The peak fitted Fe 2p spectrum (Fig.14) consists of peaks at 709.9, 711.26, 712.86, 722.74,723.97 and 725.44eV. The comparable intensities of the three Fe $2p_{3/2}$ components indicate the presence of Fe^{2+}_{oh}: Fe^{3+}_{oh}: Fe^{3+}_{td} close to the theoretical value, 1:1:1 as observed in pure Fe_3O_4. The vacancy cascade peak, which is a common occurrence in iron oxide species is spotted at ~719.2eV. A slight chemical shift to the higher binding energy for all the observed peaks from that of the pure magnetite is correlated to the capping and stabilization of SMN-12 by plant metabolites. The O 1s core-level spectrum (Fig.15) exhibits components at ~529.2, 530.1, and 531.1eV correlated to Fe-O, surface OH moieties and conjugated phytochemical fragments respectively. The C 1s profile of SMN-12 (Fig.16) was fitted into four components with binding energies ~284.2, 285.1, 286.3, and 288.2eV corresponding to C-C, C-O, C=O, and π-π interactions respectively.

The structure of Cr 2p spectra of the exhausted adsorbent, revealed the presence of Cr(III) species alone on the surface (Fig.17a). The multiplet structure of Cr 2p core level spectra, similar to that of $FeCr_2O_4$, Cr_2O_3 or $Cr(OH)_3$ displayed peaks at 576.6, 577.9 and 579.3 eV corresponding to Cr (III) indicating the complete reduction of toxic hexavalent chromium on SMN-12 surface. Pb(II) moieties were detected on the surface of SMN-Pb indicating lead adsorption. Peak fitting of the Pb 4f spectra exposed the presence of two different Pb(II) moieties along with reduced Pb(0) on the surface (Fig.17b). Accordingly, the peaks at 136.8 and 141.8eV were assigned to Pb metal whereas the peaks at 137.6 and 142.5eV represent Pb-O species. Peaks at 138.6 and 143.6 eV indicate Pb interacting with the hydroxyl groups[44]. The peak corresponding to the hydroxyl component in O 1s core spectra displayed an increase in intensity in both cases owing to the increase in the total number of metal-OH bonds formed on the adsorbent surface. The association of HMIs on the surface produced slight chemical shifts in Fe 2p and C 1s spectra of Pb-SMN-12 towards higher binding energy values. The changes in the C 1s spectra of Cr-SMN-12 may be attributed to the involvement of π electrons in the reduction process of Cr(VI) causing the dissolution of the corresponding peak along with increased intensity of C-C peak. Whereas in Pb-SMN-12 the peak is spotted at 289.1 eV owing to the weak reductive nature of the adsorption. However, there is a visible reduction in the area of the peaks in C 1s spectra suggesting the involvement of active groups from the phytoconjugate shell in the reduction process.

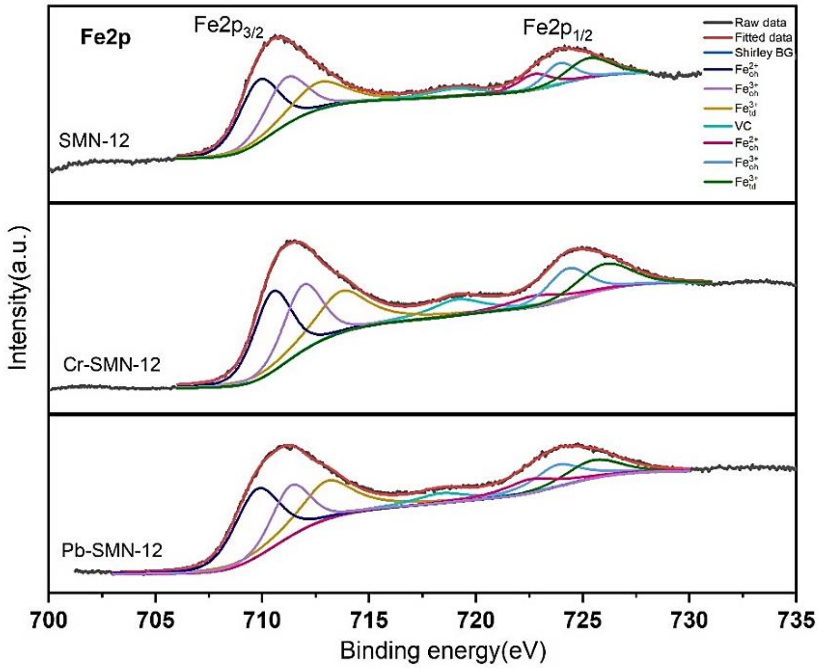

Fig. 14. Fe 2p core level spectra of SMN-12 pre and post adsorption of HMIs

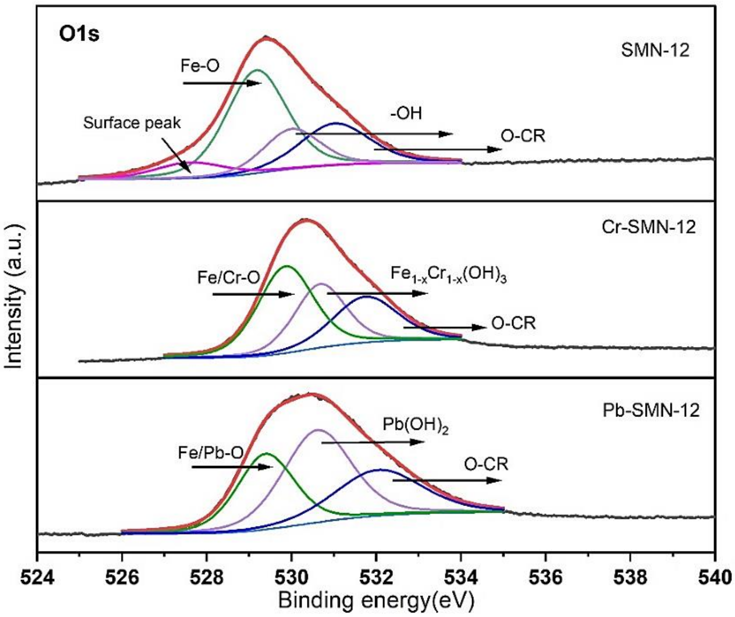

Fig.15. O 1s core level spectra of SMN-12 pre and post adsorption of HMIs

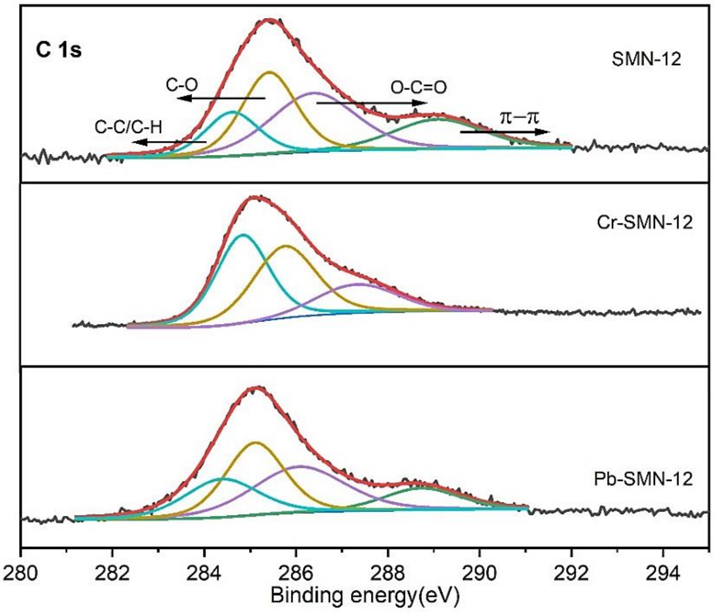

Fig.16. C 1s core level spectra of SMN-12 pre and post adsorption of HMIs

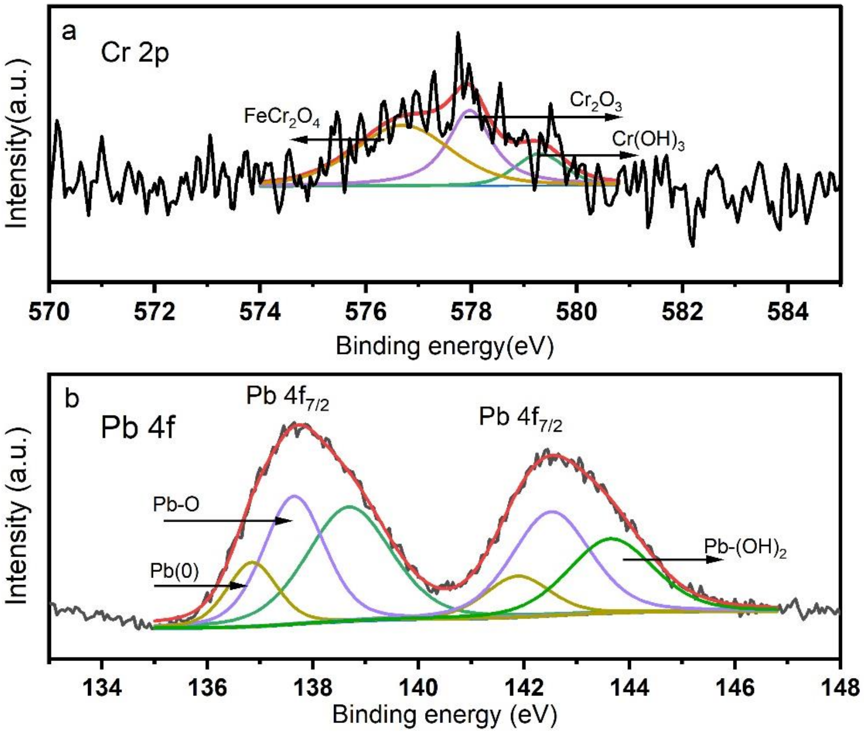

Fig.17 a) Cr 2p and b) Pb 4f core level spectra of SMN-12 post adsorption

The EDX examination provides deeper surface analysis of pure and exhausted adsorbents (Fig.18). Table 3 shows that the results are qualitatively identical with the XPS data though there is evident difference in the composition percentages. The disparity in compositional data obtained from both analyses is due to the difference in the interaction volume for both techniques. XPS analysis is restricted to the surface with a depth of 1-10nm whereas EDX can investigate elemental composition in larger depth. The increase in the percentage of oxygen after adsorption indicates the association of oxygenated chromium species on the surface. The comparably evident reduction in the amount of carbon shows that the adsorbate species are linked to the phytochemical fragments capping the magnetite core rather than directly to the iron atoms.

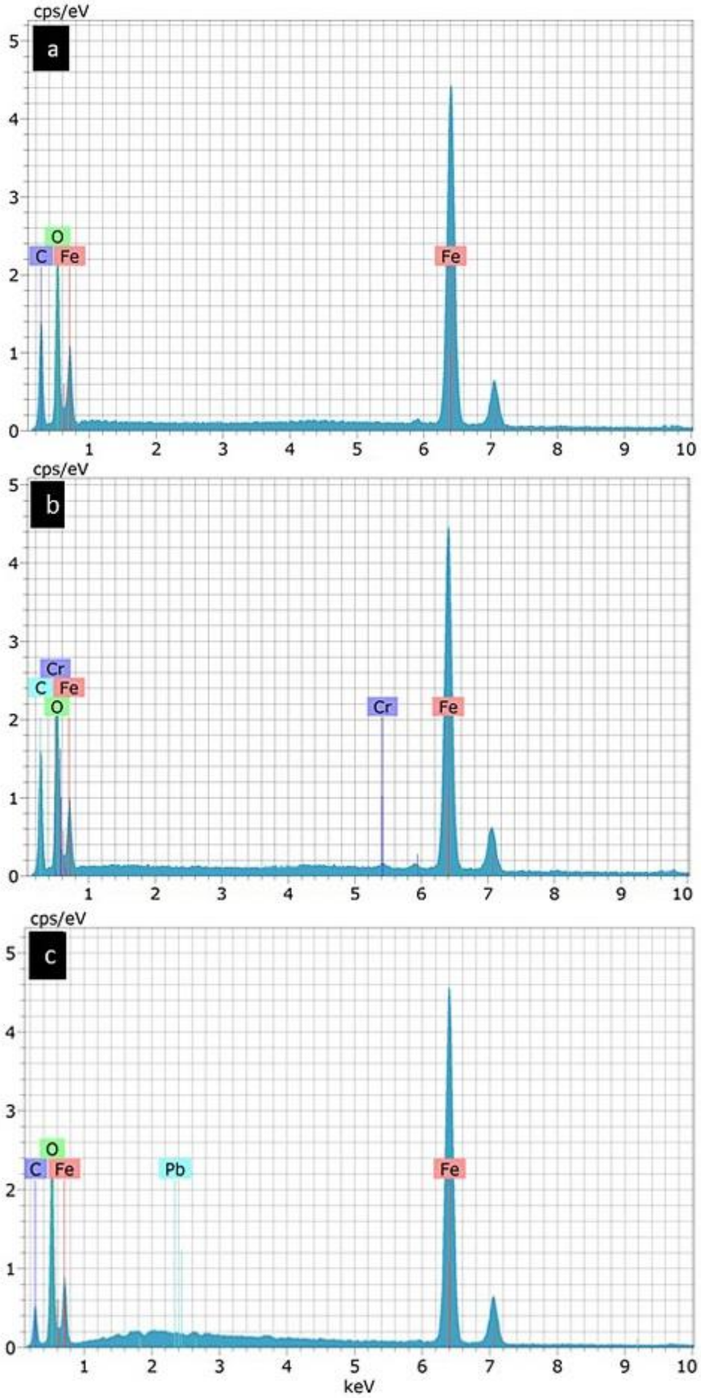

Fig.18. EDX spectrum of a) SMN-12, b) Cr-SMN-12 and c) Pb-SMN-12

Table 3. Elemental analysis of SMN-12, Cr-SMN-12 and Pb-SMN-12

	EDX (atomic wt%)				XPS (atomic wt%)			
	Fe	**O**	**C**	**Cr/Pb**	**Fe**	**O**	**C**	**Cr/Pb**
SMN-12	20.41	24.22	55.37	-	9.28	35.74	54.98	-
Cr-SMN-12	19.45	29.77	48.54	2.24	8.71	42.01	47.37	1.91
Pb-SMN-12	18.26	30.15	47.37	4.22	8.75	42.37	46.17	2.71

4.4.4 Effect of adsorption on magnetic properties.

Magnetic properties of SMN-12 before and after adsorption of HMIs (Fig.19) revealed prominent changes. Owing to the smaller size of particles, SMN-12 exhibited superparamagnetic nature with a saturation magnetization (M_s) of 21.46emug^{-1}. The lower saturation magnetisation value indicates effective coating of iron oxide nanocore by the phytoconjugates. M_s after adsorption of Cr(VI) increased up to 31.09emug^{-1}. The high magnetic moment and paramagnetic nature of chromium species deposited on the surface of SMN-12 increases the inherent M_s of the adsorbent. The coercivity is an extrinsic property of a magnet, which depends not only on the spin carrier but also on the shape or size of the magnets [31,32]. The larger coercivity and remanence magnetization for Cr-laden SMN-12 is attributed to shape and magneto-crystalline anisotropy of deposited chromium superstructures. The enhanced anisotropy prevents them from magnetizing in directions other than along their easy magnetic axes, hence leading to the higher remnant magnetization and higher coercivity. Weak ferromagnetic nature of SMN-12 post adsorption of Cr(VI) originated from the obvious interactions between bulk chromium and nano iron. The remarkable change in the hysteresis upon adsorption substantiates deposition of chromium on SMN-12 surface. The adsorption of Pb(II) also marked an increase in the M_s value as evident from Fig.19. The M_s of SMN-Pb was recorded as

$50.02emug^{-1}$. Similar rise in magnetic moment upon doping with lead has been reported elsewhere. Although the exact reason for increase in the M_s is under study, it can be speculated that the reduction of Pb(II) might have generated such a noticeable change in the total magnetic moment of the adsorbent. The small size of SMN-12 enables significant surface interactions altering the magnetic properties of the material. However, the changes in the magnetic parameters did not affect the magnetic separation of the exhausted adsorbent from the analyte. The results of the magnetic characterization are compiled in table 4.

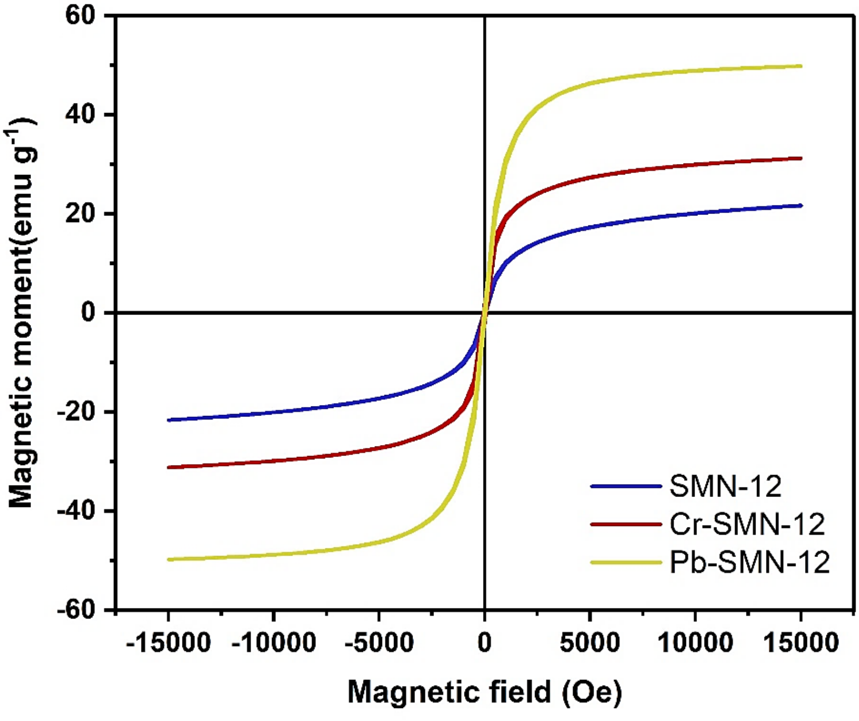

Fig.19 M-H plot of SMN-12 pre and post adsorption

Table 4. The results of the magnetic characterization of SMN-12

Sample	Coercivity (Oe)	Remenance (emu g^{-1})	Saturation magnetization (emu g^{-1})
SMN-12	41.95	0.61	21.46
SMN-Cr	67.23	2.16	31.09
SMN-Pb	34.84	1.46	50.02

4.4.5 Effect of adsorption on surface morphology

The surface morphology of the superior adsorbent, SMN-12 was examined using FESEM imaging to detect the underlying changes on the surface structure upon adsorption of HMIs. Fig.20 a-c displays FESEM micrographs of SMN-12 before adsorption. Pure SMN-12 surface contains numerous small spherical aggregates with many linked interstices across the surface. These interstices promote the transport of adsorbate species towards the active sites and provide anchoring sites to hook the adsorbed impurities. The collected exhausted adsorbent was dried at 40°C and the morphological changes were examined employing FESEM technique. The surface displayed evident morphological changes after adsorption in both cases. The adsorption of Cr(VI) caused an extensive 'bloom of spikes' on the surface owing to the deposition of amorphous Fe-Cr hydroxide species[14]. The interstices appear to have completely filled with $(Fe_{1-x}Cr_{1-x})(OH)_3$ and are no longer visible on the surface (Fig.20 d-f). The adsorption of Pb(II) also has generated extensive uniform deposition of amorphous spherical aggregates covering the interstices as seen in Fig.20 g-i. The morphological changes observed after adsorption of both metal ions indicate effective adsorption of HMIs on SMN-12. FESEM studies also underline the significance of the peculiar morphology of SMN-12 in promoting the adsorption of HMIs.

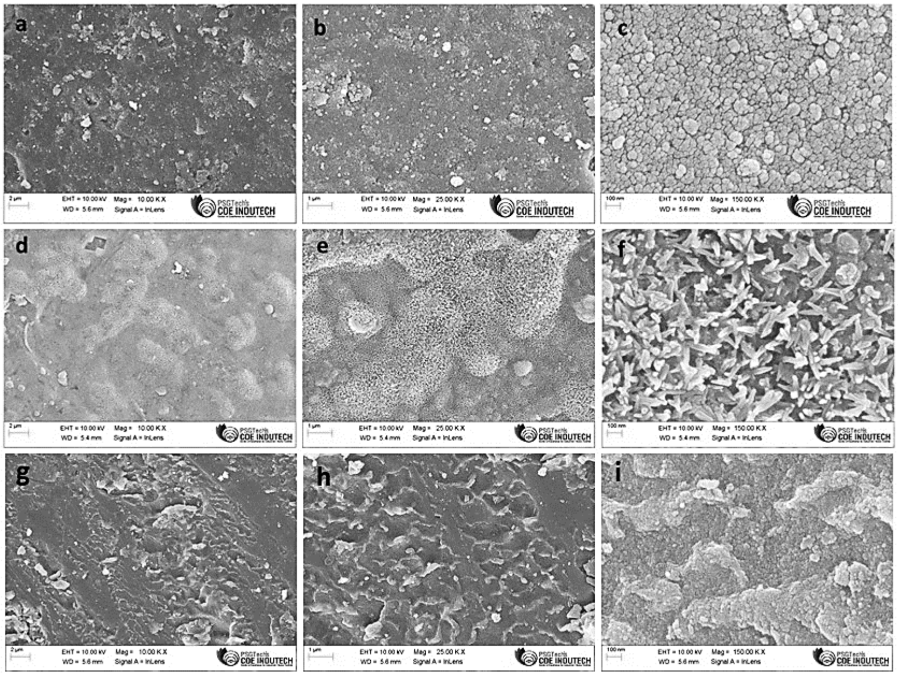

Fig.20. FESEM micrographs of a-c) SMN-12, d-f) Cr-SMN-12 and g-i) Pb-SMN-12

4.4.6 Mechanism of adsorption

A plausible mechanism of adsorption of HMIs on SMN-12 is elucidated from the above results. The hydroxyl groups and phytochemical fragments on SMN-12 surface undergo protonation under acidic environment inversing the inherent negative charge on the surface. The positive charge prevailing on the surface of SMN-12 up to pH 4.6 enables electrostatic attraction towards $HCrO_4^-$ species initiating the adsorption process. The inherent pH of the simulated Pb(II) effluent was 5.6. It is highly probable for the Pb^{2+} ions dominating in solution at this pH to get adsorbed by the negatively charged SMN-12. The above results indicated that 1) adsorptive removal of Cr(VI)/Pb(II) is initiated through electrostatic attraction, 2) the variations inflicted in XPS spectrum of SMN-12 after adsorption of chromium corroborates the role of phytoconjugates in the reduction of Cr(VI) to Cr(III) through redox reactions of surface hydroxyl groups and phytoconjugates with Cr(VI). Although phytoconjugates do not actively participate in the adsorption of Pb(II) they provided noticeable Pb(II) to Pb(0) reduction. The increased hydrothermal treatment period resulted in the enhanced incorporation of phytochemicals onto the magnetite core which in turn improved the reducing capacity of SMN-12. The increase in the intensity of -OH component in the O 1s core component of Cr/Pb-SMN-12 suggests deposition of the adsorbed metal ion as hydroxide species. XPS, EDX, VSM and FESEM suggest that there might be an amorphous deposition of the adsorbed species on the adsorbent surface. Fig.21 illustrates a schematic representation of the synthesis of SMN-12 and its HMI removal capacities.

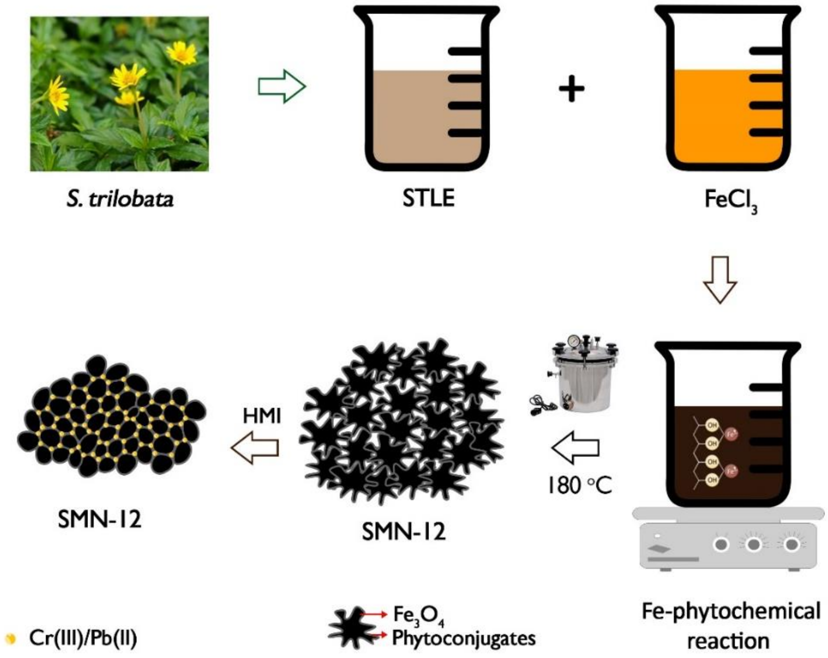

Fig.21. Schematic representation of synthesis of SMN-12 and its HMI removal capacities.

4.5 Regeneration and recyclability of SMN-12

Recyclability of adsorbent is a crucial aspect from a sustainable and economical point of view. The magnetic nature of SMN-12 not only provide prompt collection of the exhausted adsorbent from the contaminant solution but also makes the regeneration processes less tedious. Loaded SMN-12 were separated from the adsorption vessels by an external magnet for regeneration. Chromium associated SMN-12 was eluted using distilled water, the neutral pH prompted rapid desorption of the adsorbed chromium yielding pristine SMN-12. 0.2 M HCl was used as a suitable eluent to desorb lead from SMN-12. The regenerated SMN-12 were tested for five consecutive cycles of adsorption to its efficiency. As illustrated in Fig.22 the loss of adsorption efficiency was minimal for both metal ions. Interestingly, it was observed that regenerated SMN-12 exhibited comparable adsorption efficiency when the target metal ions were interchanged for the second cycle substantiating the efficacy of the adopted regeneration method.

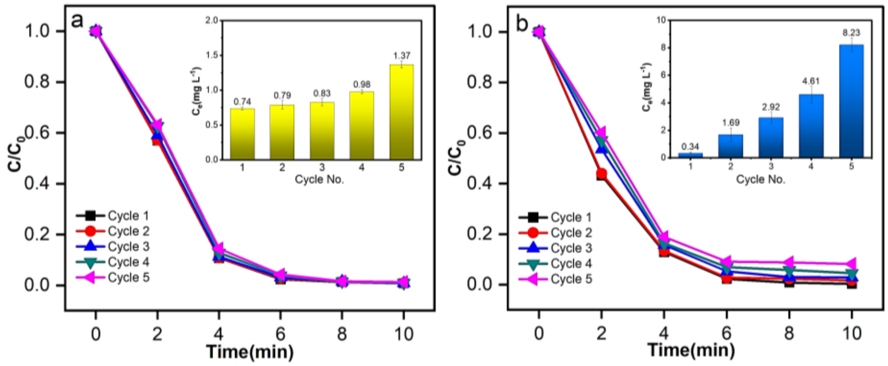

Fig.22 Recyclability studies for a) Cr(VI) removal and b) Pb(II) removal

4.6 Summary

The study explores the effectiveness of a phytoreagent derived from *S. trilobata*, commonly known as Singapore daisy. This ornamental plant was introduced and widely cultivated for its bright yellow flowers. However, the invasiveness of the plant created a havoc for the farmers and landowners. Phytochemical screening reports on the plant indicates presence of active secondary metabolites capable of binding and reducing iron. Ultrasonic assisted hydrothermal treatment using the plant extract resulted in production of magnetite NPs. Various characterization techniques confirmed the formation of phyto-conjugated superparamagnetic Fe_3O_4. An increase in the hydrothermal treatment time accelerated particle agglomeration and generated mixed morphology in the SMNs. All three SMNs displayed appreciable adsorption of Cr(VI) & Pb(II) in acidic and neutral environment respectively. Maximum adsorption capacity was recorded as 184.63mgg^{-1} for Cr(VI) and 322.03mgg^{-1} for Pb(II) removal for SMN-12 samples. Consistent performance with varied constraints along with magnetic nature and recyclability render SMN-12 superior characteristics expected for an efficient adsorbent. The use of an invasive weed to synthesize efficient and less toxic nano-adsorbent system to remove HMIs from water provide the work a circular green nature.

- *The results of this chapter are reserved for filing patent applications.*

References

[1] Chowdhury SR, Yanful EK, Pratt AR. Chemical states in XPS and Raman analysis during removal of Cr(VI) from contaminated water by mixed maghemite–magnetite nanoparticles. Journal of Hazardous Materials 2012;235–236:246–56. https://doi.org/10.1016/j.jhazmat.2012.07.054.

[2] Drits V, Środoń J, Eberl DD. XRD Measurement of Mean Crystallite Thickness of Illite and Illite/Smectite: Reappraisal of the Kubler Index and the Scherrer Equation. Clays Clay Miner 1997;45:461–75. https://doi.org/10.1346/CCMN.1997.0450315.

[3] Cai W, Wan J. Facile synthesis of superparamagnetic magnetite nanoparticles in liquid polyols. Journal of Colloid and Interface Science 2007;305:366–70. https://doi.org/10.1016/j.jcis.2006.10.023.

[4] Ricci A, Olejar KJ, Parpinello GP, Kilmartin PA, Versari A. Application of Fourier Transform Infrared (FTIR) Spectroscopy in the Characterization of

Tannins. Applied Spectroscopy Reviews 2015;50:407–42. https://doi.org/10.1080/05704928.2014.1000461.

[5] Köseoğlu Y, Alan F, Tan M, Yilgin R, Öztürk M. Low temperature hydrothermal synthesis and characterization of Mn doped cobalt ferrite nanoparticles. Ceramics International 2012;38:3625–34. https://doi.org/10.1016/j.ceramint.2012.01.001.

[6] Cacua K, Ordoñez F, Zapata C, Herrera B, Pabón E, Buitrago-Sierra R. Surfactant concentration and pH effects on the zeta potential values of alumina nanofluids to inspect stability. Colloids and Surfaces A: Physicochemical and Engineering Aspects 2019;583:123960. https://doi.org/10.1016/j.colsurfa.2019.123960.

[7] Scherdel C, Reichenauer G, Wiener M. Relationship between pore volumes and surface areas derived from the evaluation of N2-sorption data by DR-, BET- and t-plot. Microporous and Mesoporous Materials 2010;132:572–5. https://doi.org/10.1016/j.micromeso.2010.03.034.

[8] Mira L, Tereza Fernandez M, Santos M, Rocha R, Helena Florêncio M, Jennings KR. Interactions of Flavonoids with Iron and Copper Ions: A Mechanism for their Antioxidant Activity. Free Radical Research 2002;36:1199–208. https://doi.org/10.1080/1071576021000016463.

[9] Elhabiri M, Carrër C, Marmolle F, Traboulsi H. Complexation of iron(III) by catecholate-type polyphenols. Inorganica Chimica Acta 2007;360:353–9. https://doi.org/10.1016/j.ica.2006.07.110.

[10] Pan Y, Qin R, Hou M, Xue J, Zhou M, Xu L, et al. The interactions of polyphenols with Fe and their application in Fenton/Fenton-like reactions. Separation and Purification Technology 2022;300:121831. https://doi.org/10.1016/j.seppur.2022.121831.

[11] Morel I, Lescoat G, Cogrel P, Sergent O, Pasdeloup N, Brissot P, et al. Antioxidant and iron-chelating activities of the flavonoids catechin, quercetin and diosmetin on iron-loaded rat hepatocyte cultures. Biochemical Pharmacology 1993;45:13–9. https://doi.org/10.1016/0006-2952(93)90371-3.

[12] Balekar N. Wedelia trilobata L.: A Phytochemical and Pharmacological Review. Chiang Mai J Sci n.d.:16.

[13] Qiang Y, Du D-L, Chen Y-J, Gao K. ent-Kaurane Diterpenes and Further Constituents from Wedelia trilobata. Helvetica Chimica Acta 2011;94:817–23. https://doi.org/10.1002/hlca.201000301.

[14] Richard FC, Bourg ACM. Aqueous geochemistry of chromium: A review. Water Research 1991;25:807–16. https://doi.org/10.1016/0043-1354(91)90160-R.

[15] Kaushik A, Kansal A, Santosh, Meena, Kumari S, Kaushik CP. Heavy metal contamination of river Yamuna, Haryana, India: Assessment by Metal Enrichment Factor of the Sediments. Journal of Hazardous Materials 2009;164:265–70. https://doi.org/10.1016/j.jhazmat.2008.08.031.

[16] Günay A, Arslankaya E, Tosun i. Lead removal from aqueous solution by natural and pretreated clinoptilolite: Adsorption equilibrium and kinetics. Journal of Hazardous Materials 2007;146:362–71. https://doi.org/10.1016/j.jhazmat.2006.12.034.

[17] Lead: Health Problems Caused by Lead | NIOSH | CDC n.d. https://www.cdc.gov/niosh/topics/lead/health.html (accessed November 29, 2022).

[18] A.O D, Olalekan A, Olatunya A, Dada AO. Langmuir, Freundlich, Temkin and Dubinin–Radushkevich Isotherms Studies of Equilibrium Sorption of Zn 2+ Unto Phosphoric Acid Modified Rice Husk. J Appl Chem 2012;3:38–45. https://doi.org/10.9790/5736-0313845.

[19] Simonin J-P. On the comparison of pseudo-first order and pseudo-second order rate laws in the modeling of adsorption kinetics. Chemical Engineering Journal 2016;300:254–63. https://doi.org/10.1016/j.cej.2016.04.079.

[20] Kul AR, Koyuncu H. Adsorption of Pb(II) ions from aqueous solution by native and activated bentonite: Kinetic, equilibrium and thermodynamic study. Journal of Hazardous Materials 2010;179:332–9. https://doi.org/10.1016/j.jhazmat.2010.03.009.

CHAPTER 5

Phytogenic synthesis, characterization and application of iron oxide nanopigments

> The most important of my discoveries have been suggested to me by my failures.
>
> \- Humphry Davy

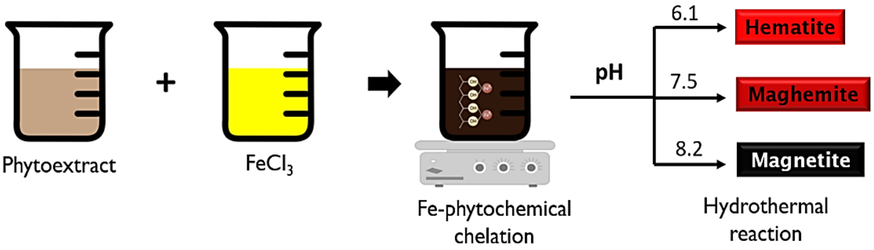

Color imparts excitement and meaning to the mundane life for all classes of people. Hematite or red ochre is one of the oldest red pigments used by mankind since antiquity. The nonrenewable nature of the source and the presence of toxic metals declined the acceptability of the pigment considerably. Phytogenic synthesis offers safe and sustainable alternatives for production of inorganic pigments. The inherent phytoconjugate capping originating from reducing phytoreagent provides the nanopigments appreciable stability and dispersibility. The possibility of transfer of medicinal properties of the plant extract to the NPs makes the approach more appealing.

Color is an essential part of human life. With the rising standards of the world, it's mandatory to produce pigments that meet ethical, environmental, and technological standards. Iron oxide-based pigments fulfill the above requirements with non-toxic nature, chemical stability, durability, variety of shades and with their low production cost. Iron oxides, though considered to have a hydrophilic surface, tend to strongly coagulate in any medium due to its ferromagnetic behavior. This gives rise to poor dispersibility with considerable viscosity changes when the formulation calls for producing different shades of cosmetics and, furthermore, color separation occurs on the surface of the cosmetics when this material is used along with other pigments such as titanium dioxide[1]. Although iron oxide pigments are extremely weather resistant, the shades are dull when compared to organic pigments. For example, hematite has a dull red color close to brown. If bright inorganic pigments based on iron oxide pigments can be realized, they could be used in various industrial sectors as economical, safe, and sustainable weather-resistant pigments.

5.1 Synthesis of iron oxide nano pigments

To 50ml of the *S. trilobata* extract, 30ml of 0.032M $FeCl_3$ solution was added under vigorous magnetic stirring. The decline in the pH of the medium was adjusted by the gradual addition of 0.186g of $NaHCO_3$. The mixture was then magnetically stirred for 1 hour at room temperature. The mixture was then exposed to hydrothermal treatment at 180°C and autogenous pressure for 12 hours. The solid product formed was collected by filtration and washed repeatedly with ethanol and water. The product was dried at 60°C to obtain a red iron oxide pigment (SR-12).

To investigate the process of formation and growth of the iron oxide nanopigments, the effect of various experimental conditions on the synthesis has been investigated. The reaction time of hydrothermal treatment and the molar ratio of $NaHCO_3$ to $FeCl_3$ has been varied to investigate systematically the parameters affecting the formation of the nanopigments. The product formed at the molar ratio of reactants 2.0 was named as SB-12.

The steps were repeated with *C. odorata* flower extract to produce red and brown pigments after hydrothermal treatment of 8 hours. The red and the brown pigment were named as CR-8 and CB-8 respectively. The effect of reactant ratio and hydrothermal reaction period was also investigated.

5.2 Characterization of iron oxide nano pigments

5.2.1 XRD analysis

The XRD analysis of SR-12 and CR-8 displayed well defined diffraction patterns of hematite NPs with corundum structure (Fig.1). All diffraction peaks matched well with the normal diffraction patterns of rhombohedral α-Fe_2O_3 and can be indexed to JCPDS file 33-0664, and no characteristic peaks of impurities were observed. Peaks formed at 2θ values of 24.2, 33.2, 35.7, 40.9, 49.6, 54.4, 57.4, 62.5 and 64.2 correspond to Miller indices of (012), (104), (110), (113), (024), (116), (018), (214) and (300) respectively. The calculated lattice parameter (a), was ~4.978 and 4.983Å for CR-8 and SR-12 respectively, confirming the hematite phase [2]. The average crystallite size obtained using Scherrer's equation [3] was 32.5 and 30.1nm for SR-12 and CR-8 respectively.

The X-ray diffractograms of SB-12 and CB-8 (Fig.2b) displayed well defined diffraction patterns at 30.2, 35.6, 43.4 54.1,57.3 and 63.1corresponding to (220), (311), (400), (422), (511), and (440) planes of spinel maghemite (JCPDS 39-1346)[4]. Due to the similarity in the crystal structure magnetite and maghemite XRD patterns are nearly identical and indistinguishable. However, a detailed analysis of (511) Bragg peak around the 2θ range 56.5–57.5° provides insight into this issue. The peak appears at a slightly higher 2θ value for maghemite than in magnetite particles where the peak appears at 2θ ~57.0. In the case of SB-12 and CB-8, the peak appears at 57.3 indicating the formation of the maghemite phase[5]. In addition to that the calculated lattice parameter (a), was ~8.338 and 8.337Å for CB-8 and SB-12 respectively, indicating the formed maghemite phase[6]. The average crystallite size obtained using Scherrer's equation was 26.3 and 21.4 nm for SB-12 and CB-8 respectively.

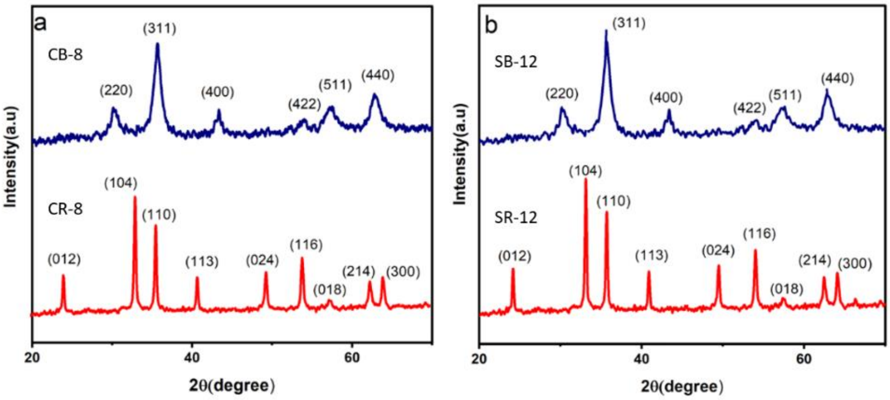

Fig.1. X-ray diffractograms of a) *C. odorata* derived and b) *S. trilobata* derived iron oxide nanopigments

5.2.2 FTIR analysis

Resonating with the existing literature, the FTIR spectra of the crude plant extracts revealed the presence of phytochemicals with assorted functional groups (see Chapter 3&4). The FTIR spectra of the obtained pigments displayed in Fig.2 confirm the conjugation of plant metabolites with the iron oxide core. The prominent peak around 3435cm^{-1} is attributed to hydroxyl groups from polyphenols. The peaks at 2927cm^{-1} and 1630cm^{-1} refer to C-H, and C=C, stretching vibrations respectively while the peaks around 1378cm^{-1} and 1058cm^{-1} correspond to –OH and C-O bending vibrations of the plant metabolites[7]. A broad peak ~547cm^{-1} in SR-12 and CR-8 is attributed to the Fe-O bonds in hematite. Whereas the peaks corresponding to

Fe-O bonds appear slightly shifted to ~693cm^{-1} for SB-12 and CB-8 suggesting formation of hematite and maghemite respectively[7].

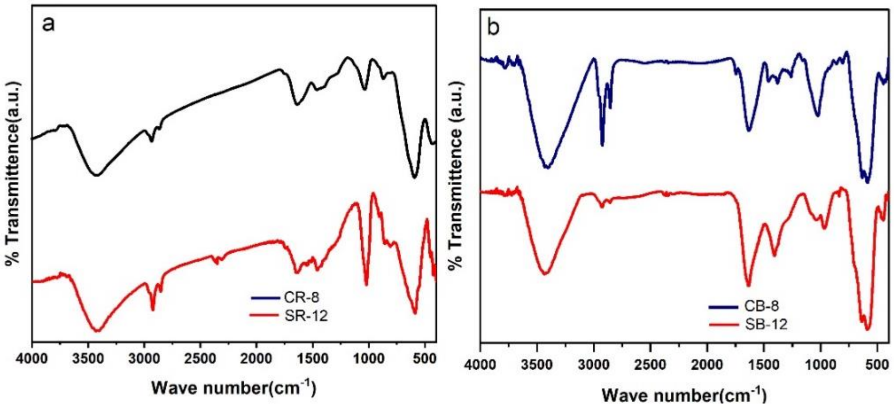

Fig.2. FTIR spectra of phytogenic iron oxide, a) red & b) brown nanopigments

5.2.3 UV-Visible spectroscopy and color evaluation

The UV-Visible analysis of the pigments was conducted (Fig.3a). The spectra reveal a continuous characteristic absorption peak covering a large range. The red pigments obtained from both extracts displayed adsorption ranging up to 535nm, attributed to the charge transfer transition from the O 2p to Fe 3d levels resulting in a red colour, whereas the brown pigments displayed an even broader spectrum. The results are comparable with similar phytogenic IONPs[8]. Table 1 presents the results of the color evaluation study of the pigments.

Table 1. Color parameters of phytogenic iron oxides pigments

	CR-8	**SR-12**	**CB-8**	**SB-12**
L^*	40.6	43.5	32.7	38.3
a^*	35.4	38.7	27.4	30.2
b^*	38.6	42.4	22.4	28.3

The color parameters of the pigments along with the images of coated pigments are given in Fig.3b. The color parameters for red pigments were superior to commercially available hematite (L^*-38.6, a^*-30.4, b^*-28.0).

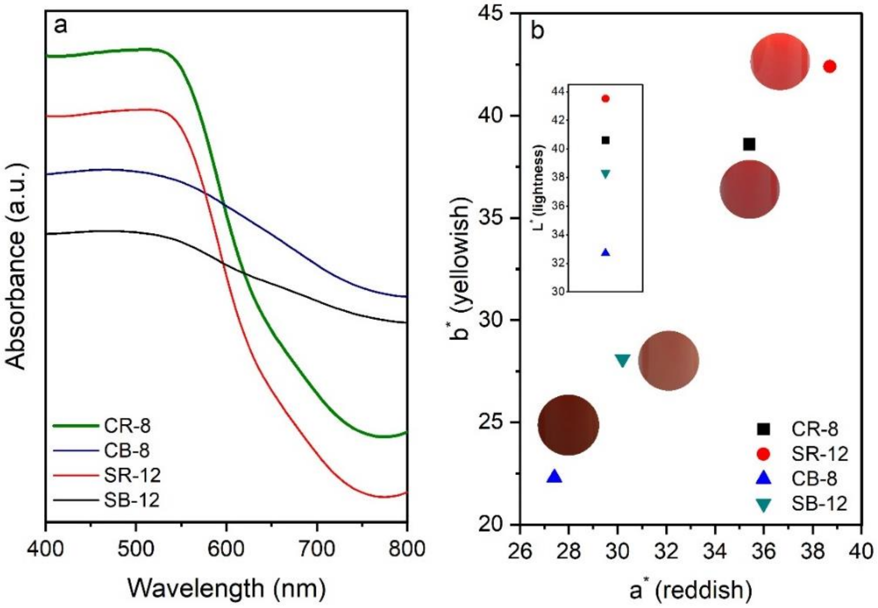

Fig.3. a) UV-Visible spectra of the pigments, b) quantitative color parameters of the pigments.

5.2.4 Morphological analysis

The morphology of the phytogenic nanopigments were examined using FESEM. The FESEM images of the pigments derived from *C. odorata* are displayed in Fig 4. Close examination of the CR-8's surface revealed protruding petal-like structures arranged randomly across the surface. The brown pigment, CB-12 displayed an extensive distribution of spherical aggregates across the surface, typical to nano iron oxide surface. Figure 5 shows the pigments surfaces made using *S. trilobata* extract. SR-12 shows an evidently distinct morphology from that of CR-12 whereas SB-12 displays a typical iron oxide morphology. These morphologies can help in sustained retention and release of active ingredients in cosmetics.

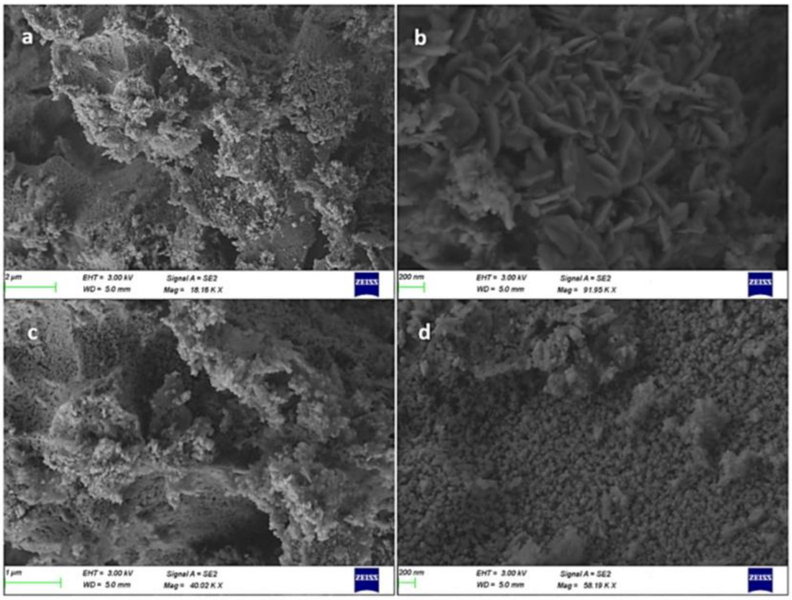

Fig.4. FESEM images of a)&b) CR-8, c)&d) CB-8

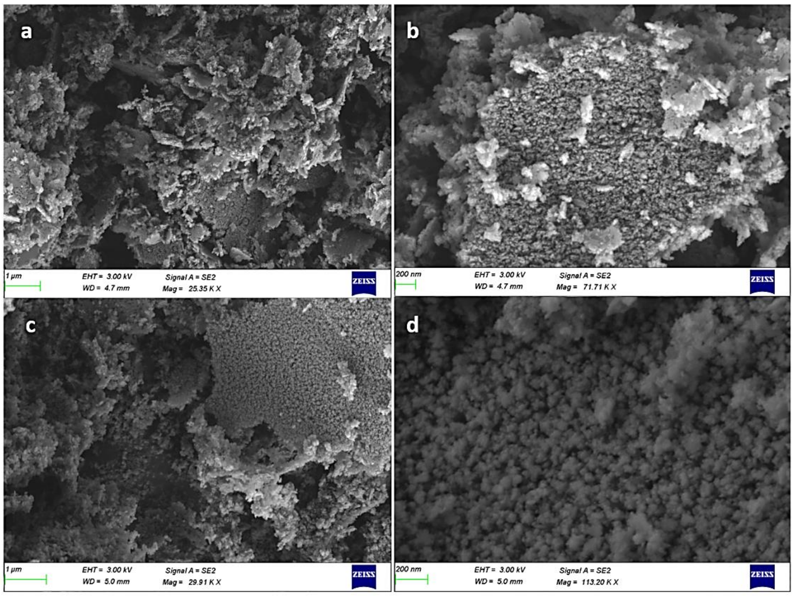

Fig.5. FESEM images of a&b) SR-12, c&d) SB-12

5.2.5 Compositional analysis

EDX was used for the primary elemental analysis of all the synthesized nanopigments and XPS analysis was employed to confirm the iron oxide phase present in the brown pigments. The EDX spectra (Fig.6) of all pigments identified the presence of Fe, O and C, confirming the presence formation of iron oxide conjugated with phytochemical fragments. The compositional analysis (Table 2) reveals that the pigments derived from *S. trilobata* extract possessed enhanced phytoconjugation owing to the prolonged optimal reaction time.

Table 2. Compositional analysis of phytogenic iron oxide pigments

Pigment	Atomic wt%		
	Fe	O	C
CR-8	18.35	24.79	56.86
CB-8	15.92	37.81	46.27
SR-12	16.02	21.39	62.59
SB-12	17.62	26.75	55.63

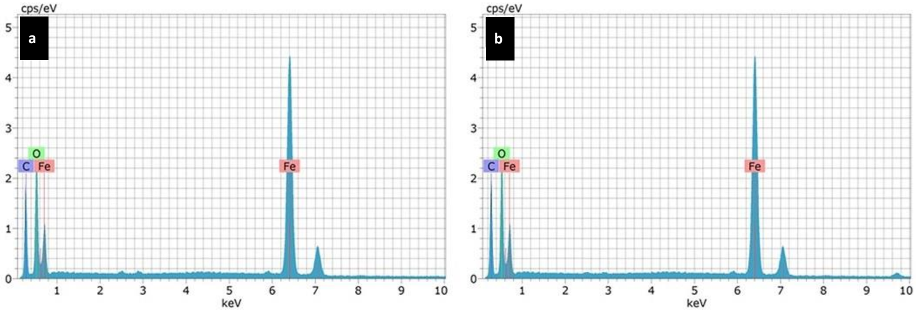

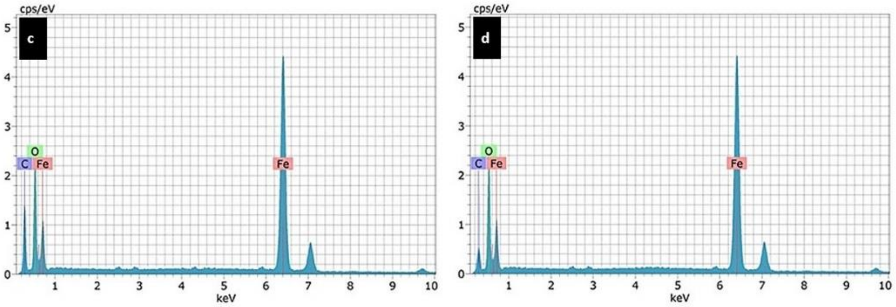

Fig.6. EDX spectra of a) CR-8 b) CB-8 c) SR-12 and d) SB-12

The XPS spectra of SB-12 and CB-8 was critically analysed to identify the surface composition in detail and to confirm the valence state of iron. All the obtained core spectra were corrected by shifting the C-C/C-H component of the C 1s peak to standard binding energy value of 285.0eV to eliminate the effects of sample charging. For both samples the XPS survey spectra showed Fe, O and C to be the main elements. Fig.7, typical high-resolution Fe 2p, C 1s and O1s responses from the pigment surfaces are shown. The core level spectra of each element in SB-12 and CB-8 were examined and peak fitted after subtraction of a Shirley-type background. The fitted components have mixed Gauss-Lorentz shapes. The four fitted components of Fe2p spectra appears at slightly higher binding energy values than that of pure iron maghemite due to the phytoconjugation. The component appearing at ~711.72 and 711.86 eV in CB-8 and SB-12 respectively identifies the presence of Fe^{3+} ions, thus confirming the formation of maghemite phase[9,10]. The O 1s peak could be described accurately using four individual peaks, corresponding to O_2^-, OH^-, -OR from phytochemicals and chemisorbed H_2O[11,12]. The C 1s peak was resolved to four components corresponding to C-C/C-H, C-O, O-C=O and π-π interactions[13]. The details of the XPS studies are listed in Table 3.

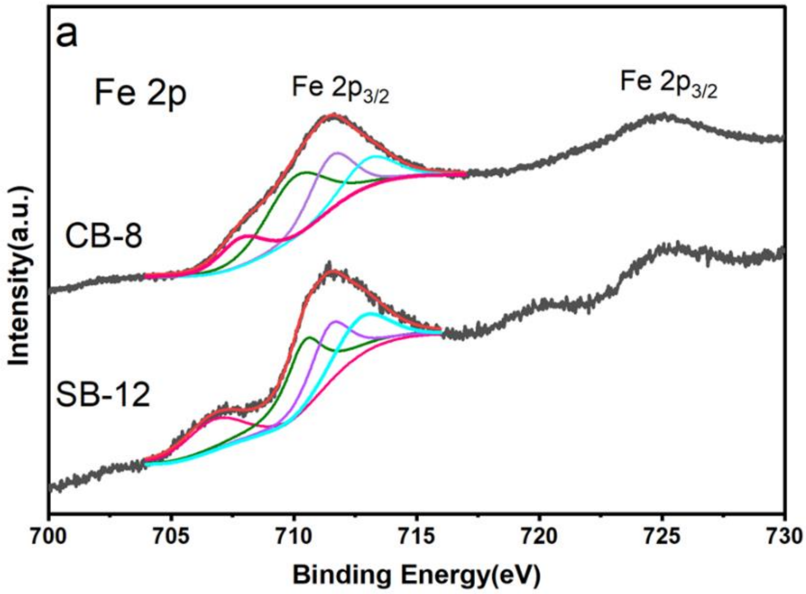

Fig.7a. Peak fitted XPS spectra of Fe 2p core level of CB-8 and SB-12

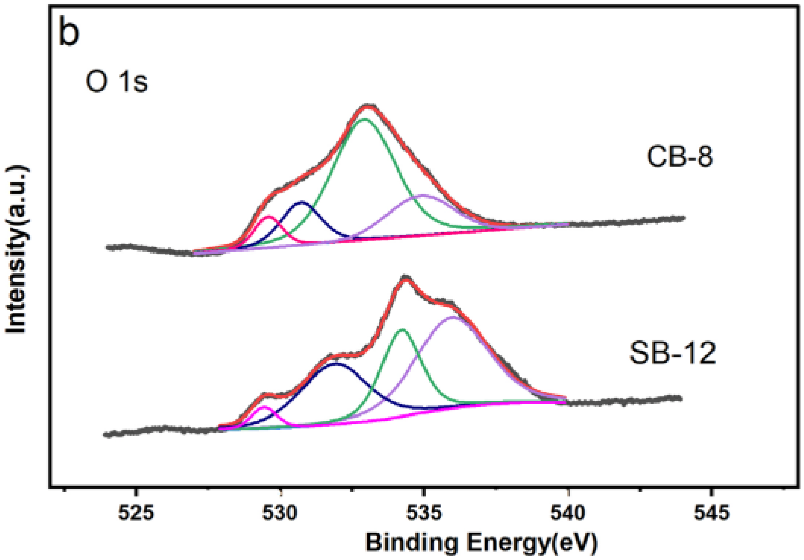

Fig.7b. Peak fitted XPS spectra of O 1s core level of CB-8 and SB-12

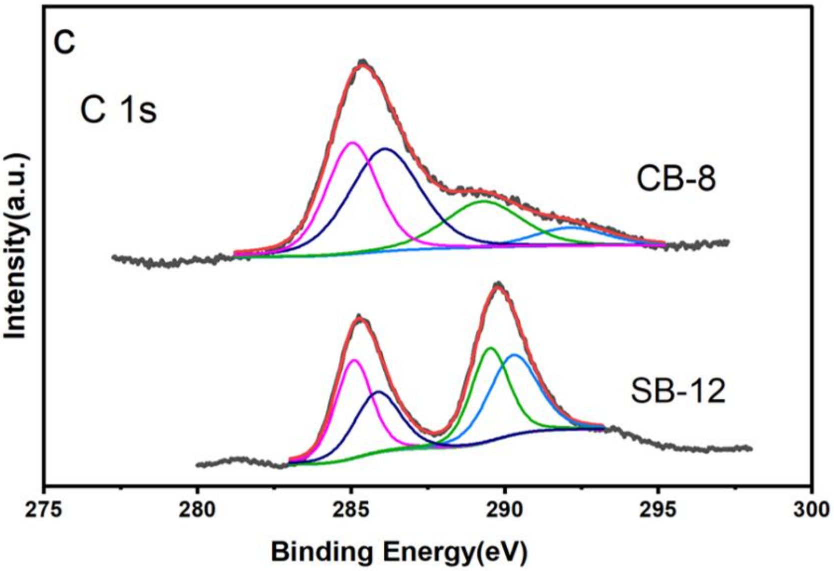

Fig.7c. Peak fitted XPS spectra of C 1s core level of CB-8 and SB-12

Table 3. Details of high resolution XPS analysis and peak fitting

Element	Peaks Binding energy(eV)		Composition Atomic wt %	
	SB-12	CB-8	SB-12	CB-8
Fe	707.71 710.22 711.86 712.95	706.91 710.51 711.72 713.01	6.37	6.56
O	529.47 531.12 534.36 535.99	529.71 530.92 533.11 535.05	37.36	42.71
C	285.0 286.01 289.51 290.2	285.0 286.12 289.31 290.21	56.27	50.73

5.3 Optimization of the synthesis of phytogenic IONPs

The effect of different physical variables including the ratio of reactants on the formed product were analyzed in detail. The instantaneous change observed in the brown colour and the transparency of the extract to dirty green precipitate upon the addition of $FeCl_3$ indicates the complexation of Fe^{3+} ions with highly active (unstable) polyphenols/flavonoids in the phytoreagents[14]. The pH drops from 6.4 to 2.1 upon addition of the iron precursor. The addition of $NaHCO_3$ neutralizes HCl formed in the reaction medium rising the pH to 6.1. Initially, the pH of the reactant system was considered as pivotal factor in obtaining the iron oxide of the desired phase[15]. The molar ratio of sodium bicarbonate and ferric chloride controls the pH of the reaction system. $NaHCO_3$ acts as a neutralizing agent against HCl formed in the reaction vessel upon addition of $FeCl_3$. To obtain hematite NPs, the ratio needed to be controlled at around 1.1 with all the other parameters fixed. At this ratio the pH of the system rises from 2.1 to 6.1. When the ratio reached between 1:2 (pH~7.5), the as-synthesized brown product was identified as maghemite NPs. In case of a higher ratio such as 3.0, where the pH reaches ~8.2, a bulky precipitate was produced, yielding black magnetite NPs (see chapter 3&4). Further increase in the pH of the system did not trigger any significant changes on the product formation. The reduction of Fe(III) under alkaline conditions is promoted by the instability of polyphenols at high pH[16]. However, the exact reactions promoting the reduction are still under investigation.

Although the dry weight of the plant parts used to prepare the phytoreagents were the same in both synthesis routes, *S. trilobata* leaves extract consumed more time to produce pure IONPs. The difference in the reaction period is attributed to low polyphenolic and flavonoid content of the *S. trilobata* leaves extract than *C. odorata* flower extract. It is generally perceived that the reproductive parts of the plant contain more active phytochemicals than the vegetative counterparts which in turn might help in the reduction of the hydrothermal reaction period. An increase in the concentration of phytoreagents resulted in the formation of a highly hygroscopic, undesirable product whereas, a reduction in the concentration of phytoextract resulted in low yield of the IONPs. Elimination of the phytoreagents from the reaction system produced an amorphous non-magnetic black amorphous solid.

An increase in the hydrothermal reaction time (24 hours) produced magnetite NPs irrespective of the pH and the extract used. However, the uniformity of nanoparticles became poor and irregular, agglomerated particles of greater size were produced. A further increase in the reaction time to 48 hours produced no significant changes.

To recognize the distinct role of $NaHCO_3$, if any, it was replaced with NaOH and Na_2CO_3 to generate the required pH for synthesis of each iron oxide phase. Surprisingly, the method yielded only black magnetite NPs irrespective of the change in initial pH. Moreover, Na_2CO_3 resulted in substantial reduction in the yield of magnetite NPs even at higher pH. In the absence of neutralizers, no product was formed indicating the significance of pH in enabling the nucleation process. Therefore, it was confirmed that pH along with CO_2 evolution plays crucial role in producing different iron oxide phases. Since the term 'hydrothermal' is of geological origin, existing literature on geological hydrothermal alterations and metamorphism were explored to understand the synthesis process in detail. The formation of iron oxide phases inside the reaction vessel mimics hydrothermal alteration called metasomatism. Metasomatism is a type of hydrothermal alteration which results in change in chemical composition of the rocks in presence of large number of fluids under high pressure and temperature. The frequent observation of saline fluids in deep seated groundwaters of metamorphic terrains indicates the crucial role of ‘brines’ in metamorphism and metasomatism[17–19]. The most abundant components in these brines are H_2O, CO_2 and NaCl. Under high temperatures and pressure brines are capable of dissolving and transporting chemical species. The salt concentrations can regulate the thermodynamic and transport properties of geofluids, the solubility of minerals, metasomatic transformations of the rocks, hydration and melting reactions of the fluids and the composition of the derived melts. Literature also suggest that the chloride richness of the brine increases the solubility and transport of most of the metals[17,20]. Researchers have identified the association of high salinity brines in iron oxide copper-gold (IOCG) deposits in different parts of the world[21–23]. A schematic illustration of the strategic synthesis and possible outcomes are represented in Fig.8.

The high affinity between iron and polyphenols facilitates instant complexation yielding colloidal iron-polyphenol complexes. The high reactivity of polyphenols also indicates their instability; thus, alkaline treatments can convert polyphenols to other compounds depending on their stability in the solution. Polyphenols containing trihydroxybenzene or catechol substructures are listed as moderately or highly unstable. Though there is ambiguity regarding the reactions and products of alkaline treatment the reduction of Fe(III) suggests that higher pH enhances the reducing power of the phytoextracts.

During the phytogenic synthesis, the coexistence of aqueous brine and a CO_2 rich vapour inside the hydrothermal vessel recreates a pseudo-metasomatic environment leading to the production of different iron oxide phases. The amount of $NaHCO_3$ added to the system regulates reducing power of the extract and the ratio of the brine yielding different iron oxides from the hydroxide precursors. Moreover, the colour tone and dispersibility of the iron oxide pigments depends on the particle size too. For example, smaller particle size imparts red colour to hematite whereas an increase in the particle size produces grey shades. The phytochemicals bind to iron controlling the morphology of the nuclei during growth yielding vivid and intense pigments. Thus, it was assumed that the reducing and stabilizing nature of the phytoextract along with the metasomatic abilities of the brine curated tailor-made IONPs of three different phases with appreciable purity.

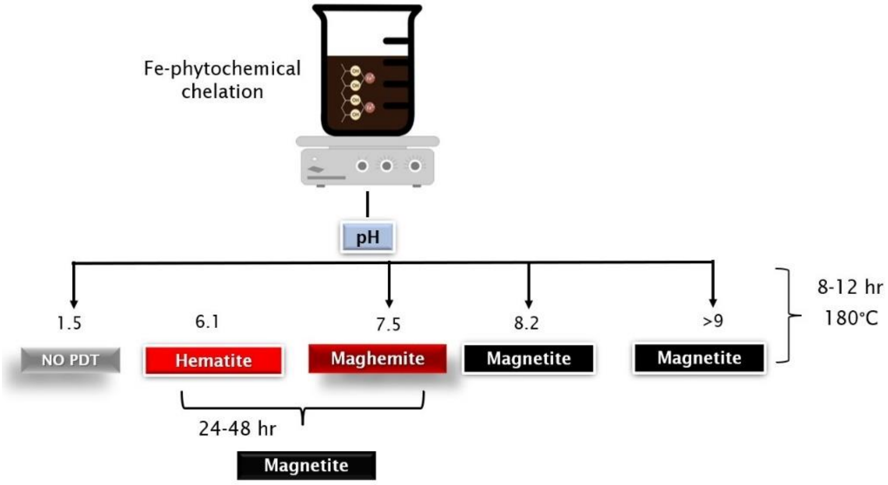

Fig.8. Schematic representation of pH manipulation yielding different IONPs

5.4 Antioxidant assay

Aging is a natural phenomenon, whereas fighting aging is a normalized phenomenon. Antioxidant cosmetics can slow down signs of aging such as wrinkles, dark spots and dull skin. The free radical scavenging activity of the pigments were determined using DPPH assay using ascorbic acid as the standard. The results are displayed in Fig.9. It is evident that all pigments possessed antioxidant capacities. It was noted that the pigments displayed antioxidant activity comparable to that of the standard, ascorbic acid at lower concentrations. It indicates that the use of these phytogenic pigments in very small quantities can impart colour as well as provide protection. The IC50 value of the pigments were calculated as1093.69, 1361.52, 1517.96 and 1866.43 μg/ml for SR-12, CR-8, SB-12 and CB-8 respectively. The high IC50 value of the pigments suggests mild antioxidant activity which in turn enables its use to create highly tinted cosmetics without causing damages to the skin with a bonus of mild antioxidant benefits, especially for sensitive skin.

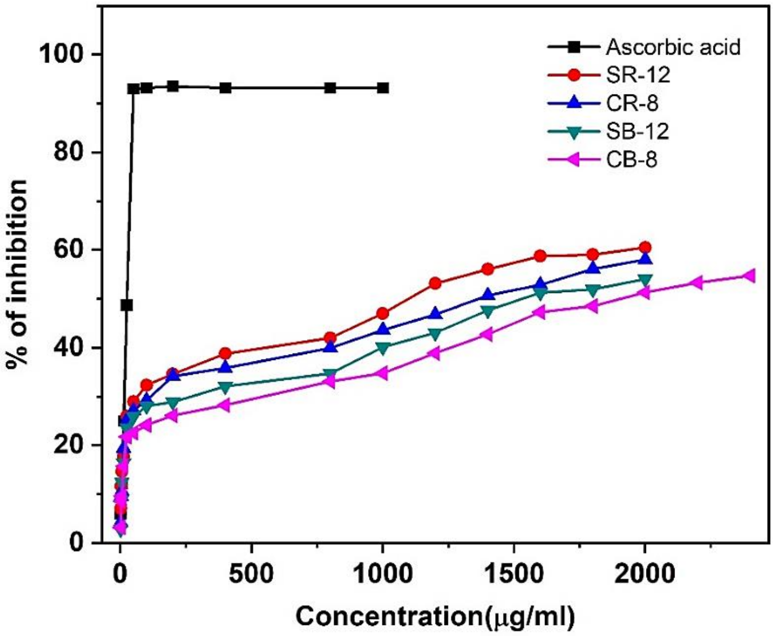

Fig.9. Antioxidant assay of the synthesized pigments

5.5 Antimicrobial assay

A diverse community of bacteria inhabits mucosal and epidermal surfaces in humans and plays a crucial role in defense against pathogens. Cosmetics containing metal oxide NPs may display a general toxicity towards skin microflora which are crucial for healthy skin. The synthesized pigments were tested for inhibitory action towards different opportunistic pathogens. *S. aureus. subsp. aureus, S. epidermis* and *P. aeruginosa* were selected for the study due to their frequent occurrence on human skin and mucosal membranes by agar-well diffusion method. The results of the antimicrobial studies are illustrated in Fig.10. At lower concentration(400μg/ml) none of the pigments showed significant inhibitory behavior towards any of the selected bacterial strains. Even at higher concentrations(800μg/ml) the pigments exhibited negligible activity against all strains except towards *P. aeruginosa*. Therefore, it can be assumed that the pigments are not a threat to human microbiome and thus can be used in cosmetics.

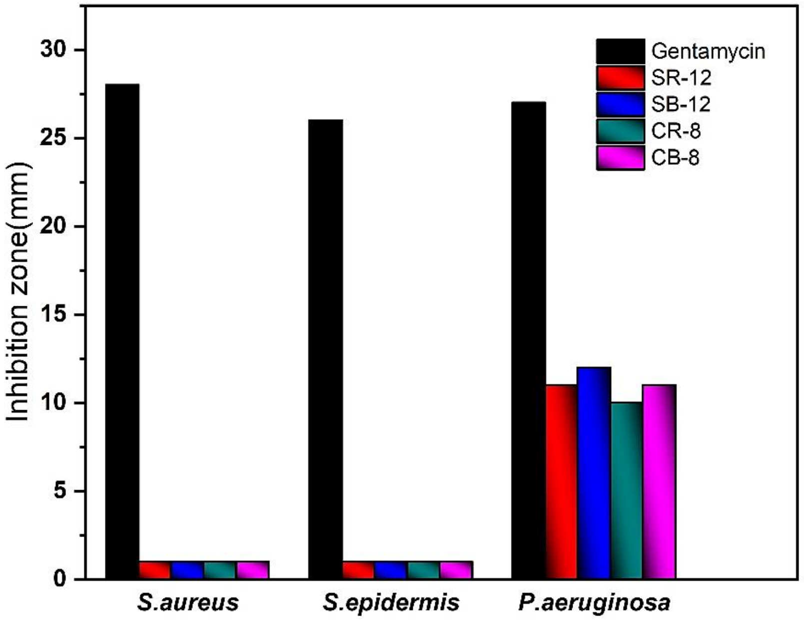

Fig.10. Antimicrobial assay of synthesized pigments

5.6 Toxicity studies

Cytotoxicity assay measures the killing capacity of the analyte against a selected cell line. Metal oxide NPs can penetrate human skin through intercellular, intracellular, or follicular pathways. Therefore, to ensure the safe use of the pigments in the cosmetic sector, the cytotoxicity of the pigments was evaluated using human skin epithelial A431 cells. MTT results showed that the cell viability was highly dependent on the pigment dosages. 96% of cell viability was detected at initial dosage of all four pigments. The viability of A431 cells decreased to 86%, and 43% for the concentrations of 500 and 1000 μg/ml respectively. The details of the study are summarized in Table 4. The primary observations suggest that pigments can be used in lifestyle products without harming human health. However, the study should be extended to more *in-vitro* and *in-vivo* analyses prior to implementation on a large scale.

Table 4. Cytotoxicity evaluation of the pigments.

Pigment	CC50(μg/ml)	SD
SR-12	857	2.4×10^{-2}
SB-12	739	5.1×10^{-2}
CR-8	825	3.6×10^{-2}
CB-8	685	2.3×10^{-2}

5.7 Formulation of cosmetics

Owing to the superior properties of pigments synthesized using *S. trilobata* leaves extract, two cosmetic formulations were prepared using SR-12 and SB-12. The details of the cosmetic recipes are presented in Table 5.

Table 5. Cosmetic recipe of the formulations.

Formulation 1	Formulation 2
Bees wax - 2g	Bees wax- 2g
Coconut oil - 4ml	Coconut oil - 4ml
SR-12 - 0.01g	SB-12 - 0.01g
Vanilla essential oil - 0.2ml	Vanilla essential oil - 0.2ml

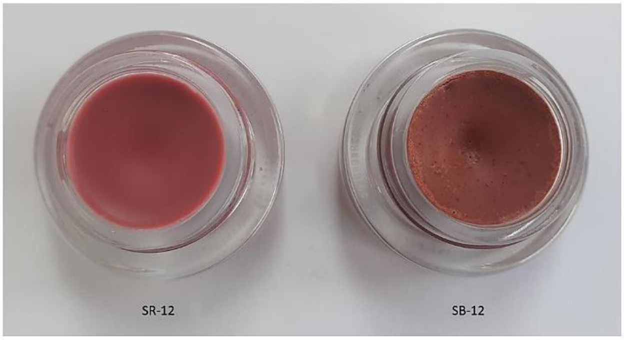

Fig.11 Cosmetics developed from *S. trilobata* derived pigments.

The formulations work as lip and cheek tints. The ingredients given in Table 4 were melted together in a double boiler. 0.2 ml of vanilla essential oil was added dropwise before solidification of the products for imparting freshness and flavor. Fig.11 displays the images of the formulated cosmetics. The tinting ability and spread ability of the formulation were physically verified to be satisfactory.

5.8 Summary

Phytoconjugated hematite and maghemite NPs were synthesized by mimicking metasomatic conditions through hydrothermal route using crude plant extracts. The exotic invasive flora was selected to prepare the phytoreagents to protect the native biodiversity in case of upscaling. The synthesized materials were characterized and screened for biological activities and toxicity. The studies revealed a promising combination of strong pigmentation along with antioxidant abilities. The research was then extended to the formulation of different lifestyle products. The in-vitro cytotoxicity analysis of the phytogenic iron oxide nanopigments revealed the nontoxic nature of the nanopigments and proved that these products can be safely used for cosmetic applications. It was noted that the pigments were of no harm to the skin microflora even at higher concentrations. The study indicates the possibility of using plant extracts as an effective and cheap alternative reagent for the preparation of antioxidant nanopigments.

- *The results of this chapter are reserved for patent filing.*

References

[1] Ali A, Zafar H, Zia M, ul Haq I, Phull AR, Ali JS, et al. Synthesis, characterization, applications, and challenges of iron oxide nanoparticles. Nanotechnol Sci Appl 2016;9:49–67. https://doi.org/10.2147/NSA.S99986.

[2] Exfoliation of hematite: Morphological, structural and magnetic investigations. Journal of Magnetism and Magnetic Materials 2022;542:168507. https://doi.org/10.1016/j.jmmm.2021.168507.

[3] Drits V, Środoń J, Eberl DD. XRD Measurement of Mean Crystallite Thickness of Illite and Illite/Smectite: Reappraisal of the Kubler Index and the Scherrer Equation. Clays Clay Miner 1997;45:461–75. https://doi.org/10.1346/CCMN.1997.0450315.

[4] Schimanke G, Martin M. In situ XRD study of the phase transition of nanocrystalline maghemite (γ-Fe2O3) to hematite (α-Fe2O3). Solid State Ionics 2000;136–137:1235–40. https://doi.org/10.1016/S0167-2738(00)00593-2.

[5] The formation mechanism of iron oxide nanoparticles within the microwave-assisted solvothermal synthesis and its correlation with the structural and magnetic properties - Dalton Transactions (RSC Publishing) n.d. https://pubs.rsc.org/en/content/articlelanding/2015/dt/c5dt03518j (accessed October 14, 2022).

[6] McElhinny MW, McFadden PL, editors. Chapter Two - Rock Magnetism. International Geophysics, vol. 73, Academic Press; 2000, p. 31–77. https://doi.org/10.1016/S0074-6142(00)80095-9.

[7] Ricci A, Olejar KJ, Parpinello GP, Kilmartin PA, Versari A. Application of Fourier Transform Infrared (FTIR) Spectroscopy in the Characterization of Tannins. Applied Spectroscopy Reviews 2015;50:407–42. https://doi.org/10.1080/05704928.2014.1000461.

[8] Rajiv P, Bavadharani B, Kumar MN, Vanathi P. Synthesis and characterization of biogenic iron oxide nanoparticles using green chemistry approach and evaluating their biological activities. Biocatalysis and Agricultural Biotechnology 2017;12:45–9. https://doi.org/10.1016/j.bcab.2017.08.015.

[9] Chowdhury SR, Yanful EK, Pratt AR. Chemical states in XPS and Raman analysis during removal of Cr(VI) from contaminated water by mixed maghemite–magnetite nanoparticles. Journal of Hazardous Materials 2012;235–236:246–56. https://doi.org/10.1016/j.jhazmat.2012.07.054.

[10] Hu J, Chen G, Lo IMC. Removal and recovery of Cr(VI) from wastewater by maghemite nanoparticles. Water Research 2005;39:4528–36. https://doi.org/10.1016/j.watres.2005.05.051.

[11] Yamashita T, Hayes P. Analysis of XPS spectra of Fe2+ and Fe3+ ions in oxide materials. Applied Surface Science 2008;254:2441–9. https://doi.org/10.1016/j.apsusc.2007.09.063.

[12] Zhao H, Zhu Q, Gao Y, Zhai P, Ma D. Iron oxide nanoparticles supported on pyrolytic graphene oxide as model catalysts for Fischer Tropsch synthesis. Applied Catalysis A: General 2013;456:233–9. https://doi.org/10.1016/j.apcata.2013.03.006.

[13] Bandara PC, Peña-Bahamonde J, Rodrigues DF. Redox mechanisms of conversion of Cr(VI) to Cr(III) by graphene oxide-polymer composite. Sci Rep 2020;10:9237. https://doi.org/10.1038/s41598-020-65534-8.

[14] Perron NR, Brumaghim JL. A Review of the Antioxidant Mechanisms of Polyphenol Compounds Related to Iron Binding. Cell Biochem Biophys 2009;53:75–100. https://doi.org/10.1007/s12013-009-9043-x.

[15] Mahdavi M, Ahmad MB, Haron MJ, Namvar F, Nadi B, Rahman MZA, et al. Synthesis, Surface Modification and Characterisation of Biocompatible Magnetic Iron Oxide Nanoparticles for Biomedical Applications. Molecules 2013;18:7533–48. https://doi.org/10.3390/molecules18077533.

[16] Deng J, Yang H, Capanoglu E, Cao H, Xiao J. 9 - Technological aspects and stability of polyphenols. In: Galanakis CM, editor. Polyphenols: Properties, Recovery, and Applications, Woodhead Publishing; 2018, p. 295–323. https://doi.org/10.1016/B978-0-12-813572-3.00009-9.

[17] Takahashi K, Tsunogae T, Ugwuonah EN. Fluid-induced high-temperature metasomatism at Rundvågshetta in the Lützow-Holm Complex, East Antarctica: Implications for the role of brine during granulite formation. Geoscience Frontiers 2018;9:1309–23. https://doi.org/10.1016/j.gsf.2017.11.010.

[18] Trommsdorff V, Skippen G. Metasomatism Involving Fluids in CO2-H2O-NaCl. In: Helgeson HC, editor. Chemical Transport in Metasomatic Processes, Dordrecht: Springer Netherlands; 1987, p. 133–52. https://doi.org/10.1007/978-94-009-4013-0_6.

[19] Aranovich LYa. The role of brines in high-temperature metamorphism and granitization. Petrology 2017;25:486–97. https://doi.org/10.1134/S0869591117050022.

[20] Manning CE, Aranovich LY. Brines at high pressure and temperature: Thermodynamic, petrologic and geochemical effects. Precambrian Research 2014;253:6–16. https://doi.org/10.1016/j.precamres.2014.06.025.

[21] Barton MD. ALTERNATIVE BRINE SOURCES FOR Fe-OXIDE(-Cu-Au) SYSTEMS: IMPLICATIONS FOR HYDROTHERMAL ALTERATION AND METALS n.d.:18.

[22] Bernal NF, Gleeson SA, Smith MP, Barnes JD, Pan Y. Evidence of multiple halogen sources in scapolites from iron oxide-copper-gold (IOCG) deposits and regional NaCl metasomatic alteration, Norrbotten County,

Sweden. Chemical Geology 2017;451:90–103. https://doi.org/10.1016/j.chemgeo.2017.01.005.

[23] Sheibi M, Mirnejad H, Moghaddam MP. Magnetic susceptibility anisotropy as a predictive exploration tool of metasomatic iron oxide deposits: Example from the Panj-Kuh iron ore body, NE Iran. Ore Geology Reviews 2016;72:612–28. https://doi.org/10.1016/j.oregeorev.2015.08.024.

CHAPTER 6

Phytogenic synthesis of nano aluminium sulphate coagulant for removal of congo red and fluoride from water

'Chemistry is all about getting lucky'

\- Robert Curl

A plethora of industries such as paper, leather, plastics, cosmetics, food, printing, pharmaceutical and textile both consume and contaminate gallons of water each day. Congo red, the selected dye for the present study is capable to release benzidine which on long-term exposure may increase the risk of cancer as per reported epidemiological studies. Coagulation is usually preferred in dye removal due to its ease of operation, high efficiency, and comparatively low cost. The process intends to destabilize the dissolved pollutant instantaneously (coagulation) using coagulants to form aggregates of small particles which can be removed upon settling.

Currently, over 7000 types of synthetic dyes are used by the paper, leather, ceramics, and textile industries. Despite the existence of stringent waste management policies, nearly 10% of the dyes are released into waterbodies during their production and use. Dye wastewater is characterized by deep colour, high toxicity, high chemical oxygen demand (COD) and biochemical oxygen demand (BOD) values, complex composition, large discharge, wide distribution, and difficult degradation[1]. Moreover, most synthetic dyes used in the textile industry contain azo functions often linked to an aromatic ring which makes them highly toxic, non-biodegradable, carcinogenic, and mutagenic for human and aquatic life[2,3]. Congo red, the selected dye for the present study is capable to release benzidine which on long-term exposure may increase the risk of cancer as per reported epidemiological studies[4–6]. Another contaminant discussed in this chapter, fluoride is known to cause teeth and skeletal fluorosis, crippling bone deformities, cancer and decreased cognitive ability upon prolonged ingestion in higher levels than recommended(>1ppm)[7,8]. Coagulation-flocculation methods are widely recognized and adopted owing to their simple operation, large processing capacity and low investment cost. This chapter presents the attempts undertaken to synthesize an efficient nanocoagulant from bulk aluminium sulphate using *Hemigraphis alternata* leaves extract. The chapter further discusses the potential of the obtained aluminium sulphate NPs to coagulate aqueous solutions of congo red and fluoride.

6.1 Synthesis

20mL of 0.55M aluminium sulphate solution was added dropwise to 25mL of the *H. alternata* leaf extract kept at room temperature. The system was stirred for 3 hours and kept overnight for aging. The aged mixture was then dried at 150°C and calcined at 600 and 1000°C for 2 hours. The obtained products were ground to fine powder for characterization and decontamination studies. The samples were named as AS-6 and AS-10.

6.2 Characterization

6.2.1 XRD and SAED analysis

The XRD profiles of the AS-6 and AS-10 are shown in Fig.1. The crystalline diffraction patterns obtained exactly similar to the bulk aluminium sulphate, with broader peaks, confirms the sample formed at 600°C to be aluminium sulphate NPs[9] The sharp peaks indicate a high crystallinity of the as-synthesized product. Diffraction patterns of AS-10 confirms the transformation of the sulphate precursor into γ-alumina phase having spinel lattice [JCPDS File no. 29-63] and pure crystalline nature at higher temperatures[10]. Moreover, the absence of additional diffractions reveals the formation of pure particles free from extract residues/binders. The average crystallite size calculated using Scherrer's equation was 13nm and 20 nm for AS-6 and AS-10. The SAED pattern of the products are displayed in Fig.2. The increased crystallinity attained at higher temperature is evident in the SAED monograph of AS-10.

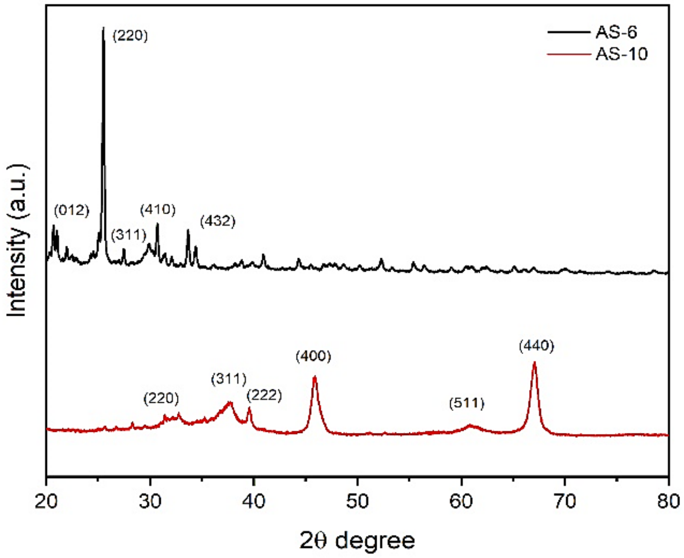

Fig.1. XRD patterns of AS-6 & AS-10

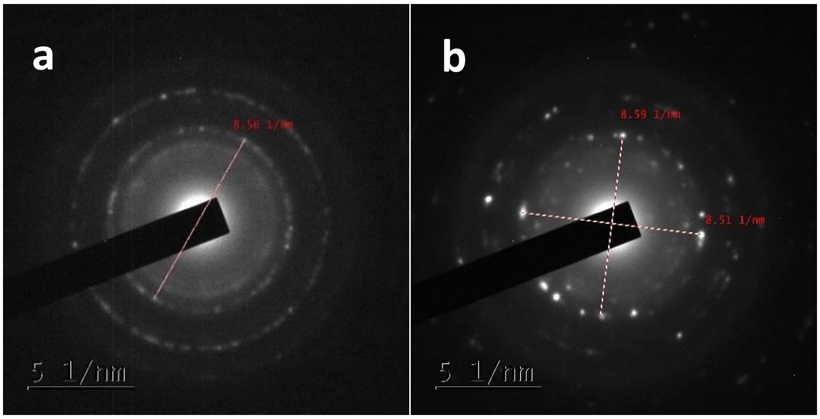

Fig.2. SAED patterns of a) AS-6 and b) AS-10

6.2.2 FTIR analysis

Phytoconstituents in *H. alternata* leaves include flavonoids, poly-phenols, tannin, alkaloids, steroids, xanthoprotein, carbohydrates and carboxylic acids[11,12]. They are believed to act as binders to facilitate the formation of metal/metal oxide NPs. FTIR studies were conducted to identify the composition and purity of the synthesized nanocoagulant. FTIR spectra of the AS-6 and AS-10 are displayed in Fig.3. The vibrational bands obtained around 3440 and 3016cm^{-1} are assigned to the –OH stretching vibrations and –OH bending vibrations appeared ~1685cm^{-1}. The sharp intense peak at 1150cm^{-1} and the peak around 978cm^{-1} were attributed to SO_4^{2-} stretching vibrations. The peak observed at around 689cm^{-1} was identified to be SO_4^{2-} bending vibrations [13,14]. The spectra devoid of any other characteristic vibrations imply the removal of binders and the absence of residues from the plant extract.

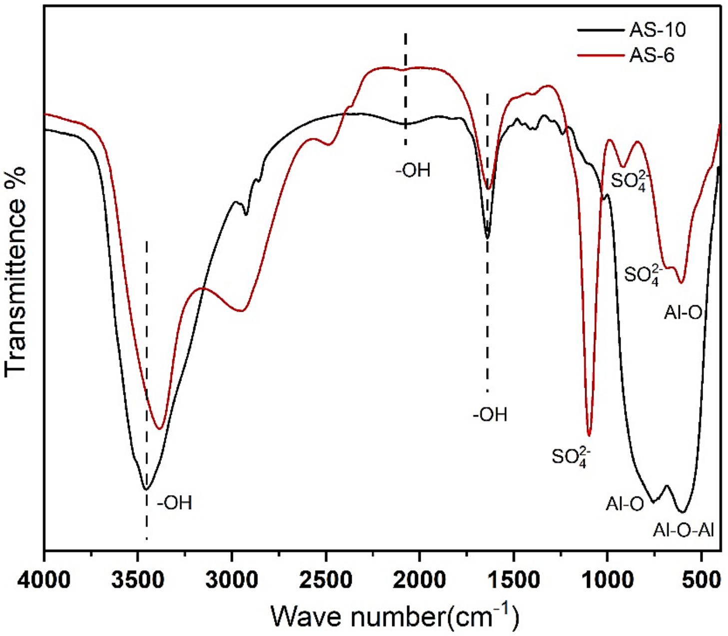

Fig.3. FTIR spectra of AS-6 & AS-10

6.2.3 Evolution of surface morphology

To identify the evolution of hierarchical structures on products the precursor and products calcined at different temperatures were examined using FESEM. The FESEM images of bulk precursor and the calcined products recorded are shown in Fig.4. Morphological changes to the precursor associated with the *H. alternata* leaf extract treatment was evident from the enhanced hierarchy of NPs. The FESEM micrographs of the precursor displayed solid abstract structures on the surface. Whereas the calcined products at 200 and 400°C showed developing web-like three dimensional structures. As the calcination temperature increased the surface of the product was observed to comprise popcorn- like particles (at 600°C) of assorted sizes. At temperature >800˚C the popcorn morphology starts to deteriorate, and tiny aggregates starts to appear extensively throughout the surface. The changes on the product surface can be attributed to the disintegration of phytoconjugates from the precursor with rising temperature.

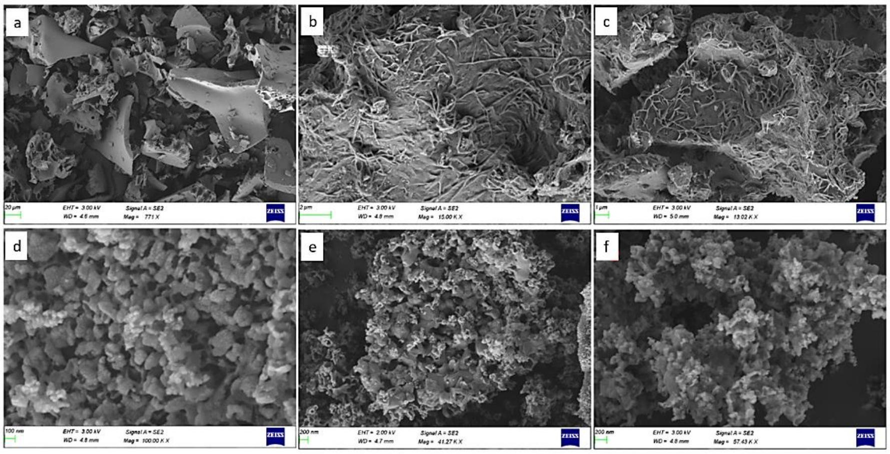

Fig.4. FESEM micrographs of, a) dried sample, samples calcined at b) 200°C c) 400°C d) 600°C (AS-6) e) 800°C and f)1000°C (AS-10)

The EDX profile of the crude precursor after drying, AS-6 and AS-10 are depicted in Fig 5. AS-6 spectra encounter the characteristic elemental peak line of Al (Kα1, Kβ1), O (Kα1) and sulphur (Kα, Kβ1, Lα) in 12.46%, 77.89%, and 9.65% atomic weight percentage respectively. The absence of other elemental peak lines, especially of carbon residues implies the sample purity of AS-6. The elemental composition details are displayed in table 1.

Table 1. Elemental composition of precursors, AS-6 and AS-10

Sample	Atomic wt %				
	Al	O	S	C	N
Precursor	5.46	65.8	10.35	12.74	5.65
AS-6	12.46	77.89	9.65	-	-
AS-10	29.66	70.34	-	-	-

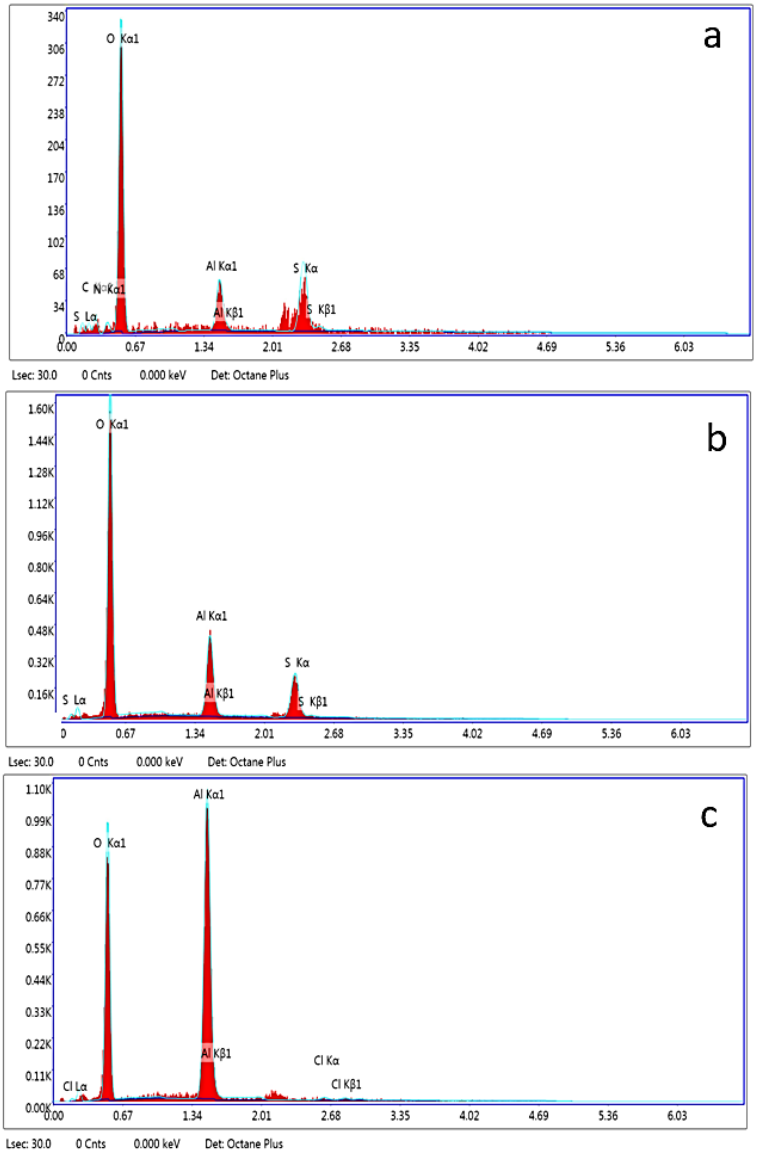

Fig.5.EDX spectra of a) dried AS, b) AS-6 and c) AS-10

To investigate further the morphology and size of the nanoparticles HR-TEM analysis was employed. HRTEM micrographs of AS-6 displayed a collection of polydispersed nearly spherical particles with average particle size ~17.4nm (Fig.6 a, b). Whereas AS-10 contained particles of irregular shapes with an average particle size of 23.3nm (Fig.6 d, e).

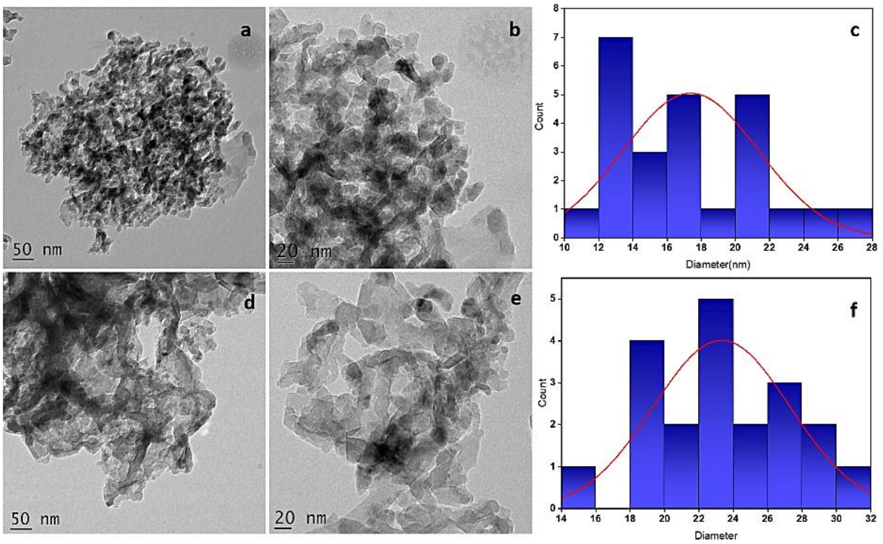

Fig.6. HRTEM images of a,b) AS-6, c) size distribution analysis of AS-6, d,e) HRTEM images of AS-10 and f) size distribution analysis of AS-10

The characterization studies confirmed that the product formed at 600 and 1000°C was aluminium sulphate NPs and γ-alumina NPs respectively. Phytochemicals in the leaf extract are incapable of facilitating the formation of aluminium oxide from the sulphate precursor at the lower temperature. This can be attributed to the mild reducing nature of phytochemicals in general towards a hard metal ion like Al^{3+}. Therefore, the probable mechanism of formation of AS-6 is through the recrystallisation of solvated bulk aluminium sulphate precursor in the phytochemical medium. In contrary to similar reports of green synthesis[15,16] where the phytoconstituents act as both reducing and capping agents in this study, the phytochemicals solely act as capping agents. This in turn resulted in efficient size reduction of the particles instigating the formation of the NPs.

6.3 Coagulation batch studies

6.3.1 Effect of coagulant dosage and initial concentration

The bulk aluminium sulphate, dried sample and the sample calcined at 400 °C was devoid of any visible coagulation ability. But the coagulation of congo red dye and fluoride solution by AS-6 was instantaneous. Initially, the efficiency of the pollutant removal increased with the addition of AS-6 eventually attaining complete coagulation. The solution encircling the flocs appeared clear on introducing the nanocoagulant of the optimum dose into the dye solution. The addition of the nanocoagulant past the optimum dosage did not result in any significant changes in the coagulation efficiency. This behaviour may be attributed to the increase in the number of cationic active sites in the solution with an increase in the coagulant dosage which in turn promotes destabilization through charge neutralisation [54]. The effect of initial concentration on coagulation efficiency was monitored for both contaminants (Table 2 & 3). The study revealed that there exists an ideal dosage for the coagulant corresponding to the concentration of the contaminant solution, below which the coagulation is incomplete. Incomplete coagulation was visible in case of congo red solution due to strong colour. The coagulation of congo red dye solution attained 99.5% efficiency at a dose of 140mgL^{-1} for 100mgL^{-1} dye solution of pH 7 at room temperature. Whereas 2.5mgL^{-1} of AS-6 removed 99.8% of 10mgL^{-1} of fluoride solution. These findings were set as standards for further set of experiments. AS-10 did not exhibit any coagulant activity towards congo red dye instead it displayed adsorptive removal towards the dye. However, 140mgL^{-1}(same dosage as AS-6) of AS-10 removed only 82.6% of dye from 100mgL^{-1} of dye solution in under 30 minutes, even under vigorous stirring (Fig.7). Also, it was noticed that the adsorptive ability decreased with an increase in the pH. Owing to the superior performance of AS-6 over AS-10 only the former was investigated further.

Table 2. Effect of initial concentration of congo red on optimum dosage and coagulation efficiency of ASNPs

Initial Concentration (ppm)	Coagulant Dosage (mg L^{-1})	Coagulation Efficiency %
50	60	92.46
	80	97.37
	100	99.59
	120	99.59
100	100	94.32
	120	97.47
	140	99.51
	160	99.54
150	240	95.35
	260	97.11
	280	99.52
	300	99.60
200	340	94.15
	360	95.93
	380	99.67
	400	99.79

Table 3. Effect of initial concentration of fluoride on optimum dosage and coagulation efficiency of ASNPs

Initial Concentration (ppm)	Coagulant Dosage (mg L^{-1})	Coagulation Efficiency %
5	0.5	90.36
	1.0	99.71
	1.5	99.68
10	1.5	92.78
	2.0	93.47
	2.5	99.81
	3.0	99.83
15	1.5	87.41
	2.0	94.85
	2.5	99.75
	3.0	99.68
20	3.0	79.35
	3.5	96.87
	4.0	99.62
	4.5	99.85

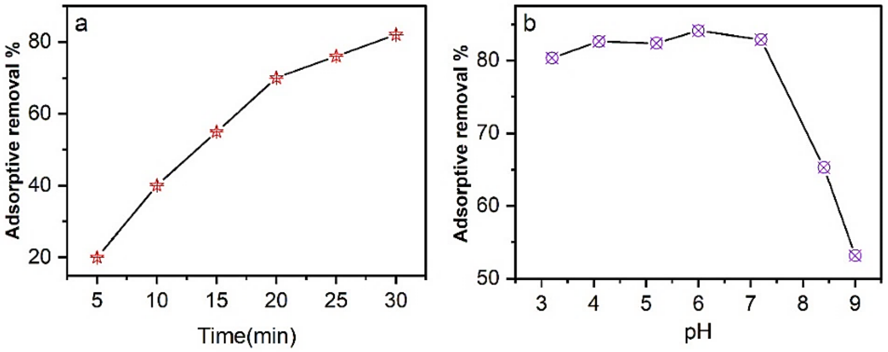

Fig.7. a) Adsorptive removal of congo red by AS-1, b) adsorptive performance of AS-10 with pH.

The synthesis strategy was repeated on chloride and nitrate salts of aluminium using the same plant extract. The samples calcined at 600°C, AC-6 & AN-6, represented recrystallized nanoform of the bulk precursor whereas calcination at higher temperature yielded alumina NPs, AC-10 & AN-10 (Fig.8.). This confirmed that the *H. alternata* leaves extract are incapable of reducing aluminium. The samples were tested against organic/inorganic water contaminants for possible coagulation properties but in vain. The samples reacted with Ferron reagent with no specific complexation indicating the absence of active Al-coagulant species. Whereas addition of AS-6 to Ferron reagent displayed instant complexation due to the presence of mono/di/oligomeric hydrolysed Al-species capable of triggering coagulation[17]. AC-10 and AN-10 displayed mild adsorption activity (<52%) towards congo red however, removal capacity was much lower than the removal percentage of AS-6 and was discarded.

6.3.2 Effect of pH and temperature

The pH of the contaminant solution is a major factor in determining the efficacy of a coagulant[18]. The efficiency of the nanocoagulant towards both pollutants under varying pH was hence estimated. 0.25molL^{-1} HCl and 0.25 molL^{-1} NaOH was used to adjust the pH accordingly. The experiments revealed that within the investigated range the influence of pH on the efficiency of the nanocoagulant is negligible (Fig.8a,9a). The plot also depicts the trend of residual turbidity of the dye solution with a change in pH for congo red solution. Zeta potential analysis detected a surface charge of 7 mV on the nanocoagulant at neutral pH. This cationic surface facilitates instant electrostatic attraction of the anionic pollutants on to the surface ultimately leading to charge neutralization. The introduction of hydrogen and hydroxyl ions in the tested range do not interfere with the interaction between cationic nanocoagulant and anionic contaminants probably owing to the amphoteric nature of hydrolysed Al species. The effect of temperature on the efficiency of the nanocoagulant was investigated and it was found that the temperature variations do not influence the coagulation efficiency of AS-6 (Fig.8b & 9b). Therefore, it was inferred that the synthesized nanocoagulant does not undergo any compositional changes during temperature rise and provides consistent removal efficiency.

6.3.3 Effect of interfering anions

All the experiments were conducted using tap water which may contain several inorganic ions and organic matter. But to detect any specific intervention by inorganic ions, the effect of sulphate, sulphite, nitrate, nitrite, chloride, and bromide ions on the efficiency of the nanocoagulant was investigated. Equimolar solutions of the chosen anions were prepared for the purpose, coagulant dosage and other experimental conditions were kept the same. Fig.8c & 9c concludes that these ions have no significant influence on coagulation efficiency of the nanocoagulant. Therefore, it can be proposed that Na^+ and K^+ cations and SO_4^{2-}, SO_3^{2-}, NO_3^-, NO_2^-, Cl^- and Br^- anions do not interfere with the coagulation of the selected contaminants by AS-6.

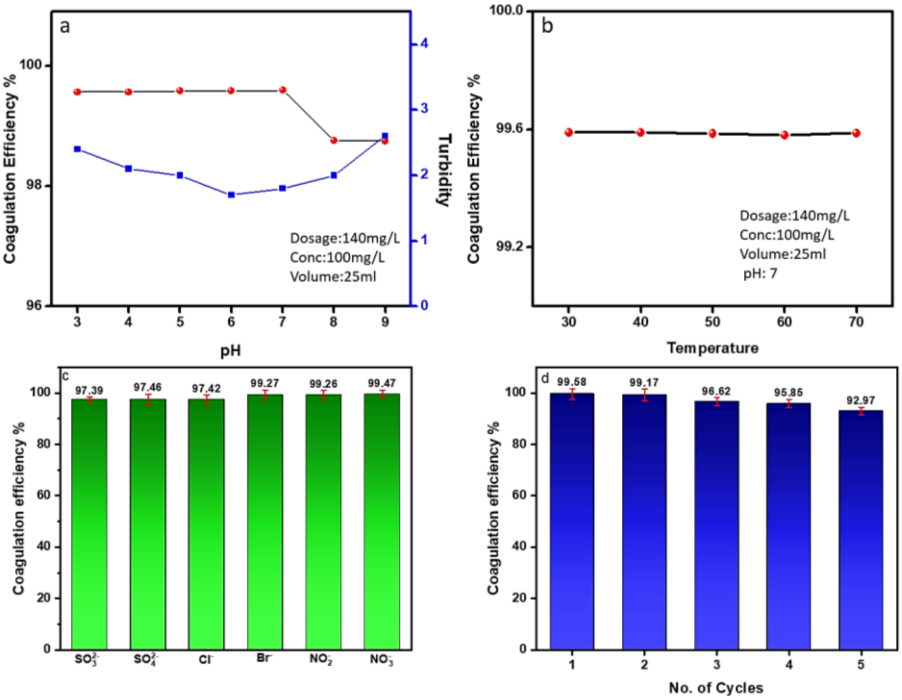

Fig.8. Coagulation of congo red a) with pH, b) with temperature, c) interfering anions and d) recycling ability of AS-6

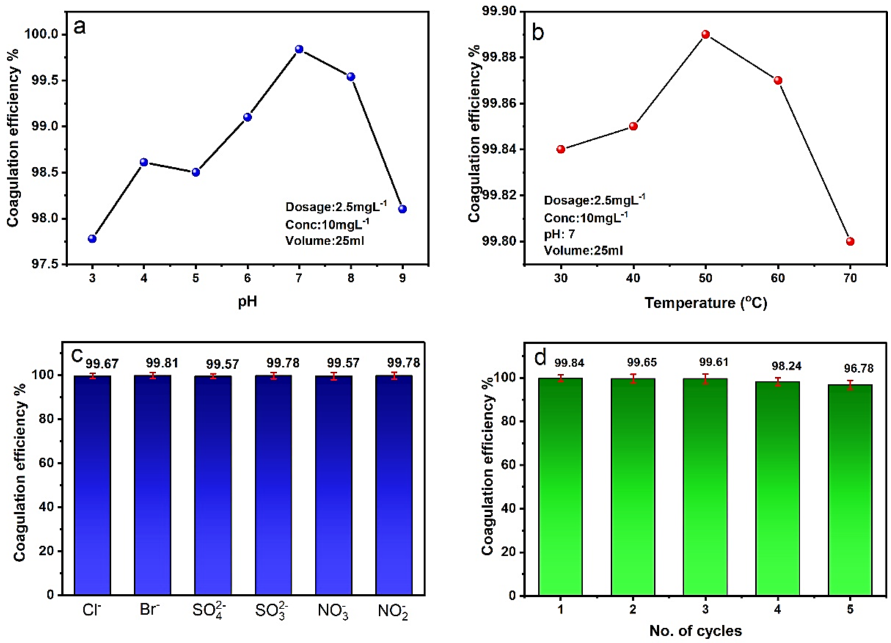

Fig.9. Coagulation of fluoride a) with pH, b) with temperature, c) interfering anions and d) recycling ability of AS-6.

6.3.4 Sedimentation, sludge characteristics and recyclability

The settling time required for complete sedimentation after coagulation was monitored. It was observed that under optimum conditions the flocs formed were considerably thick and consequently, settled faster. The microscopic images of flocs formed at optimal dosage, reveal substantial floc population promoting fast sedimentation (Fig.10). The period after which the sludge volume and coagulation efficiency remained constant was taken as the optimum settling period, which in this case was 30 and 10 minutes for congo red and fluoride respectively. At this point, the separation between the treated clear supernatant solution and the settled sludge becomes evident. The increased surface area attained through size reduction may have resulted in the exposure of more cationic active sites forcing the anionic pollutants in the solution to coagulate without an external flocculant aid thus accelerating the entire process. The inherent tendency of nanoparticles to agglomerate might have supported the effective flocculation within a short period.

The sludge volume index (SVI) less than 80mLg^{-1}represent a good sludge and a value around 50mLg^{-1}indicates a very good sludge. An SVI greater than 120mLg^{-1} indicates poor settling characteristics[19]. The low dosage of the nanocoagulant used, aided in the significant reduction of sludge generation. The SVI was found to be 31 and 16mLg^{-1} for congo red and fluoride solutions respectively. Lower SVI values indicate appreciable settling ability of the sludge. It was found that with increasing initial concentration, SVI value also increased. Coagulants with low SVI values are preferred for industrial applications as they offer easy sludge management.

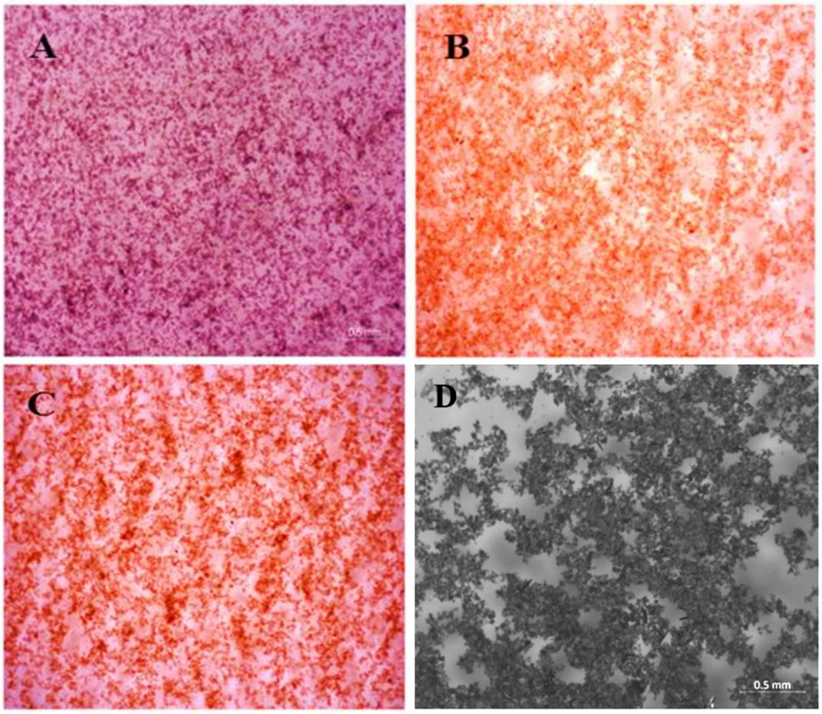

Fig.10. Microscopic images of flocs from congo red at A) acidic B) neutral, C) alkaline, and D) fluoride in neutral solution

The dried sludge of congo red (AS-6/CR) and fluoride (AS-6/F) was characterized using FTIR, FESEM and HRTEM techniques. The presence of inherent peaks along with peaks characteristic of the pollutant in the FTIR spectra confirms the conjugation of the pollutant on the surface of AS-6 (Fig.11). Both coagulated samples possessed peaks at ~3385,1634 and 610cm^{-1} pertaining to AS-6. The peaks at ~2848,2369 and 1200cm^{-1} in AS-6/CR confirms the presence of the dye on AS-6 surface. Such prominent peaks corresponding to fluoride are absent in AS-6/F owing to the lower concentration of the sample solution. The FESEM images of the sludge revealed drastic morphological changes after the extensive deposition of the pollutant masking the AS-6's surface (Fig.12 a-c). The HRTEM images of the dried sludge displayed in Fig.12 d-f reveals the amorphous nature of the sludge formed.

To evaluate the reusability of the nanocoagulant for practical applications the recycled AS-6 were tested using fresh congo red/fluoride solutions. The coagulation experiments were repeated for five cycles using the recycled coagulant. It was observed that the coagulation efficiency of the synthesized nanocoagulant was retained even after five cycles (Fig.8d & 9d). A trivial reduction in the efficiency may be correlated to the loss of coagulant during the repeated washing and drying processes.

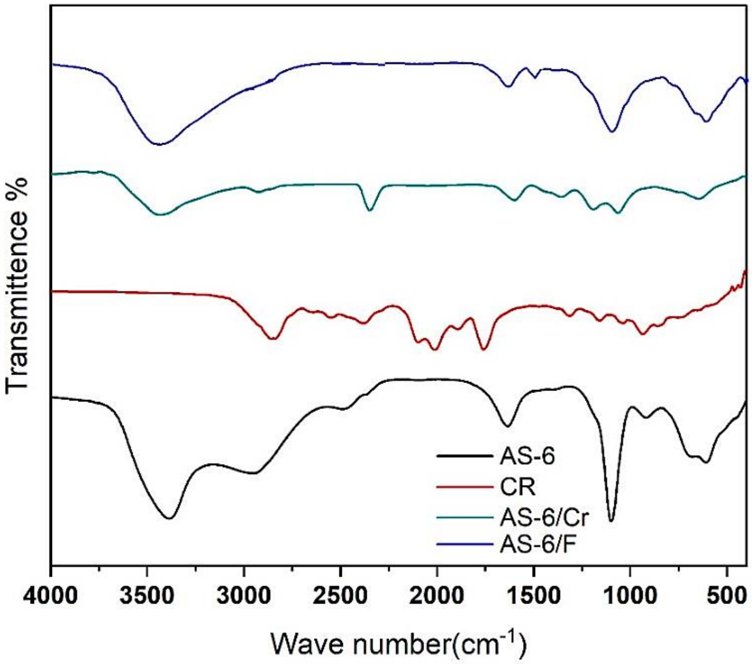

Fig. 11. FTIR spectra of sludge

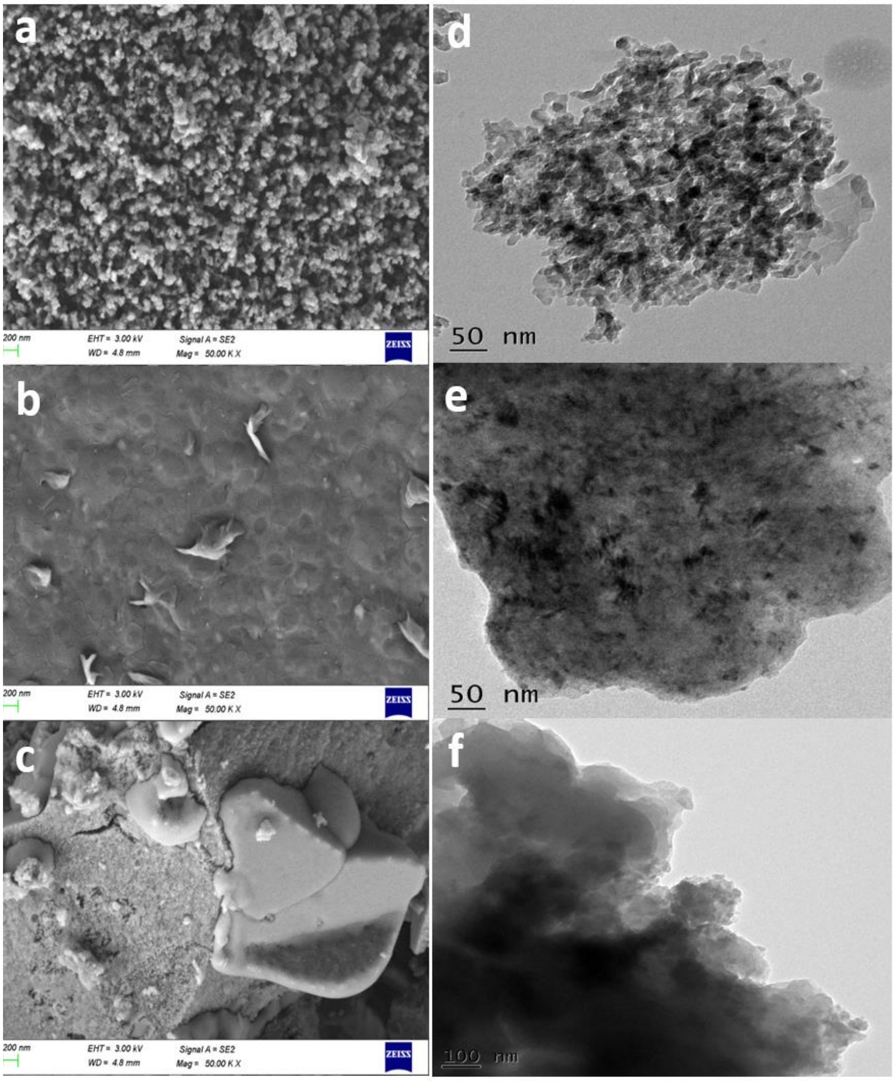

Fig.12. FESEM image of a) AS-6, b) AS-6/CR and c) AS-6/F and HRTEM images of d) AS-6, e) AS-6/CR and f) AS-6/F

6.3.5 Coagulation mechanism

For practical applications, the efficiency of a chemical substance to destabilize and coagulate targeted particles is the result of a combination of several mechanisms[19-21]. Fig.13 shows a schematic representation of the coagulation/flocculation process by AS-6. AS-6 hydrolyses and produces cationic mononuclear hydroxy aluminium complexes (Al^{3+}, $Al(OH)^{2+}$,$Al(OH)_2^+$ and $Al(OH)_4$) and primary aggregates($Al_2(OH)_2^{4+}$, $Al_2(OH)_5^+$ and $Al_3(OH)_8^+$, etc.) which are responsible for the event of coagulation[17]. The coagulation is assumed to be triggered by adsorption of anionic pollutant molecules on the cationic surface of AS-6 followed by charge neutralization. The swelling of the nanocoagulant helps in holding the complex structure of congo red dye molecules and large fluoride anion thus making it available for the charge neutralization process. Then, the cationic Al species rapidly bridges the anionic pollutant molecules and aids in flocculation. The surface of the nanocoagulant abundant with cationic active sites sufficiently neutralizes the less charged pollutant species. Once the charge neutralization is complete, van der Waal's forces take over and initiates coalescence of molecules. Initial coagulation results in formation of mesh like frames around the coagulant particle. The nanocoagulant particles entrapped in these frames cause more coagulation of the dye/fluoride molecules producing larger aggregates like sweep flocs. The process continues, and more dye molecules get trapped in this enmeshment. Moreover, the nano size of the coagulant induces self-assembly to form larger aggregates that facilitate bridging among molecules. As the bridging progresses, larger molecules cumulate at each active site causing complete and instantaneous coagulation of the pollutant solution. The negligible variations in the coagulation efficiency of the nanocoagulant under different conditions suggest that the coagulation properties are results of surface-to-surface physical interactions. Rapid flocculation and settling behaviour of AS-6 without any flocculant aids confirm high aggregation capacity of the nanocoagulant.

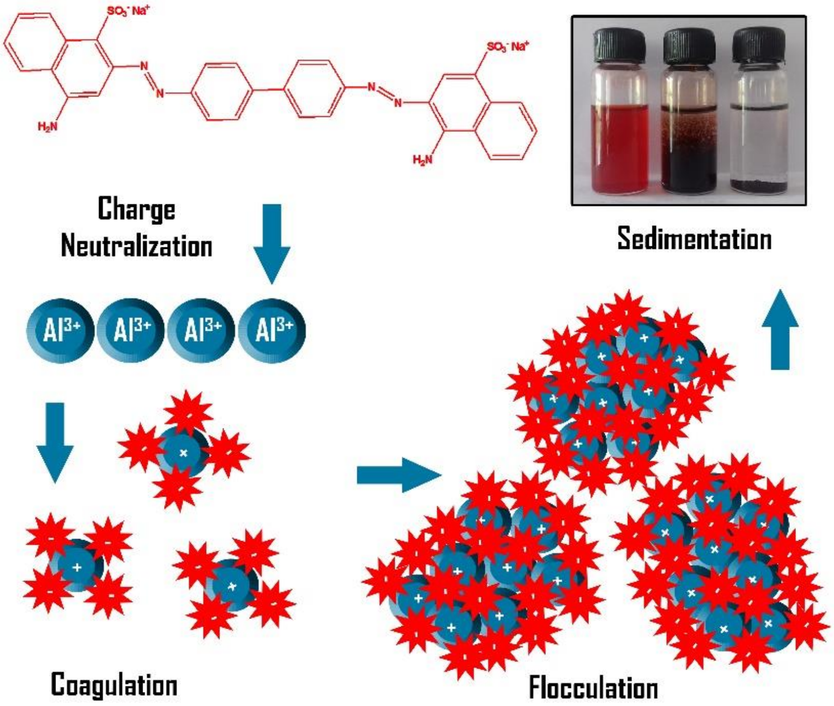

Fig.13. Schematic representation of the coagulation and flocculation process by AS-6

6.4 Summary

Phytogenic aluminium sulphate NPs were synthesized with an average dimension of ~17.4nm employing *H. alternata* leaf extract through dry combustion followed by calcination. The prepared sample was employed as a nanocoagulant for the removal of hazardous congo red dye and high fluoride content from aqueous solutions. The coagulation of congo red dye solution attained 99.5% efficiency at a dose of 140mgL^{-1} for 100mgL^{-1} dye solution of pH 7 at room temperature. Whereas 2.5mgL^{-1} of AS-6 removed 99.8% of 10mgL^{-1} of fluoride solution. The coagulation efficiency was found to be consistent with the changes in pH and temperature. The presence of various ions (Na$^+$ and K$^+$ cations and SO_4^{2-}, SO_3^{2-}, NO_3^-, NO_2^-, Cl$^-$ and Br$^-$ anions) did not interfere the coagulation efficiency of the material.

The AS-6 also displayed high coagulation efficiency and rapid settling ability. The sludge produced is less and thermally decomposable. The coagulant can be reused up to five cycles with negligible compromise in the efficiency. Thus, phytogenic AS-6 is a promising candidate for the removal of congo red and fluoride in terms of cost efficiency, low dose, high coagulation efficiency, sludge management, and shelf life. The novel synthesis route adapted also lights up the sparsely investigated area of phytogenic synthesis of $Al_2(SO_4)_3$/ Al_2O_3 NPs, its possibilities, and challenges.

- *The results presented in this chapter is partially published in Materials Chemistry and Physics.*

References

[1] Yusuf M. Synthetic Dyes: A Threat to the Environment and Water Ecosystem. Textiles and Clothing, John Wiley & Sons, Ltd; 2019, p. 11–26. https://doi.org/10.1002/9781119526599.ch2.

[2] Pinheiro HM, Touraud E, Thomas O. Aromatic amines from azo dye reduction: status review with emphasis on direct UV spectrophotometric detection in textile industry wastewaters. Dyes and Pigments 2004;61:121–39. https://doi.org/10.1016/j.dyepig.2003.10.009.

[3] Chung K-T. Azo dyes and human health: A review. Journal of Environmental Science and Health, Part C 2016;34:233–61. https://doi.org/10.1080/10590501.2016.1236602.

[4] Afkhami A, Moosavi R. Adsorptive removal of Congo red, a carcinogenic textile dye, from aqueous solutions by maghemite nanoparticles. Journal of Hazardous Materials 2010;174:398–403. https://doi.org/10.1016/j.jhazmat.2009.09.066.

[5] Hairom NHH, Mohammad AW, Kadhum AAH. Influence of zinc oxide nanoparticles in the nanofiltration of hazardous Congo red dyes. Chemical Engineering Journal 2015;260:907–15. https://doi.org/10.1016/j.cej.2014.08.068.

[6] Gray LE, Ostby JS, Kavlock RJ, Marshall R. Gonadal effects of fetal exposure to the azo dye Congo red in mice: Infertility in female but not male offspring. Fundamental and Applied Toxicology 1992;19:411–22. https://doi.org/10.1016/0272-0590(92)90180-P.

[7] Yadav KK, Kumar S, Pham QB, Gupta N, Rezania S, Kamyab H, et al. Fluoride contamination, health problems and remediation methods in Asian groundwater: A comprehensive review. Ecotoxicology and Environmental Safety 2019;182:109362. https://doi.org/10.1016/j.ecoenv.2019.06.045.

[8] Ali S, Thakur SK, Sarkar A, Shekhar S. Worldwide contamination of water by fluoride. Environ Chem Lett 2016;14:291–315. https://doi.org/10.1007/s10311-016-0563-5.

[9] Garvasis J, Prasad AR, Shamsheera KO, Jaseela PK, Joseph A. Efficient removal of Congo red from aqueous solutions using phytogenic aluminum sulfate nano coagulant. Materials Chemistry and Physics 2020;251:123040. https://doi.org/10.1016/j.matchemphys.2020.123040.

[10] Parida KM, Pradhan AC, Das J, Sahu N. Synthesis and characterization of nano-sized porous gamma-alumina by control precipitation method. Materials Chemistry and Physics 2009;113:244–8. https://doi.org/10.1016/j.matchemphys.2008.07.076.

[11] Annapoorna M, Sudheesh Kumar PT, Lakshman LR, Lakshmanan V-K, Nair SV, Jayakumar R. Biochemical properties of Hemigraphis alternata incorporated chitosan hydrogel scaffold. Carbohydrate Polymers 2013;92:1561–5. https://doi.org/10.1016/j.carbpol.2012.10.041.

[12] Adangampurath S, Sudhakaran S. Antiinflammatory potential of flavonoids from Hemigraphis colorata. Int J of Life Sciences 2018;6:569–74.

[13] Frost RL, Xi Y, Scholz R, López A, Granja A. Infrared and Raman spectroscopic characterisation of the sulphate mineral creedite – Ca3Al2SO4(F,OH)·2H2O – and in comparison with the alums. Spectrochimica Acta Part A: Molecular and Biomolecular Spectroscopy 2013;109:201–5. https://doi.org/10.1016/j.saa.2013.02.029.

[14] Frost RL, López A, Scholz R, Wang L. A Raman and infrared spectroscopic study of the sulphate mineral aluminite Al2(SO4)(OH)4·7H2O. Spectrochimica Acta Part A: Molecular and Biomolecular Spectroscopy 2015;148:232–6. https://doi.org/10.1016/j.saa.2015.04.011.

[15] Prasad AR, Garvasis J, Oruvil SK, Joseph A. Bio-inspired green synthesis of zinc oxide nanoparticles using Abelmoschus esculentus mucilage and selective degradation of cationic dye pollutants. Journal of Physics and Chemistry of Solids 2019;127:265–74. https://doi.org/10.1016/j.jpcs.2019.01.003.

[16] Suresh J, Pradheesh G, Alexramani V, Sundrarajan M, Hong SI. Green synthesis and characterization of zinc oxide nanoparticle using insulin plant (Costus pictus D. Don) and investigation of its antimicrobial as well as anticancer activities. Adv Nat Sci: Nanosci Nanotechnol 2018;9:015008. https://doi.org/10.1088/2043-6254/aaa6f1.

[17] Zhou W, Gao B, Yue Q, Liu L, Wang Y. Al-Ferron kinetics and quantitative calculation of Al(III) species in polyaluminum chloride coagulants. Colloids and Surfaces A: Physicochemical and Engineering Aspects 2006;278:235–40. https://doi.org/10.1016/j.colsurfa.2005.12.024.

[18] Li H, Liu S, Zhao J, Feng N. Removal of reactive dyes from wastewater assisted with kaolin clay by magnesium hydroxide coagulation process. Colloids and Surfaces A: Physicochemical and Engineering Aspects 2016;494:222–7. https://doi.org/10.1016/j.colsurfa.2016.01.048.

[19] Oladoja NA, Aliu YD. Snail shell as coagulant aid in the alum precipitation of malachite green from aqua system. Journal of Hazardous Materials 2009;164:1496–502. https://doi.org/10.1016/j.jhazmat.2008.09.114.

[20] Liu B, Zheng H, Wang Y, Chen X, Zhao C, An Y, et al. A novel carboxyl-rich chitosan-based polymer and its application for clay flocculation and cationic dye removal. Science of The Total Environment 2018;640–641:107–15. https://doi.org/10.1016/j.scitotenv.2018.05.309.

[21] Lam S-M, Low X-ZD, Wong K-A, Sin J-C. Sequencing coagulation–photodegradation treatment of Malachite Green dye and textile wastewater through ZnO micro/nanoflowers. Chemical Engineering Communications 2018;205:1143–56. https://doi.org/10.1080/00986445.2018.1434163

Outlook

Nothing in life is to be feared, it is only to be understood.
Now is the time to understand more, so that we may fear less.

\- Marie Curie

Weed control is an expensive annual ritual around the globe. Kerala, known for its wide array of flora and fauna, has been facing extreme climatic events recently. The recurring landslides and floods have led to the introduction/re-introduction of various alien invasive flora disturbing the native biodiversity and ecological services. Weed control includes laborious physical, chemical, and biological methods of eliminating the whole/parts of the plant from the affected area. Another major concern rising at alarming pace is the increased contamination of water resources. Synthetic colorants, heavy metal ions, micro/nanoplastics, leached pesticides and other inorganic pollutants restrict access to clean drinking water for our future generations. Development of efficient, economical, and sustainable water treatment strategies are in high demand than ever.

The thesis has presented a sustainable approach connecting weed control with nanomaterial engineering and water remediation. The synthesized nanoparticles show promising results in removal of HMI (CMNs & SMNs) and other water pollutants (AS-6). The cost effectiveness, efficiency and recyclability of these materials call for extensive research on utilizing more invasive species found in the State for synthesis. Based on results of the study and current reports on water and soil pollution, the research can be extended to the following,

1. Investigation of AS-6 as an alternative for alum in water treatment sector to remove natural organic substances.
2. Exploring the coagulating properties of AS-6 towards hazardous pollutants like micro and nanoplastics in fresh water and in marine environment.
3. Incorporation of IONPs into AS-6 to magnetize the latter and to study the effect of Fe composition on coagulation properties.
4. Possible manipulation of IONPs surface so that it can be used as a sink for several HMIs.
5. Unlike many reports, CMN-8 & SMN-12 shows very fast adsorption towards HMIs, which suggest a possibility of employing these materials as electrochemical sensors for detecting HMIs
6. Identifying more AIS in the State to synthesize IONPs and to establish a mechanism for the binding of iron with phytochemicals with the help of computational techniques.
7. The synthesis method can be modified by replacing the crude phytoextract with isolated flavonoids or other economic biomolecules to produce SPIONs which can be tested for biomedical applications like MRI contrast agent and hyperthermia.

LIST OF PUBLICATIONS & PRESENTATIONS

Garvasis J, Prasad AR, Shamsheera KO, Roy TN, Joseph A. A facile one-pot synthesis of phyto-conjugate superparamagnetic magnetite nanoparticles for the rapid removal of hexavalent chromium from water bodies. Materials Research Bulletin. 2022 Dec 17:112130.

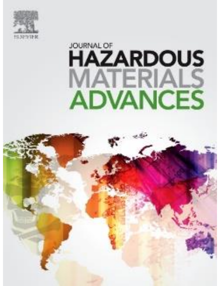

Garvasis J, Prasad AR, Shamsheera KO, Roy TN, Joseph A. Weed to nano seeds: Ultrasonic assisted one-pot fabrication of superparamagnetic magnetite nano adsorbents from Siam weed flower extract for the removal of lead from water. Journal of Hazardous Materials Advances. 2022 Nov 1;8:100163.

Garvasis J, Prasad AR, Shamsheera KO, Jaseela PK, Joseph A. Efficient removal of Congo red from aqueous solutions using phytogenic aluminum sulfate nano coagulant. Materials Chemistry and Physics. 2020 Sep 1;251:123040.

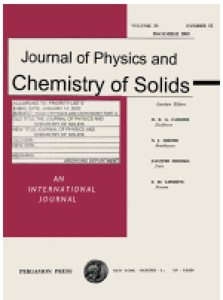

Prasad AR, Garvasis J, Oruvil SK, Joseph A. Bio-inspired green synthesis of zinc oxide nanoparticles using Abelmoschus esculentus mucilage and selective degradation of cationic dye pollutants. Journal of Physics and Chemistry of Solids. 2019 Apr 1;127:265-74.

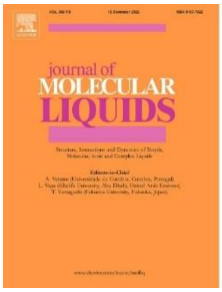

Jaseela PK, Garvasis J, Joseph A. Selective adsorption of methylene blue (MB) dye from aqueous mixture of MB and methyl orange (MO) using mesoporous titania (TiO_2)-poly vinyl alcohol (PVA) nanocomposite. Journal of Molecular Liquids. 2019 Jul 15;286:110908.

Prasad AR, Williams L, Garvasis J, Shamsheera KO, Basheer SM, Kuruvilla M, Joseph A. Applications of phytogenic ZnO nanoparticles: A review on recent advancements. Journal of Molecular Liquids. 2021 Jun 1;331:115805.

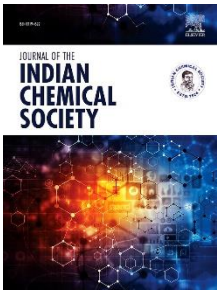

Prasad AR, Sowmya P, Garvasis J, Joseph A. Gamma-ray induced thermoluminescence emission of green synthesized zinc oxide nanophosphors. Journal of the Indian Chemical Society. 2021 Oct 1;98(10):100153.

KO S, Prasad AR, Garvasis J, Basheer SM, Joseph A. Stearic acid grafted chitosan/epoxy blend surface coating for prolonged protection of mild steel in saline environment. Journal of Adhesion Science and Technology. 2019 Oct 18;33(20):2250-64.

Erandapurathukadumana Sreedharan H, Cherukara Chellappan H, Selvanesan P, Garvasis J. Quorum sensing mediated response of Achromobacter denitrificans SP1 towards prodigiosin production under phthalate stress. Journal of basic microbiology. 2020 Sep;60(9):758-67.

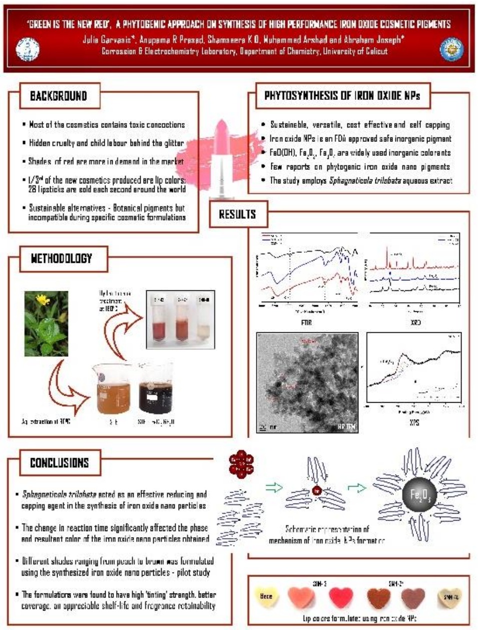

'GREEN IS THE NEW RED', A PHYTOGENIC APPROACH ON SYNTHESIS OF HIGH PERFORMANCE IRON OXIDE COSMETIC PIGMENTS

Julia Garvasis*, Anupama R Prasad, Shamseera K O, Muhammed Arshad and Abraham Joseph*
Corrossion & Electrochemistry Laboratory, Department of Chemistry, University of Calicut

BACKGROUND

- Most of the cosmetics contains toxic concoctions
- Hidden cruelty and child labour behind the glitter
- Shades of red are more in demand in the market
- 1/3rd of the new cosmetics produced are lip colors: 28 lipsticks are sold each second around the world
- Sustainable alternatives - Botanical pigments but incompatible during specific cosmetic formulations

PHYTOSYNTHESIS OF IRON OXIDE NPs

- Sustainable, versatile, cost effective and self capping
- Iron oxide NPs is an FDA approved safe inorganic pigment
- FeO(OH), Fe_2O_3, Fe_3O_4 are widely used inorganic colorants
- Few reports on phytogenic iron oxide nano pigments
- The study employs *Sphagneticola trilobata* aqueous extract

METHODOLOGY

RESULTS

FTIR

XRD

HR TEM

XPS

CONCLUSIONS

- *Sphagneticola trilobata* acted as an effective reducing and capping agent in the synthesis of iron oxide nano particles
- The change in reaction time significantly affected the phase and resultant color of the iron oxide nano particles obtained
- Different shades ranging from peach to brown was formulated using the synthesized iron oxide nano particles - pilot study
- The formulations were found to have high 'tinting' strength, better coverage, an appreciable shelf-life and fragrance retainability

Schematic representation of mechanism of iron oxide NPs formation

Lip colors formulated using iron oxide NPs

'Green Is The New Red', A Phytogenic Approach on Synthesis of High-Performance Iron Oxide Cosmetic Pigments

Julia Garvasis*, Anupama R Prasad, Shamseera K O, Muhammed Arshad and Abraham Joseph*

Frontiers in Chemical Sciences (FCS 2022), Department of Chemistry, University of Calicut

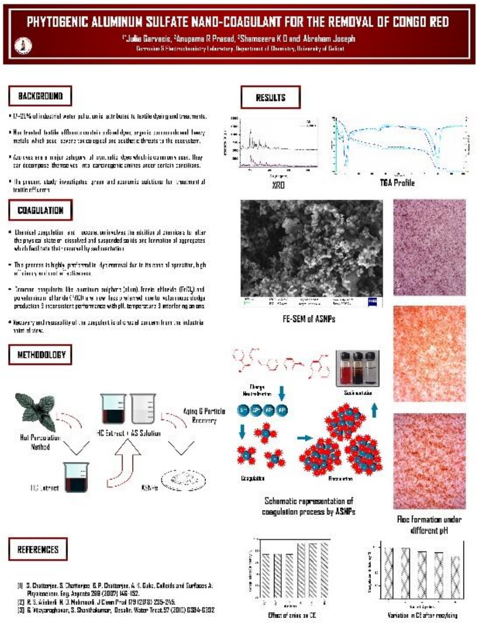

PHYTOGENIC ALUMINUM SULFATE NANO-COAGULANT FOR THE REMOVAL OF CONGO RED

[1]*Julia Garvasis, [2]Anupama R Prasad, [3]Shamseera K O and Abraham Joseph
Corrosion & Electrochemistry Laboratory, Department of Chemistry, University of Calicut

BACKGROUND

COAGULATION

METHODOLOGY

RESULTS

XRD

TGA Profile

FE-SEM of ASNPs

Schematic representation of coagulation process by ASNPs

Floc formation under different pH

Effect of anion on CE

Variation in CE after recycling

REFERENCES

[1] S. Chatterjee, S. Chatterjee, B. P. Chatterjee, A. K. Guha, Colloids and Surfaces A: Physicochem. Eng. Aspects 299 (2007) 146-152.
[2] R. S. Alisbefi, N. O. Mahmoodi, J Clean Prod 179 (2018) 235-245.
[3] G. Vijayaraghavan, S. Shanthakumar, Desalin. Water Treat.57 (2016) 6384-6392

Phytogenic Aluminum Sulfate Nano-Coagulant for The Removal of Congo Red

Julia Garvasis*, Anupama R Prasad, Shamseera K O and Abraham Joseph*

Frontiers in Chemical Sciences (FCS 2019), Department of Chemistry, University of Calicut

- Won 1st Prize